UNIVERSITY OF OKLAHOMA

GRADUATE COLLEGE

# POLARIMETRIC AND RAPID-SCAN RADAR OBSERVATIONS OF TORNADOES

A DISSERTATION

SUBMITTED TO THE GRADUATE FACULTY

in partial fulfillment of the requirements for the

Degree of

DOCTOR OF PHILOSOPHY

By

CASEY BENJAMIN GRIFFIN
Norman, Oklahoma
2019

POLARIMETRIC AND RAPID-SCAN RADAR OBSERVATIONS OF TORNADOES

A DISSERTATION APPROVED FOR THE
SCHOOL OF METEOROLOGY

BY

Dr. Robert D. Palmer, Chair

Dr. David J. Bodine, Co-Chair

Dr. Caleb J. Fulton

Dr. Guifu Zhang

Dr. Phillip B. Chilson

## Acknowledgments

First and foremost, I'd like to thank my wife Suzanne whose love and support helped me get through all of the difficult stretches of this journey. You sacrificed much so that I could achieve this degree and I will spend my whole life in your debt. Second, I'd like to thank my co-Chair and advisor Dr. David Bodine who painstakingly helped me become a better scientist and on countless occasions over the last four years put aside his own work to prioritize my growth and success. But, even more importantly, your friendship and kindness far exceeds your exemplary mentorship and I'll value your friendship long beyond the years of my scientific career. Third, I'd like to thank my advisor and Chair Dr. Bob Palmer who provided me with the once-in-a-lifetime opportunity to study and work at the Advanced Radar Research Center. I'm exceptionally fortunate to work for you and am grateful that you took a chance on me. You have been an amazing model of leadership and professionalism to which I can only hope and aspire to replicate in my career. I'd also like to thank my committee members, Drs. Guifu Zhang, Phillip Chilson, and Caleb Fulton who have selflessly volunteered their expertise and time to guide me through my final years as a student. I could not have asked for a better group of mentors to shepherd me through this rigorous task. In addition to my committee members Drs. David Bodine, Bob Palmer, and Caleb Fulton, I'd like to thank my fellow NSF Debris group members Dr. Boon Leng Cheong and Dr. Sebastian Torres. I greatly enjoyed our weekly research meetings and I appreciate all of the feedback and encouragement you provided to me each step of the way during my Ph.D.

I am fortunate to have two parents who have supported and encouraged me in every endeavor. To you I owe my love of learning and my drive to improve myself. While I cannot put into words how much I've learned from you and how much I appreciate everything you have done for me, I would like to say how proud I am to be your son. I

also am grateful for my Aunt Debbie, who fostered my love of science from a very young age. You gave me my spirit of adventure and my endless curiosity. I am grateful for my grandparents, who provided me with as many happy experiences as I could ever wish for, and then some. You have been amazing examples of work ethic and thoughtfulness.

I'd like to thank the friends that I've made in the school of meteorology and ARRC, especially, Andrew Mahre, Andrew Byrd, Javier Lujan, Hong Jiang, Zach Wienhoff, Arturo Umeyama, and Javier Ortiz for making coming into work everyday a welcoming and enjoyable experience. Many of you also provided many helpful discussions that aided in my research. I'd like to thank the ARRC staff, especially Jo Ann Mehl and Kayla Cervi for providing me with nearly endless administrative support and keeping the ARRC from descending into chaos. I'd also like to thank the ARRC engineers and technical staff, especially Danny Feland, John Meier, Kyle Keys, and Redmond Kelley for helping to maintain the AIR. Also, I'd like to thank Christie Upchurch in the school of meteorology for helping me with anything and everything at a moment's notice. I appreciate you always being there to help me both professionally and personally and am grateful for the amount you care for all of the SoM students and hard work you put in to see us succeed.

I'd like to thank all of the teachers who have taught me over the course of nearly three decades. There are too many to list, but you all shared your passion and love of learning with me and have inspired me on every step of my journey as a student and I appreciate the nearly countless hours you have invested in me and all your other students. I'd like to thank Dr. Adam Houston and Dr. Christopher Weiss who have been and continue to be such great examples of scholarship and mentorship for me. Finally, I would like to thank my high school math teacher, Dr. Darren Holley for being the first to tell me that I could get a Ph.D. I believed you and I would not be here without your belief in me.

This work was supported by National Science Foundation grants AGS-1303685 and AGS-1823478.

# Table of Contents

**Acknowledgments** **iv**

**List of Tables** **xi**

**List of Figures** **xii**

**Abstract** **xxiv**

**1 Introduction** **1**

**2 Background** **11**

2.1 Tornado Lifecycle . . . . . 11

2.1.1 Tornadogenesis . . . . . 11

2.1.2 Tornado Maintenance and Tornado Decay . . . . . 17

2.2 Tornado Dynamics . . . . . 21

2.2.1 Tornado Structure . . . . . 21

2.2.2 Swirl Ratio . . . . . 26

2.2.3 Debris Loading and Centrifuging . . . . . 27

2.3 Polarimetric Signatures in Supercells . . . . . 32

2.3.1 Polarimetric Variable Overview . . . . . 33

2.3.1.1 Radar Reflectivity Factor . . . . . 33

2.3.1.2 Differential Reflectivity . . . . . 35

2.3.1.3 Co-polar Cross-correlation Coefficient . . . . . 37

2.3.1.4 Differential Phase and Specific Differential Phase . . . . 37

2.3.2 $Z_{DR}$ Column . . . . . 38

2.3.3 $Z_{DR}$ Arc . . . . . 40

2.3.4 $K_{DP}$ Foot . . . . . 42

**3 Kinematic and Polarimetric Radar Observations of the 10 May 2010, Moore-Choctaw, Oklahoma, Tornadic Debris Signature 44**

3.1 Introduction . . . . . 44

3.2 Methods . . . . . 45

3.2.1 Radar Data . . . . . 45

3.2.2 TDS Criteria . . . . . 46

3.2.3 Dual-Doppler Analysis . . . . . 47

3.2.4 Axisymmetric Wind Retrieval . . . . . 51

3.3 Results . . . . . 52

3.3.1 Spatial distribution of polarimetric variables . . . . . 52

3.3.2 Tornado subvortices . . . . . 56

3.3.3 Polarimetric vs. kinematic variables . . . . . 59

3.4 Discussion . . . . . 66

3.4.1 Polarimetric observations . . . . . 66

3.4.2 Comparison of single- and dual- Doppler analyses . . . . . 68

3.5 Conclusions . . . . . 72

**4 Polarimetric Radar Observations of Simultaneous Tornadoes on 10 May 2010 near Norman, Oklahoma 75**

4.1 Introduction . . . . . 75

4.2 Methods . . . . . 76

4.2.1 Case Overview . . . . . 76

4.2.2 Radar Data and Dual-Doppler Synthesis . . . . . 76

4.2.3 Debris Classification . . . . . 78

4.3 Results . . . . . 80

4.3.1 Polarimetric and Dual-Doppler Observations of Tornadic Debris . 80

4.3.2 Comparison of Simultaneous TDSs . . . . . 84

4.3.3 Debris Sedimentation . . . . . 93
4.3.4 Dual-Wavelength Observations of Inner vs. Outer Debris . . . . . 97
4.4 Discussion . . . . . 102
4.4.1 TDS Rotation . . . . . 102
4.4.2 Temporal Evolution of Polarimetric Profiles . . . . . 105
4.5 Conclusions . . . . . 107

**5 High-Temporal Resolution Observations of the 27 May 2015 Canadian, Texas, Tornado Using the Atmospheric Imaging Radar 111**

5.1 Introduction . . . . . 112
5.2 Methods . . . . . 113
5.2.1 Atmospheric Imaging Radar and Case Overview . . . . . 113
5.2.2 Time-Height Plots . . . . . 114
5.2.3 Axisymmetric Wind Retrieval . . . . . 115
5.2.4 Angular Momentum Budget . . . . . 116
5.3 Results . . . . . 117
5.3.1 High-Temporal Resolution Observations . . . . . 117
5.3.2 Rapid Tornado Evolution . . . . . 127
5.3.3 Angular Momentum Budget . . . . . 132
5.3.4 Tornado Tilt . . . . . 135
5.3.5 Vertical Cross-Sections . . . . . 138
5.4 Discussion . . . . . 142
5.4.1 Persistent Vortex Tilt Layer and Tornado Decay . . . . . 142
5.4.2 Vertical Correlation in Vortex Intensity . . . . . 147
5.5 Conclusions . . . . . 151

**6 Conclusions and Recommendations for Future Work 155**

6.1 Conclusions . . . . . 155
6.2 Recommendations for Future Work . . . . . 158

6.2.1 Polarimetric Atmospheric Imaging Radar . . . . . 158
6.2.2 SimRadar . . . . . 162

**Reference List** **165**

**Appendix A**

List of Acronyms . . . . . 177

**Appendix B**

List of Symbols . . . . . 179

## List of Tables

2.1 Typical values of polarimetric variables for a selection of precipitation types at S band adapted from Doviak and Zrnić (1993). . . . . 36

3.1 A selection of radar characteristics for OU-PRIME, KTLX, and KOUN. . 46

## List of Figures

1.1 The PAIR concept courtesy of J. Salazar (personal communication). . . . 9

2.1 Illustration of the dynamic pipe effect. The "L" represents the perturbation pressure deficit associated with a vortex. The vertical lines represent the air response to the vertical pressure gradient force associated with the low pressure. The horizontal lines represent convergence to replace the vertically displaced air. Figure courtesy of Bluestein (2013). . . . . 13

2.2 An illustration of how transient enhanced vertical vorticity within a mid- and low-level mesocyclone might appear as a descending incipient tornado in WSR-88D data. The black bar indicates a tornado and the dotted horizontal line marks the level of free convection. Gray (dark green) shading represents mesocyclone-scale (tornadic) vertical vorticity. Light green shading highlights areas (top) of locally enhanced vertical vorticity and (bottom) where TVS criteria are met based on the given vertical vorticity distribution. The black dots indicate the approximate center beam locations from a WSR-88D scanning a storm 60 km away using VCP 212. Figure courtesy of French et al. (2013). . . . . 14

2.3 Schematic showing how cyclonic vorticity may be generated near the updraft-downdraft interface. (Top) Top-down schematic of steamlines representing streamwise vorticity approaching the mesocyclone from the forward flank. (Bottom) Vorticity vectors, which are tilted downward by the downdraft (anticyclonic vorticity) becomes tilted upward (becoming cyclonic vorticity) as it is advected faster below than it is aloft, as happens at the "foot" of a density current. This cyclonic vertical vorticity enters the base of the updraft where it is stretched. Figure courtesy of Bluestein (2013). . . . . 16

2.4 Horizontal cross section of (a) model-simulated reflectivity at 500 m (dBZ; shaded) and manually annotated boundaries. (d) The 10-m vertical vorticity ($s^{-1}$; shaded), 10-dBZ reflectivity at 500m AGL (black contour), and 10-m storm-relative, horizontal vorticity vectors. Figure adapted from Coffer and Parker (2017). . . . . 17

2.5 Schematic representations of five tornado maintenance mechanisms: (a) the observed relationship between the rear-flank downdraft and gust fronts, mesocyclone; (b) the relationship between tornado strength and changes in the strength of the low-level mesocyclone and convergence; (c) the relationship between tornado strength and its position relative to the primary updraft; (d) the relationship between tornado longevity and temperature deficit of the outflow; and (e) the relationship between tornadogenesis and the tilting of an initially sinking baroclinically generated vortex ring. Figure courtesy of Marquis et al. (2012). . . . . 19

2.6 An axisymmetric vertical cross section schematic of the four regions of a tornado. Orange contours indicate lines of constant angular momentum. Figure adapted from Bluestein (2013). . . . . 22

2.7 Lines of constant angular momentum in a vertical cross section of an idealized tornado. Figure adapted from Lewellen et al. (2000) by Bluestein (2013). . . . . 23

2.8 Radial profile of tangential velocity in the (a) Rankine combined, (b) Burgers–Rott, and (c) Sullivan vortex models. $R_{core}$ is the core radius and $V_{max}$ is the maximum in tangential velocity. Figure adapted from Brown and Wood (2012). . . . . 25

2.9 Idealized force diagrams for (a) low and (b) high swirl ratio tornadoes. Radius from the center of the tornado increases from left to right. Figure adapted from Bluestein (2013). . . . . 28

2.10 Vertical cross-sections through idealized tornadoes with (a) low, (b) medium, and (c) high swirl ratio. Arrows indicate the associated secondary circulations. Figure adapted from Bluestein (2013). . . . . 29
2.11 Idealized depiction of a vortex sheet (dashed line) that arises from the radial gradient in tangential velocities in a high-swirl tornado. Figure courtesy of Bluestein (2013). . . . . 30
2.12 Photograph of the 11 May 1982 Friendship, Oklahoma, multiple-vortex tornado. Photo courtesy of Bluestein (2013). . . . . 31
2.13 Photograph (copyright D. Dowell) of a tornado near Fulton, SD on 31 May 1998. The arrow marks a curl in the debris cloud that may indicate debris fallout and recirculation. Figure courtesy of Dowell et al. (2005). . . . . 33
2.14 Vertical cross-section of Doppler-on-Wheels reflectivity (dBZ) in the 3 June 1995 Dimmitt, Texas, tornado illustrating a WEC. Figure adapted from Wurman et al. (1996). . . . . 34
2.15 A vertical cross section of $Z_{DR}$ (dB) through a supercell updraft illustrating a prominent $Z_{DR}$ column. Black contours represent values of reflectivity (dBZ). Figure courtesy of Kumjian and Ryzhkov (2008). . . . . 39
2.16 PPI plots of OU-PRIME (a) reflectivity (dBZ) and (c) differential reflectivity (dB) illustrating a prominent $Z_{DR}$ arc in the 10 May 2010 Norman-Little Axe supercell. Figure adapted from Palmer et al. (2011). . . . . 41
2.17 A conceptual model illustrating the relative position of the $K_{DP}$ foot to other features within the supercell. Figure courtesy of Romine et al. (2008). 43

3.1 Dual-Doppler winds (arrows) overlaid on 2223 UTC 1° elevation PPIs of OU-PRIME (a) reflectivity (dBZ), (b) correlation coefficient, and (c) differential reflectivity (dB), and (d) a CAPPI of dual-Doppler derived vertical vorticity ($s^{-1}$) valid at 250 m ARL. The solid black contours represent the 15 dBZ isodop. . . . . 49

3.2 PPIs of 1° elevation OU-PRIME (a) reflectivity (dBZ), (b) radial velocity (m $s^{-1}$), (c) correlation coefficient, and (d) differential reflectivity (dB) valid at 2231 UTC. Arrows highlight the pockets of low $\rho_{hv}$ and $Z_{DR}$ in (c) and (d). The plus sign in (c) represents the subjectively determined TDS center. . . . . 50

3.3 Scatter plots of objectively analyzed (a) correlation coefficient, and (b) differential reflectivity (dB), and raw (c) correlation coefficient, and (d) differential reflectivity (dB) vs. radial distance (km) valid at 2231 UTC. Blue dots indicate non-TDS flagged points and red dots indicate TDS flagged points. The black line is the second order polynomial fit for all points and the red line is the second-order polynomial fit for TDS flagged points. . . . . 54

3.4 OU-PRIME axisymmetric (a) reflectivity (dBZ), (b) correlation coefficient, (c) differential reflectivity (dB), and (d) tangential velocity (m $s^{-1}$) valid at 2231 UTC. Dashed lines represent isopleths of axisymmetric correlation coefficient. . . . . 55

3.5 (a) A PPI of OU-PRIME radial velocity (m $s^{-1}$) and (b) a CAPPI of dual-Doppler vertical vorticity ($s^{-1}$) valid at 2231 UTC. The hatched blue contour in (b) represents areas where reflectivity exceeds 40 dBZ. . . . . 57

3.6 KOUN axisymmetric (a) tangential velocity (shaded, m $s^{-1}$), (b) angular momentum (shaded, $m^2$ $s^{-1}$), (c) correlation coefficient (shaded), and (d) differential reflectivity (shaded, dB) valid at 2230 UTC. Dashed lines represent isopleths of axisymmetric correlation coefficient. Arrows represent secondary circulation wind vectors comprised of radial and vertical velocities from the axisymmetric wind retrieval. . . . . 58

3.7 Scatter plots of vertical vorticity ($s^{-1}$) vs. OU-PRIME (a) reflectivity (dBZ) and (b) correlation coefficient valid at 2223 UTC. No significant relationship is observed between either radar variable and vertical vorticity. 60

3.8 Scatter plots of vertical vorticity ($s^{-1}$) vs. OU-PRIME reflectivity (dBZ) at (a) 250 m ARL and (b) 1000 m ARL, and CAPPIs of OU-PRIME reflectivity (shaded, dBZ) overlaid with dual-Doppler winds (arrows) at (c) 250 m ARL, and (d) 1000 m ARL valid at 2231 UTC. Blue dots in (a) and (b) represent non-TDS flagged points and red dots indicate TDS flagged points. The black lines in (a) and (b) represent the second order polynomial fit for all points and the red lines are the second-order polynomial fits for TDS flagged points. . . . . 61

3.9 As in Fig. 3.8 except for OU-PRIME correlation coefficient at (a,c) 250 m ARL and (b,d) 1000 m ARL valid at 2231 UTC. . . . . 63

3.10 As in Fig. 3.9 except for vertical velocity (m $s^{-1}$) instead of vertical vorticity. 64

3.11 As in Fig. 3.9 except with differential reflectivity (dB) instead of correlation coefficient. Polynomial fits for TDS flagged points were not included due to poor fit. . . . . 65

3.12 Dual-Doppler derived vertical vorticity (shaded, $s^{-1}$) and OU-PRIME objectively analyzed differential reflectivity (black contours, dB) contoured every 0.3 dB from -0.9 dB valid at 2231 UTC. The hatched blue contour represents the 40 dBZ reflectivity isopleth. . . . . 67

3.13 Axisymmetric tangential velocity (shaded, m $s^{-1}$) from (a) KOUN and (b) a dual-Doppler analysis between OU-PRIME and KTLX valid at 2230 and 2231 UTC, respectively. Difference plots between the KOUN and dual-Doppler (c) tangential velocity (shaded, m $s^{-1}$), (d) radial velocity (shaded, m $s^{-1}$), and (e) vertical velocity (shaded, m $s^{-1}$), and (f) a CAPPI of dual-Doppler perturbation vertical velocity (shaded, m $s^{-1}$) based on the axisymmetric mean. . . . . 70

3.14 Conceptual diagrams of polarimetric signatures associated with large tornado subvortices displayed as (a) a PPI and (b) an axisymmetrically averaged vertical cross-section along line c-d in panel (a). Panel (a) illustrates the high $Z_H$, low $\rho_{hv}$, and near zero $Z_{DR}$ observed within the high $\zeta$ regions associated with the largest two subvortices in the 10 May 2010 Moore-Choctaw tornado. Also illustrated is the trailing region of negative $Z_{DR}$. Panel (b) illustrates the annulus of $Z_H$ associated with debris centrifuging and the annuli of low $\rho_{hv}$ and $Z_{DR}$ associated with the tornado subvortices and bound by the radius of maximum winds (RMW, white dashed line). 73

4.1 Tornado damage paths in Cleveland County, Oklahoma, on 10 May 2010. Figure courtesy of the National Weather Service Office in Norman. Available online at `https://www.weather.gov/oun/`events-20100510-maps. The red star indicates the track of the Norman–Little Axe tornado and the blue star indicates the track of the landspout tornado. . . . . 77

4.2 OU-PRIME PPI plots of (a–c) reflectivity (dBZ), (d–f) correlation coefficient, (g–i) differential reflectivity (dB), and (j–l) debris classification at 1.0°, 2.0°, and 3.0° elevation (from left to right) for the Norman-Little Axe tornado (western TDS only) valid at 2242 UTC. . . . . 81

4.3 OU-PRIME PPI plots at 1.0° elevation of (a-b) $Z_H$ (dBZ) and (c-d) $\rho_{hv}$ overlaid with dual-Doppler derived (a,c) storm-relative horizontal winds (arrows) and (b,d) vertical velocity at 250 m ARL valid at 2242 UTC. . . 82

4.4 Same as Fig. 2 except at 4.0°, 5.0°, and 6.5° elevation (from left to right) valid at 2242 UTC. . . . . 85

4.5 Same as Fig. 2 except at 1.0°, 2.0°, and 4.0° elevation (from left to right) valid at 2244 UTC. . . . . 86

4.6 Same as Fig. 2 except valid at 2247 UTC. . . . . 88

4.7 OU-PRIME PPI plots at 1.0° elevation of (a) reflectivity (dBZ), (b) correlation coefficient, and (c) differential reflectivity (dB) overlaid with dual-Doppler derived storm-relative horizontal winds (arrows) at 250 m ARL valid at 2247 UTC. . . . . 89

4.8 OU-PRIME PPI plots of (a–b) reflectivity (dBZ) and (c–d) correlation coefficient at (a,c) 1.0° and (b,d) 2.0° elevation valid at 2249 UTC. . . . 91

4.9 Composite profiles of OU-PRIME (a) reflectivity (dBZ), (b) differential reflectivity (dB), and (c) correlation coefficient vs. height (km) valid from 2244–2247 UTC. Red lines indicate the profiles of the western tornado and blue lines indicate the profiles of the eastern tornado. Light colors represent median values and dark colors represent 90th percentile values. 92

4.10 (a) OU-PRIME areal extent ($km^2$) of debris at 1.0°, 2.0°, 3.0°, 4.0°, 5.0°, and 6.5° in the northern (green), eastern (red), southern (blue), and western (black) quadrants. Quadrants are defined relative to the center of the tornado. Dark colors represent area with reflectivity >30 dBZ and light colors represent area with <30 dBZ reflectivity. (b) Area ($km^2$) of debris exhibiting $Z_H > 30$ dBZ vs. height (km) valid at 2242 UTC (blue line), 2244 UTC (orange line), 2247 UTC (green line), and 2249 UTC (red line). 94

4.11 OU-PRIME PPI plots of (a–c) reflectivity (dBZ), (d–f) correlation coefficient, and (g–i) Norman-Little Axe tornado debris classification at (a,d,g) 2.0°, (b,e,h) 3.0°, and (c,f,i) 4.0° elevation valid at 2247 UTC. . . . . 96

4.12 Same as Fig. 2 except at 4.0°, 5.0°, and 6.5° elevation (from left to right) valid at 2249 UTC. . . . . 98

4.13 Dual-Doppler-derived mean storm relative horizontal wind profile, computed within a 3-km radius of the Norman-Little Axe tornado valid at 2247 UTC. . . . . 99

4.14 Composite profiles of (a,d) reflectivity (dBZ), (b,e) differential reflectivity (dB), and (c,f) correlation coefficient vs. height (km) for the western tornado valid from 2242–2249 UTC. Profiles in (a–c) are for inner debris (debris within a 1-km radius of the tornado center) and profiles in (d–f) are for debris farther than 1 km from the tornado center. Red lines indicate profiles from KOUN (S band) and blue lines are from OU-PRIME (C band). Light colors represent median values and dark colors represent median values. . . . . 101

4.15 PPI plots of KTLX (a–c) reflectivity (dBZ) and (d–f) correlation coefficient at (a,d) 5°, (b,e) 6.5°, and (c,f) 8° elevation valid at 2336 UTC for the 19 May 2013 Shawnee, Oklahoma, tornado. Figures generated by the NOAA Weather and Climate Toolkit, available online at `https://www.ncdc.noaa.gov/wct/`. Rings represent range to radar (km). . . . . 104

4.16 OU-PRIME (a) 90th percentile reflectivity (dBZ) and (b) median correlation coefficient vs. height (km) valid at 2242 UTC (blue line), 2244 UTC (orange line), 2247 UTC (green line), and 2249 UTC (red line) for debris within 1 km of the Norman-Little Axe tornado. . . . . 106

5.1 PPI plots of (a,c,e,g) reflectivity (dBZ) and (b,d,f,h) radial velocity (m $s^{-1}$) at 1° elevation at (a-b) 22:03:52, (c-d) 22:04:13, (e-f) 22:04:56, and (g-h) 22:05:18 UTC. White pixels here and elsewhere represent censored data. 119

5.2 PPI plots of (a,c,e,g) reflectivity (dBZ) and (b,d,f,h) radial velocity (m $s^{-1}$) at (a-b) 1°, (c-d) 4°, (e-f) 7°, and (g-h) 10° elevation valid at 22:03:52 UTC. The elevations roughly correspond with 100 m, 400 m, 750 m, 1000 m ARL. 120

5.3 PPI plots of (a,c) spectrum width (m $s^{-1}$) and (b,d) radial velocity (m $s^{-1}$), at (a-b) 1.5° and (c-d) 5° elevation valid at 22:04:13 UTC. . . . . 122

5.4 PPI plots of radial velocity (m $s^{-1}$) at (a) 22:04:02, (b), 22:04:13, (c) 22:04:24, (d) 22:04:35, (e) 22:04:45, (f) 22:04:56, (g) 22:05:07, and (h) 22:05:18 UTC at 3.5° elevation. Arrows indicate the location of the shed vortices. Maximum $\Delta V$ of each vortex is shown after it has been shed. . 124

5.5 Time-height plot of maximum $\Delta V$ (m $s^{-1}$) within the tornado. Overlaid are the 55 m $s^{-1}$, 30 m $s^{-1}$, and 20 m $s^{-1}$ $\Delta V$ contours. Note that sampling of tornado intensity was not continuous, but rather there is approximately 10.5 s between each estimate of $\Delta V$. . . . . 125

5.6 Axisymmetric tangential velocity (shaded, m $s^{-1}$) at (a) 22:03:52, (b) 22:04:13, (c) 22:04:24, and (d) 22:04:45 UTC. Arrows represent secondary circulation wind vectors (m $s^{-1}$) comprised of radial and vertical velocities from the axisymmetric wind retrieval. . . . . 128

5.7 The same as Fig. 5.6 except for axisymmetric reflectivity (shaded, dBZ). 131

5.8 Axisymmetric angular momentum (shaded, $m^2$ $s^{-1}$) at (a) 22:04:02, (b) 22:04:13, (c) 22:04:35, and (d) 22:04:56 UTC. Arrows represent secondary circulation wind vectors ($m^2$ $s^{-1}$) comprised of radial and vertical velocities from the axisymmetric wind retrieval. . . . . 132

5.9 Axisymmetric (a,d,g,j) time rate of change (shaded, $m^2$ $s^{-2}$), (b,e,h,k) advection (shaded, $m^2$ $s^{-2}$), and (c,f,i,l) eddy flux convergence (shaded, $m^2$ $s^{-2}$) of angular momentum valid for the (a-c) 22:03:52–22:04:56 UTC timeframe, (d-f) 22:03:52–22:04:13 UTC timeframe, (g-i) 22:04:13–22:04:35 UTC timeframe, and (j-l) 22:04:35–22:04:56 UTC timeframe. The left column represents the time rate of change of angular momentum calculated by taking difference in the angular momentum field between the first and last time in the analysis window. The middle column represents the average advection of angular momentum by the secondary circulation during the analysis window. The right column is largely representative of the turbulent creation and dissipation of angular momentum. . . . . 133

5.10 (a) Tornado tilt (°) between the lowest elevation angle (∼ 0.1 km) and 0.5 km (blue), 1.0 km (orange), 1.5 km (green), and 2.0 km (red). (b) Tornado center at the lowest elevation angle (black) and mean tornado center in the 0.1–1.0 km layer (blue) and 1.0–2.0 km layer (red). Storm motion is from right to left at all levels. . . . . 136

5.11 Direction of vortex tilt between 0.1 and 2.0 km ARL in clockwise degrees from north. Radial axis is time in UTC. . . . . 137

5.12 Photographs at (a) 2204, (b) 2206, and (c) 2207 UTC and (d) a time-height plot of filtered vortex tilt (°). Vertical lines i, ii, iii in (d) correspond with (a-c) respectively. Photographs adapted from Kurdzo et al. (2017). . . . 139

5.13 (a) PPI plot of reflectivity (dBZ) at 1° elevation and (b) RHI of reflectivity (dBZ) valid at 22:03:52 UTC. Black line in (a) represents the location of the RHI in (b). . . . . 140

5.14 (a,c,d) PPI plots of reflectivity (dBZ) at 1°, 8°, and 10° respectively and (b) AHI of reflectivity (dBZ) valid at 22:03:52 UTC. Horizontal lines i, ii, iii in (b) correspond with (a,b,d) respectively. Black lines in (a,c,d) represent the location of the AHI in (b). . . . . 141

5.15 RHI plots of (a) radial velocity (m $s^{-1}$) and (b) reflectivity (dBZ) and PPI plots of radial velocity (m $s^{-1}$) at (c) 2° and (d) 6.5° elevation valid at 22:06:44 UTC. The tornado is very tilted through the 400–700 m layer (see Fig. 5.12d) as evidenced by the shift in vortex position between (c) and (d). Strong horizontal vorticity is evident through this layer with slightly larger $\Delta V$ in the RHI scan compared to the PPI scans. Black lines i and ii in (b) correspond with the elevation angles in (c-d) respectively. Black lines in (c-d) correspond with the location of the RHIs in (a-b). . . . . 143

5.16 Storm Prediction Center mesoanalysis of (a) surface temperature (red lines, °F), mean sea level pressure (black lines, mb), and dewpoint temperature (shaded, °F), (b) 700 mb height (black lines, m), temperature (red lines, °C), and 700-500 mb mean RH (shaded, %), and (c) 500 mb height (black lines, m) and temperature (red lines, °C) valid at 2200 UTC on 27 May 2015. The star indicates the location of Canadian, Texas, and the circle indicates the location of Dodge City, Kansas. Archived mesoananalyses are available online at `http://www.spc.noaa.gov/exper/ma_archive/`. (d) Skew-T diagram of the vertical sounding launched at Dodge City, Kansas, valid at 00 UTC on 28 May 2015. Archived soundings are available online at `http://weather.uwyo.edu/upperair/sounding.html`. . . . . 145

5.17 Time-height plots of (a) maximum $\Delta$V (m s$^{-1}$) as in Fig. 5.5 and (b) the distance (km) separating maximum inbound and maximum outbound velocities used to calculate $\Delta$V in (a). Vortex diameter is thresholded on $\Delta$V beneath 40 m s$^{-1}$ where diameter calculations became much noisier. 148

5.18 Cross-correlation at lag 0 of $\Delta$V at each height (km) with the 0.5° scan. The calculation was performed over the 22:03:52–22:07:37 UTC time period when $\Delta$V exceeded 40 m s$^{-1}$ throughout the majority of the observed depth. High correlation at lag 0 suggests that changes in vortex intensity occur largely simultaneously in the vertical. . . . . 150

6.1 PPI plot of (a) OU-PRIME reflectivity overlaid with forward trajectories for leaves color coded by height above ground level and (b) binned $\log_{10}$(debris count) for leaves in a tornado relative reference frame. . . . . 160

6.2 (a) Time-height plot of maximum $\Delta$V (m s$^{-1}$) and (b) the distance between the mean position of the Woodward tornado in the lowest 1 km and the mean position of the vortex between 1-2 km (blue), 2-3 km (orange), and 3-4 km (green). . . . . 161

6.3 Graphical output from SimRadar showing the vertical plane of an LES tornado simulation with lofted raindrops (purple) and leaves (green). . . 163
6.4 Simulated $Z_H$ for a high-swirl LES. Arrows indicate the position of large tornado subvortices. . . . . 164

## Abstract

Tornadoes are capable of lofting large pieces of debris that present irregular shapes, near-random orientations, and a wide range of dielectric constants to polarimetric radars. While ties between tornadic debris signature (TDS) characteristics and tornado- and storm-scale kinematic processes have been speculated upon or investigated using photogrammetry and single-Doppler analyses, little work has been done to relate the three-dimensional wind field to TDS characteristics and behavior. Additionally a knowledge gap in larger-scale transport and sedimentation of debris exists within the literature. This study utilizes data collected by the University of Oklahoma's Advanced Radar Research Center's OU-PRIME C-band radar as well as KTLX and KOUN WSR-88D S-band radars to study three tornadoes that occurred in Central Oklahoma on 10 May 2010. The relationship between polarimetric and kinematic variables are interrogated revealing an instance where large tornado subvortices were associated with comparatively high reflectivity, low correlation coefficient, and were surrounded by negative differential reflectivity. Comparisons of the polarimetric characteristics of two tornadoes interacting with similar land cover but with different intensities are documented. Also, the storm-scale sedimentation of debris within the supercell is investigated revealing a novel observation of TDS rotation and elongation with height. Additionally, a novel dual-wavelength comparison of debris within the tornado to debris in the near-tornado environment is presented revealing larger dual-wavelength differences in polarimetric variables for debris within the tornado and increasingly similar inner and out debris characteristics as height increases.

While new insight into the behavior of tornadic debris is elucidated in this study, tornadoes themselves evolve on much shorter timescales than what can be resolved by traditional, mechanically steered radars. In order to illustrate the benefit of rapid-scan

radars for the study of tornado evolution and to motivate future rapid-scan polarimetric radar observations of tornadoes and debris, high-temporal resolution observations of the 27 May 2015 Canadian, Texas, tornado collected by the Atmospheric Imaging Radar (AIR) are presented. A 10-s resolution time-height investigation of vortex tilt and differential velocity ($\Delta$V) is presented and illustrates an instance of upward vortex intensification as well as downward tornado decay. Changes in tornado intensity over periods of less than 30 s coincided with rapid changes in tornado diameter. At least two small-scale vortices were observed being shed from the tornado during a brief weakening period. A persistent layer of vortex tilt was observed near the level of free convection, which separated two layers with contrasting modes of tornado decay. Finally, the vertical cross-correlation of vortex intensity reveals that apart from the brief instances of upward vortex intensification and downward decay, tornado intensity was highly correlated throughout the observation period.

# Chapter 1

# Introduction

Tornadoes are capable of causing considerable loss of life and destruction of property on timescales much shorter than most natural disasters. For example, three recent events, the 22 May 2011 Joplin tornado, the 27 April 2011 Dixie outbreak, and the 2013 Newcastle-Moore tornado resulted in a combined 500 fatalities and between $14–16 billion in direct losses (NCDC 2015). While the number of significant tornadoes has remained relatively constant over the past 50 years (Coleman and Dixon 2014), the risk for major tornado disasters has increased due to growing population and urban development in tornado-prone regions (Ashley and Stradler 2016). These urban areas provide a source for considerable amounts of lofted tornadic debris, which are the primary cause of fatalities within tornadoes (Bohonos and Hogan 1999). Additionally, airborne debris can increase the damage potential of a tornado by increasing its near-surface total momentum (e.g., Lewellen et al. 2008).

The advent and operational implementation of dual-polarization radar has led to vast improvements in hydrometeor classification (e.g., Vivekanandan et al. 1999; Bringi and Chandrasekar 2001; Ryzhkov et al. 2005a; Park et al. 2009; Kumjian 2013a,b) as well as improvements in the ability to differentiate between meteorological and non-meteorological scatterers (e.g., Zrnić and Ryzhkov 1999), which facilitates the identification of tornadic debris (Ryzhkov et al. 2002, 2005b). The tornadic debris signature (TDS) is characterized by low values of co-polar cross-correlation coefficient at lag 0 $\rho_{hv}$, and is often accompanied by a local maximum in reflectivity factor at horizontal polarization $Z_H$[1] and near-zero values in differential reflectivity $Z_{DR}$ (Ryzhkov et al. 2002, 2005b).

[1]TDSs have been noted to exhibit a wide range of $Z_{HH}$ values (∼20-70 dBZ) by the Warning Decision Training Division (WDTB 2013).

The polarimetric signature is often, but not always, collocated with a tornadic vortex signature (e.g., Van Den Broeke and Jauernic 2014; Skow and Cogil 2017).

Attempts to algorithmically detect tornadic debris have been made, with future work expected to optimize and improve the application to operations (Snyder and Ryzhkov 2015; Wang and Yu 2015). However, there are many caveats to polarimetric tornadic debris detection (Schultz et al. 2012b). Most notably, attenuation and differential attenuation may lead to erroneous values of $Z_H$ and $Z_{DR}$. However, $\rho_{hv}$ is still a reliable indicator of tornadic debris provided that there is uniform beam filling up-radial and in the target volume and noise correction is applied in regions of low signal-to-noise ratio (Bluestein et al. 2007a). Additionally, tornadoes must be strong enough to loft debris to a height where it can be sampled by a radar, and the debris field must be large enough to be spatially resolved (Kumjian and Ryzhkov 2008). Both of these conditions are modulated by the range that a tornado is from the radar and the scanning strategy chosen. Finally, the presence of a TDS does not necessarily mean that a tornado is ongoing. TDSs sometimes precede tornadogenesis (e.g., Saari et al. 2014; Van Den Broeke 2015) and persist after tornado demise (e.g., Van Den Broeke 2015; Houser et al. 2016). However, accounting for these considerations, the TDS can be used, with caution, to operationally confirm the presence of ongoing tornadoes (Schultz et al. 2012a,b).

An understanding of how the TDS relates to tornado characteristics can expand the utility of polarimetric radars, and recently, the focus of TDS research has broadened from tornado detection to include the relationship between the behavior or tornadic debris and tornado- and storm-scale kinematic processes. If relationships between the distribution of polarimetric radar variables and tornado structure can be documented, more accurate inferences can be made about tornadoes in real time. This would be particularly useful for processes that are not resolved in the Doppler velocity field. For example, tornado- and sub-tornado-scale processes would need to be several beamwidths in diameter in order to be properly sampled in Doppler velocity; however, only a few resolution volumes would be needed to capture debris processes associated with these under-resolved features.

Recently, it has been determined that longer-lived and more-intense tornadoes have been observed to have TDSs with larger volumes and TDSs that extend to higher altitudes than comparatively weaker tornadoes (Bodine et al. 2013; Van Den Broeke and Jauernic 2014; Van Den Broeke 2015), while many tornadoes with EF-scale ratings of EF-2 or less may not exhibit any TDS (Kumjian and Ryzhkov 2008; Van Den Broeke and Jauernic 2014). Additionally, studies have shown that seasonal and regional differences in land type and usage modify some of the characteristics of a TDS, including the height to which debris are lofted and likelihood that a tornado of a given intensity will exhibit a TDS (Van Den Broeke and Jauernic 2014; Van Den Broeke 2015). The life-cycle stage of a tornado may also influence whether a tornado exhibits a TDS, with the probability of a TDS increasing during the first five minutes following tornadogenesis and decreasing between the five minutes preceding and five minutes following the dissipation of a tornado (Van Den Broeke 2015). Bodine et al. (2013) found that large areas of debris fallout occurs as tornadoes weaken and updrafts can no longer suspend as much debris. Houser et al. (2016) found that the area of the low levels of the TDS associated with the 2011 El Reno, Oklahoma, tornado increased while the upper levels of the TDS narrowed as tornado intensity decreased. The El Reno TDS also exhibited vertically propagating wave-like bulges along its periphery, which may be indicative of centrifugal waves within the tornado (Houser et al. 2016).

Stronger tornadoes often exhibit TDSs with higher values of $Z_H$, lower values of $Z_{DR}$, and lower values of $\rho_{hv}$ (Bodine et al. 2013; Van Den Broeke 2015). Bodine et al. (2014) found that values of $Z_H$ and $\rho_{hv}$ were larger at S band within the TDS compared to at C band due to non-Rayleigh scattering effects and that the dual-wavelength differences were larger when the tornado was producing more damage. Within the TDS, $Z_H$ was found to decrease with height and $\rho_{hv}$ was found in increase with height, presumably because large, heavy debris falls out at lower altitudes than light debris (Bodine et al. 2014).

Recently, TDS research has expanded to include observations of debris immediately adjacent to the tornado. For example, Wakimoto et al. (2015) used rapid-scan polarimetric radar data in conjunction with photogrammetric data to document the evolution of the spatial distribution of debris in the 31 May 2013, El Reno, Oklahoma (OK) tornado, noting many features, such as the weak echo hole (WEH), "debris overhang", and "pockets" of low-level debris associated with the rear-flank gust front (RFGF). Similarly, Kurdzo et al. (2015) note instances during the 20 May 2013, Moore, OK tornado where debris are ejected from the tornado preferentially in one direction coinciding with internal momentum surge in the rear flank downdraft (RFD) or occlusions. Appendages to the TDS could also be the result of light debris being lofted by convergent inflow into the tornado (Houser et al. 2016). Similarly, an extension to the TDS aloft, called a 'debris overhang,' could indicate a near-tornado updraft is suspending light debris that are falling out of the tornado (Wakimoto et al. 2015).

It is hypothesized that negative $Z_{DR}$ observed within tornadoes might be attributed to a certain degree of common debris alignment (Ryzhkov et al. 2005b; Bluestein et al. 2007a). Recently, coherent regions of negative $Z_{DR}$ have been observed at the periphery and in the wake of large tornado subvortices (Griffin et al. 2017) and near the radius of maximum winds (RMW) of tornado vortices (Wakimoto et al. 2018). Modeling work using SimRadar (Cheong et al. 2017), a physically based radar simulator that combines large-eddy simulation, air drag models, and radar cross-section measurements of debris, has determined that common debris alignment within tornadoes can theoretically occur (Umeyama et al. 2018). Umeyama et al. (2018) found that debris tended to be aligned such that the major axis was perpendicular to the local wind vector. Therefore, in the observations where negative $Z_{DR}$ occurred near the periphery of tornado vortices, it can be inferred that the local winds were largely horizontal in direction.

While many studies have focused on the near-tornado debris field, comparatively little research has explored the larger-scale transport and sedimentation of debris. Damage and debris surveys suggest that light debris are transported farther than heavy debris, while

the majority of debris fall out to the left of the tornado track due to storm-relative wind shear (Snow et al. 1995). Trajectory calculations using a near-storm sounding confirm these previous observations (Magsig and Snow 1998) and provide insight into how debris can sediment in the rear-flank, left-flank, and forward-flank of storms. Knox et al. (2013) confirmed that the majority of debris sediment to the left of the tornado track using the Hybrid Single-Particle Lagrangian Integrated Trajectory (HYSPLIT) model and a large dataset of debris items obtained from social media postings in the aftermath of the 27 April 2011 tornado outbreak. However, Knox et al. (2013) also found that the debris that were transported the farthest actually travelled to the right of tornado motion, perhaps due to being lofted to higher altitudes and experiencing more westerly winds. Van Den Broeke (2015) provided polarimetric radar observations of debris fallout both downstream of the storm-relative flow and on the northwest periphery of supercells. Fallout of debris has also been documented by polarimetric radar within the RFD in the wake of the tornado (Ryzhkov et al. 2005b; Bodine et al. 2013). Additionally, lofted light debris is often observed within storm inflow and along the rear-flank gust front (RFGF, e.g., Ryzhkov et al. 2005b; Wakimoto et al. 2015). Much of this light debris may not have been lofted by the tornado, but rather by strong winds in the near-tornado environment. However, this debris may also be entrained into the TDS (Houser et al. 2016).

As the previous discussion illustrates, pencil-beam radars have facilitated considerable progress toward a better understanding of tornadoes, especially radars with dual-polarimetric capabilities for the study of tornadic debris. However, the need for mechanical steering confines these radars to a series of designated beam sweeps in space, called volume coverage patterns (VCPs), in order to obtain a three-dimensional dataset. As a result, volumetric updates of traditional, scanning radars are limited to around 4 min (Zrnić et al. 2007). However, tornadoes intensify and weaken on timescales much shorter than 4 min, and many weak tornadoes have entire lifecycles that are much shorter than the volumetric update time of traditional, mechanically-steered radars. Volumetric update times much less than one minute are required to properly sample the evolution

of tornadoes, with temporal resolution of 10 s or less necessary to capture some of the more rapidly evolving features (Bluestein et al. 2010). Mobile radars currently capable of volumetric updates of ∼30 s or less include the Rapid-scan Doppler on Wheels (Wurman and Randall 2001), the Mobile Weather Radar 2005 X-band Phased Array (MWR-05XP, Bluestein et al. 2010), the Rapid X-band polarimetric radar (RaXPol, Pazmany et al. 2013), and the Atmospheric Imaging Radar (AIR, Isom et al. 2013; Kurdzo et al. 2017). In addition to high-temporal resolution, these radars have the advantage of close-range deployments (Wurman et al. 1996), which allow for much better spatial and low-level sampling of tornadoes and mesocyclones compared to stationary radars (e.g., Wurman and Gill 2000; Bluestein and Pazmany 2000; Bluestein et al. 2007a; Kosiba and Wurman 2013; Wurman and Kosiba 2013; Weiss et al. 2014). The finescale spatial resolution provided by mobile radars maximizes the benefits of high-temporal updates for tornado applications by allowing radars to observe rapidly evolving small-scale phenomena.

Recent tornado studies using rapid-update radars have illustrated the importance of short-lived tornadic subvortices on a tornado's intensity and damage potential (Snyder and Bluestein 2014; Wakimoto et al. 2016). Rapid-scan radars are also uniquely capable of providing observations to interrogate the vertical evolution of rotation during tornadogenesis (Houser et al. 2015; French et al. 2013) and tornado decay (French et al. 2014). Houser et al. (2015) found that subtornadic rotation in the 24 May 2011 El Reno, Oklahoma, EF-5 tornado first developed below 1 km and then intensification of rotation to tornadic intensity occurred simultaneously throughout the column when rotation increased aloft (e.g., above 3 km). During decay, French et al. (2014) found that the 5 June 2009 Goshen County, Wyoming, tornado first dissipated near a height of 1.5 km and then proceeded to decay in an "inside out" manner at progressively higher and lower elevations. The level where dissipation first occurred was found to be just above where the tornado motion was most influenced by strong rear-flank gust front outflow. Houser et al. (2015) also noted a similar decay mechanism in the El Reno tornado with tornado dissipation first occurring in a stable layer between 1.5 and 3 km above the ground.

Rapid-update radars have observed that tornado intensity can be highly variable, and sometimes periodic, over short timescales (e.g., Wurman and Kosiba 2013) and that tornado intensity in the low levels (e.g., below 1 km) may be uncorrelated from tornado intensity aloft (French et al. 2014; Mahre et al. 2018). Additional topics of recent investigation using high-temporal resolution radar data include the impact that rapidly evolving storm-scale processes, such as rear-flank gust front surges, have on the tornado lifecycle (Houser et al. 2015) and the rapid evolution of the distribution of tornadic debris (Kurdzo et al. 2015; Houser et al. 2016; Mahre et al. 2018). However, the number of high-temporal resolution tornado cases is still extremely limited, and thus it remains unclear whether or not these past findings can be generalized. A range of tornado cases of varying tornado size and intensity are needed to better understand the diversity of tornado behavior and document whether similarities exist in tornadogenesis and tornado dissipation modes.

In addition to aiding in the understanding of the physical processes that occur during tornadogenesis and tornado decay, documenting the rapid evolution of tornadoes may also inform future weather warning decisions. Forecasters will soon have the ability to better resolve the tornado lifecycle once the current weather surveillance radar network is upgraded to polarimetric phased array radars. If reliable indicators of tornado formation, intensification, and decay can be documented, then it is expected that the quality and lead time of tornado warnings will significantly improve.

The ideal radar for they study of tornadoes would provide the high-temporal resolution volumetric observations necessary to document rapid changes in tornado behavior while also providing the polarimetric diversity needed to identify tornadic debris. The AIR is the only mobile radar currently capable of resolving changes in tornado behavior on timescales less than 10 s, but it is not dual polarimetric. However, in the near future the Advanced Radar Research Center (ARRC) will complete the construction of a Polarimetric Atmospheric Imaging Radar (PAIR, Yu et al. 2015; Salazar-Cerreño et al. 2017). The PAIR will be a mobile, C-band Imaging Radar (Fig. 1.1) that will provide similar volumetric update times to the AIR and will improve upon the sensitivity of

the AIR by using higher-gain solid-state power amplifiers (Yu et al. 2015). The C-band transmit frequency of the PAIR will experience less attenuation than the AIR as well and will therefore be better suited to observe tornadoes wrapped in rain and observe forward-flank downdraft precipitation often missed by attenuated observations at shorter wavelengths. Toward the goal of motivating future research using the PAIR, this study utilizes data from OU-PRIME, a C-band polarimetric radar, to relate the behavior and polarimetric characteristics of tornadic debris to tornado- and storm-scale kinematics and utilizes high-temporal resolution mobile radar observations from the AIR to interrogate rapidly-evolving tornado behavior.

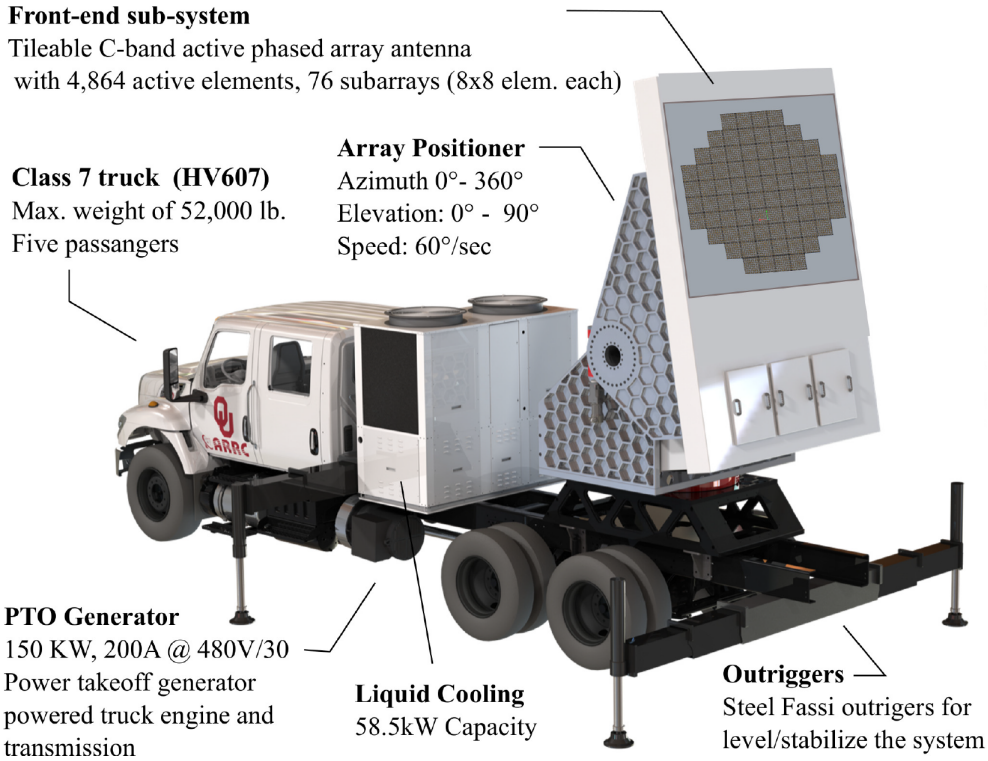


Figure 1.1: The PAIR concept courtesy of J. Salazar (personal communication).

In Chapter 2, an overview of tornado dynamics is presented, including a discussion of the tornado lifecycle, tornado structure, and swirl ratio. The tornado dynamics discussion is followed by an overview of selected polarimetric signatures in supercells with a focus on the relationship between the polarimetric signatures and storm-scale kinematic processes. In Chapter 3, tornado-scale kinematic processes are related to TDS structure for the 10

May 2010 Moore-Choctaw EF-4 tornado. Chapter 4 contains observations of debris sedimentation within the 10 May 2010 Norman-Little Axe EF-4 tornado. A dual-wavelength comparison of debris within the tornado to debris in the near-tornado environment is presented and a comparison of the polarimetric characteristics of the Norman-Little Axe tornado to a nearby landspout tornado is performed. In Chapter 5, high-temporal resolution observations of the late-mature and decay periods of the 27 May 2015 Canadian, Texas, tornado using the AIR are presented. An analysis of tornado tilt with fine-scale vertical resolution is performed, observations of small-scale vortices being shed by the tornado are presented, and the vertical evolution of tornado decay is interrogated. An overview of the findings of this study and recommendations for future work that are motivated by these conclusions are presented in Chapter 6.

# Chapter 2

# Background

In this chapter, an overview of the tornado lifecycle is presented and tornado dynamics is discussed. The regions of the tornado are discussed as well as how the swirl ratio of a tornado governs tornado structure. Finally, a brief overview of polarimetric radar signatures in supercells is discussed with special attention given to the kinematic processes that can be inferred from their presence.

## 2.1 Tornado Lifecycle

### 2.1.1 Tornadogenesis

At the most basic level, tornadogenesis is a process that generates and intensifies vertical vorticity near the ground. In a Lagrangian reference frame (air parcel relative) and ignoring friction, the time rate of change of vertical vorticity is given as:

$$\frac{D\zeta}{Dt} = -\zeta\left(\vec{\nabla}\cdot\vec{V}\right) + \hat{k}\cdot\left(\frac{\partial\vec{V_h}}{\partial z}\times\vec{\nabla}_h \mathrm{w}\right) + \hat{k}\cdot\left[\vec{\nabla}p^{'}\times\vec{\nabla}\frac{1}{\bar{\rho}}\right]. \tag{2.1}$$

The first term on the right-hand side is the vorticity stretching term. It is simply velocity divergence acting on existing vertical vorticity $\zeta$. The negative sign implies that velocity convergence acts to intensify vertical vorticity. The second term is known as vorticity tilting. This is simply the cross product of horizontal vorticity ($\frac{\partial\vec{V_h}}{\partial z}$) and the horizontal gradient in vertical velocity (w). It can be thought of as horizontal gradients in vertical velocity tilting horizontal vorticity into a vertical axis of rotation. In a 'barotropic' atmosphere (ignoring density gradients), this horizontal vorticity is generated mechanically by vertical gradients in horizontal velocity (i.e., vertical wind shear). The last term on the right-hand side is known as the solenoidal term. It can be thought of as the vorticity generated by gradients in atmospheric pressure and density. In supercell thunderstorms, the solenoidal term may not directly generate a large proportion of the vertical vorticity,

but rather horizontal vorticity is 'baroclinically' generated at the edge of the cold pool (e.g., along the forward- and rear-flank gust fronts), a region of large horizontal pressure and density gradients, and this vorticity can then be tilted by the second term into the vertical plane.

Mass continuity dictates that supercell updrafts, enhanced by a dynamically induced vertical perturbation pressure gradient force by the mesocyclone, are a region of strong horizontal convergence, which acts to intensify vertical vorticity (Rotunno 1986; Rasmussen et al. 1994). Moreover, the edge of the supercell updraft is a region of strong horizontal gradients in vertical velocity, which convert horizontal vorticity into vertical vorticity. However, vertical vorticity generated from tilting and stretching of vorticity solely by an updraft quickly advects vorticity upward, away from the ground, violating a necessary requirement for a tornado.

One possible mechanism for bringing vertical vorticity near the ground is the dynamic pipe effect (DPE, Leslie 1971; Smith and Leslie 1978). The DPE centers on the fact that a rotating fluid is associated with a perturbation pressure deficit ($p^{'} \propto -\zeta^2$). This perturbation pressure deficit drives an upward directed pressure gradient force beneath the rotating fluid (Fig. 2.1). Mass continuity dictates that air must replace the vertically displaced air, leading to convergence beneath the level of rotation. This convergence acts to intensify vorticity via stretching at the level beneath the original level of strong rotation creating a feedback that gradually lowers strong vorticity over time. However, Trapp and Davies-Jones (1997) found that the DPE would take approximately 15–20 min to form a tornado from a mesocyclone, and rapid-scan observations (e.g., French et al. 2013; Houser et al. 2015) have only shown simultaneous or slightly upward modes of tornadogenesis that occurs on timescales of seconds to 1 min. French et al. (2013) illustrated how transient strong vorticity within a broader and weaker mesocyclone may appear to descend when under sampled in time by a WSR-88D (Fig. 2.2). This potential sampling artifact may have led to erroneous observational evidence of the DPE mode of tornadogenesis in the past. In real thunderstorms, it may be that the DPE is responsible

for bringing mesocyclone-scale vorticity near the surface, as illustrated in Fig. 2.2; but, the strengthening of that vorticity to tornadic intensity is done by a different process that occurs much more rapidly than can be explained solely by the DPE.

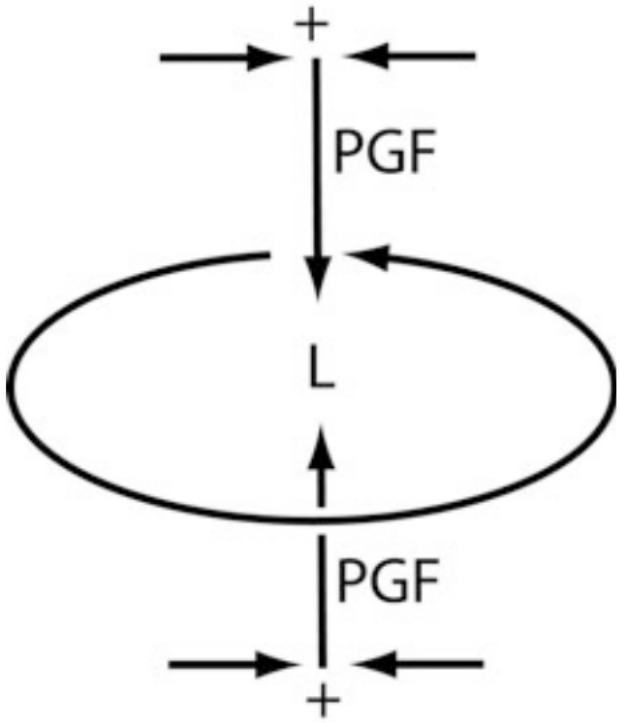


Figure 2.1: Illustration of the dynamic pipe effect. The "L" represents the perturbation pressure deficit associated with a vortex. The vertical lines represent the air response to the vertical pressure gradient force associated with the low pressure. The horizontal lines represent convergence to replace the vertically displaced air. Figure courtesy of Bluestein (2013).

Downdrafts likely play an important role in transporting vorticity near the surface (Markowski 2002). However, in isolation downdrafts tilt streamwise vorticity (vorticity with the axis of rotation parallel to the local motion vector) downward and create anti-cyclonic (clockwise) vertical vorticity, whereas the majority of tornadoes are cyclonic (counter-clockwise rotating) in the northern hemisphere. But, near the interface that occurs near the intersection of the rear-flank downdraft and the updraft beneath the mesocyclone, cyclonic vertical vorticity can be generated (Fig. 2.3). In region of wind

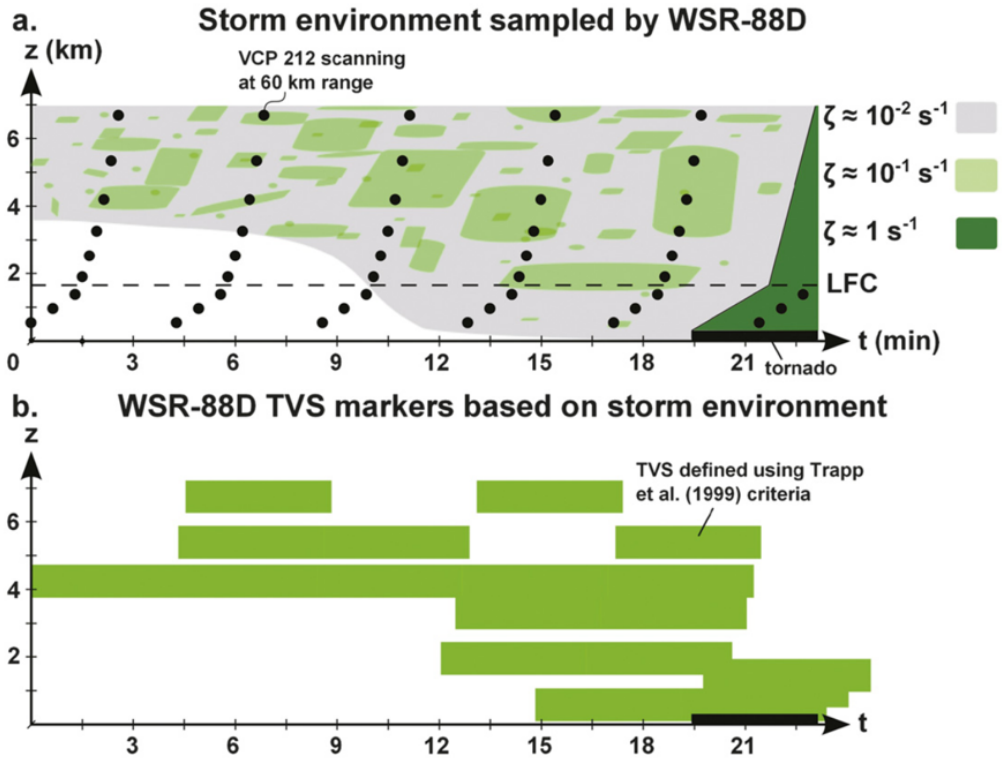


Figure 2.2: An illustration of how transient enhanced vertical vorticity within a mid- and low-level mesocyclone might appear as a descending incipient tornado in WSR-88D data. The black bar indicates a tornado and the dotted horizontal line marks the level of free convection. Gray (dark green) shading represents mesocyclone-scale (tornadic) vertical vorticity. Light green shading highlights areas (top) of locally enhanced vertical vorticity and (bottom) where TVS criteria are met based on the given vertical vorticity distribution. The black dots indicate the approximate center beam locations from a WSR-88D scanning a storm 60 km away using VCP 212. Figure courtesy of French et al. (2013).

shear, vorticity vectors can be tilted away from the streamlines they are following. This means that if horizontal velocity decreases with height, as if often observed near the top of a density current like the rear-flank downdraft, the anticyclonic vertical vorticity generated by the downdraft can be tilted to become cyclonic vertical vorticity prior to entering the updraft beneath the mesocyclone (Fig. 2.3). This cyclonic vorticity can be immediately stretched by the the updraft beneath the mesocyclone near the surface. One consideration for this processes is the temperature of the cold pool and its impact on the buoyancy of parcels entering the updraft. Markowski et al. (2002) found that there was an ideal range of potential temperature deficits in tornadic supercells. If the RFD is too warm, then it is not a significant source of baroclinic vorticity generation; however, if the RFD is too cold, then parcels entering the updraft are too negatively buoyant and hinder the ability of the updraft to stretch and intensify vertical vorticity. The temperature of the downdraft is further discussed in the next subsection.

Recently, the source of the horizontal vorticity within the forward flank of supercells as in (Fig. 2.3) has been a topic of particular interest. High-resolution simulations (e.g., Dahl et al. 2014; Coffer and Parker 2017) indicate that concentrated streams of vorticity, called 'vorticity rivers', feed the low-level mesocyclone preceding tornadogenesis and help maintain ongoing simulated tornadoes (Fig. 2.4). This vorticity forms along a density gradient, which baroclinically generates streamwise horizontal vorticity. Recent observational field campaigns, RiVorS and TORUS, have targeted the forward flank of supercells in order to verify this source of vorticity. Preliminary observations (e.g., Schueth and Weiss 2018) indicate that vorticity rivers may indeed be present in real-world supercells and play a vital role in tornadogenesis. This is one significant illustration of the recent progress made, not only in the understanding of tornadoes, but also in the ability to numerically simulate supercells and tornadoes.

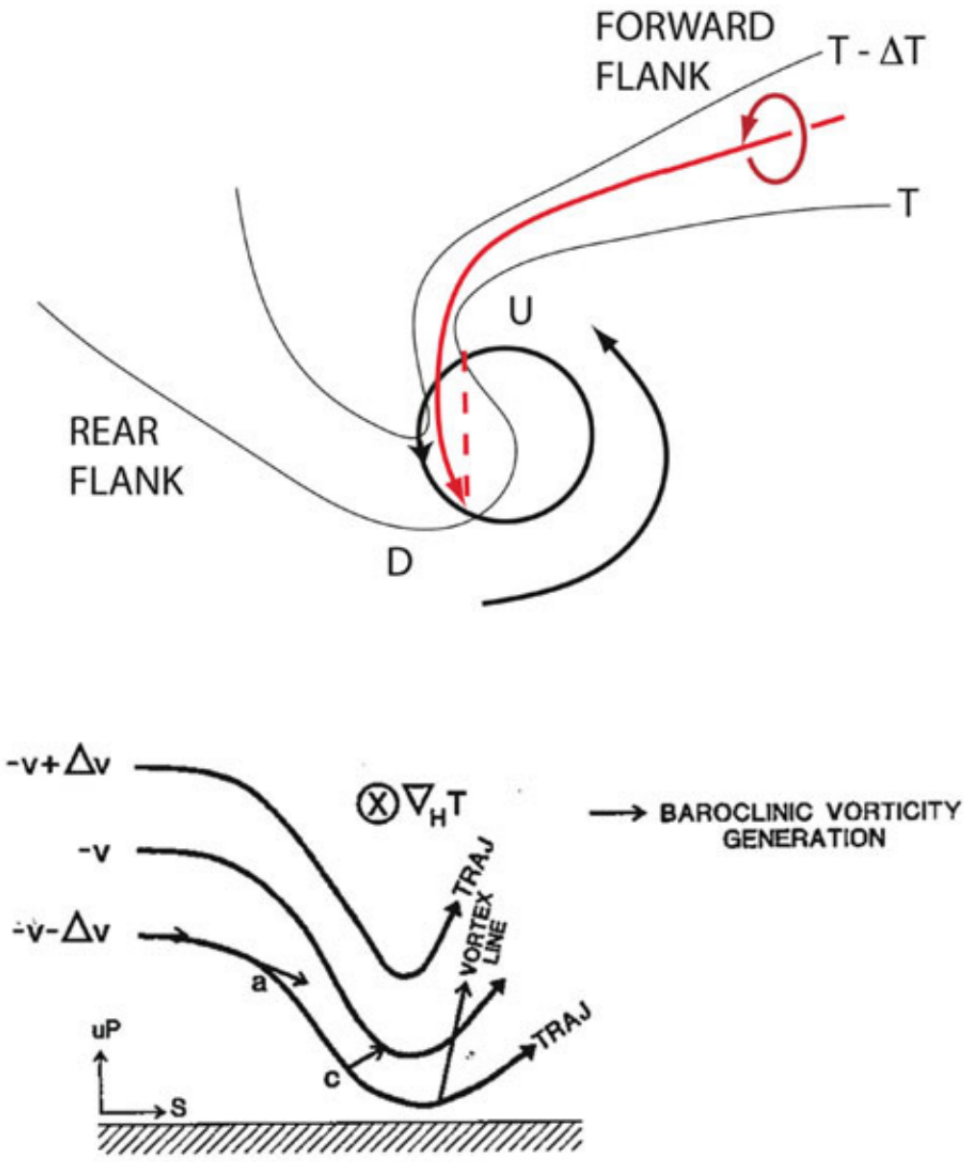


Figure 2.3: Schematic showing how cyclonic vorticity may be generated near the updraft-downdraft interface. (Top) Top-down schematic of steamlines representing streamwise vorticity approaching the mesocyclone from the forward flank. (Bottom) Vorticity vectors, which are tilted downward by the downdraft (anticyclonic vorticity) becomes tilted upward (becoming cyclonic vorticity) as it is advected faster below than it is aloft, as happens at the "foot" of a density current. This cyclonic vertical vorticity enters the base of the updraft where it is stretched. Figure courtesy of Bluestein (2013).

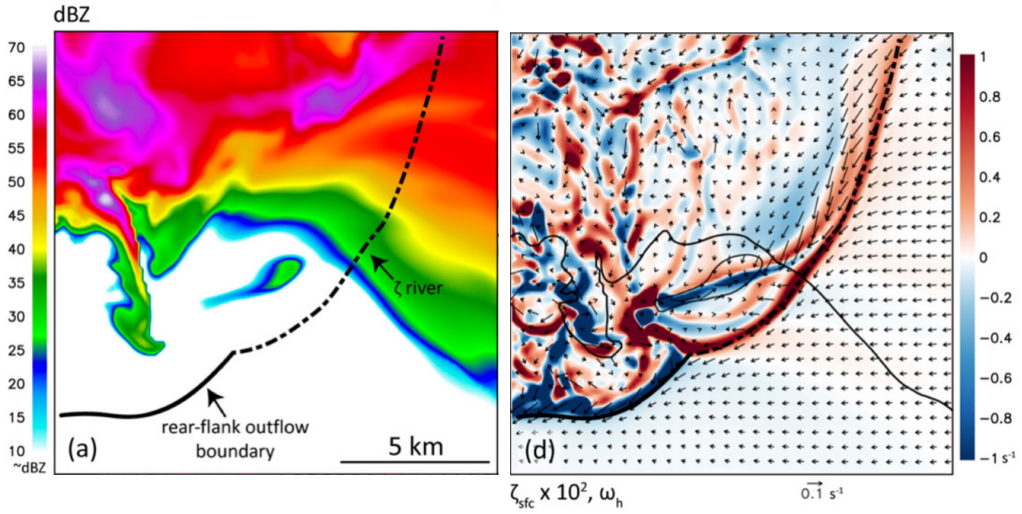


Figure 2.4: Horizontal cross section of (a) model-simulated reflectivity at 500 m (dBZ; shaded) and manually annotated boundaries. (d) The 10-m vertical vorticity ($s^{-1}$; shaded), 10-dBZ reflectivity at 500m AGL (black contour), and 10-m storm-relative, horizontal vorticity vectors. Figure adapted from Coffer and Parker (2017).

### 2.1.2 Tornado Maintenance and Tornado Decay

Tornado maintenance requires the continued collection and intensification of vertical vorticity near the tornado through tilting and stretching. As reviewed by Marquis et al. (2012), there are approximately five known storm-scale processes that help maintain a tornado, each of which has an inherent failure mechanism which can lead to tornado decay. The first requirement for tornado longevity is that it maintains its position at the intersection of the rear and forward-flank gust fronts (Fig. 2.5a). The forward and rear-flank gust fronts are regions with large density gradients where horizontal vorticity is generated. This horizontal vorticity often converges at the intersection of these boundary beneath the mesocyclone where it can be tilted and stretched by gradients in vertical velocity (e.g., Lemon and Doswell 1979; Brandes 1978, 1984; Wicker and Wilhelmson 1995; Alderman et al. 1999; Marquis et al. 2016). If a tornado becomes displaced from this favorable location through a process known as occlusion (Fig. 2.5a), it may gradually lose its source of low-level vorticity and the warm, buoyant inflow necessary to sustain

its updraft. However, there are exceptions to this decay mode where convergence and baroclinic generation of vorticity along a secondary, internal momentum surge within the rear-flank downdraft (RFD) allowed the tornado to collect and stretch vorticity and persist for a prolonged period of time (Marquis et al. 2008, 2012).

In addition to a tornado maintaining its position relative to the forward and rear-flank gust fronts, high angular momentum air must also converge into the tornado from the far field (Fig. 2.5b). While mesocyclone intensity is not necessarily directly correlated with tornado intensity (e.g., Atkins et al. 2012), a persistent mesocyclone is required in order to maintain convergence of a pool of high angular momentum air. Due to the conserved nature of angular momentum and the inverse relationship between the radius of the rotation and the rotational velocity, the convergence of high angular momentum air helps maintain the strongly rotating flow within tornadoes. Rasmussen and Straka (2007) found that low-level divergence reduced the angular momentum near the axis of rotation in the 2 June 1995 Dimmit, Texas, tornado, which led to the weakening and eventual dissipation of that tornado. Angular momentum and it role in tornado maintenance is further discussed in Chapter 4.

The third requirement for long-lived tornadoes is that their updraft-relative motion remains near zero (Fig. 2.5c). Dowell and Bluestein (2002) found in a cyclic tornadogenesis case that tornado maintenance was interrupted when the balance between storm inflow and outflow became imbalanced, separating the tornadoes from regions of strong vorticity tilting and stretching. Along with the previously discussed occlusion process, which occurs when storm inflow exceeds storm outflow, tornado decay via the displacement of the low-level vortex ahead of the mesocyclone by strong outflow has also been observed using mobile radars (e.g., French et al. 2014).

The fourth requirement for tornado maintenance is that the thermodynamic characteristics of the rear-flank downdraft must continue to be favorable for strong vertical velocities within the tornado (Fig. 2.5d). Markowski et al. (2002) found that the likelihood of a supercell producing a tornado and the longevity of a tornado increased both

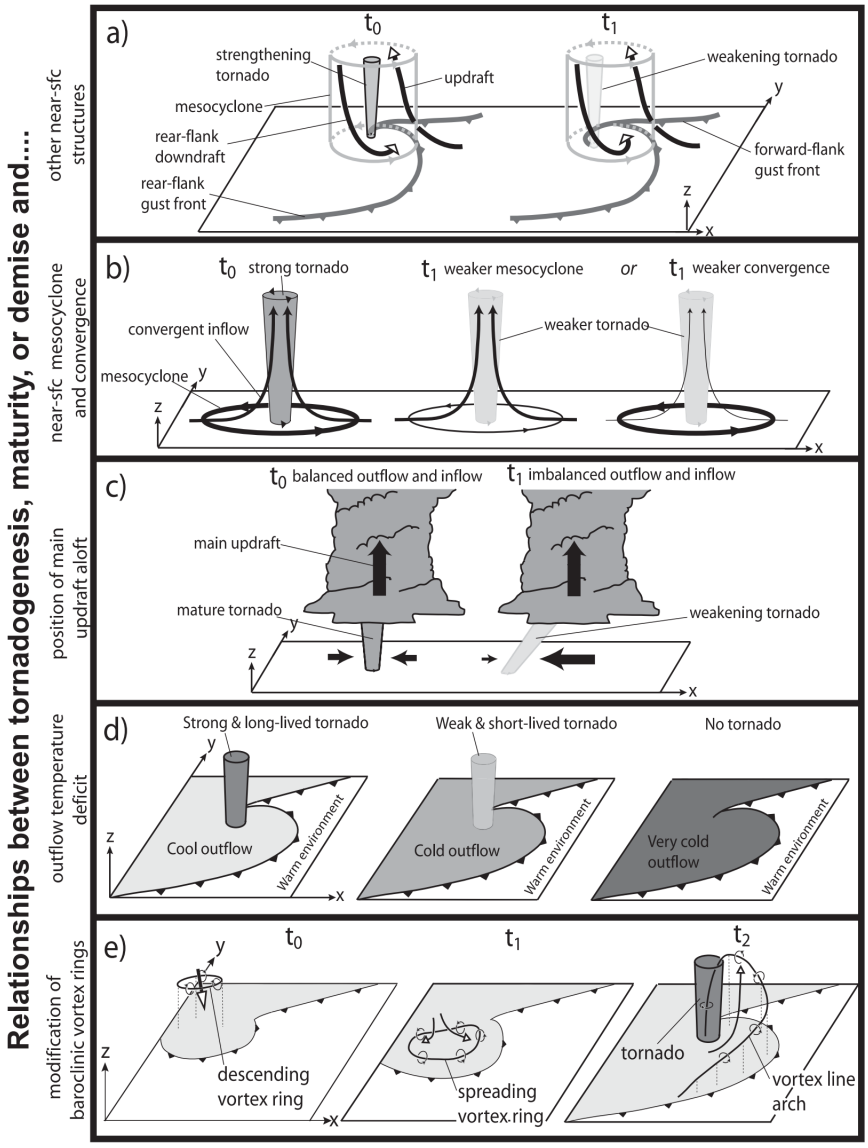


Figure 2.5: Schematic representations of five tornado maintenance mechanisms: (a) the observed relationship between the rear-flank downdraft and gust fronts, mesocyclone; (b) the relationship between tornado strength and changes in the strength of the low-level mesocyclone and convergence; (c) the relationship between tornado strength and its position relative to the primary updraft; (d) the relationship between tornado longevity and temperature deficit of the outflow; and (e) the relationship between tornadogenesis and the tilting of an initially sinking baroclinically generated vortex ring. Figure courtesy of Marquis et al. (2012).

increased as the relative buoyancy of the RFD increased. While RFD air is always negatively buoyant, downdraft air ingested into the mesocyclone that is only weakly negatively buoyant can by lifted by the nonlinear vertical perturbation pressure gradient force and will not significantly inhibit strong vertical accelerations necessary for tornado maintenance. While the perturbation pressure deficit in ongoing tornadoes is capable of lifting progressively colder air (Marquis et al. 2012), there may be a point where the buoyancy deficit within the RFD is a greater detriment to tornado maintenance than its counteracting contribution to the baroclinic generation or vorticity also necessary to maintain a strong vortex (e.g., Marquis et al. 2016).

Finally, baroclinically-generated vortex rings within the RFD, which are tilted by an elongated updraft to form vortex line arches that may play a role in tornadogenesis (Straka et al. 2007), may periodically generate and supply vertical vorticity in the vicinity of the tornado (Fig. 2.5e). It is uncertain whether this mechanism plays a significant role in generating the vorticity necessary to maintain a tornado; however, Marquis et al. (2012) found that in two of the four cases they investigated that secondary gust fronts generated vertical vorticity within the tornado via vortex line arches in conjunction with the primary rear-flank gust front. It was also speculated that divergence in the wake of the secondary gust front led to tornado decay in these tornadoes.

## 2.2 Tornado Dynamics

### 2.2.1 Tornado Structure

Tornadoes are typically broken up into four regions (Fig. 2.6), each with their own flow structure. The first region is called the outer flow region and is characterized by cyclostrophic balance where a radially inward directed pressure gradient force is balanced by a radially outward centrifugal force. Angular momentum is assumed to be constant within the outer flow region and is provided by the parent mesocyclone. This flow structure of constant angular momentum is known as a 'potential vortex.' The perturbation

pressure gradient force associated with this potential vortex is what drives low-level inflow into the tornado.

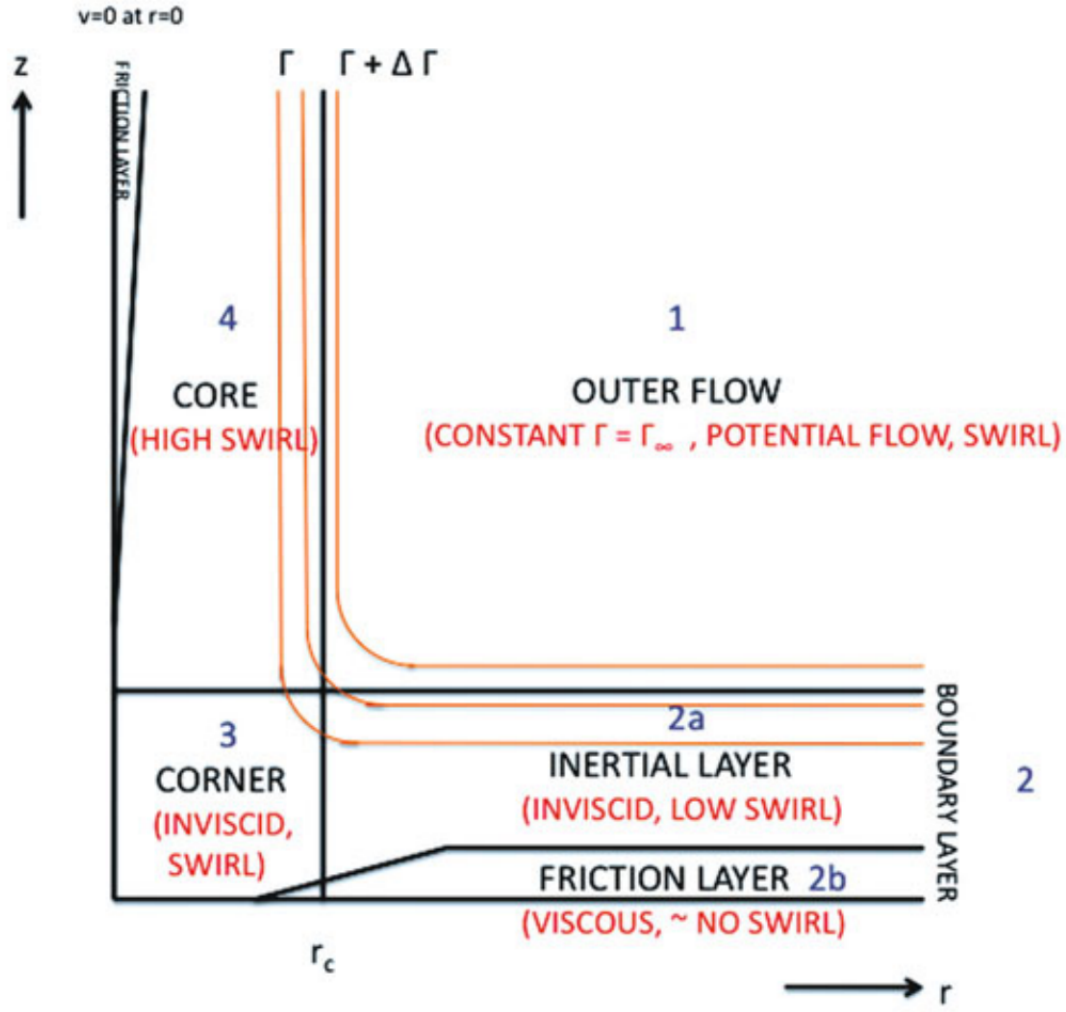


Figure 2.6: An axisymmetric vertical cross section schematic of the four regions of a tornado. Orange contours indicate lines of constant angular momentum. Figure adapted from Bluestein (2013).

The region of the tornado close to the surface is known as the 'tornado boundary layer.' In this layer, surface drag slows the tangential wind speeds resulting in a vertical gradient in angular momentum (Fig. 2.7). The largest vertical gradients in angular momentum occur in the layer nearest the surface where air is in direct contact with the ground. This

layer is known as the 'friction layer' and is only on the order of 10 m in depth (Kosiba and Wurman 2013), but decreases in depth toward the center of the tornado (Fig. 2.6). The friction layer is characterized by downward transport of angular momentum by turbulence and radial inflow into the tornado. Above the friction layer, the vortex deviates from cyclostropic balance due to the decrease in the centrifugal force owing to surface drag. As a result, air parcels are accelerated inward by the pressure gradient force. This region of inflow into the tornado is called the 'inertial layer.' The strongest winds within tornadoes occur within the inertial layer (Lewellen et al. 2000; Kosiba and Wurman 2013), likely near the top of the friction layer where angular momentum in the far field is still appreciable and strong, frictionally induced inflow occurs allowing for the convergence of angular momentum and subsequent increase in tangential flow.

Near the center of the tornado, the inward accelerating air within the tornado boundary layer converges, decelerates, and turns upward owing to continuity considerations. The place where air turns upward is called the 'corner region.' In the corner region, friction is negligible compared to other forces and flow is essentially laminar. Angular momentum impinges farther toward the axis of rotation in the corner region than above the tornado boundary layer. This 'inertial overshoot' of relatively high angular momentum at small radii (Fig. 2.7) is why the greatest tangential velocities occur within this region. Tornado structure and intensity are very sensitive to the the magnitude of tangential velocities within the corner region and their subsequent impact on swirl ratio (Lewellen et al. 2000). Swirl ratio will be further discussed in the next subsection.

Above the corner region is the 'tornado core.' The tornado core is characterized by solid body rotation where tangential velocity is a linear function of the radius from the axis of rotation and the angular momentum is a function of $r^2$. Therefore, the tornado core is characterized by radial gradients in tangential velocity and angular momentum (Fig. 2.7). Additionally, the core often has strong vertical velocities from the end-wall updraft generated in the corner region. In and ideal sense, the tornado core for low-swirl tornadoes is largely laminar, with the exception of a very narrow, conically-shaped

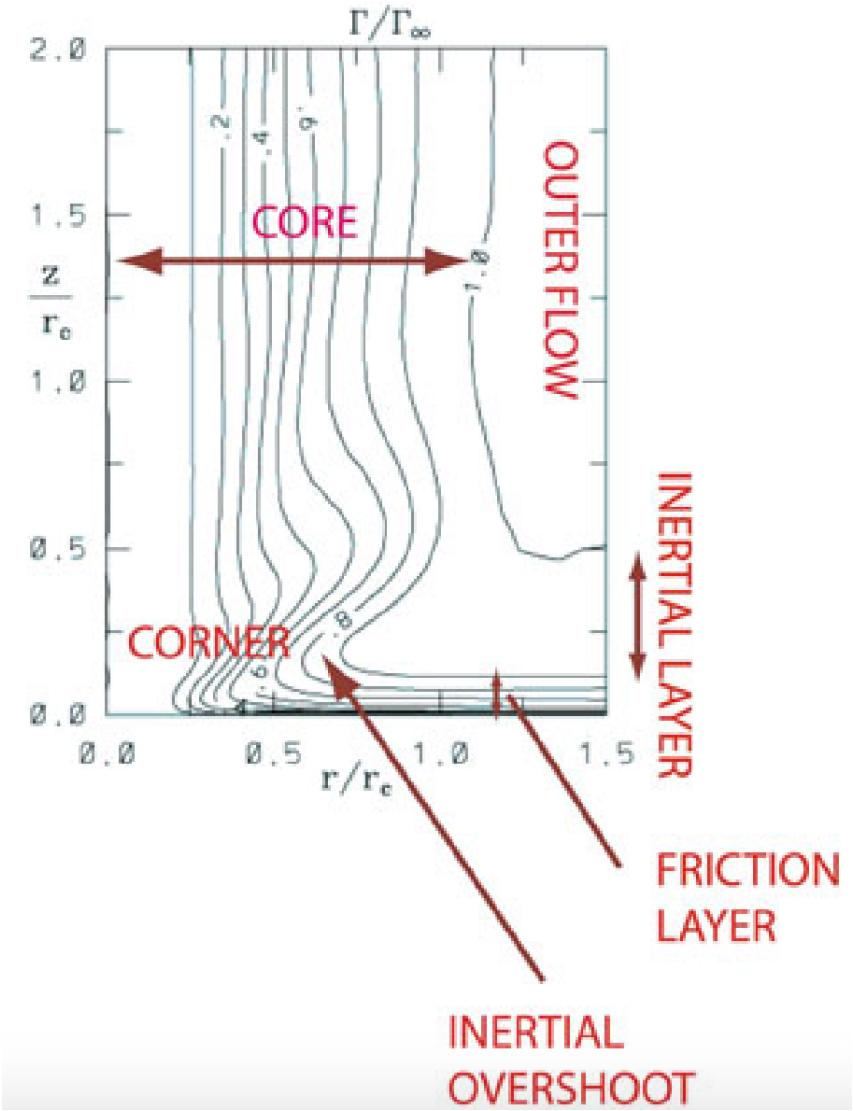


Figure 2.7: Lines of constant angular momentum in a vertical cross section of an idealized tornado. Figure adapted from Lewellen et al. (2000) by Bluestein (2013).

viscous layer immediately near the axis of rotation (Fig. 2.6). High-swirl tornadoes, however, can be highly turbulent. The horizontal extent of the core or 'core radius' is defined by the radius where angular momentum becomes approximately constant (i.e., where the tornado becomes a potential vortex in the outer flow region). This core radius is approximately the same as the depth of the tornado boundary layer. At the interface between the core and outer flow region, tangential velocity is maximized; thus, the the core radius is also known as the radius of maximum winds (RMW).

As the previous discussion infers, the radial profile of tangential velocity in a tornado is comprised of two main regimes. Near the center of the tornado, radial velocity increases linearly to the core radius, where tangential velocity is maximized, as prescribed by solid body rotation; then, tangential velocity decreases as a function of $\frac{1}{r}$ to satisfy the criteria for potential vortex flow. This simple model of a tornado is known as the 'Rankine combined' model (Rankine 1882), which satisfies the equations of motion for a steady-state vortex with no vertical motion (Fig. 2.8a). Observations of tornadoes (e.g., Tanamachi et al. 2007), indicate that the transition from solid body rotation to potential vortex flow is much smoother than the Rankine vortex indicates owing to diffusion (Fig. 2.8b). This tornado model, which allows for the radial diffusion of azimuthal momentum, is known as a 'Burgers–Rott' vortex (Burgers 1948). This steady-state vortex model allows for upward vertical motion, but vertical motion varies only as a function of height and radial velocity only varies as a function of radius. A vortex model that does satisfy the Navier-Stokes equations for an axisymmetric vortex while allowing for both upward and downward motion is the 'Sullivan' vortex (Sullivan 1959). The Sullivan vortex also allows for radial variations in vertical velocity, and apart from very small radii, is extremely similar to the Burgers-Rott vortex (Fig. 2.8c). However, it must be remembered that real-world tornadoes are neither axisymmetric nor steady state, so deviations from this vortex model are expected to occur.

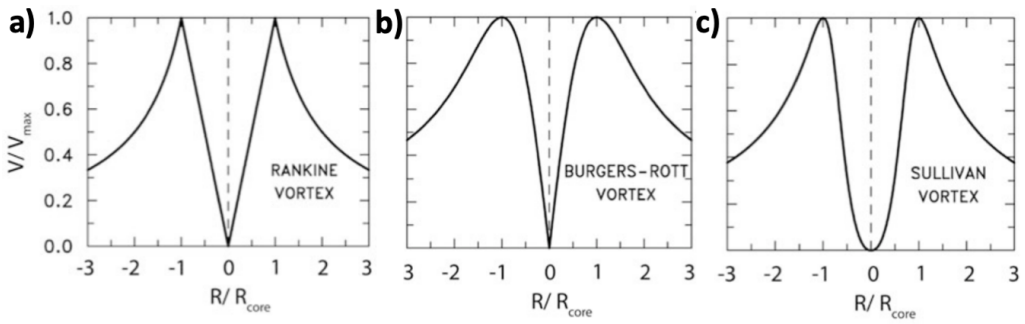


Figure 2.8: Radial profile of tangential velocity in the (a) Rankine combined, (b) Burgers–Rott, and (c) Sullivan vortex models. $R_{core}$ is the core radius and $V_{max}$ is the maximum in tangential velocity. Figure adapted from Brown and Wood (2012).

### 2.2.2 Swirl Ratio

The most important parameter defining the behavior and structure of tornadoes is the 'swirl ratio.' Swirl ratio is defined as:

$$S = \frac{R\Gamma}{2M}, \tag{2.2}$$

where R is the radius of the updraft, $\Gamma$ is the the circulation at the edge of the updraft ($2\pi$ multiplied by the angular momentum), and M is the volume flow rate of the updraft ($w\pi R^2$). Physically, swirl ratio can be thought of as the relationship between the rotational velocity within the tornado to the vertical mass flux. If the rotational velocity of a tornado is high, the perturbation pressure deficit will also be large, which can can slow or even reverse the direction of the vertical perturbation pressure gradient force if the circulation of the tornado exceeds the circulation of the mesocyclone. If the swirl ratio is large, this means that the resultant downward directed perturbation pressure gradient force is large relative to the strength of the updraft, which results in an axial downdraft in the center of the tornado.

When discussing tornado structure, it is useful to consider the 'secondary circulation' within the tornado (i.e., the radial and vertical velocity profiles). To interrogate this, it is necessary to define the equation of motion for radial velocity $u$. For an axisymmetric

vortex in an inviscid, constant density, incompressible fluid, the time rate of change of $u$ is defined as:

$$\frac{Du}{Dt} = \frac{v^2}{r} - \frac{1}{\rho}\frac{\partial p'}{\partial r}. \tag{2.3}$$

where the first term on the right hand side is the centripetal acceleration and the second term is the pressure gradient force. For low swirl tornadoes, the pressure gradient force is directed outward at extremely small radii (Fig. 2.9a), but the radius where the pressure gradient force switches from radially outward to radially inward is relatively small resulting in air being allowed to converge into the core of the tornado before decelerating and turning upward. This configuration of inflow impinging to the core of the tornado with an axial updraft is known as a 'single-cell' vortex (Fig. 2.10a). As swirl ratio increases, the radius where the pressure gradient forces changes sign decreases until it is always directed inward. However, for high swirl tornadoes the centrifugal acceleration term dominates at small radii resulting in the outward acceleration of air (Fig. 2.9b). The pressure gradient force only begins to dominate at large radii leading to convergence and upward motion displaced from the center of the vortex. The axial downdraft, divergence at small radii, and displaced updraft structure is known as 'two-cell' vortex flow (Fig. 2.10c). For medium swirl ratios, the downdraft may only impinge part way to the surface, leading to a vortex flow structure called a 'drowned vortex jump' (Fig. 2.10b). This flow structure is a special case of vortex breakdown, where the breakdown occurs displaced from the surface.

Because the net radial force is outward at small radii for high swirl tornadoes, high angular momentum air is not allowed to converge toward the center of the vortex. This leads to a relatively stagnant core with weak tangential velocities. Near the radius where high angular momentum can no longer converge, a circular vortex sheet arises from the strong radial gradient in tangential velocity (Fig. 2.11). Because this radius is also a region of strong convergence and vertical motion capable of stretching vorticity, this vortex sheet is unstable and breaks down into multiple intense smaller vortices, or 'suction vortices' (Fig. 2.12).

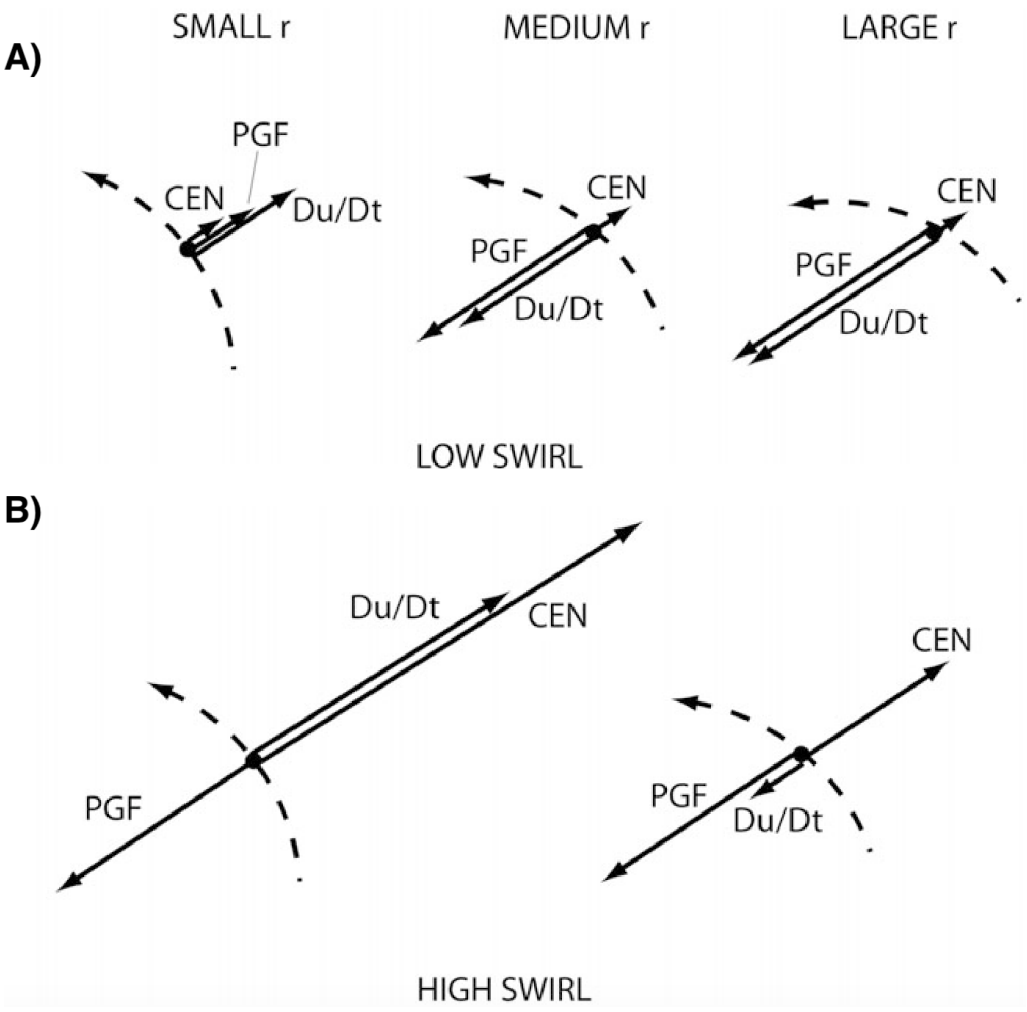


Figure 2.9: Idealized force diagrams for (a) low and (b) high swirl ratio tornadoes. Radius from the center of the tornado increases from left to right. Figure adapted from Bluestein (2013).

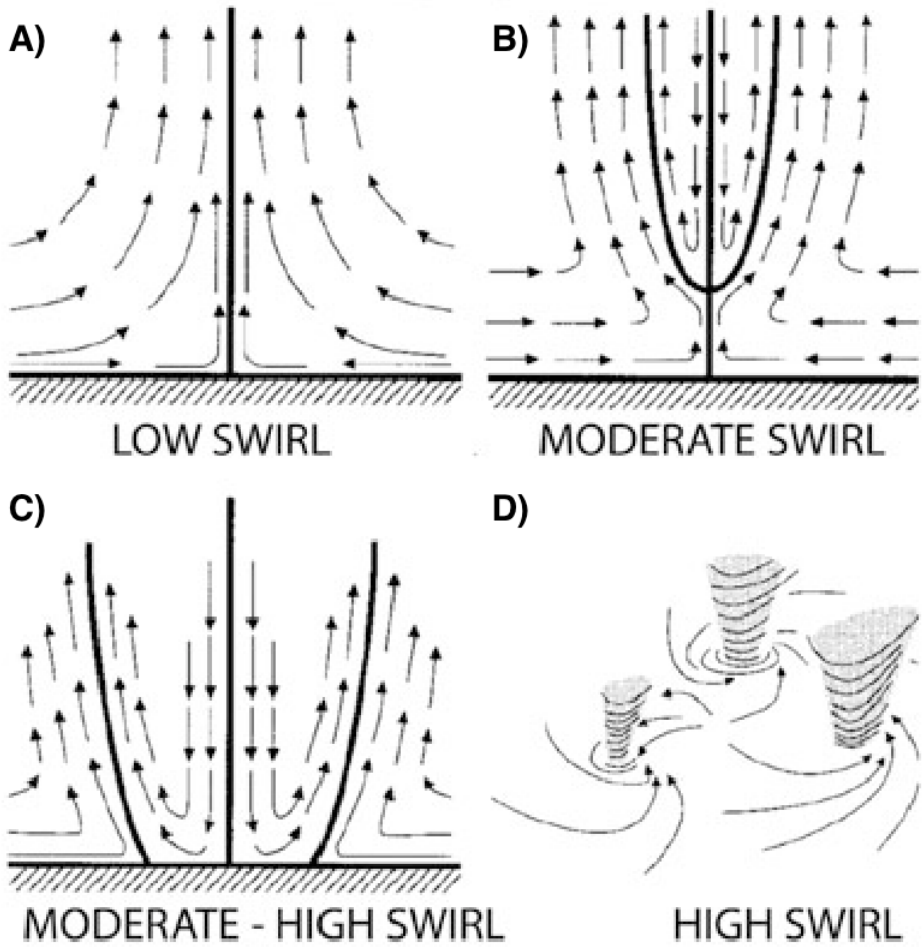


Figure 2.10: Vertical cross-sections through idealized tornadoes with (a) low, (b) medium, and (c) high swirl ratio. Arrows indicate the associated secondary circulations. Figure adapted from Bluestein (2013).

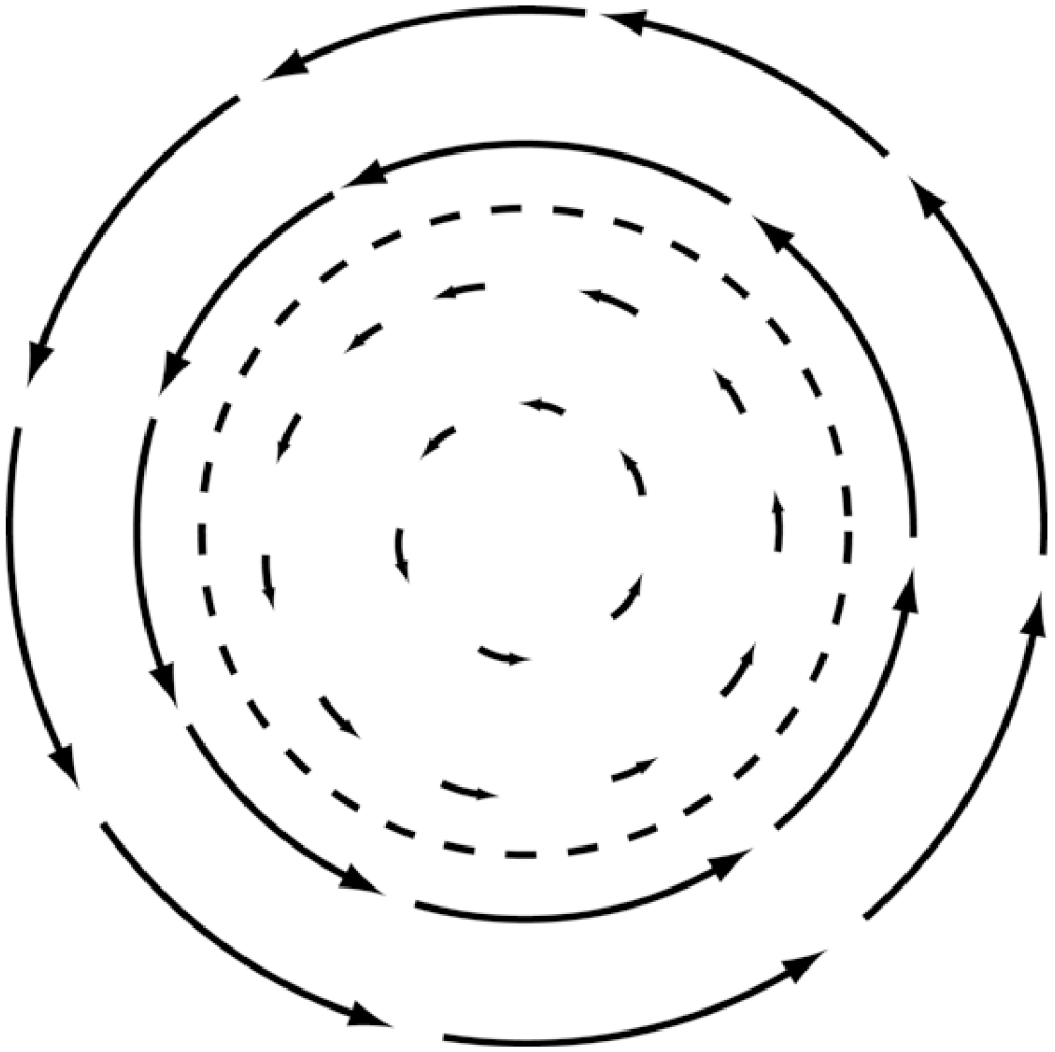

Figure 2.11: Idealized depiction of a vortex sheet (dashed line) that arises from the radial gradient in tangential velocities in a high-swirl tornado. Figure courtesy of Bluestein (2013).

Figure 2.12: Photograph of the 11 May 1982 Friendship, Oklahoma, multiple-vortex tornado. Photo courtesy of Bluestein (2013).

### 2.2.3 Debris Loading and Centrifuging

Radar measurements of the wind field within tornadoes are inherently biased because radars measure a power-weighted average velocity of scatterers within the a resolution volume and not the air velocity itself. As a result, measured velocities above the surface layer[1] within a tornado are likely an underestimation of the actual wind speeds, with the largest differences between air and scatterer velocities occurring within the corner flow and near-surface inflow regions (Lewellen et al. 2008). Larger differences occurs when scatterers, such as tornadic debris, are larger and more dense (Dowell et al. 2005). The lofting of large quantities of debris, known as debris loading, results in the transfer of momentum from the air to the debris, which may directly reduce the wind velocities by up to 50% (Lewellen et al. 2008; Bodine et al. 2016a). A slowing of the wind speeds in the corner flow region of tornadoes due to debris loading can alter a tornado's corner flow swirl ratio (Lewellen et al. 2008), which in turn can significantly alter the flow structure of the tornado (Lewellen et al. 2000; Lewellen and Lewellen 2007a,b). The reduction of the

[1]In the surface layer, stationary clutter may lead to an underestimate of Doppler velocity.

rotational velocity within a tornado can also increase the pressure within a tornado, which reduces the radial and vertical pressure gradient forces. This reduction of the pressure gradient force can decrease air velocities even where debris are not present (Lewellen et al. 2008; Bodine et al. 2016a). However, the introduction of debris may also significantly increase the total combined momentum of air and debris despite reducing the momentum of the air itself, which can increase the damage potential of the tornado (Lewellen et al. 2008). It is noteworthy that observational evidence of debris loading effects has yet to be noted. In a tornado crossing dirt fields with a large visible debris cloud, tornado velocities increased as debris loading increased, suggesting that storm-scale driven changes dominated debris-loading induced changes (Wakimoto et al. 2018).

Because debris have large radial outward momentum and the inward pressure gradient force is not strong enough to overcome this, debris move radially outward relative to the air within a tornado (Dowell et al. 2005). This behavior is known as debris centrifuging. Debris centrifuging results in the maximum tangential object motion being displaced outward from the maximum tangential air motion (Dowell et al. 2005) and an outward bias in Doppler velocity measured by a radar (Wakimoto et al. 2012; Nolan 2013; Bodine et al. 2016b). The centrifuging of debris and hydrometeors leaves a column void of many scatterers surrounded by an annulus of high power returns and high particle concentrations that usually expands with height (Dowell et al. 2005). This feature is known as a weak-echo column (WEC) when observing a vertical cross section or a weak-echo hole (WEH) when viewing a horizontal cross section or plan position indicator (PPI). Debris centrifuging also acts to transport angular momentum away from the tornado, and may either act to weaken a tornado by inhibiting the inward transport of angular momentum, or increase tornado intensity by recirculating debris (Fig. 2.13) with high momentum into the near-surface inflow (Lewellen et al. 2008). Low-level inflow and recirculation of debris may also explain the tapering and cutoff of the WEC (Fig. 2.14), since debris concentrations near the tornado core in the low levels can be orders of magnitude greater than elsewhere within the tornado (Dowell et al. 2005).

Figure 2.13: Photograph (copyright D. Dowell) of a tornado near Fulton, SD on 31 May 1998. The arrow marks a curl in the debris cloud that may indicate debris fallout and recirculation. Figure courtesy of Dowell et al. (2005).

## 2.3 Polarimetric Signatures in Supercells

This section overviews the polarimetric variable used in this study as well as summarizing a subset of polarimetric signatures commonly observed in supercells. While other polarimetric signatures exist, this section focuses on ones with well-established relationships with supercell kinematics. The reader is referred to Kumjian and Ryzhkov (2008) for more details on supercell polarimetric radar signatures that are beyond the scope presented here.

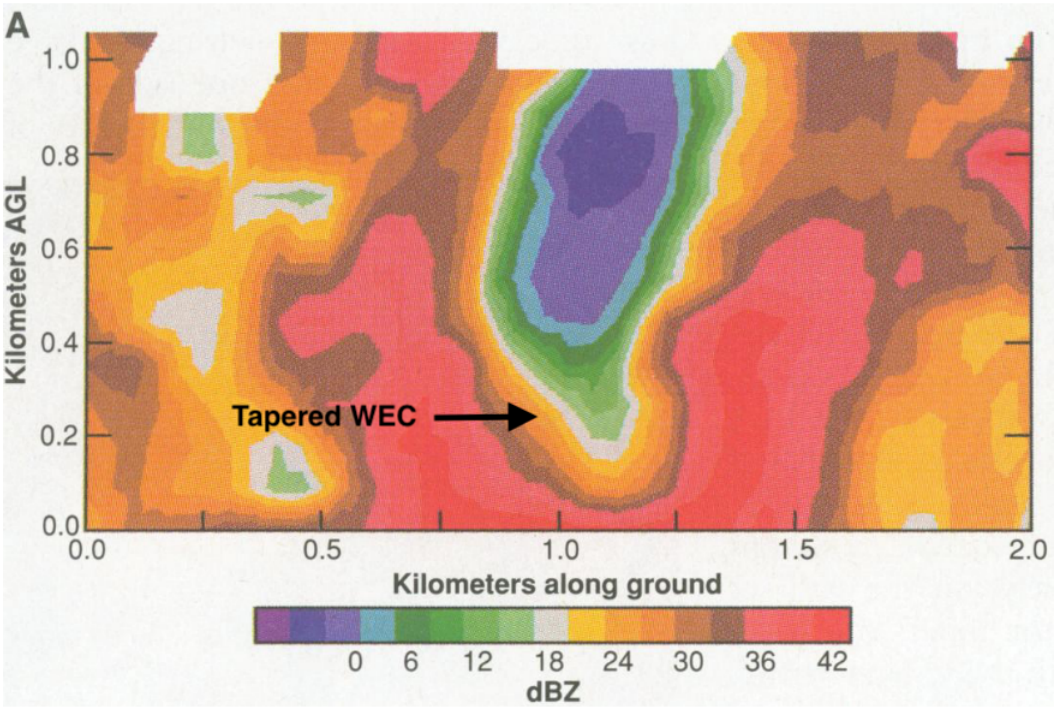


Figure 2.14: Vertical cross-section of Doppler-on-Wheels reflectivity (dBZ) in the 3 June 1995 Dimmitt, Texas, tornado illustrating a WEC. Figure adapted from Wurman et al. (1996).

### 2.3.1 Polarimetric Variable Overview

#### 2.3.1.1 Radar Reflectivity Factor

For Rayleigh scatterers, whose diameters are smaller than $\lambda/16$, where $\lambda$ is the transmit wavelength of the radar, radar reflectivity factor at horizontal polarization $Z_{hh}$ is given by:

$$Z_{hh} = \frac{4\lambda^4}{\pi^4 |K_m|^2} \langle N |S_{hh}|^2 \rangle, \tag{2.4}$$

where $K_m$ is the dielectric constant of the scatterers, N is the number of scatterers, and $S_{hh}$ is the scattering amplitude given by:

$$S_{hh} = \left(\frac{2\pi}{\lambda}\right)^2 c_m D^3, \tag{2.5}$$

where $c_m$ is a constant and $D$ is the diameter of the scatterer. It can be seen that reflectivity is a function of $D^6$ and is sensitive to particle size. However, particle concentrations within a radar resolution volume can vary by many orders of magnitude and the dielectric constant can range from ∼0.2 for ice to ∼0.9 for liquid water and potentially even larger for non-meteorological scatterers.

The reflectivity factor can be related to the reflectivity $\eta$ measured by the radar through the equation:

$$\eta = \frac{\pi^5}{\lambda^4} |K_m|^2 Z_{hh}, \tag{2.6}$$

and $\eta$ can be related to the power received by the radar through the weather radar equation:

$$E\big[P(r_0)\big] = \frac{P_t g^2 \lambda^2 \eta c \tau \pi \theta_1^2}{(4\pi)^3 r_0^2 l^2 16 \ln(2)}, \tag{2.7}$$

where $P(r_0)$ is the power received as a function of range $r_0$, $P_t$ is the transmit power, $g$ is the system gain, $c$ is the speed of light, $\tau$ is the pulse length, $\theta_1$ is the beamwidth, and $l$ are the one-way losses due to attenuation.

#### 2.3.1.2 Differential Reflectivity

The ratio of radar reflectivity factors at horizontal and vertical polarization is called differential reflectivity or $Z_{DR}$ and is defined as:

$$Z_{DR} = 10 \log_{10} \left( \frac{\langle |S_{hh}|^2 \rangle}{\langle |S_{vv}|^2 \rangle} \right). \tag{2.8}$$

Differential reflectivity is a measure of the aspect ratio of the scatterers within a resolution volume. For oblate (prolate) particles, where the horizontal (vertical) axis is greater than the vertical (horizontal) axis, $Z_{DR}$ will be positive (negative). Differential reflectivity is particularly useful for determining the median drop size of rain within a resolution volume since rain becomes increasingly oblate as its diameter increases (e.g., Seliga and Bringi 1976). Examples of prolate hydrometeors include conical graupel and ice needles. Therefore, outside the presence of strong vertical motion, the sign of $Z_{DR}$ can sometimes be used to discriminate between liquid and ice phase hydrometeors[2]. For spherical particles, or for a volume of scatterers with near-random orientations, $Z_{DR}$ will be near zero. For example, a volume of large hail, which tends to tumble as it falls, would present a near-random average orientation to the radar resulting in $Z_{DR}$ near zero. A selection of typical ranges of $Z_{DR}$ and other polarimetric variables for hydrometeors can be found in Table 2.1. One advantage of differential reflectivity is that it is independent of the concentration of scatterers and is therefore not affected by partial beam blockage or non-uniform beam filling.

#### 2.3.1.3 Co-polar Cross-correlation Coefficient

Co-polar cross-correlation coefficient or $\rho_{hv}$ is the measure of the correlation between the vertically and horizontally polarized received signals $S_{hh}$ and $S_{vv}$ and is defined as:

$$\rho_{hv}(0) = \frac{\langle S_{vv} S_{hh}^* \rangle}{\langle |S_{hh}|^2 \rangle^{0.5} \langle |S_{vv}|^2 \rangle^{0.5}}. \tag{2.9}$$

[2]The exception to this being hexagonal plates, which are roughly oblate

Table 2.1: Typical values of polarimetric variables for a selection of precipitation types at S band adapted from Doviak and Zrnić (1993).

| Precipitation type | $Z_{hh}$ (dBZ) | $Z_{DR}$ (dB) | $\rho_{hv}$ | $K_{DP}$ ($^\circ$ km$^{-1}$) |
|---|---|---|---|---|
| Drizzle | <25 | 0 | >0.99 | 0 |
| Rain | 25 – 60 | 0.5 – 4 | >0.97 | 0 – 10 |
| Dry snow | <35 | 0 – 0.5 | >0.99 | 0 – 0.5 |
| Melting snow | <45 | 0 – 3 | 0.8 – 0.95 | 0 – 2 |
| Graupel | 40 – 55 | -0.5 – 3 | >0.99 | -0.5 – 2 |
| Small, wet hail | 50 – 60 | -0.5 – 0.5 | >0.95 | -0.5 – 0.5 |
| Large, wet hail | 55 – 70 | <-0.5 | >0.96 | -1 – 1 |
| Rain and hail | 50 – 70 | -1 – 1 | >0.9 | 0 – 10 |

The numerator of the equation is the covariance of the returned horizontally and vertically polarized signals and the denominator is the product of the respective variances of the two signals. Typically, $\rho_{hv}$ is estimated at zero lag and only the magnitude is considered. For a distribution of scatterers, $\rho_{hv}$ is dependent upon the diversity of particle sizes, orientations, shapes, irregularities, and phase compositions within the sampling volumes (e.g., Ryzhkov et al. 2005b; Kumjian and Ryzhkov 2010). Correlation coefficient is particularly useful in discriminating between meteorological and non-meteorological scatterers. Hydrometeors are relatively uniform in their shape and orientation, and thus usually exhibit $\rho_{hv}$ >0.9. Non-meteorological scatters such as biological scatterers or debris tend to be more randomly shaped and oriented and thus have lower values of $\rho_{hv}$, often below 0.5 (e.g., Ryzhkov et al. 2002). However, mixed-phase precipitation such as rain mixed with hail can also have low $\rho_{hv}$, but values approaching those produced by non-meteorological scatterers are rare. The effects of resonance scattering can also significantly reduce correlation coefficient for large particle and is highly sensitive to the

the wavelength of the radiated signal and the dielectric constant of the scatterer (e.g., Kumjian et al. 2010a; Ryzhkov et al. 2013; Bodine et al. 2016b).

#### 2.3.1.4 Differential Phase and Specific Differential Phase

Differential propagation phase $\Phi_{DP}$ is a measure of the phase lag between horizontally and vertically polarized signals and varies based on waves encountering non-spherical scatterers. Differential phase is calculated using:

$$\Phi_{DP} = \Phi_H - \Phi_V, \tag{2.10}$$

where $\Phi_H$ and $\Phi_V$ are the respective phases of the signals at horizontal and vertical polarizations. As an example, a radar beam traveling through heavy rain will encounter more oblate hydrometeors than prolate hydrometeors and thus the phase of the horizontally polarized wave will begin to lag increasingly behind the phase of the vertically polarized wave. This lag results in the received phase from horizontal polarization being greater than the phase of the vertically polarized wave for the same volume of targets and the differential phase becoming increasingly positive with range from the radar.

The phase shift measured by $\Phi_{DP}$ is cumulative along the two-way path of the radar beam. The local phase shift owing to a single volume of scatterers is called specific differential phase or $K_{DP}$ and is calculated using the range derivative of $\Phi_{DP}$:

$$K_{DP} = 0.5\frac{\partial\big(\Phi_{DP}\big)}{\partial r}. \tag{2.11}$$

For practical purposes, $K_{DP}$ is calculated using a linear regression of range-filtered $\Phi_{DP}$. Specific differential phase is a useful tool for quantitatively estimating precipitation rates and correctiung for attenuation and differential attenuation due to its immunity to errors in radar calibration, attenuation, beam blockage, and noise (e.g., Kumjian and Ryzhkov 2010).

### 2.3.2 $Z_{DR}$ Column

Differential reflectivity is a useful tool for identifying the location of thunderstorm updrafts aloft. Relatively narrow (4–8 km wide) columns of positive $Z_{DR}$, known as $Z_{DR}$ columns (Fig. 2.15) are the result of positive temperature perturbations associated with warm, buoyant air within thunderstorm updrafts. As a result of the positive temperature perturbation, liquid rain that exhibits positive $Z_{DR}$ can reside well above the freezing level (e.g., Caylor and Illingworth 1987; Conway and Zrnić 1993). $Z_{DR}$ columns are located on the inflow side of the storms and are slightly displaced from the largest magnitudes of vertical velocity because the largest raindrops fall out at the periphery of the updraft (Kumjian and Ryzhkov 2008). Similar to $Z_{DR}$ columns, $K_{DP}$ columns are often displaced slightly to the west of $Z_{DR}$ columns where greater liquid water content exists. Documenting the temporal evolution of $Z_{DR}$ columns may be useful as changes in column height may indicate strengthening updrafts and subsequent storm intensification (Hubbert et al. 1998; Kumjian et al. 2014; Snyder et al. 2017). For example, the maximum altitude of the $Z_{DR}$ column above the freezing level may be able to distinguish strongly tornado storms, from weakly tornadic or non-tornadic storms (Van Den Broeke 2017).

### 2.3.3 $Z_{DR}$ Arc

The '$Z_{DR}$ arc' is a region of enhanced $Z_{DR}$ along the forward flank reflectivity gradient of supercells (Fig. 2.16) that is formed by hydrometeor size sorting (Kumjian and Ryzhkov 2008). Small raindrops with slow terminal fall velocities have large residence times in vertical layers with strong storm-relative winds. These small raindrops are transported farther from the supercell updraft compared to large raindrops (Dawson II, D. T. et al. 2014). This process leaves a shield of raindrops with large median drop sizes and inherently large $Z_{DR}$ on the inflow side of the supercell forward flank due to strong southerly storm-relative winds that are usually found in in the lowest 1-2 km of supercell environments. The magnitude of $Z_{DR}$ within the arc may be modified by the

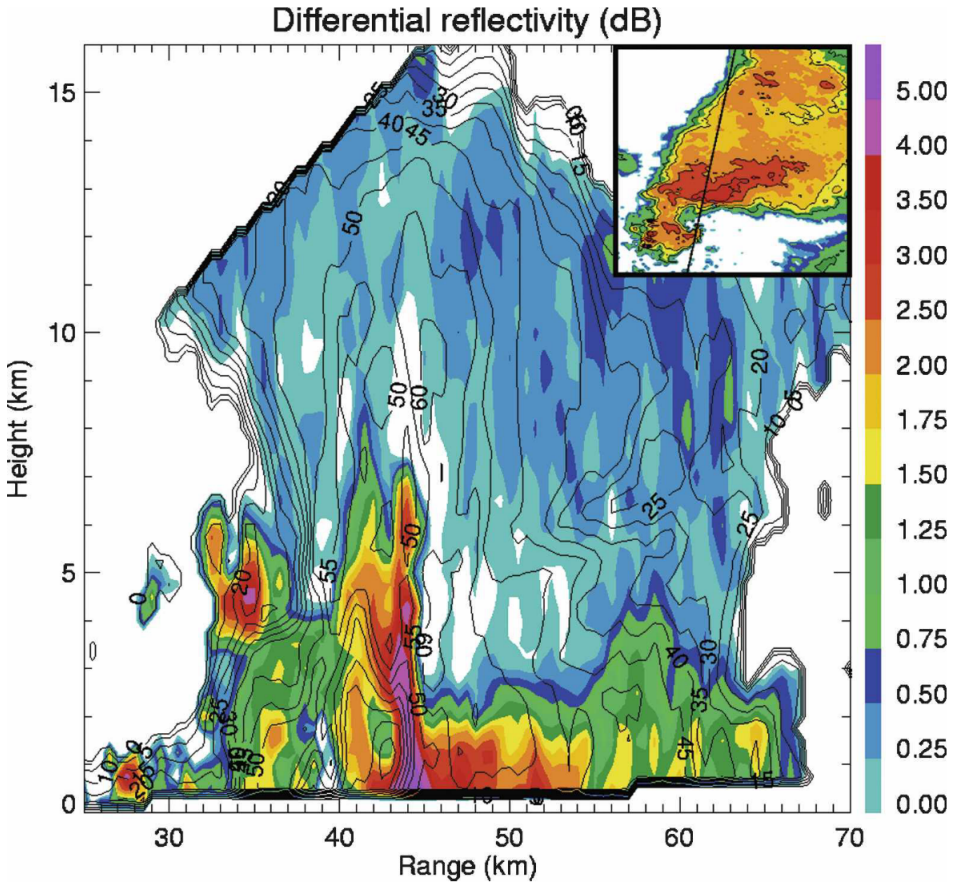


Figure 2.15: A vertical cross section of $Z_{DR}$ (dB) through a supercell updraft illustrating a prominent $Z_{DR}$ column. Black contours represent values of reflectivity (dBZ). Figure courtesy of Kumjian and Ryzhkov (2008).

amount of low-level storm-relative helicity (SRH) (Kumjian and Ryzhkov 2009) or simply the magnitude of the storms relative winds within the layer of size sorting (Dawson II, D. T. et al. 2014). Additionally, the storm-relative winds dictate the sedimentation and size sorting of hail within a supercell, which in turn impacts the representation of the $Z_{DR}$ arc since the presence of large, dry hail can significantly lower the $Z_{DR}$ within a resolution volume (Dawson II, D. T. et al. 2014). Because of its relationship with low-level wind shear and inflow strength, the $Z_{DR}$ arc could potentially be used to discriminate between tornadic and non-tornadic storms. Van Den Broeke (2017) found that $Z_{DR}$ arcs in tornadic storms had higher mean $Z_{DR}$ and larger areal extent than arcs in non-tornadic storms, partly due to tornadic storms having smaller, more concentrated hail cores.

Disruptions in the $Z_{DR}$ arc near the storm updraft may indicate that large hail is falling out near the updraft (e.g., Kumjian and Ryzhkov 2009; Tanamachi and Heinselman 2016) or that mesocyclone occlusion is occurring (Kumjian et al. 2010b; Palmer et al. 2011; Kurdzo et al. 2015). In the case of mesocyclone occlusion, the $Z_{DR}$ arc shrinks as a result of decreased storm-relative inflow in the low levels from a weakening updraft, decreasing size sorting of hydrometeors (Kumjian et al. 2010b). Additionally, an influx of small drops from the rear-flank downdraft into the supercell forward flank occurs (Kumjian 2011). If another mesocyclone forms, a new $Z_{DR}$ arc redevelops along the forward flank (e.g., Kumjian et al. 2010b; Palmer et al. 2011; Kurdzo et al. 2015).

### 2.3.4 $K_{DP}$ Foot

Within the precipitation core of supercells, a downshear-elongated region of enhanced $K_{DP}$ is sometimes referred to as the '$K_{DP}$ foot' (Romine et al. 2008). The $K_{DP}$ foot is located to the left of the storm updraft and adjacent to or slightly overlapping with the $Z_{DR}$ arc (Fig. 2.17). The high values of $K_{DP}$ indicates that the $K_{DP}$ foot has a high liquid water content, but its displacement from the largest values of $Z_{DR}$ along the forward flank reflectivity gradient suggest it is composed of large concentrations of small raindrops. An increase in the separation between the maxima in $Z_{DR}$ and $K_{DP}$ would

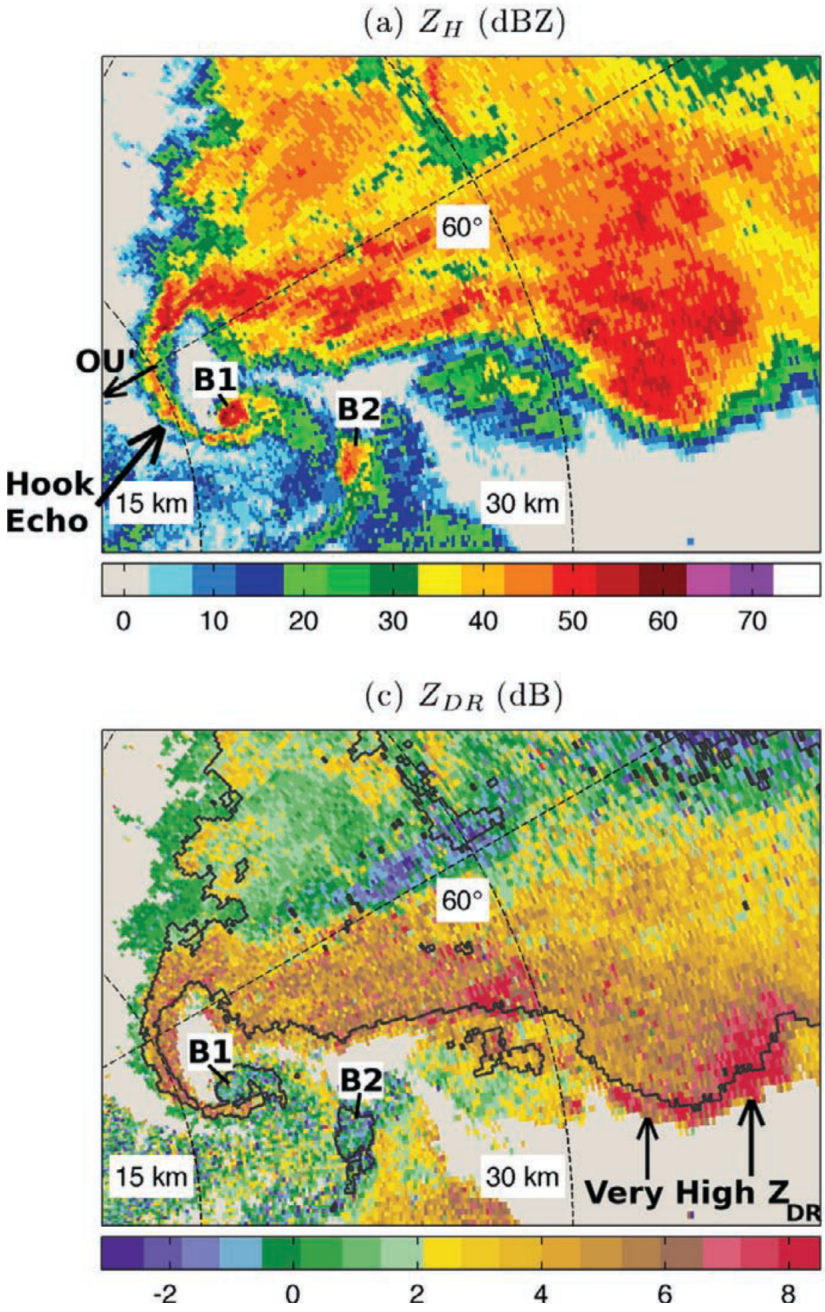


Figure 2.16: PPI plots of OU-PRIME (a) reflectivity (dBZ) and (c) differential reflectivity (dB) illustrating a prominent $Z_{DR}$ arc in the 10 May 2010 Norman-Little Axe supercell. Figure adapted from Palmer et al. (2011).

indicate that greater size sorting of small and large raindrops is occurring, which may be the result of increased SRH (e.g., Kumjian and Ryzhkov 2009) or storm-relative inflow (e.g., Dawson II, D. T. et al. 2014). Observational studies have documented increasing separation between the $K_{DP}$ foot and the $Z_{DR}$ arc near the time of tornadogenesis in supercell cases (Romine et al. 2008; Crowe et al. 2012) and in non-supercell cases (Loeffler and Kumjian 2018), suggesting that the $K_{DP}$ foot and the $Z_{DR}$ arc may have operational utility in aiding forecasters' warning decisions.

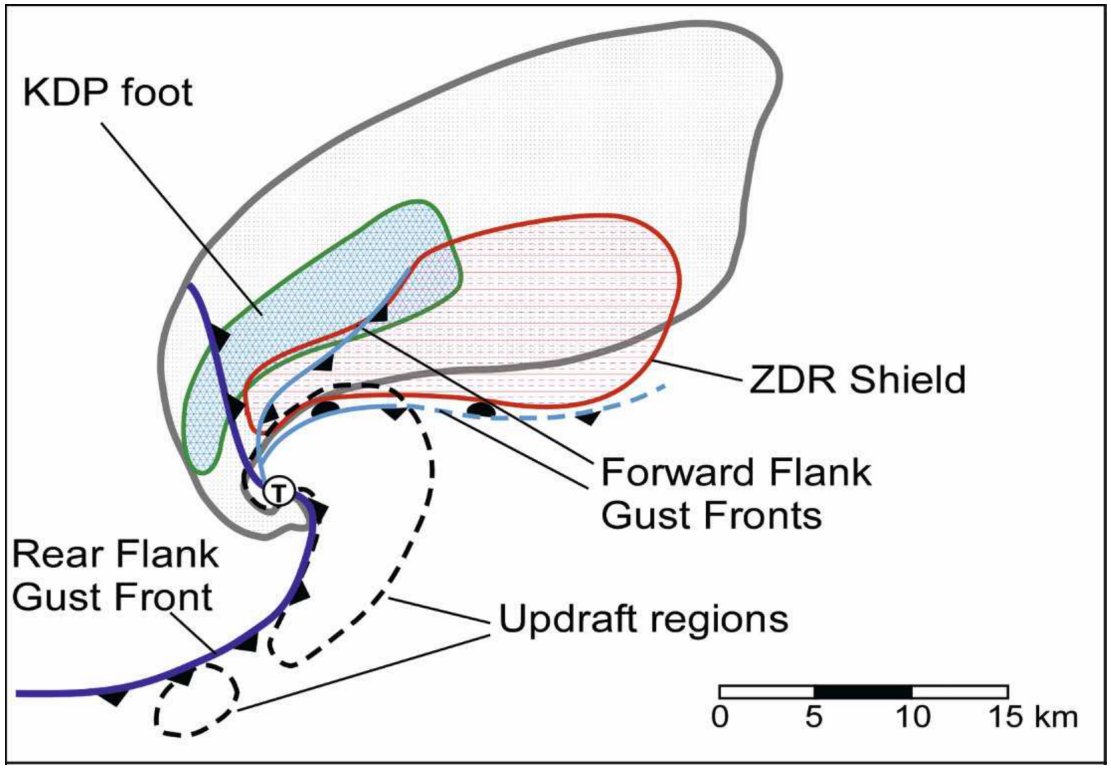


Figure 2.17: A conceptual model illustrating the relative position of the $K_{DP}$ foot to other features within the supercell. Figure courtesy of Romine et al. (2008).

# Chapter 3

# Kinematic and Polarimetric Radar Observations of the 10 May 2010, Moore-Choctaw, Oklahoma, Tornadic Debris Signature

In this chapter, data collected by the University of Oklahoma's Polarimetric Radar for Innovations in Meteorology and Engineering (OU-PRIME) C-band radar as well as KTLX and KOUN WSR-88D S-band radars are used to construct single- and dual-Doppler analyses of a tornadic supercell that produced an EF-4 tornado near Moore and Choctaw, Oklahoma, on 10 May 2010. The spatial distribution of polarimetric radar variables and how each variable relates to kinematic fields such as vertical velocity and vertical vorticity are documented. Special consideration is given to polarimetric signatures associated with subvortices within the tornado. An observation of negative $Z_{DR}$ at the periphery of tornado subvortices is presented and discussed. Finally, dual-Doppler wind retrievals are compared to single-Doppler axisymmetric wind fields to illustrate the merits of each method.

## 3.1 Introduction

The 10 May 2010, OK tornado outbreak produced 55 tornadoes, including 36 in the Norman Weather Forecast Office's county warning area and two tornadoes rated 4 on the Enhanced Fujita (EF) scale. This case provides a rare opportunity to perform dual-Doppler polarimetric radar analyses on large, debris-lofting tornadoes and compare the results of dual-Doppler analyses to those performed by single-Doppler methods. The serendipitous collection of data at relatively close range by KTLX and KOUN WSR-88D S-band radars, and OU-PRIME C-band radar operated by the Advanced Radar Research Center (ARRC), briefly provide a favorable dual-Doppler lobe for the interrogation of the Moore-Choctaw, OK tornado, which will be the focus of this study.

While previous studies have focused primarily on single radar representations of the TDS, little work has been done to document the two- and three-dimensional wind field associated with a large, heterogeneous TDS using two radars. The use of dual-Doppler derived data may provide insight to some of the kinematic processes that have been hypothesized in prior literature that utilized single-Doppler radar data. Further details regarding the 10 May 2010 outbreak can be found in Palmer et al. (2011).

## 3.2 Methods

### 3.2.1 Radar Data

The polarimetric radar data used in this project were collected by OU-PRIME, located near the National Weather Center, and by KOUN, which is located at Westheimer airport in Norman, OK. Supplementary velocity data for dual-Doppler analyses were provided by KTLX, a WSR-88D radar. Selected specifications for each radar appear in Table 3.1. For a full system overview of OU-PRIME and details regarding system performance during the event, please refer to Palmer et al. (2011). At its closest range, the Moore-Choctaw tornado was sampled as low as ∼100 m above radar level (ARL) by OU-PRIME. Late in the period, the lowest OU-PRIME scan available (1.0°) sampled the Moore-Choctaw tornado at an altitude of ∼400 m. KTLX sampled the Moore-Choctaw tornado as close as ∼5 km, with a beam height as low as ∼75 m at the range of the center of the tornado.

Radar data editing for this project was completed using the National Center for Atmospheric Research Earth Observing Lab's Solo3 editing software (Oye et al. 1995) available online at https://www.eol.ucar.edu/software/solo3. Clutter, identified by regions of stationary high power returns with near-zero radial velocity, and erroneous data, most often in the form of azimuths affected by partial beam blockage or multiple-trip contamination, were subjectively removed. Low values of signal-to-noise ratio (SNR) were objectively thresholded below 0.3. No $\rho_{hv}$ thresholding was performed, which potentially introduces error to the analyses due to variance in radar measurements increasing as $\rho_{hv}$ decreases

Table 3.1: A selection of radar characteristics for OU-PRIME, KTLX, and KOUN.

| **Radar Characteristic** | **OU-PRIME** | **KOUN** | **KTLX** |
|---|---|---|---|
| Operating Frequency | 5510 MHz | 2705 MHz | 2700-3000 MHz |
| Peak Power | 1000 kW | 760 kW | 750 kW |
| Beam Width | 0.45° | 0.93° | 0.93° |
| Gate Length | 125 m | 250 m | 250 m |
| Nyquist Velocity | 16.06 m $s^{-1}$ | 26.92 m $s^{-1}$ | 26.92 m $s^{-1}$ |
| Volumetric update time | 2 min 50 s | 4 min 18 s | 4 min 18 s |
| Polarization | STSR | STSR | N/A |
| Scanning Strategy | 1.0°, 2.0°, 3.0°, 4.0°, 5.0°, 6.5°, and 9.0° | VCP 12 | VCP 12 |

(Bringi and Chandrasekar 2001). However, a $\rho_{hv}$ threshold would eliminate many desirable volumes containing debris and bias the distribution of polarimetric variables in the TDS. Solo3 was also used to subjectively dealias radial velocity prior to performing the dual-Doppler and axisymmetric analyses. Values of differential phase in the vicinity of the TDS ranged between -20° and 0° and a simple differential attenuation correction calculation (not shown) created no appreciable changes in the polarimetric fields near the tornado. Thus, no differential attenuation correction was applied to the data presented.

### 3.2.2 TDS Criteria

The original criteria for a TDS at S band proposed by Ryzhkov et al. (2005b) were values of $\rho_{hv} < 0.8$, $Z_{DR} < 0.5$ dB, and $Z_H > 45$ dBZ collocated with a vortex signature in radial velocity ($V_r$). The criteria for $Z_H$ were relaxed by Schultz et al. (2012a) to 30 dBZ and were further relaxed by Van Den Broeke and Jauernic (2014) to 20 dBZ given the Warning Decision Training Branch (WDTB 2013) recommendation based on numerous tornadic events exhibiting $Z_H < 30$ dBZ. In order to include the WEH, the $Z_H$

threshold for tornadic debris is 10 dBZ. Radar volumes with $Z_H$ in the 10-20 dBZ range were screened to ensure that they were representative of tornadic debris. This project uses the original $\rho_{hv} < 0.8$ and $Z_{DR} < 0.5$ dB thresholds as additional constraints. Finally, pixels also had to be within 5 km of the tornado center to be included. These constraints perform well in spatially identifying tornadic debris in the Moore-Choctaw tornado (not shown); however, for many TDSs, an upper $\rho_{hv}$ threshold of 0.8 may be too restrictive. Additionally, a $Z_{DR}$ threshold may perform poorly if too much precipitation is present from entrainment Bodine et al. (2014). Therefore, the authors do not recommend these thresholds for TDS identification in all circumstances. Other TDS identification methods have been implemented with success in the past, including using percentile-based polarimetric thresholds as opposed to specific value thresholds (Bodine et al. 2014) and using an adaptive fuzzy logic system (Wang and Yu 2015).

### 3.2.3 Dual-Doppler Analysis

Dual-Doppler and objective analyses are performed using the Observation Processing and Wind Synthesis (OPAWS) code developed by David Dowell (NOAA/Earth System Research Laboratory) and Lou Wicker (National Severe Storms Laboratory). Documentation and source code can be found at http://code.google.com/p/opaws/. Radar data are first objectively analyzed on a 30 km x 30 km domain using a two-pass Barnes method (Barnes 1964) with a second pass convergence parameter $\gamma$ of 0.3 used to further recover the amplitudes of smaller-scale spatial structures (Barnes 1973; Majcen et al. 2008). The limiting spatial resolution ($\delta$) in the vicinity of the tornado was ∼350 m. A smoothing parameter [$\kappa = (1.33\delta)^2$] of 0.216 km$^{-2}$ (Pauly and Wu 1990) was chosen. A horizontal and vertical grid spacing of 250 m was chosen to accommodate coarser limiting spatial resolution in other parts of the analysis domain[1]. Motion of the supercell between each radar sweep in a volume is linearly corrected within the objective analyses prior

[1]We used the formula for grid spacing ($\Delta = \delta/2.5$) based on Koch et al. (1983) where values of $\delta$ exceeded 600 m in parts of the analysis domain.

to performing the dual-Doppler synthesis using a translation velocity determined by a comparison between the mesocyclone location at the previous time to its location at the analysis time. While correcting for advection partially mitigates errors in the analyses caused by propagation between elevation scans and mismatched temporal sampling by the two radars, the mesocyclone motion may not be representative of tornado motion at all heights and can introduce errors in the analyzed location of the tornado at some levels.

Dual-Doppler wind syntheses are performed in regions where the look angle difference between OU-PRIME and KTLX is between 20 and 160 degrees. Vertical velocities are calculated using upward integration of the mass continuity equation with the implementation of a $w = 0$ at $z = 0$ boundary condition. Density is assumed to decrease exponentially with height. Hydrometeor fall speeds are corrected using the terminal fall velocity-reflectivity relationships[2] obtained from Joss and Waldvogel (1970) and implemented by OPAWS (Potvin et al. 2012). It is noted that OU-PRIME did not sample the mass field below 400 m in the vicinity of the tornado, which may lead to large errors in the vertical velocity estimates, however, KTLX sampled the wind field below 75 m, which may partially mitigate this issue.

A major crux in the dual-Doppler assumption is that the two radars are observing the same volume of space at nearly the same time. Because this study does not use coordinated radar scans, and OU-PRIME was running a different scanning strategy than the WSR-88D radars, only two analysis times approached synchronization. The first analysis time began at approximately 2223 UTC approximately 3 min after tornadogenesis when scan times between OU-PRIME and KTLX varied between 3-10 s. The 2223 dual-Doppler analysis (Fig. 3.1) illustrates some interesting features, including a cyclonic-anticyclonic vortex pair and small raindrops in the rear-flank downdraft. However, these topics are beyond the scope of this paper, and the lack of a TDS in the early lifecycle of

[2]These relationships were derived for precipitation, and are likely to be underestimates of the fall speeds for debris. However, no alternative methods for debris exists.

the Moore-Choctaw tornado dictates that this time serve only as comparison to a later time with a TDS. Nonetheless, the 2223 UTC time serves as a quality control check of the methodology, confirming the locations of supercell structures, like the rear-flank gust front and a strong cyclonic vortex, consistent with theoretical models (e.g., Lemon and Doswell 1979; Bluestein 2013).

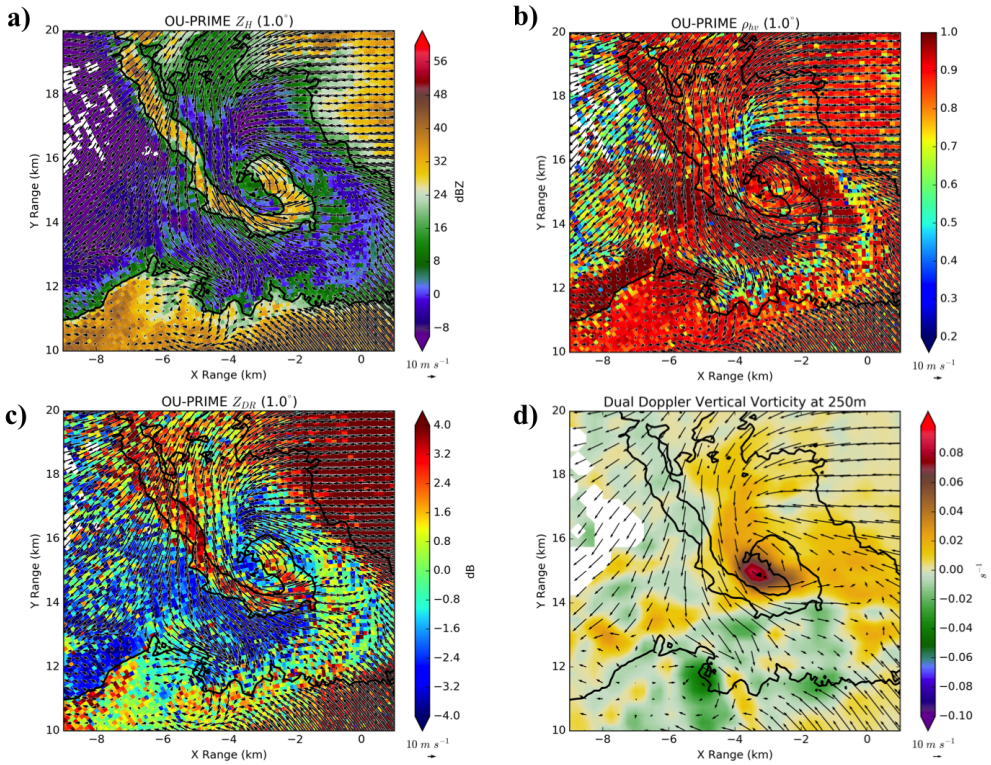


Figure 3.1: Dual-Doppler winds (arrows) overlaid on 2223 UTC 1° elevation PPIs of OU-PRIME (a) reflectivity (dBZ), (b) correlation coefficient, and (c) differential reflectivity (dB), and (d) a CAPPI of dual-Doppler derived vertical vorticity ($s^{-1}$) valid at 250 m ARL. The solid black contours represent the 15 dBZ isodop.

The other time that approximately fulfills the simultaneous observation requirement is the volume beginning at approximately 2231 UTC, when the difference between scan

times[3] is on the order of ∼30 s. The Moore-Choctaw tornado exhibits a large, inhomogeneous TDS at 2231 UTC (Fig. 3.2), which will be the main focus of this study. Due to the main circulation being near the edge of the dual-Doppler lobe, kinematic analyses only cover the lowest ∼1 km of the tornado. The lowest scans of KTLX and OU-PRIME are also the most synchronized.

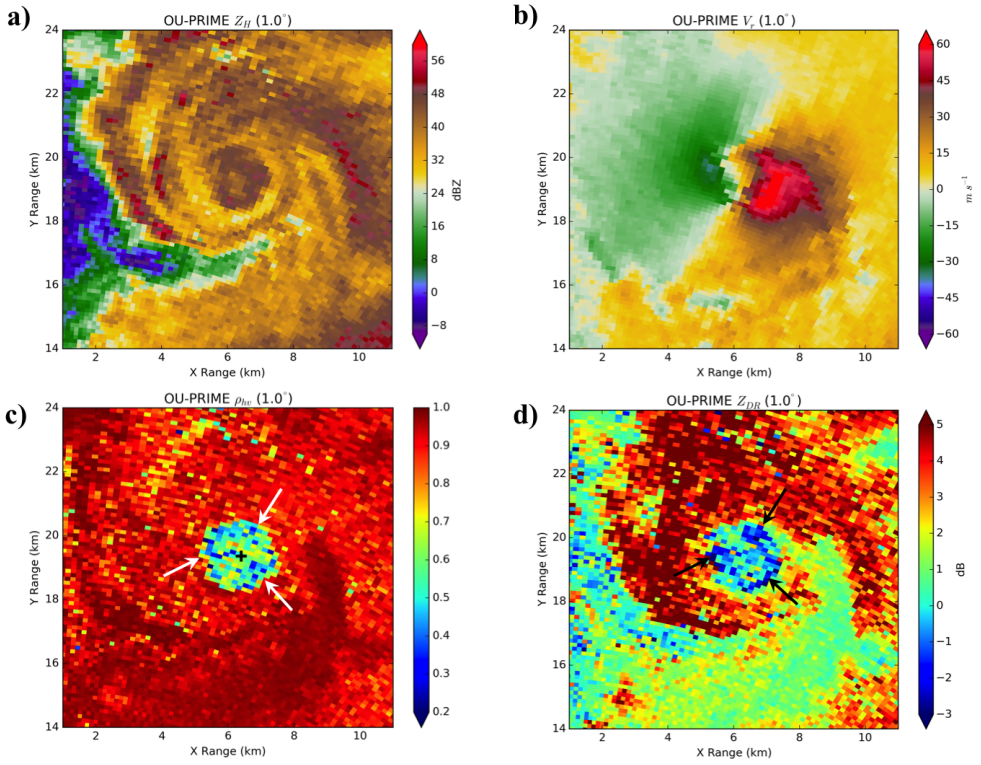


Figure 3.2: PPIs of 1° elevation OU-PRIME (a) reflectivity (dBZ), (b) radial velocity (m $s^{-1}$), (c) correlation coefficient, and (d) differential reflectivity (dB) valid at 2231 UTC. Arrows highlight the pockets of low $\rho_{hv}$ and $Z_{DR}$ in (c) and (d). The plus sign in (c) represents the subjectively determined TDS center.

[3]For other potential dual-Doppler analyses, the scan times between KOUN and KTLX are on the order of ∼2 min, which is well beyond the length of time where we can assume steady-state for processes within supercells (Taylor 1938)

### 3.2.4 Axisymmetric Wind Retrieval

Using the assumption of axis symmetry, Lee et al. (1999) developed a method to diagnose mean three-dimensional motion within tropical cyclones. This technique was called the ground-based velocity track display (GBVTD) method and has later been successfully applied to tornado vortices (e.g., Bluestein et al. 2003; Lee and Wurman 2005; Tanamachi et al. 2007; Kosiba and Wurman 2010; Wakimoto et al. 2012). This paper uses the simplified single-Doppler wind retrieval similar to the GBVTD defined by Dowell et al. (2005) eqs. (25-27) that recovers only the azimuthally averaged (zero wavenumber) radial and tangential velocities, u and v. This method has previously been used by Kosiba et al. (2008) to derive axisymmetric wind fields for a tornado near Harper, Kansas and by Bodine et al. (2014) to interrogate the Moore-Choctaw, OK tornado of interest to this study. For KOUN and OU-PRIME, $u$ and $v$ are calculated for 250-m-wide annuli, at 125-m intervals. Vertical velocities are computed by vertically integrating radial mass flux using eq. (2.2) from Nolan (2013). KOUN did not sample the lowest 150 m of the tornado, which as noted in Nolan (2013) could result in significant errors in the retrieved vertical velocities due to insufficient observations of the low-level mass flux. However, circumstantial evidence supporting the derived vertical velocities will be discussed in conjunction with the results in future sections.

Radar-derived wind fields are known to have a radially outward bias owing to objects within tornado vortices undergoing centrifugal accelerations (Dowell et al. 2005; Bodine et al. 2016b). In the absence of debris, centrifuging can be corrected using the terminal fall velocities of radar-derived drop size distributions (Wakimoto et al. 2012). However, since the radar volumes in this study are filled with debris, we use the method described by Nolan (2013) eq. (3.1) that accounts for the velocity owing to the centrifugal force at each location as a component of the biased radial wind field $U_{mod}$:

$$U_{mod} = U + U_{bias} = U + C_{max}\frac{v^2/r}{max(v^2/r)}, \tag{3.1}$$

where $C_{max}$ is a specified maximum flow-relative radially outward velocity estimate, $v$ is the tangential velocity, and $r$ is the radius from the center of the vortex. For the purposes of this study, a conservative value of $C_{max} = 8.0$ m s$^{-1}$ was chosen, similar to the maximum positive bias in radial velocity found by Wakimoto et al. (2012) (see their Fig. 9) and similar to values for centrifuging tested by Kosiba and Wurman (2013). The correction for centrifuging recovered low-level inflow without dramatically changing the rest of the analysis. The analyses were not qualitatively sensitive to values of $C_{max}$ between 4 and 12 m s$^{-1}$.

## 3.3 Results

### 3.3.1 Spatial distribution of polarimetric variables

At 2231 UTC, areas of high $Z_H$ surround a region of strong azimuthal shear in $V_r$ associated with the Moore-Choctaw, OK tornado (Fig. 3.2a,b). Large rain drops, with $\rho_{hv}$ values of ∼0.95 and $Z_{DR}$ values in excess of 4 dB, enshroud the tornado (Fig. 3.2c,d). Small rain drops exhibiting $\rho_{hv} > 0.98$ and $Z_{DR}$ of approximately 0.5 dB are located farther to the south in the rear flank downdraft, as noted by Kumjian (2011) and French et al. (2015). The tornado exhibits a TDS in excess of 2 km in diameter. While this TDS has been examined statistically by Bodine et al. (2014), the spatial distribution of polarimetric variables was not the focus. Thus, of particular interest to this study are the local minima in $Z_{DR}$ and $\rho_{hv}$, which are not located in the center of the TDS, but rather are concentrated in pockets near the periphery of the TDS (Fig. 3.2c-d). In contrast, values of $Z_{DR}$ and $\rho_{hv}$ are locally maximized near the center of the TDS.

Plots of both raw and two-pass Barnes analyzed $Z_{DR}$ and $\rho_{hv}$ vs. distance from the subjectively defined center of the TDS (Fig. 3.3) indicate that the lowest values of both polarimetric variables occur 500-1000 m from the center of the TDS. Data points flagged

as part of the TDS are plotted in red.[4] Within volumes containing considerable amounts of debris (red lines[5]), there is a weak tendency for $Z_{DR}$ and $\rho_{hv}$ to decrease with distance from the center of the tornado. Some of the points in the outer half of the TDS exhibit values of $\rho_{hv}$ below 0.3 and values of $Z_{DR}$ less than -2 dB. As expected, the trend lines have a better fit to the objectively analyzed data (Fig. 3.3a-b) than the noisier raw data (Fig. 3.3c-d).

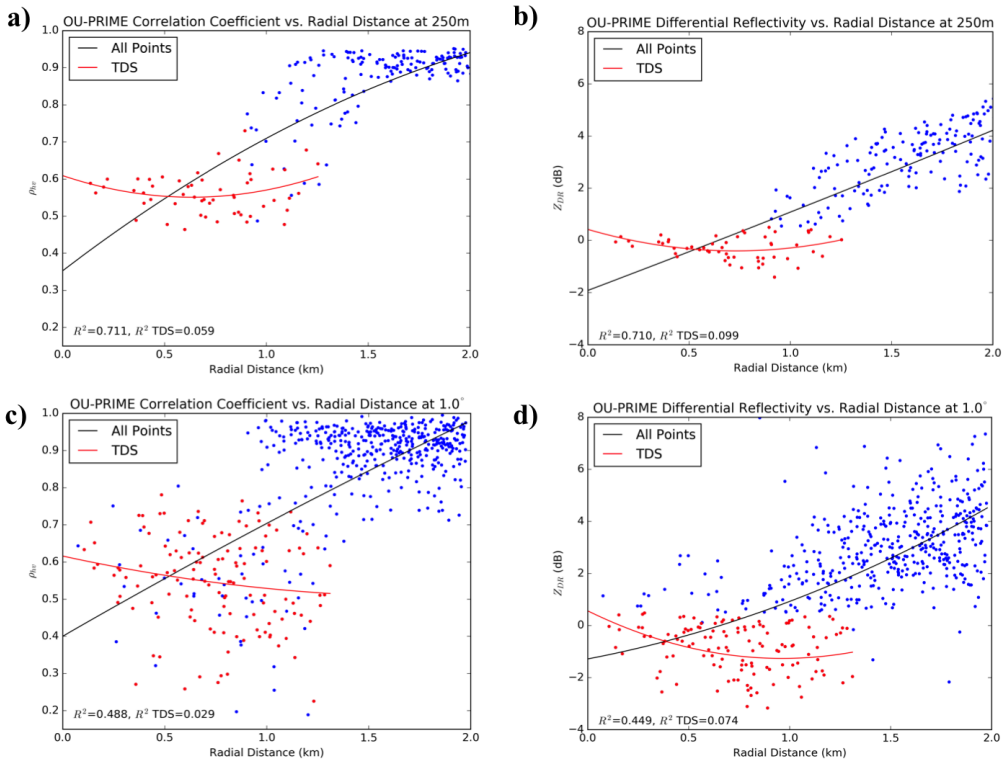


Figure 3.3: Scatter plots of objectively analyzed (a) correlation coefficient, and (b) differential reflectivity (dB), and raw (c) correlation coefficient, and (d) differential reflectivity (dB) vs. radial distance (km) valid at 2231 UTC. Blue dots indicate non-TDS flagged points and red dots indicate TDS flagged points. The black line is the second order polynomial fit for all points and the red line is the second-order polynomial fit for TDS flagged points.

[4]It is possible that some of the bins exhibiting low values of $\rho_{hv}$ at small radii in Fig. 3.3c also contain small concentrations of debris but did not meet the 15 dBZ reflectivity threshold.

[5]All scatter plots in this study are fitted to second-order polynomials.

Axisymmetric cross sections are used to gain a better perspective on how mean radial profiles of polarimetric variables change with height (Fig. 3.4). The cross section of reflectivity (Fig. 3.4a) illustrates that the radius of the maximum in reflectivity within the TDS increases with height associated with the centrifuging of debris, similar to what has been noted previously within tornadoes (e.g., Wurman and Gill 2000; Dowell et al. 2005; Bodine et al. 2014). As seen in Fig. 3.3, the minimum in $\rho_{hv}$ occurs at approximately 750 m from the center of the TDS. The local minimum extends up from the lowest analysis level and is largely confined to below 1.0 km ARL (Fig. 3.4b), similar to what was seen in the photogrammetric analyses performed by Wakimoto et al. (2015) (e.g. their Fig. 5d). Unlike the cross sections presented by Wakimoto et al. (2015), a secondary minimum in $\rho_{hv}$ is absent from the center of the TDS aloft. This may be due to greater precipitation entrainment in the Moore-Choctaw tornado (Schwarz and Burgess 2011; Bodine et al. 2014), as suggested by the large raindrops surrounding the tornado in Fig. 3.2 or simply due to a higher SNR in the Moore-Choctaw tornado.

The minimum in $Z_{DR}$ below 0.8 km ARL occurs approximately 800 m from the center of the TDS. Above 0.8 km ARL, the minimum in $Z_{DR}$ is located closer to the center of the TDS (Fig. 3.4c). Axisymmetric $v$ is plotted in Fig. 3.4d and illustrates that the TDS, as approximately defined by the dashed 0.8 $\rho_{hv}$ contour, is largely constrained within the radius of maximum winds (RMW) similar to what was found in Houser et al. (2016). Heights where the TDS extends beyond the RMW exhibit $v$ in excess of 40 m s$^{-1}$. Strong $v$ are likely necessary in order for debris to be centrifuged to such a large radius. The radius of the TDS increases with height, which is likely the result of continued debris centrifuging in combination with a vertically increasing core diameter of the tornado and low-level mesocyclone (Fig. 3.4d). Because of the lack of low-level coverage provided by OU-PRIME, supplemental axisymmetric analyses from KOUN are used. These are interrogated in the next subsection. Included in these analyses is the secondary circulation, which is omitted from Fig. 3.4.

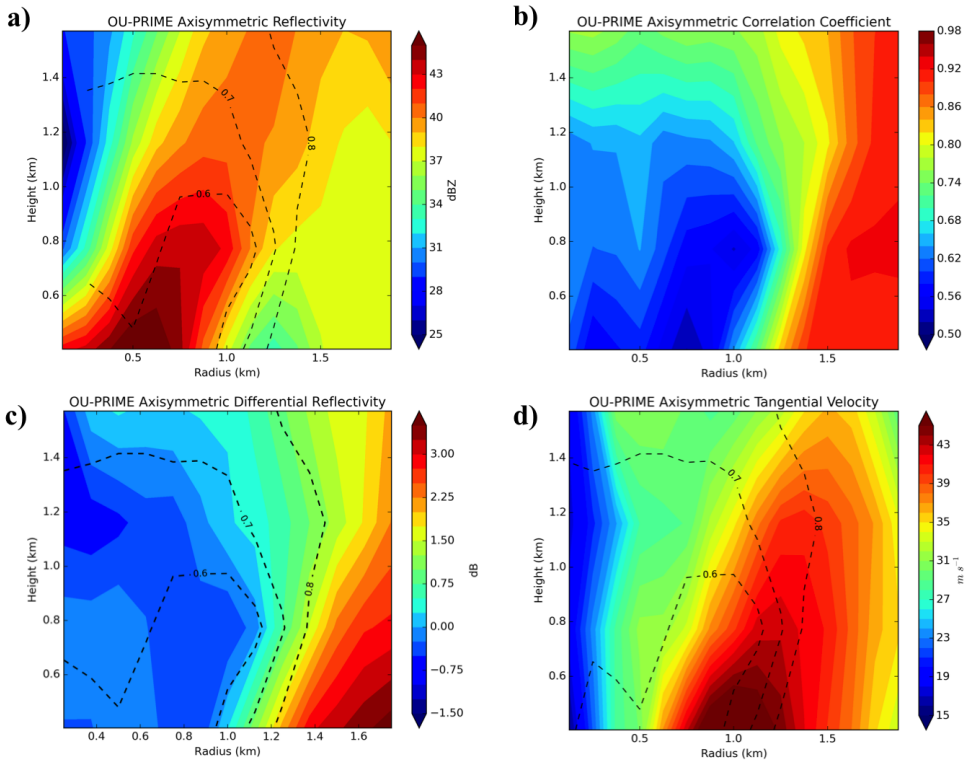


Figure 3.4: OU-PRIME axisymmetric (a) reflectivity (dBZ), (b) correlation coefficient, (c) differential reflectivity (dB), and (d) tangential velocity (m $s^{-1}$) valid at 2231 UTC. Dashed lines represent isopleths of axisymmetric correlation coefficient.

### 3.3.2 Tornado subvortices

The PPI of $V_r$ at 2231 UTC (Fig. 3.5a) indicates at least two regions of locally enhanced radial shear, likely associated with tornado subvortices (e.g., Wurman 2002; Wurman and Kosiba 2013). Dual-Doppler analysis with KTLX at this time (Fig. 3.5b) indicate two regions of locally enhanced vertical vorticity oriented in the same manner as the regions of enhanced shear in Fig. 3.5a. It is possible that the dual-Doppler analysis is only resolving the two largest subvortices, and that more are present at the sub-grid scale.

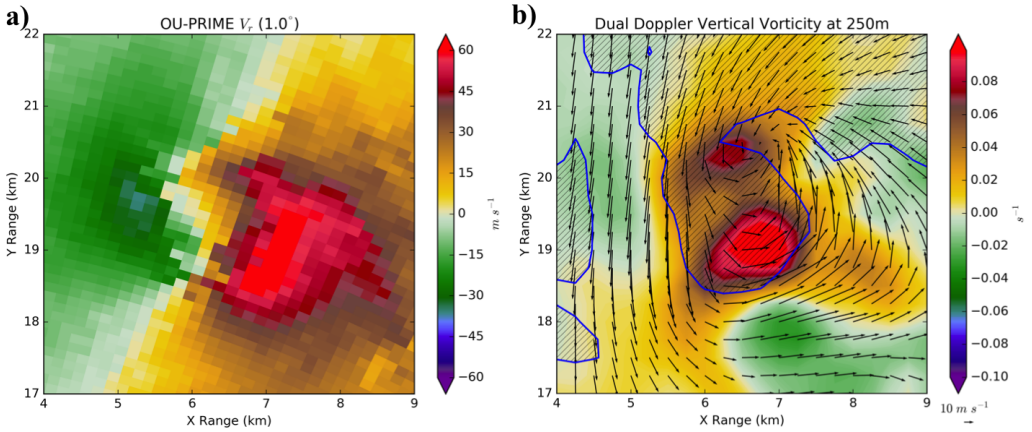


Figure 3.5: (a) A PPI of OU-PRIME radial velocity (m $s^{-1}$) and (b) a CAPPI of dual-Doppler vertical vorticity ($s^{-1}$) valid at 2231 UTC. The hatched blue contour in (b) represents areas where reflectivity exceeds 40 dBZ.

Axisymmetric wind fields were retrieved from the Moore-Choctaw tornado using KOUN data beginning at 2229 UTC (Fig. 3.6). The secondary circulation (arrows), comprised of radial and vertical velocities, provides evidence of a central downdraft, with upward vertical velocities displaced to ∼1 km in radius from the center of the tornado. This observed secondary circulation closely resembles the model for moderate to high swirl, two-celled vortices seen in previous studies (e.g., Church et al. 1979; Davies-Jones 1986; Wakimoto and Liu 1998; Lewellen et al. 2004, 2008) and conceptually summarized by Bluestein (2013). It is possible that the low-level divergence field, which is poorly

sampled at ∼17 km in range, offsets or supersedes the divergence and convergence of u at higher altitudes rendering the secondary circulation erroneous. However, the Moore-Choctaw tornado exhibited tornado subvortices and a RMW of ∼1 km, which is consistent with a moderate-to-high swirl ratio vortex that should likely contain a central downdraft. Regardless, the authors caution that magnitude of the downdraft may be exaggerated by the absence of boundary layer inflow, similar to what was noted by Kosiba and Wurman (2010) and shown by Nolan (2013).

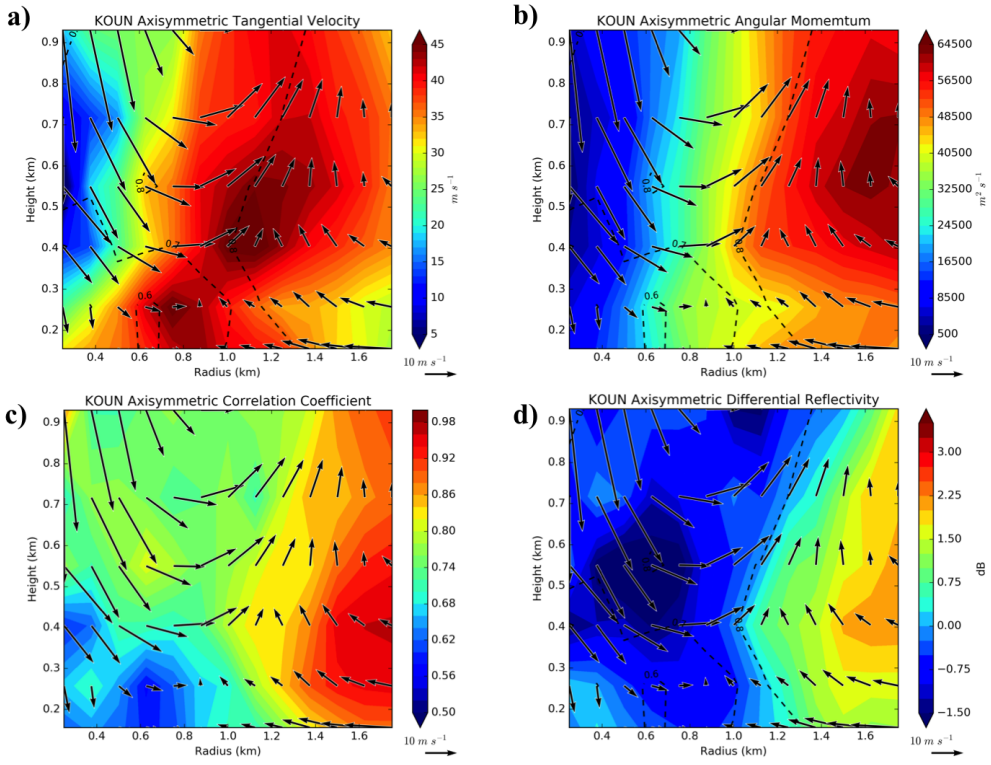


Figure 3.6: KOUN axisymmetric (a) tangential velocity (shaded, m $s^{-1}$), (b) angular momentum (shaded, $m^2$ $s^{-1}$), (c) correlation coefficient (shaded), and (d) differential reflectivity (shaded, dB) valid at 2230 UTC. Dashed lines represent isopleths of axisymmetric correlation coefficient. Arrows represent secondary circulation wind vectors comprised of radial and vertical velocities from the axisymmetric wind retrieval.

The axisymmetric analyses capture the top of an inflow layer, which extends to at least 300 m in height. The low levels are characterized by radial inflow and a strong

vertical gradient in angular momentum (Fig. 3.6b). Radial inflow also extends into the radius of maximum $v$ at higher altitudes (Fig. 3.6a), similar to what was noted by Nolan (2013). The maximum in $v$ is observed at approximately 1100 m in radius at 500 m ARL, with values exceeding 45 m $s^{-1}$. A secondary maximum in $v$ exists at 250 m ARL at 800 m in radius. At this height, radial inflow extends in to the radius of maximum $v$, impinging farther than inflow aloft. The 0.8 $\rho_{hv}$ contour, which serves as a proxy for the TDS, is confined within the radius of maximum $v$ at a given level for analyses above $\sim$ 400 m ARL, but the 0.8 $\rho_{hv}$ contour extends beyond the radius of maximum $v$ at lower altitudes. This may be the result of enhanced debris lofting and loading at lower levels due to strong inflow (e.g., Lewellen et al. 2008; Bodine et al. 2016a), lofting of light debris from high near-surface inflow winds, or fallout of debris from aloft (e.g., Bodine et al. 2013; Kurdzo et al. 2015; Van Den Broeke 2015; Houser et al. 2016). However, the lowest values of $\rho_{hv}$ are confined within the RMW throughout the column.

As noted in the previous subsection, the lowest values of $\rho_{hv}$ in the TDS are displaced $\sim$ 600 m from the center of the tornado (Fig. 3.6c). The 0.8 $\rho_{hv}$ contour exists near the radius where vertical motion becomes directed upward due to radial convergence. This pocket of low $\rho_{hv}$ does not extend as high as in Fig. 3.4, however this may be due to the difference in transmit frequency[6] between the radars or the difference in analysis times, which is approximately one minute. The lowest values of $Z_{DR}$ are located at 500 m in altitude and 600 m in radius in a region of downward vertical velocity (Fig. 3.6d). At this same altitude, there is a strong gradient in $Z_{DR}$ between 700-1100 m in radius corresponding with a strong gradient in vertical velocity. This region has low values of $\rho_{hv}$ throughout, which may mean that the gradient in $Z_{DR}$ is due to differences in debris type/orientation between the updraft and downdraft. Locally reduced values of $Z_{DR}$ also extend vertically above and below 500 m ARL and between 600 and 1000 m in radius.

[6]PPIs of KOUN data are not shown, but $Z_H$ is $\sim$10 dBZ higher at S-band than at C-band within the TDS at this time.

### 3.3.3 Polarimetric vs. kinematic variables

In order to gain a better understanding of what underlying processes may be responsible for the aforementioned distribution of polarimetric variables, scatter plots of $Z_H$, $\rho_{hv}$, and $Z_{DR}$ vs. dual-Doppler kinematic variables are presented in this section. Spatial correlation between vertical vorticity ($\zeta$) and each of the polarimetric fields interrogated is observed. Additionally, there is an observed relationship between vertical velocity and $\rho_{hv}$.

Prior to the Moore-Choctaw tornado exhibiting a TDS, there is no relationship between the radar variables and $\zeta$ in the vicinity of the tornado (Fig. 3.7). At 2223 UTC, all values of $Z_H$, $\rho_{hv}$, and $Z_{DR}$ (not shown) are almost equally likely to be collocated with positive and negative values of $\zeta$. By 2231 UTC, the Moore-Choctaw tornado has strengthened to the point where debris is lofted to altitudes where it can be sampled by the radars, and the distribution of $\zeta$ vs. $Z_H$ has been significantly modified from the earlier analysis (Fig. 3.8). At 250 m ARL, $\zeta$ increases with increasing values of $Z_H$ for all points within 5 km of the TDS center (Fig. 3.8a). There is also a tendency within the TDS for higher $Z_H$ to be associated with greater cyclonic $\zeta$. Recall that the greatest cyclonic $\zeta$ at 250 m ARL is found within the tornado subvortices (Fig. 3.5b). Thus, this result can be interpreted as the tornado subvortices exhibiting the highest $Z_H$, likely due to locally enhanced debris lofting. It is possible that the subvortices exhibit a minimum in $Z_H$ at their center due to centrifuging on a smaller scale (e.g., Wurman 2002; Wakimoto et al. 2016), but the range to the tornado prevents this from being resolved by OU-PRIME.

Among all data points at 1000 m ARL, there is perhaps a weak maxima in $\zeta$ around 40 dBZ (Fig. 3.8b), but the overall relationship between $Z_H$ and $\zeta$ is much weaker than at lower levels. However, within the TDS, there is a clear inverse relationship between $Z_H$ and $\zeta$. The distribution of $\zeta$ is opposite of what was observed at lower levels, and is a representation of a WEH (Fig. 3.8d) (e.g., Wurman and Gill 2000). The transition from a relatively uniform region of high $Z_H$ (Fig. 3.8c) into a WEH is the result of centrifuging

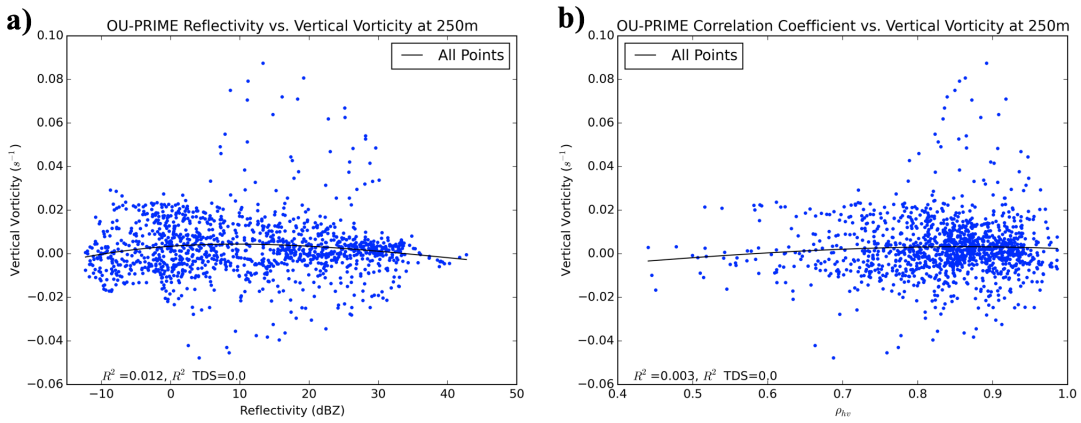


Figure 3.7: Scatter plots of vertical vorticity ($s^{-1}$) vs. OU-PRIME (a) reflectivity (dBZ) and (b) correlation coefficient valid at 2223 UTC. No significant relationship is observed between either radar variable and vertical vorticity.

(Dowell et al. 2005), which causes the manifestation of the weak echo column (WEC) observed in this study and others (e.g., Tanamachi et al. 2012; Bodine et al. 2014).

A scatter plot of all points within 5 km of the TDS center indicates that the largest values of $\zeta$ are associated with the lowest values of $\rho_{hv}$ at 250 m ARL, with a tendency for increasing $\zeta$ to be associated with decreasing $\rho_{hv}$ within the bins flagged as tornadic debris (Fig. 3.9a). Similar to the pattern observed within the $Z_H$ data, this result can be interpreted as the lowest $\rho_{hv}$ being associated with the tornado subvortices similar to what was observed by Wakimoto et al. (2016). Overlays of $\zeta$ onto constant altitude PPIs (CAPPIs) of $\rho_{hv}$ support the collocation of locally reduced pockets of $\rho_{hv}$ with the tornado subvortices (Fig. 3.9c).

At 1000 m ARL, there is still an inverse relationship between $\rho_{hv}$ and $\zeta$ among all points within 5 km of the TDS (Fig. 3.9b). However, there is no longer a relationship between $\rho_{hv}$ and $\zeta$ among TDS flagged points. This is likely because tornado subvortices are confined to a relatively shallow layer near the surface (Wurman 2002), and thus the debris associated with the lowest values of $\rho_{hv}$ are no longer tied to its lofting mechanism. A CAPPI of $\rho_{hv}$ overlaid with $\zeta$ indicates the presence of a dominant, central vortex, associated with the parent circulation (Fig. 3.9d).

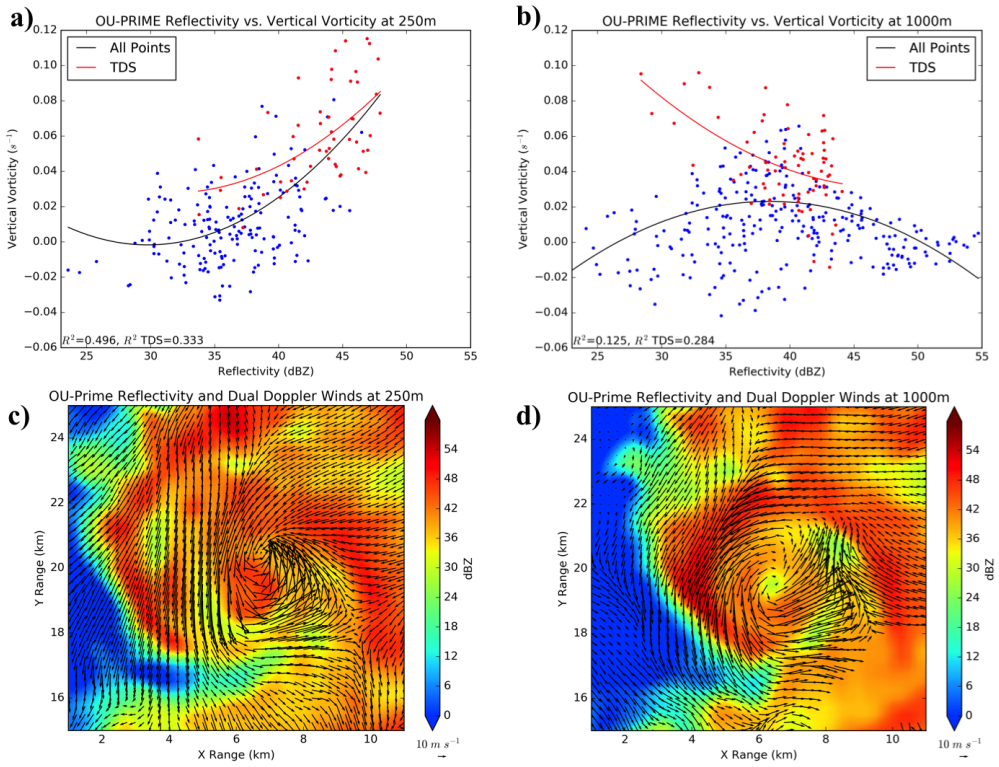


Figure 3.8: Scatter plots of vertical vorticity ($s^{-1}$) vs. OU-PRIME reflectivity (dBZ) at (a) 250 m ARL and (b) 1000 m ARL, and CAPPIs of OU-PRIME reflectivity (shaded, dBZ) overlaid with dual-Doppler winds (arrows) at (c) 250 m ARL, and (d) 1000 m ARL valid at 2231 UTC. Blue dots in (a) and (b) represent non-TDS flagged points and red dots indicate TDS flagged points. The black lines in (a) and (b) represent the second order polynomial fit for all points and the red lines are the second-order polynomial fits for TDS flagged points.

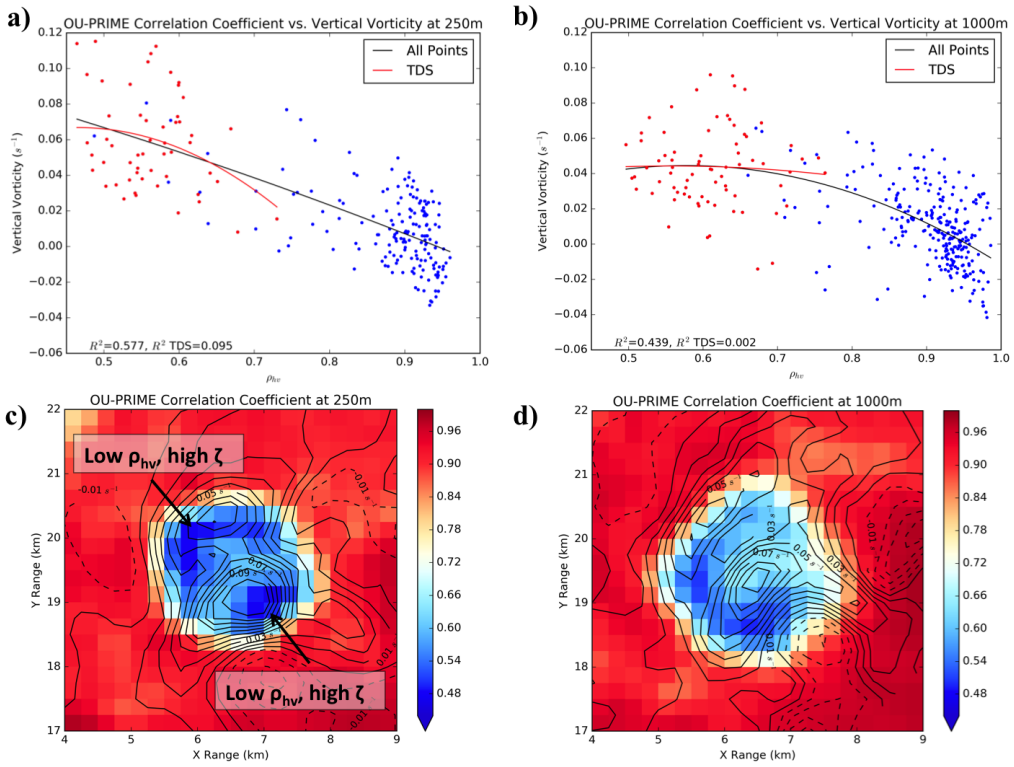


Figure 3.9: As in Fig. 3.8 except for OU-PRIME correlation coefficient at (a,c) 250 m ARL and (b,d) 1000 m ARL valid at 2231 UTC.

Within the TDS, a direct relationship exists between $\rho_{hv}$ and vertical velocity at 1000 m ARL (Fig. 3.10a). The lowest values of $\rho_{hv}$ are associated with downward vertical velocity with magnitudes[7] from 0-40 m s$^{-1}$. Higher values of $\rho_{hv}$, but still sufficiently low to be classified as debris, are associated with upward motion in excess of 40 m s$^{-1}$. A downdraft is located in the southwest half of the TDS (Fig. 3.10b) collocated with a half annulus of low $\rho_{hv}$. It is possible that these bins of low $\rho_{hv}$ represent a separate regime of debris falling out from aloft (e.g., Houser et al. 2016) compared to the relatively higher $\rho_{hv}$ bins that are collocated with the updraft in the northeast half of the TDS. For example, the downdraft may aid the fallout of larger debris whereas smaller debris can be lofted into the storm-scale updraft on the northeast side. However, differential sedimentation of debris cannot be confirmed. The northeast to southwest decrease in $\rho_{hv}$ is also seen above 1000 m (not shown), but the lack of a sufficient look angle difference for analysis aloft prevents the confirmation of a similar bifurcation in vertical velocity.

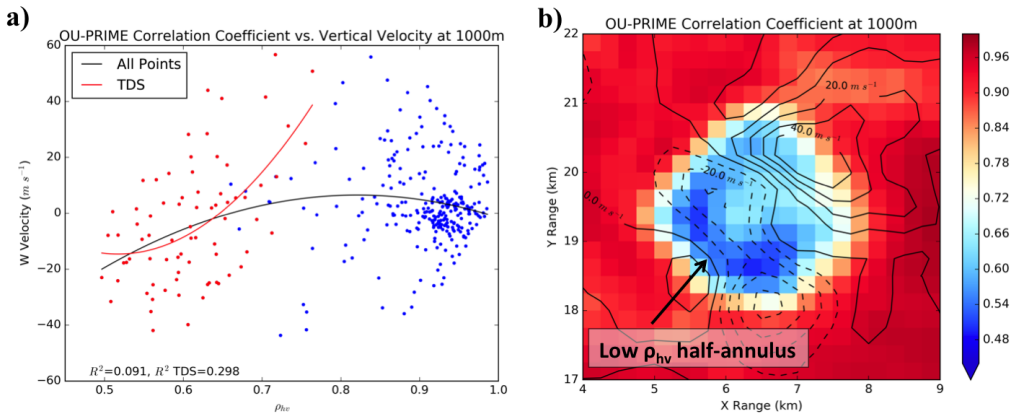


Figure 3.10: As in Fig. 3.9 except for vertical velocity (m s$^{-1}$) instead of vertical vorticity.

In general, the lowest values of $Z_{DR}$ are associated with the largest values of $\zeta$ at 250 m ARL (Fig. 3.11a). As previously noted, precipitation exhibiting high values of $Z_{DR}$

[7]A bias in the divergence field due to debris centrifuging may impact the magnitudes of vertical velocity in the dual-Doppler analyses. Additionally, poor sampling of the lowest 100 m of the storm may also affect the magnitude of retrieved vertical velocity. Finally, the analyses do not capture sub-grid scale features, like suction vortices, which may exhibit larger vertical velocity magnitudes.

surrounds the TDS at 2231 UTC (Fig. 3.11c). Thus, it is unsurprising that $Z_{DR}$ decreases when approaching the tornado. Many of the largest values of $\zeta$ in the tornado correspond to near-zero values of $Z_{DR}$. Figure 3.11c illustrates $Z_{DR}$ values near zero in the center of the tornado subvortices, with lower, negative values of $Z_{DR}$ located at the periphery of the vortices. The near-zero values of $Z_{DR}$ in the center of the subvortices are possibly due to nearly random particle orientation. At 1000 m ARL, the relationship between $\zeta$ and $Z_{DR}$ is similar to what was observed at low levels (Fig. 3.11b). Unlike at 250 m ARL, however, the near-zero values of $Z_{DR}$ and surrounding annulus of negative $Z_{DR}$ are associated with the parent vortex at the center of the TDS (Fig. 3.11d) as opposed to with the tornado subvortices. The observation of negative values of $Z_{DR}$ at the periphery of the vortices will be a subject of discussion in the next section.

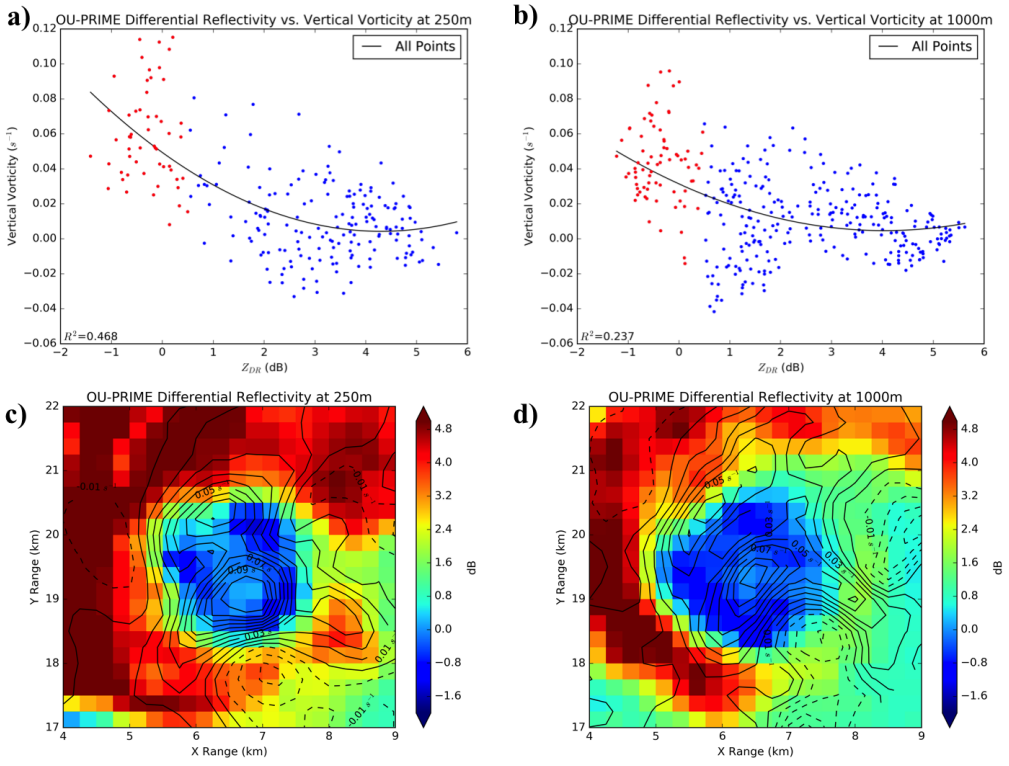


Figure 3.11: As in Fig. 3.9 except with differential reflectivity (dB) instead of correlation coefficient. Polynomial fits for TDS flagged points were not included due to poor fit.

## 3.4 Discussion

### 3.4.1 Polarimetric observations

The previous section illustrates that the subvortices in the Moore-Choctaw tornado at 2231 UTC are associated with locally enhanced $Z_H$, locally reduced $\rho_{hv}$, and near-zero $Z_{DR}$. The enhanced $Z_H$ is likely due to locally enhanced concentrations of debris. It is speculated that subvortices are capable of lofting the largest debris, which could lead to lower $\rho_{hv}$ (e.g., through resonance scattering effects). If the large debris were effectively random in orientation, $\rho_{hv}$ would be further reduced and backscattered power would be nearly equal in the horizontal and vertical polarizations, resulting in the near 0 dB $Z_{DR}$ that was observed.

Regions of negative $Z_{DR}$ within the TDS exist near the periphery of the tornado subvortices (Fig. 3.12). A region of negative $Z_{DR}$, with values below -0.6 dB, is located just to the east of the largest vortex (#1), with another, larger area of negative $Z_{DR}$ with values below -0.9 dB located to the northwest of vortex #1. The third region of negative $Z_{DR}$ is located just to the east of the smaller subvortex (#2) with values also below -0.9 dB. Since the subvortices rotate cyclonically around a common center, the second and third areas of negative $Z_{DR}$ are located in regions just vacated by the subvortices (vortex 'wakes'). It is possible that the regions outside of the subvortices are associated with less turbulence and allow for recently ejected, trailing debris to become oriented in a less random manner. Alternatively, the vortex wakes could contain a different concentration of debris compared to the subvortices leading to differences in the relative contribution of debris to the returned signal, or vortex wakes could contain a different debris regime than the subvortices due to size sorting. We speculate that the region of negative $Z_{DR}$ to the east of vortex #1 may be associated with an unresolved subvortex, debris fallout from aloft, or perhaps is associated with an eastward debris ejection from vortex #1, similar to what was observed by Kurdzo et al. (2015).

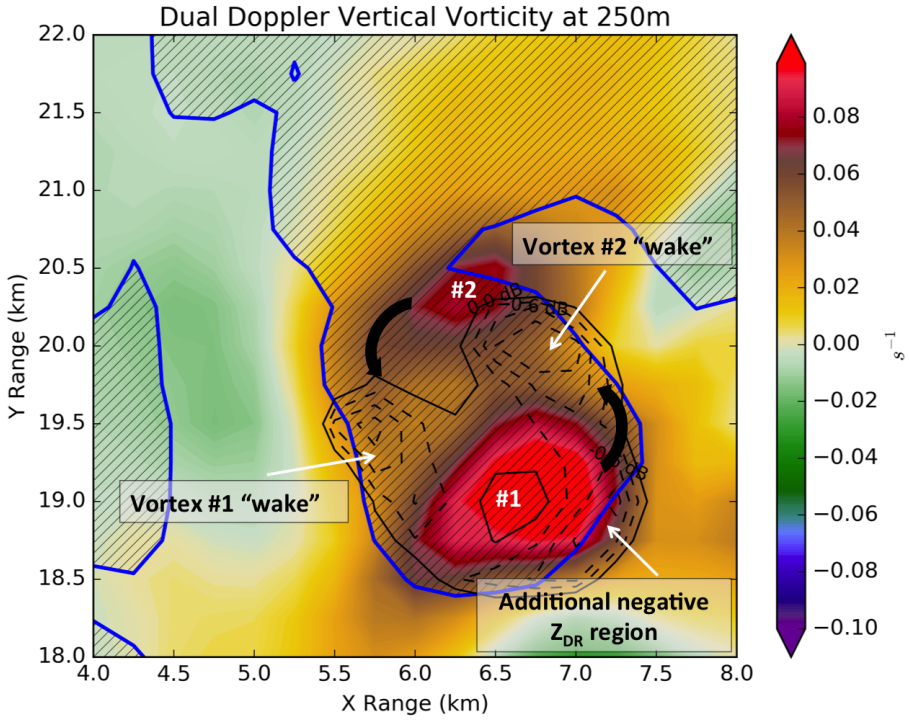


Figure 3.12: Dual-Doppler derived vertical vorticity (shaded, $s^{-1}$) and OU-PRIME objectively analyzed differential reflectivity (black contours, dB) contoured every 0.3 dB from -0.9 dB valid at 2231 UTC. The hatched blue contour represents the 40 dBZ reflectivity isopleth.

The final topic of discussion regarding polarimetric variables is the WEC illustrated in Fig. 3.4 and Fig. 3.6. Similar to what was observed by Wakimoto et al. (2015) in the 2013 El Reno, OK tornado, the region of low $Z_H$ and $\rho_{hv}$ at the center of the 2010 Moore-Choctaw tornado is also characterized by $Z_{DR} < 0$ dB. As discussed by Wakimoto et al. (2015), this region is likely composed of low concentrations of small, randomly oriented debris. However, unlike what was observed in the El Reno tornado (which contained $\rho_{hv}$ as low as 0.1 in the WEC), values of $\rho_{hv}$ were greater than 0.5 in both the KOUN and OU-PRIME analyses. Part of the differences in $\rho_{hv}$ values may be due to differences in particle scattering between the X-band radar used by Wakimoto et al. (2015) and the S- and C- band radars used in this study. However, as noted by Bodine et al. (2014), the Moore-Choctaw tornado likely entrained considerable amounts of precipitation, whereas it was hypothesized by Wakimoto et al. (2015) that few hydrometeors were present in the El Reno WEC. It is possible that precipitation found in the Moore-Choctaw WEC was transported from aloft by the central downdraft illustrated in Fig. 3.6.

### 3.4.2 Comparison of single- and dual- Doppler analyses

It is important to recognize the tradeoffs and differing utility of the single- and dual-Doppler techniques used in this study. In order to better understand some of the strengths of each method, a brief direct comparison of the analyses created by each technique was performed. By radially averaging the dual-Doppler analyses and vertically interpolating the data, a mean, axisymmetric wind profile is created that is similar to the one made by the single-Doppler technique[8] (Fig. 3.13a,b). The magnitude of tangential velocities is greater in the single-Doppler analysis than the dual-Doppler analysis at almost every point with the greatest velocity difference ($V_{single} - V_{dual}$) occurring at the RMW (Fig. 3.13c). However, the two analyses are qualitatively similar with a radius of maximum wind at approximately 1 km and the strongest winds occurring between 200-500 m ARL. It is

[8]No correction for centrifuging was applied to either the single- or dual- Doppler analyses for the comparison in Fig. 3.13a,b.

likely that the difference in tangential velocity magnitude between the analyses is the result of the single-Doppler analysis having finer grid spacing (∼100 m) compared to the dual-Doppler analysis (250-m grid spacing), which allows the single-Doppler method to better sample the peak velocities.

In most places, the difference in radial velocity between the single- and dual- Doppler analyses is $< 10$ m s$^{-1}$ (Fig. 3.13d). The largest difference is between 1-2 km in radius at the lowest two analysis levels where the single-Doppler method exhibits stronger negative radial velocity, which represents stronger low-level inflow into the tornado. It is likely that these differences are due to the better native resolution of the single-Doppler analysis in addition to the dual-Doppler analysis being constrained by the data horizon of two radars, which may limit the sampling of the inflow layer. The other region of large radial velocity difference is between 150-1000 m in radius and 300-800 m ARL where the single-Doppler analysis has much higher outward radial velocities than the dual-Doppler analysis. The single-Doppler technique better samples the peak radial velocities, which may be most biased by the effects of debris centrifuging. The region of maximum velocity difference is similar to the region found to contain the largest difference in radial velocity between air and debris by Dowell et al. (2005), which supports the hypothesis that centrifuging may account for some of the observed differences. However, it is also possible that the observed differences are the result of the single-Doppler technique better sampling the radial divergence associated with a stronger two-celled vortex.

Both Fig. 3.13a and Fig. 3.13b capture a downdraft near the center of the tornado with vertical velocity becoming directed upward near the RMW. Recall that both the dual-Doppler and axisymmetric analyses may have significant errors in vertical velocity due to poor sampling of the low-level wind field. Thus, while they are qualitatively similar, it must be cautioned that their agreement cannot be used as validation for the derived secondary circulation. Similar to tangential and radial velocities, the single-Doppler technique exhibits larger magnitude vertical velocity than the dual-Doppler

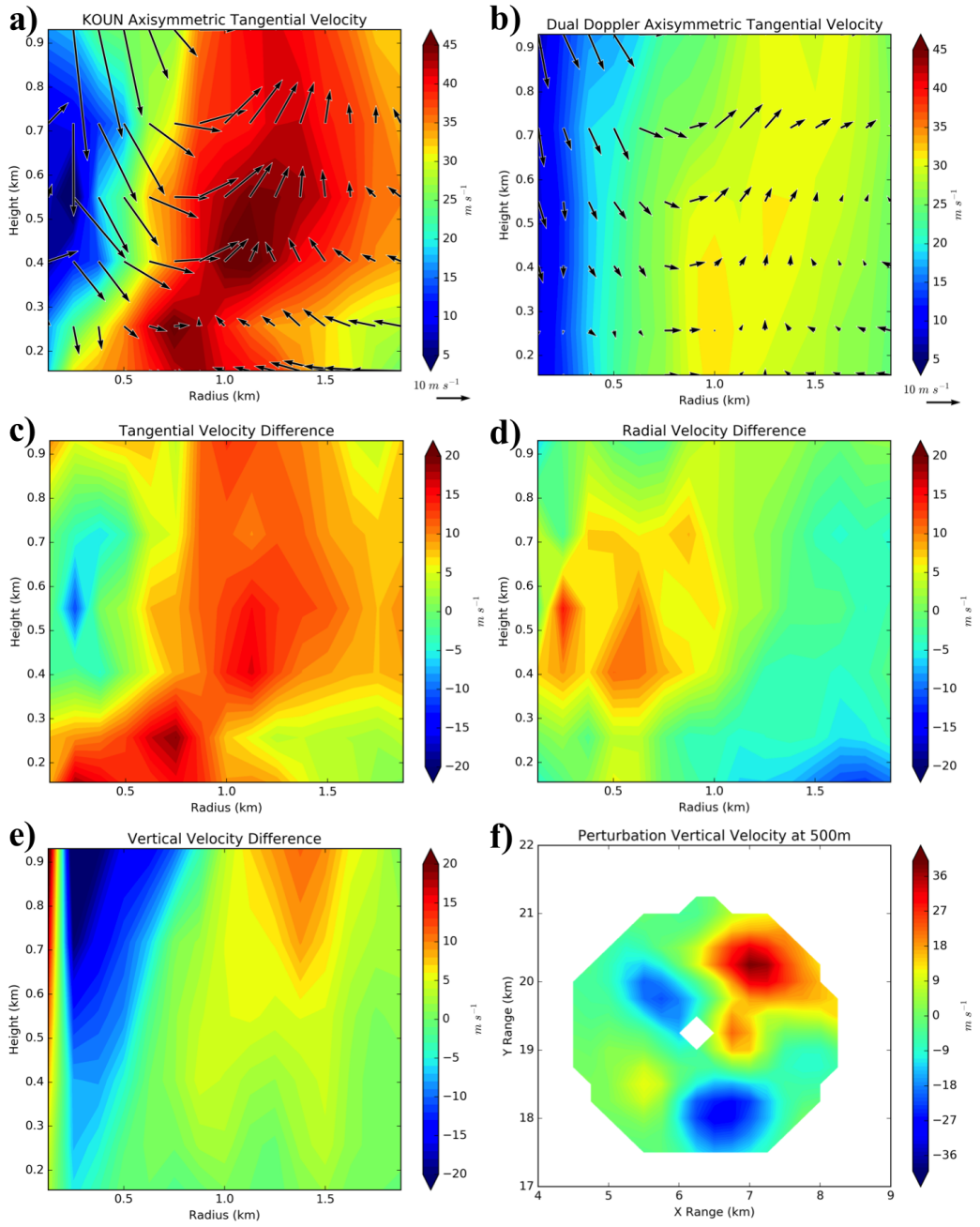


Figure 3.13: Axisymmetric tangential velocity (shaded, m $s^{-1}$) from (a) KOUN and (b) a dual-Doppler analysis between OU-PRIME and KTLX valid at 2230 and 2231 UTC, respectively. Difference plots between the KOUN and dual-Doppler (c) tangential velocity (shaded, m $s^{-1}$), (d) radial velocity (shaded, m $s^{-1}$), and (e) vertical velocity (shaded, m $s^{-1}$), and (f) a CAPPI of dual-Doppler perturbation vertical velocity (shaded, m $s^{-1}$) based on the axisymmetric mean.

method (Fig. 3.13e). The underestimate of vertical velocity in the dual-Doppler analysis is likely due to poor sampling of the low-level flow, as can be seen in Fig. 3.13d, where stronger radial inflow exists beneath the updraft and stronger radial outflow exists beneath the axial downdraft in the single-Doppler analysis. One more takeaway from the vertical velocity comparison is that the dual-Doppler solution is much more stable near the center of the vortex. This is likely due to errors in the single-Doppler technique that arise from using a small number of datapoints near the center of the vortex, which is less of an issue when subsetting and radially averaging dual-Doppler data from a larger domain.

While the single-Doppler technique has the advantage of better capturing the mass flux, the dual-Doppler technique is not constrained by an axisymmetric assumption and clearly illustrates an asymmetric vortex (e.g., Fig. 3.5b). Thus, the assumption of axisymmetry is violated in this case. However, the axisymmetric mean is still useful and can be used as a base state to linearize the dual-Doppler wind field in the vicinity of the tornado and provide a meaningful visualization of the asymmetries in the Moore-Choctaw tornado (Fig. 3.13e). The CAPPI of perturbation vertical velocity (Fig. 3.13f) illustrates that the Moore-Choctaw tornado may not be characterized simply by a downdraft at its center and updraft at approximately 1 km in radius. Rather, the Moore-Choctaw tornado may be comprised of at least two concentrated downdrafts, one near the center of the vortex, and one in the southern portion of the tornado. Likewise, there may be at least two concentrated updrafts, with the strongest one in the northeast quadrant of the vortex. Thus, even though the dual-Doppler axisymmetric analysis undersamples the largest magnitude vertical velocities, the dual-Doppler technique still captures one updraft and two downdrafts within the tornado.

## 3.5 Conclusions

The 10 May 2010 Moore-Choctaw tornado produced a large, heterogeneous TDS. Within the TDS, values of $Z_H$, $Z_{DR}$, and $\rho_{hv}$ varied considerably. The highest values

of $Z_H$, and lowest values of $Z_{DR}$ and $\rho_{hv}$, were displaced 500-1000 m from the center of the TDS. Both axisymmetric and dual-Doppler analyses suggest the presence of an axial downdraft within the center of the TDS, characteristic of a two-celled vortex. Single-Doppler $V_r$ and dual-Doppler $\zeta$ provide evidence for the presence of two large tornado subvortices that were located at approximately the radius of maximum $Z_H$ and minimum $Z_{DR}$ and $\rho_{hv}$.

The maxima in dual-Doppler $\zeta$ associated with the two large subvortices are collocated with two polarimetric variable extrema within the TDS (Fig. 3.14a). At low levels, the tornado subvortices are associated with the highest values of $Z_H$ and the lowest values of $\rho_{hv}$, likely due to locally enhanced debris concentrations. The subvortices are also associated with near-zero values of $Z_{DR}$, likely due to near-random particle orientation. Negative regions of $Z_{DR}$ were constrained to the periphery and trailing regions of the subvortices. At 1000 m, a bifurcated distribution of $\rho_{hv}$ was observed, with higher values of $\rho_{hv}$ collocated with a strong updraft in the northeast part of the TDS and lower values of $\rho_{hv}$ collocated with a downdraft in the southwest portion of the TDS.

Axisymmetric cross-sections of the Moore-Choctaw tornado (Fig. 3.14b) illustrate an annulus of $Z_H$ caused by centrifuging and results in the WEC. Axisymmetric cross-sections also capture the reduced $Z_{DR}$ and $\rho_{hv}$ in the tornado subvortices, which manifest as annuli near the RMW. A direct comparison of the single- and dual- Doppler axisymmetric cross-sections was made. When the additional axisymmetric constraint was applied to the dual-Doppler data, the two analyses were qualitatively similar. Both methods agreed on the placement of updrafts and downdrafts and had similar RMWs. The single-Doppler method better sampled the high-magnitude velocities and low-level mass flux than the dual-Doppler method, and thus exhibited stronger radial and vertical velocities. But, the dual-Doppler method is not constrained by the axisymmetric assumption and was used to provide insight into asymmetries in the tornado by utilizing the axisymmetric mean to linearize the wind field in the vicinity of the tornado.

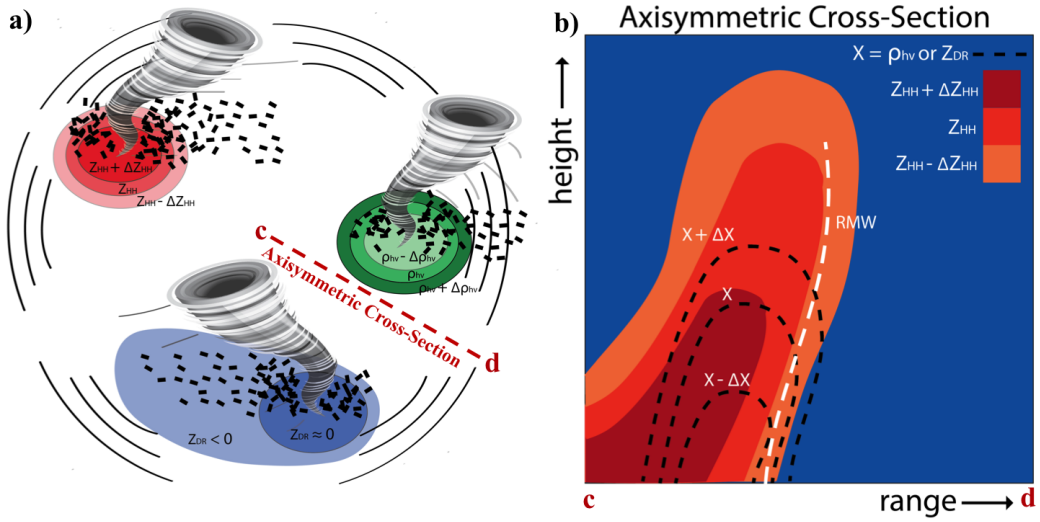


Figure 3.14: Conceptual diagrams of polarimetric signatures associated with large tornado subvortices displayed as (a) a PPI and (b) an axisymmetrically averaged vertical cross-section along line c-d in panel (a). Panel (a) illustrates the high $Z_H$, low $\rho_{hv}$, and near zero $Z_{DR}$ observed within the high $\zeta$ regions associated with the largest two subvortices in the 10 May 2010 Moore-Choctaw tornado. Also illustrated is the trailing region of negative $Z_{DR}$. Panel (b) illustrates the annulus of $Z_H$ associated with debris centrifuging and the annuli of low $\rho_{hv}$ and $Z_{DR}$ associated with the tornado subvortices and bound by the radius of maximum winds (RMW, white dashed line).

Additional dual-Doppler datasets of TDSs are needed, especially ones with the high spatial- and temporal-resolution that are provided by mobile radars. Expansion on the findings of this paper will further the understanding of how debris is distributed by the three-dimensional winds in the vicinity of tornadoes, which, in turn, will facilitate more accurate inference of tornado structure using polarimetric radars.

# Chapter 4

# Polarimetric Radar Observations of Simultaneous Tornadoes on 10 May 2010 near Norman, Oklahoma

This chapter utilizes data collected by the OU-PRIME C-band radar as well as KTLX and KOUN WSR-88D S-band radars to study a tornadic supercell that simultaneously produced a long-track EF-4 and an EF-2 landspout tornado near Norman, Oklahoma, on 10 May 2010. The dataset contains two TDSs in close proximity to one another that merge into the same parent updraft aloft, and eventually merge into one large TDS. Contrasting polarimetric characteristics of two tornadoes over similar land cover but with different intensities are documented. Also, the storm-scale sedimentation of debris within the supercell is investigated, which includes observations of rotation and elongation of a TDS with height. Additionally, a novel dual-wavelength comparison of debris within the tornado to debris in the near tornado environment is presented. Finally, the temporal evolution of the vertical structure of polarimetric variables within the TDS is discussed.

## 4.1 Introduction

This study documents debris sedimentation within the 10 May 2010 Norman–Little Axe EF-4 tornado using data collected by the OU-PRIME C-band radar (Palmer et al. 2011). OU-PRIME's 0.45° beamwidth provides finescale observations of tornadic debris and enables a novel statistical comparison of debris characteristics within the tornado and debris in the near-tornado environment, which includes debris fallout from the tornado and debris lofted along the RFGF. Additionally, this study documents novel observations of TDS rotation with height and the elongation of the TDS as debris are ingested into the storm-scale updraft. Finally, this case provides a unique opportunity to compare

TDS characteristics of two tornadoes in close proximity to one another. In addition to the Norman–Little Axe tornado, an EF-2-rated landspout tornado formed along the RFGF of the parent supercell to the Norman–Little Axe tornado and eventually passed within a few km of the Norman tornado. As discussed in Chapter 1, tornadoes with different intensities broadly exhibit differences in TDS characteristics and behavior. In this instance, the two tornadoes are encountering similar landcover, which modifies TDS properties through the scattering characteristics of debris available to be lofted (Van Den Broeke and Jauernic 2014; Van Den Broeke 2015); therefore any differences in the two TDSs are likely due to tornado- and storm-scale processes.

## 4.2 Methods

### 4.2.1 Case Overview

This study investigates two tornadoes in Cleveland County that occurred just after 5:30 pm local time on 10 May 2010 (Fig. 4.1). The Norman-Little Axe tornado (red star) occurred from 2232–2259 UTC and was rated EF-4. It had a 35-km path length, ∼2000-m maximum damage width, and caused 2 of the 3 fatalities that occurred for the event and injured 22 additional people. The landspout tornado (blue star) associated with the Norman-Little Axe supercell formed at 1639 UTC and dissipated at 1659 UTC. It was rated EF-2 and caused 3 additional injuries. The landspout tornado had a path length of 17 miles and a maximum damage width of 440 yd. More details on the event can be found online at `https://www.weather.gov/oun/events-20100510` and in Palmer et al. (2011).

### 4.2.2 Radar Data and Dual-Doppler Synthesis

Polarimetric radar data used for this project were collected by OU-PRIME. Supplementary velocity data for dual-Doppler synthesis was collected by the KTLX WSR-88D radar located just east of Oklahoma City. At its closest range of 15 km, the Norman-Little

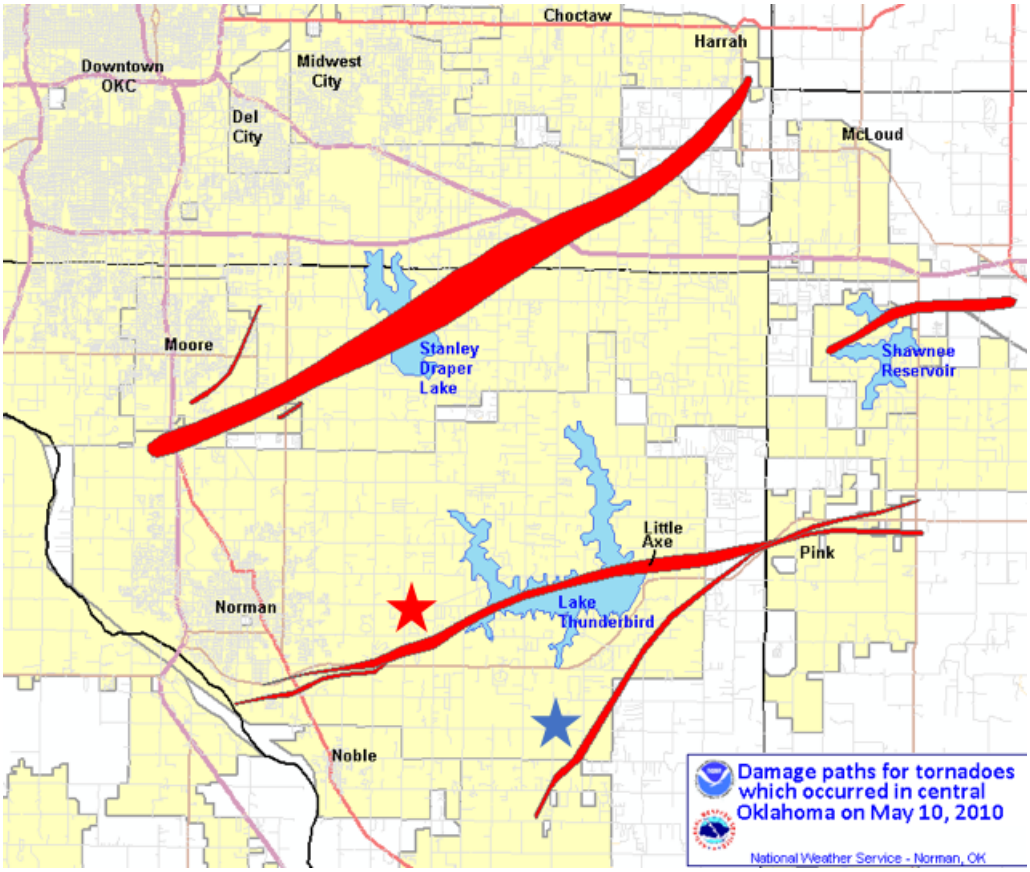


Figure 4.1: Tornado damage paths in Cleveland County, Oklahoma, on 10 May 2010. Figure courtesy of the National Weather Service Office in Norman. Available online at `https://www.weather.gov/oun/`events-20100510-maps. The red star indicates the track of the Norman–Little Axe tornado and the blue star indicates the track of the landspout tornado.

Axe tornado was sampled as low as ∼300 m above radar level (ARL) by OU-PRIME and as low as ∼230 m by KOUN. Additional details for the radar data used in this case can be found in Table 1 of Griffin et al. (2017) and further details regarding OU-PRIME and its observations during the event can be found in Palmer et al. (2011).

Radar data editing for this project was completed using the National Center for Atmospheric Research Earth Observing Laboratory's Solo3 editing software (Oye et al. 1995). Dual-Doppler and objective analyses were performed using the Observation Processing and Wind Synthesis (OPAWS) code developed by D. Dowell (NOAA/Earth System Research Laboratory) and L. Wicker (National Severe Storms Laboratory). Source code can be found online at `http://code.google.com/p/opaws/`. Detailed explanation of the dual-Doppler syntheses and data quality control are provided in Griffin et al. (2017). Values of differential phase in the vicinity of the tornado ranged between -20° and 0° with initial differential phase near 0° and a simple differential attenuation correction calculation (not shown) created no appreciable changes in the polarimetric fields. Thus, no differential attenuation correction was applied to the data. The limiting spatial resolution was similar in both cases so none of the objective analysis parameters in this study differs from what is discussed in Griffin et al. (2017). In this study, dual-Doppler analyses are conducted at 2242 and 2247 UTC. For both of these analyses, the difference in low-level scan times between KTLX and OU-PRIME was ∼20–40 s. Additional analyses are available at 2255 and 2259 UTC and may be used in future studies. Note that OU-PRIME did not sample the low-level mass flux below 300 m in the vicinity of the tornado, which may lead to large errors in the vertical velocity estimates. However, vertical velocity is only used qualitatively in this study.

### 4.2.3 Debris Classification

Originally, the criteria for a TDS at S band were values of $Z_H > 45$ dBZ, $Z_{DR} < 0.5$ dB, and $\rho_{hv} < 0.8$ collocated with a vortex signature in radial velocity $V_r$ (Ryzhkov et al. 2005b). The criteria for $Z_H$ has since been relaxed (e.g., Schultz et al. 2012a;

WDTB 2013; Van Den Broeke and Jauernic 2014) based on numerous observations of tornadoes exhibiting lower values of $Z_H$. For this case, in order to capture lower debris concentrations within the WEH and elsewhere outside of the tornado a C band, a 10 dBZ threshold for tornadic debris was implemented, similar to what was used in Griffin et al. (2017) for this same day. An upper $\rho_{hv}$ threshold of 0.82 was used based on the Bodine et al. (2013) finding of increasing contribution of precipitation above this threshold. No $Z_{DR}$ threshold was imposed in order to include resolution volumes where debris and precipitation are both present. These criteria performed well compared to subjective debris identification (not shown).

Debris in and near the Norman-Little Axe tornado are separated into 'inner' and 'outer' debris based on whether resolution volumes are within 1 km of the subjectively identified tornado center or between 1 and 3 km from the tornado center. The inner debris classification can be thought of as a traditional TDS since the debris are collocated with the tornado vortex. The 1-km threshold was chosen because it approximately represents the radius of the maximum damage swath in the tornado. Outer debris is a combination of debris falling out of the tornado, debris lofted by inflow into the tornado, and debris lofted along the gust front near the tornado. The 3-km maximum radius for outer debris was chosen to prevent debris associated with the landspout tornado from being erroneously identified as debris falling out of the Norman-Little Axe tornado. In a few instances, debris are separated into 'light' vs. 'heavy' debris classifications based on a subjective threshold of 30 dBZ. Examples of the debris classification can be seen in Fig. 4.2j-l. These classifications can be thought of as a combination of debris size and concentration contributing to the magnitude of $Z_H$.

## 4.3 Results

### 4.3.1 Polarimetric and Dual-Doppler Observations of Tornadic Debris

At 2242 UTC, the first observation time, the Norman-Little Axe tornado had already been in progress[1] for 10 min. At this time, the tornado exhibited a TDS with a 1.5-km diameter and a large appendage of debris extending to the east and south from the northeast side of the TDS (Fig. 4.2). This 'tail' of debris became shorter with height (Fig. 4.2j-l), suggesting that either debris were not being lofted as high in the southern part of the debris tail, or that debris were being transported toward the tornado with height. Additionally, the location where the debris connected with the TDS rotated counter clockwise with height, connecting on the northeast side of the TDS at 1° elevation (Fig. 4.2a,d,g,l) and connecting with the north side at 3° elevation (Fig. 4.2c,f,i,l). Dual-Doppler winds in the northern portion of (Fig. 4.3a,c) did show westward storm-relative winds in the northern portion of the debris tail, supporting the hypothesis that debris in the northern part of the tail were being ingested into the 'inner' debris region in Fig. 4.2j-l. However, the shortening of the debris tail could also have been an artifact of the temporal differences between the scans. While much of the debris tail exhibited $Z_H$ $>$ 30 dBZ, a large shield of debris with lower $Z_H$ values surrounded it on the east side of the tornado (Fig. 4.2j).

The debris tail appeared to be part of a larger linear region of low $\rho_{hv}$ extending to the south of the tornado. Another similar line of low $\rho_{hv}$ was present to the east of the tornado. This region of low $\rho_{hv}$ to the east was collocated with the RFGF in the dual-Doppler analyses (Fig. 4.3a). While the dual-Doppler analyses did not show a secondary gust front associated with the debris tail, there may have been a shallow or under-resolved feature, such as a rear-flank gust front surge, that was responsible for ejecting the debris to the east similar to what was seen in Kurdzo et al. (2015). Interestingly, $Z_{DR}$ along

[1]OU-PRIME was operating in a sector scanning mode. Prior to 2242 UTC it was collecting data on the Moore-Choctaw tornado (Griffin et al. 2017) and not scanning the Norman-Little Axe tornado.

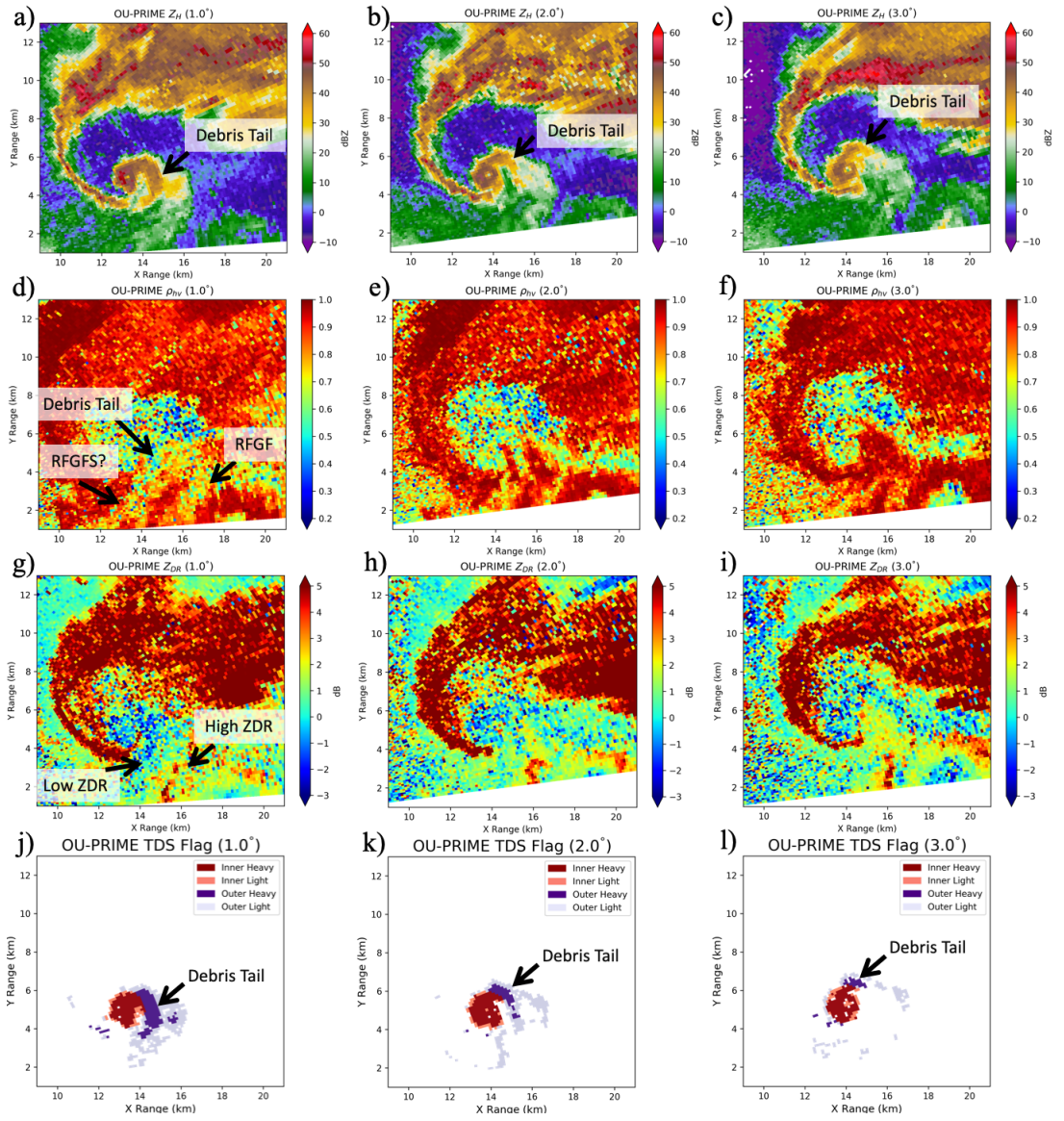


Figure 4.2: OU-PRIME PPI plots of (a–c) reflectivity (dBZ), (d–f) correlation coefficient, (g–i) differential reflectivity (dB), and (j–l) debris classification at 1.0°, 2.0°, and 3.0° elevation (from left to right) for the Norman-Little Axe tornado (western TDS only) valid at 2242 UTC.

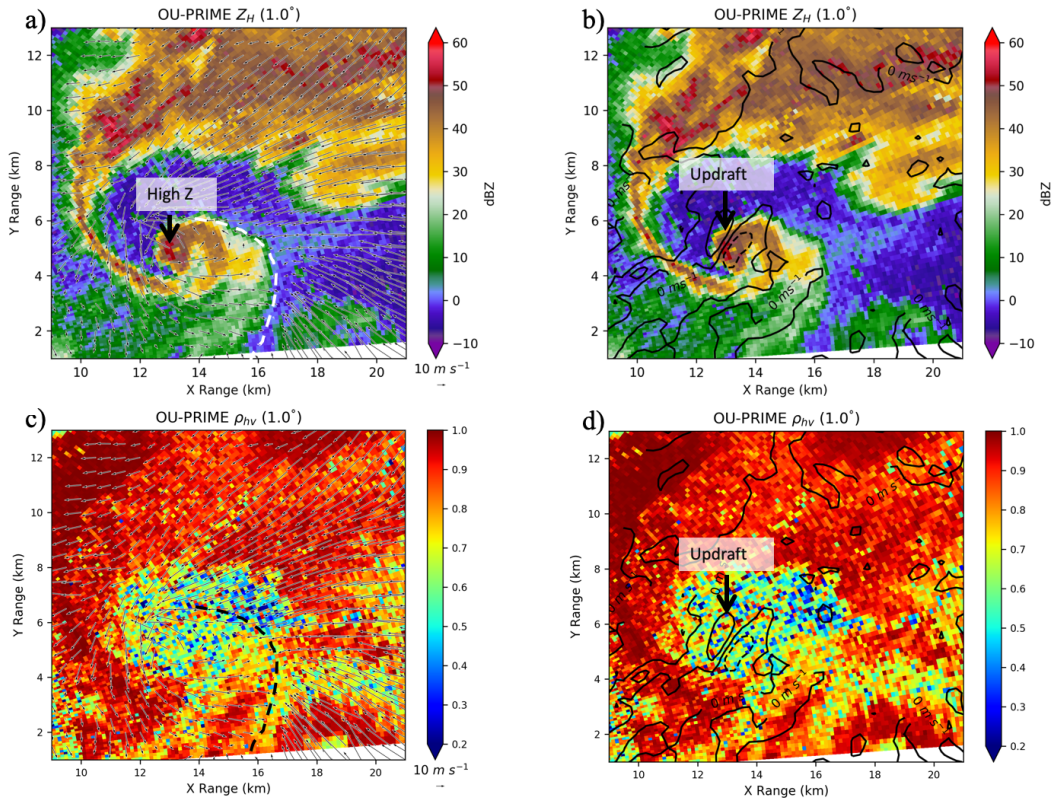


Figure 4.3: OU-PRIME PPI plots at 1.0° elevation of (a-b) $Z_H$ (dBZ) and (c-d) $\rho_{hv}$ overlaid with dual-Doppler derived (a,c) storm-relative horizontal winds (arrows) and (b,d) vertical velocity at 250 m ARL valid at 2242 UTC.

the RFGF was positive, whereas $Z_{DR}$ within and extending southward from the debris tail was negative (Fig. 4.2g) suggesting different types or orientations of scatterers along each of the linear features. Likely, light debris and insects were concentrated along the RFGF and tornadic debris mostly made up the debris tail.

At 1° elevation, the highest $Z_H$ within the TDS was on the west side of the tornado (Fig. 4.2a). The most negative values of $Z_{DR}$ were also located on the west side of the TDS (Fig. 4.2g). Dual-Doppler derived vertical velocities (Fig. 4.3b) were most positive on the west side of the tornado, which may indicate that enhanced debris lofting occurred in this region. A small WEH was present throughout the entire observed depth of the storm and becomes more prominent with height, suggesting debris and hydrometeors were being centrifuged from the tornado (Dowell et al. 2005). Also of interest for operational purposes was that due to the presence of the debris tail and inflow, the area of low $\rho_{hv}$ was large at low levels and therefore $Z_H$ must be used in order to distinguish high concentrations of debris from areas of smaller SNR and light debris concentrations. This was unlike the Moore-Choctaw TDS on the same day where the area of low $\rho_{hv}$ associated with debris was entirely surrounded by precipitation making the TDS easy to identify (Griffin et al. 2017).

Farther aloft, precipitation wrapped around the TDS, making it much more distinct (Fig. 4.4). A large band of mostly small drops with low, yet positive $Z_{DR}$ and high $\rho_{hv}$ was present to the south and southeast of the TDS and began to fill in the area of inflow to the northeast of the tornado at 5.0° and 6.5° (Fig. 4.4e-f). A very narrow band of large raindrops nearly encompassed the TDS. These large drops were an extension of a thin hook echo, which was almost entirely comprised of large drops on the inner side. Interestingly, the hook echo had a much larger width in $Z_{DR}$ than it had in $Z_H$ suggesting that there were smaller concentrations of large drops along the inside of the hook echo, similar to what was observed in Kumjian (2011) and French et al. (2015). At 5.0° and 6.5° elevation, a band of precipitation wrapped into the TDS. The narrow band of precipitation exhibited moderately high values of $Z_{DR}$ (Fig. 4.4h-i) suggesting

that perhaps it was comprised of a mixture of large drops and debris. The entrainment of large drops could potentially raise the values of $Z_{DR}$ and $\rho_{hv}$ throughout the entire TDS even when they are not the dominant scatterers (Bodine et al. 2014). Bulk TDS statistical properties will be a subject of discussion in the next two subsections. Unlike at lower levels, nearly all of resolution volumes containing debris at upper levels exhibited $Z_H <$ 30 dBZ (Fig. 4.4j-l), perhaps because debris were not lofted as high at distances from the tornado where 'light' debris concentrations were observed at lower scans (Fig. 4.2j-l).

### 4.3.2 Comparison of Simultaneous TDSs

At 2244 UTC, a landspout tornado located along the RFGF to the east of the Norman-Little Axe tornado entered OU-PRIME's observation domain (Fig. 4.5). Prior to entering the domain, this tornado had already been in progress for approximately 5 min (not shown) and had already begun lofting large quantities of debris (TDS #2 in Fig. 4.5a). This eastern TDS was elongated such that the major axis was along the gust front with a north-south orientation. The landspout tornado did not exhibit a WEH, although this could be because the diameter was too small to be resolved so far from the radar. An annulus of low $\rho_{hv}$ (Fig. 4.5d) was present in the eastern TDS, similar to what was observed in the Moore tornado on this same day (Griffin et al. 2017); however, it is unlikely this is associated with large tornado subvortices like were observed in the Moore tornado near its RMW. Meanwhile, the western TDS associated with the Norman-Little Axe tornado still exhibited a well-defined WEH and, at 2° elevation, still had much higher $Z_H$ on its western side (Fig. 4.5b). The TDS was elongated such that the major axis was oriented east-west, which paralleled the local RFGF orientation in the dual-Doppler analyses performed before (Fig. 4.3) and after this time (Fig. 4.7). No small-scale coherent features were observed at low levels in $\rho_{hv}$ or in $Z_{DR}$ for the Norman-Little Axe tornado. Similar to at the previous time, a region of 'light' debris concentrations extended to the east of the Norman-Little Axe tornado, but at higher elevations nearly all of the resolution volumes containing debris exhibited $Z_H >$ 30 dBZ (Fig. 4.5j-l).

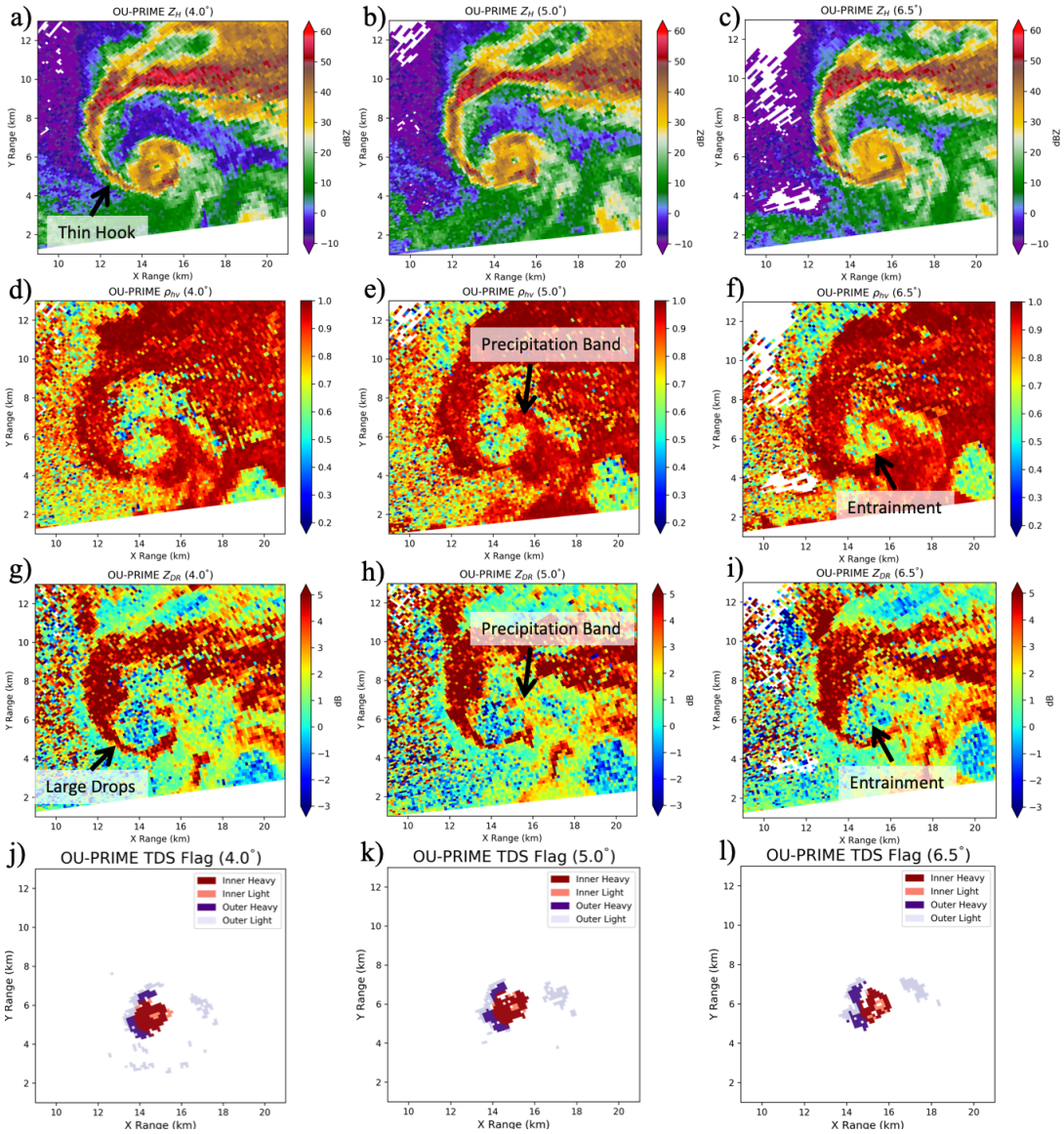


Figure 4.4: Same as Fig. 2 except at 4.0°, 5.0°, and 6.5° elevation (from left to right) valid at 2242 UTC.

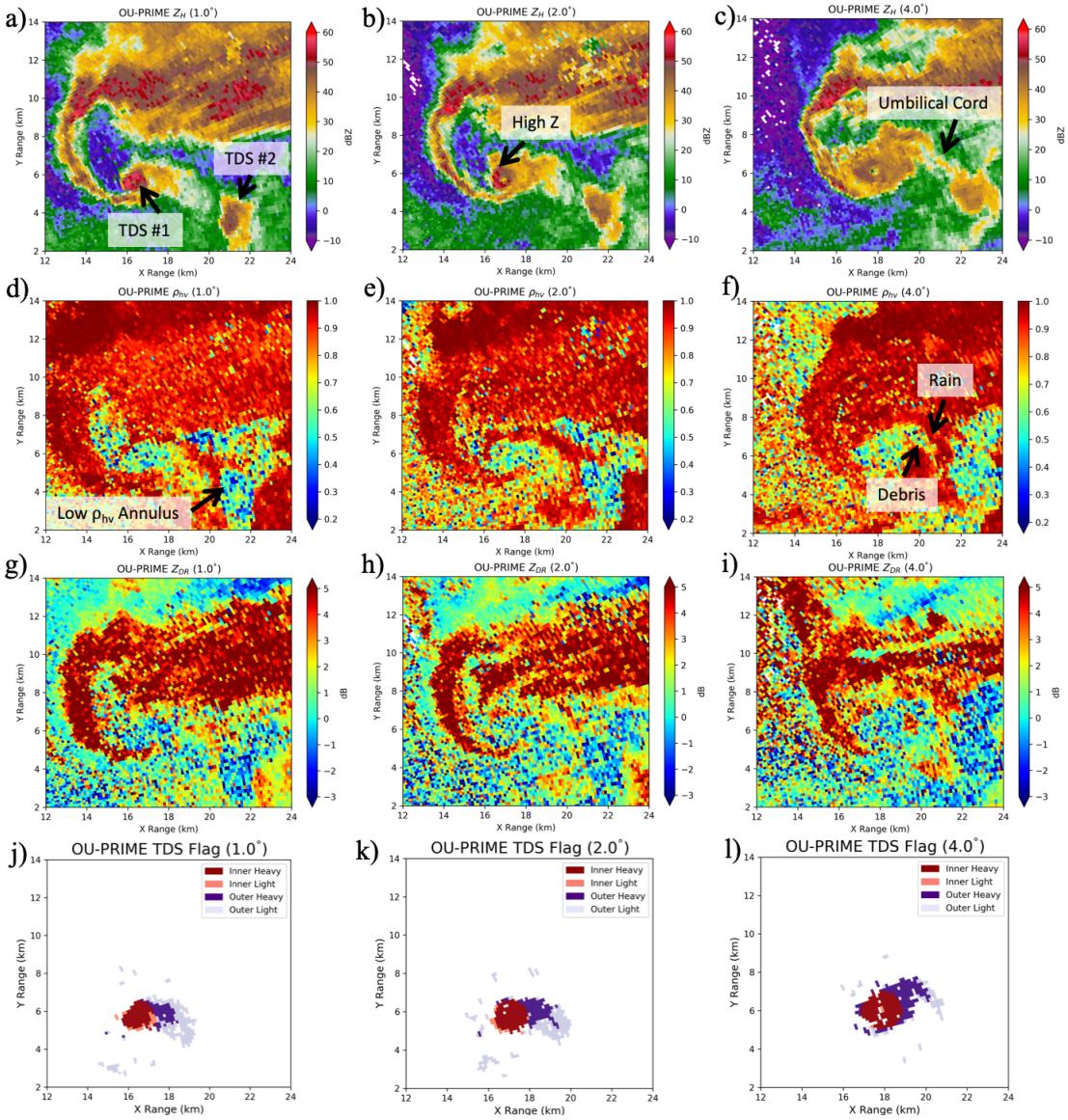


Figure 4.5: Same as Fig. 2 except at 1.0°, 2.0°, and 4.0° elevation (from left to right) valid at 2244 UTC.

Aloft at 4°, the eastern TDS exhibited slightly lower $Z_H$ compared to at low levels and had a much larger area than in the low levels (Fig. 4.5c,f,i,l). The TDS extended well to the north of the location of the tornado, with the northern portion of the TDS having relatively lower $Z_H$ while maintaining similar values of $Z_{DR}$ and $\rho_{hv}$ as the rest of the TDS. Perhaps this was the result of smaller concentrations of debris being advected to the north and ingested by the storm-scale updraft. A similar elongation of the Norman-Little Axe TDS to the northeast was also observed at this time (Fig. 4.5f). The storm-scale sedimentation of debris is discussed in the next two subsections. In addition to the northeast extension of the Norman-Little Axe TDS, a northwest-southeast oriented appendage to the TDS was also present at 4° elevation on its northeast side (Fig. 4.5f). Immediately to the north of this appendage was an 'umbilical cord' comprised of rain that connected the Norman-Little Axe TDS to the TDS associated with the landspout tornado. Unfortunately, there were no dual-Doppler analyses available at this time to definitively investigate kinematic relationships of these features to the TDS; however, the umbilical cord did approximately parallel the RFGF in the dual-Doppler analyses performed at the previous and subsequent analysis times (-2 min and +2 min, respectively).

At 2247 UTC, the landspout tornado had moved north and west in a storm-relative sense and was less than 5 km from the Norman-Little Axe tornado (Fig. 4.6). The very close proximity of the two tornadoes can also be seen in their respective damage surveys (Fig. 4.2). At this time, the two TDSs still exhibited contrasting $Z_H$ structures. The Norman-Little Axe tornado still had a WEH, whereas the landspout tornado had the highest $Z_H$ at its center and decreasing $Z_H$ with radius from the center of the tornado (Fig. 4.6a). An area of 'light' debris extended to the east of the Norman-Little Axe tornado Fig. 4.6j). This region of debris increased in $Z_H$ with height while maintaining a similar shape and area (Fig. 4.6l), perhaps due to large amounts of debris that was previously within the tornado being redistributed eastward. The landspout TDS exhibited two appendages, one on its northwest side and one on its southeast side. Dual-Doppler analyses (Fig. 4.7) suggest that the southeastern appendage was associated with inflow

into the tornado along the RFGF similar to the sawtooth features observed by Houser et al. (2016). It is likely that this appendage was made up of lighter debris lofted along the gust front and ingested into the TDS by strong inflow. Conversely, the appendage on the northwest side of the TDS was associated with outflow from the tornado and was likely comprised of debris lofted by the tornado. This is similar to the debris ejections documented by Kurdzo et al. (2015), except they noted predominantly southward and eastward ejections.

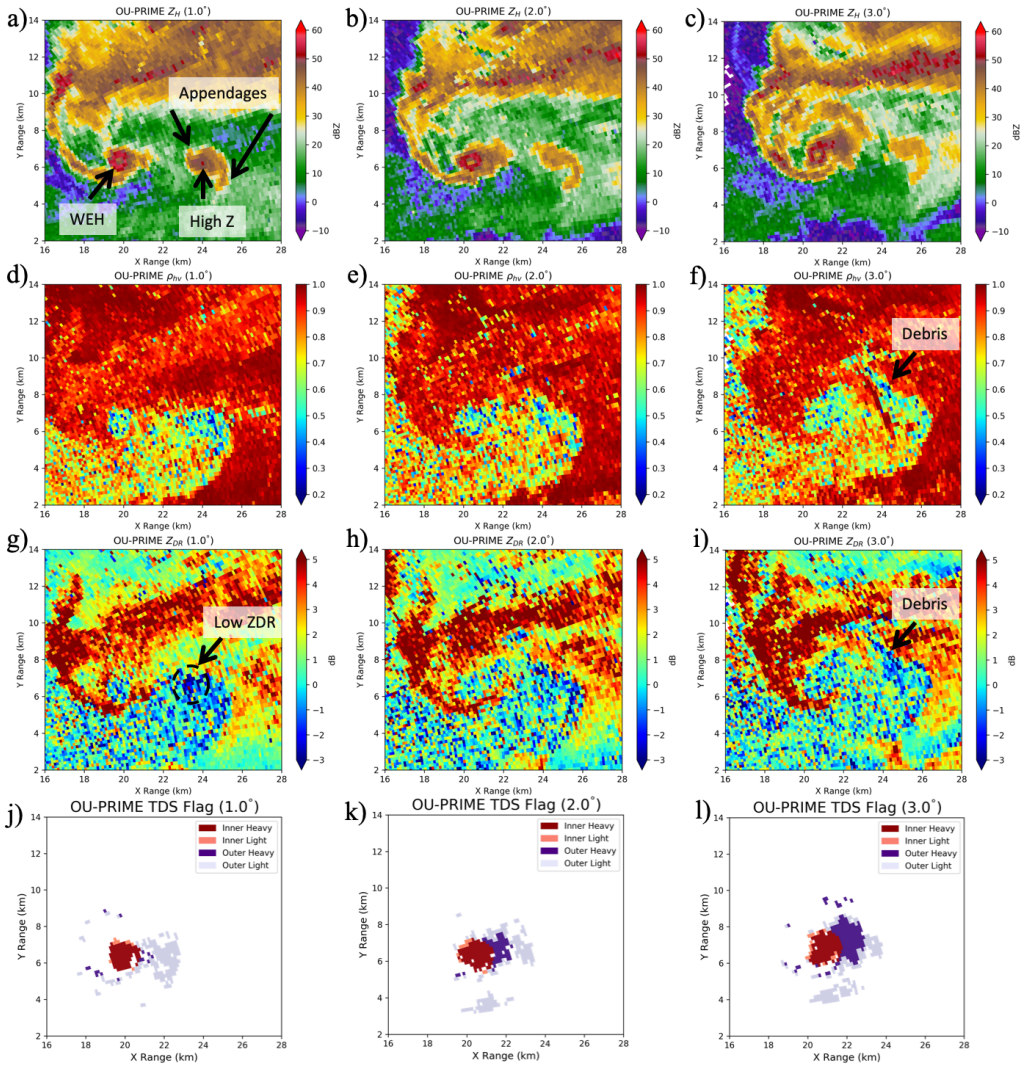


Figure 4.6: Same as Fig. 2 except valid at 2247 UTC.

Differential reflectivity less than -2 dB was observed in the northwest portion of the landspout TDS, which is associated with the debris tail made up of ejected debris

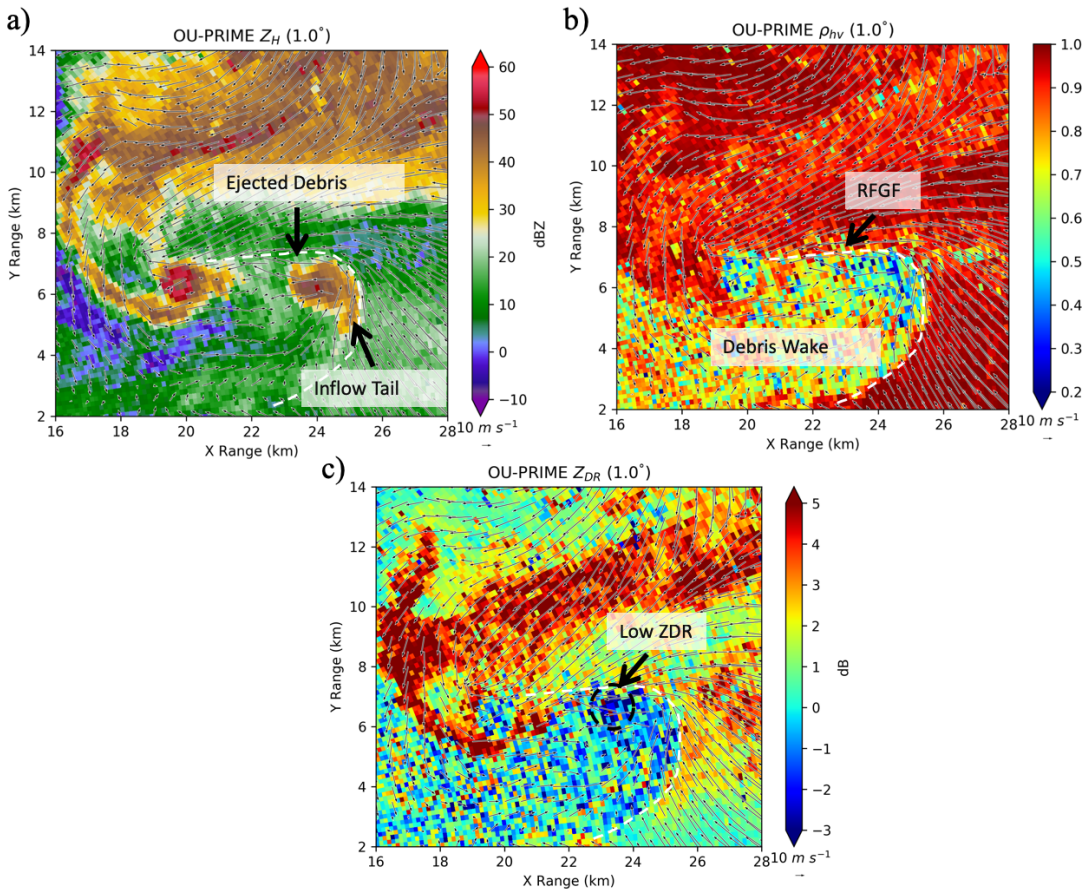


Figure 4.7: OU-PRIME PPI plots at 1.0° elevation of (a) reflectivity (dBZ), (b) correlation coefficient, and (c) differential reflectivity (dB) overlaid with dual-Doppler derived storm-relative horizontal winds (arrows) at 250 m ARL valid at 2247 UTC.

(Fig. 4.6g and Fig. 4.7c). Recent studies (e.g., Ryzhkov et al. 2005b; Bluestein et al. 2007a; Griffin et al. 2017; Umeyama et al. 2018; Wakimoto et al. 2018) have hypothesized that this negative $Z_{DR}$ is the result common debris alignment. Consistent with the observations of Griffin et al. (2017) and Wakimoto et al. (2018), the negative $Z_{DR}$ was observed at the periphery of the tornado, perhaps where tangential velocities were much larger than vertical velocities (Umeyama et al. 2018). While dual-Doppler analyses were performed for this case, they do not have the necessary resolution to interrogate this hypothesis. Similar to what was observed in Wakimoto et al. (2018), the extremely low $Z_{DR}$ was only present in the low levels with most resolution volumes exhibiting $Z_{DR} <$ -2 dB confined to the lowest elevation scan (Fig. 4.6g–i).

By 2249 UTC, the two TDSs began to merge at low levels (Fig. 4.8). For this reason, this time is excluded from the subsequent statistical comparison of the two TDSs at the end of this subsection. At 2° elevation, the TDS associated with the landspout tornado had a maximum width of ∼5 km (Fig. 4.8c,d) compared to ∼3 km at the previous times (e.g., Fig. 4.6b) and was more diffuse. It is possible that this was due to a weakening of the updraft associated with the tornado at this time (Bodine et al. 2013; Houser et al. 2016). Conversely, the Norman-Little Axe TDS maintained a similar size at low levels compared to previous times. In addition to debris concentrated near the tornadoes, a large area of lighter concentrations of debris could be seen in the wake of the two tornadoes. Debris filled the RFD (Fig. 4.8c) with its outer bounds to the east and north presumably being constrained by the RFGF similar to what was observed at the previous time (Fig. 4.7b).

Statistical analyses were conducted to compare the polarimetric characteristics of the two TDSs at 2244 and 2247 UTC using the criteria in Section 4.2.3. Median OU-PRIME $Z_H$ of resolution volumes identified as debris within 1 km of the Norman-Little Axe tornado was 5–9 dBZ higher than in the landspout tornado (Fig. 4.9a). In the landspout tornado, median $Z_H$ decreased slightly with height, whereas median $Z_H$ was relatively constant with height in the Norman-Little Axe tornado. However, these observations were all above 300 m ARL, below which is where we typically expect the largest decrease in $Z_H$

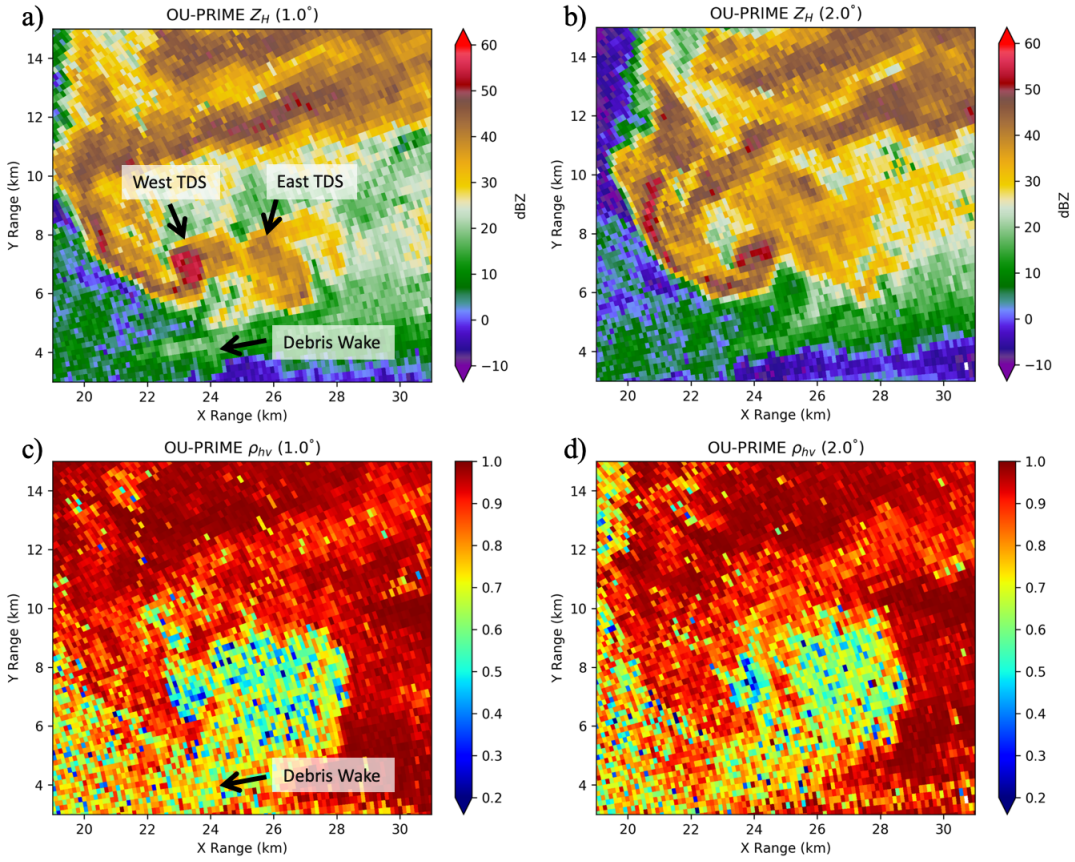


Figure 4.8: OU-PRIME PPI plots of (a–b) reflectivity (dBZ) and (c–d) correlation coefficient at (a,c) 1.0° and (b,d) 2.0° elevation valid at 2249 UTC.

to have occurred (e.g., Wurman et al. 1996; Dowell et al. 2005; Wakimoto et al. 2018). 90th percentile $Z_H$ was approximately 7 dBZ higher in the Norman-Little Axe tornado than the landspout tornado, and in both tornadoes 90th percentile $Z_H$ decreased with height. This suggests that the fallout rate of the largest debris was greater than for smaller debris, which is consistent with previous observations by Bodine et al. (2014). Both tornadoes were interacting with similar landcover, so therefore the differences in median and 90th percentile $Z_H$ between tornadoes are more likely attributed to differences in tornado intensity rather than landcover (Bodine et al. 2013; Van Den Broeke and Jauernic 2014; Van Den Broeke 2015). The Norman-Little Axe tornado produced EF-4 damage and likely lofted larger and greater quantities of debris than the landspout tornado, which produced EF-2 damage.

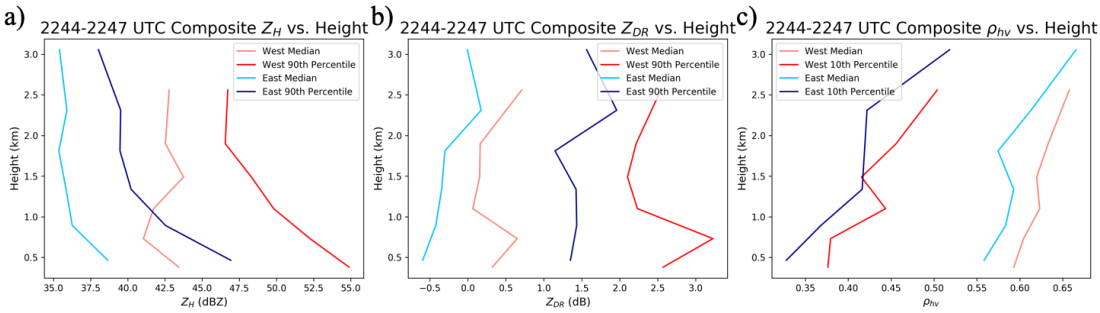


Figure 4.9: Composite profiles of OU-PRIME (a) reflectivity (dBZ), (b) differential reflectivity (dB), and (c) correlation coefficient vs. height (km) valid from 2244–2247 UTC. Red lines indicate the profiles of the western tornado and blue lines indicate the profiles of the eastern tornado. Light colors represent median values and dark colors represent 90th percentile values.

Median and 90th percentile OU-PRIME $Z_{DR}$ for tornadic debris was approximately 0.5–1.0 dB higher in the Norman-Little Axe tornado than the landspout tornado (Fig. 4.9b). For both tornadoes, median $Z_{DR}$ increased slightly with height and 90th percentile $Z_{DR}$ exhibited no appreciable trend. Median and 10th percentile $\rho_{hv}$ was approximately 0.05 higher in the Norman-Little Axe tornado and for both tornadoes median and 10th percentile $\rho_{hv}$ increased with height (Fig. 4.9c). The increase in $\rho_{hv}$ coupled with the decrease

in $Z_H$ with height is likely due to the fallout and centrifuging of the largest scatterers as altitude increases (Bodine et al. 2014). It is also likely that the previously discussed precipitation entrainment was responsible for the higher $Z_{DR}$ as well as the higher $\rho_{hv}$ in the Norman-Little Axe tornado, similar to what was observed in Bodine et al. (2014). While differences in the magnitudes of polarimetric variables exist due to differences in tornado intensity and precipitation entrainment, the behavior of the vertical profiles of polarimetric variables within the two tornadoes were similar.

### 4.3.3 Debris Sedimentation

In an effort to understand how tornado debris are dispersed into adjacent updraft and downdraft regions, the areal extent of debris was calculated in each quadrant relative to the tornado's position in order to quantify the distribution of debris with height. In the low levels, the majority of the near-tornado debris field for the Norman-Little Axe tornado was located to the east of the tornado center (Fig. 4.10a). Comparatively little debris were located to the north and south of the tornado, with nearly no debris located to the west of the tornado other than debris within the annulus of high reflectivity that surrounded the WEH. The area of debris located to the east of the tornado center decreased significantly with height from an average of 3.5 km$^2$ at 1.0° to less than 1 km$^2$ at 6.5°. The area of debris to the south of the tornado remained relatively constant up to 4.0° (∼1.5 km ARL) before it decreased slightly at 5.0° (∼ 2 km ARL) and 6.5° (∼ 2.75 km ARL) elevation. In contrast, the areal extent of debris to the north and west of the tornado increased with height up to 5.0° before decreasing slightly at 6.5°, likely due to an overall decrease in total debris area at higher elevations.

Apart from the first observation time, the total area of 'heavy' debris concentrations lofted near the Norman-Little Axe tornado increased with height (Fig. 4.10b). Additionally, the volume of lofted debris increased with time. It is likely that the change in the vertical distribution of debris after 2242 UTC was due to the increased centrifuging of

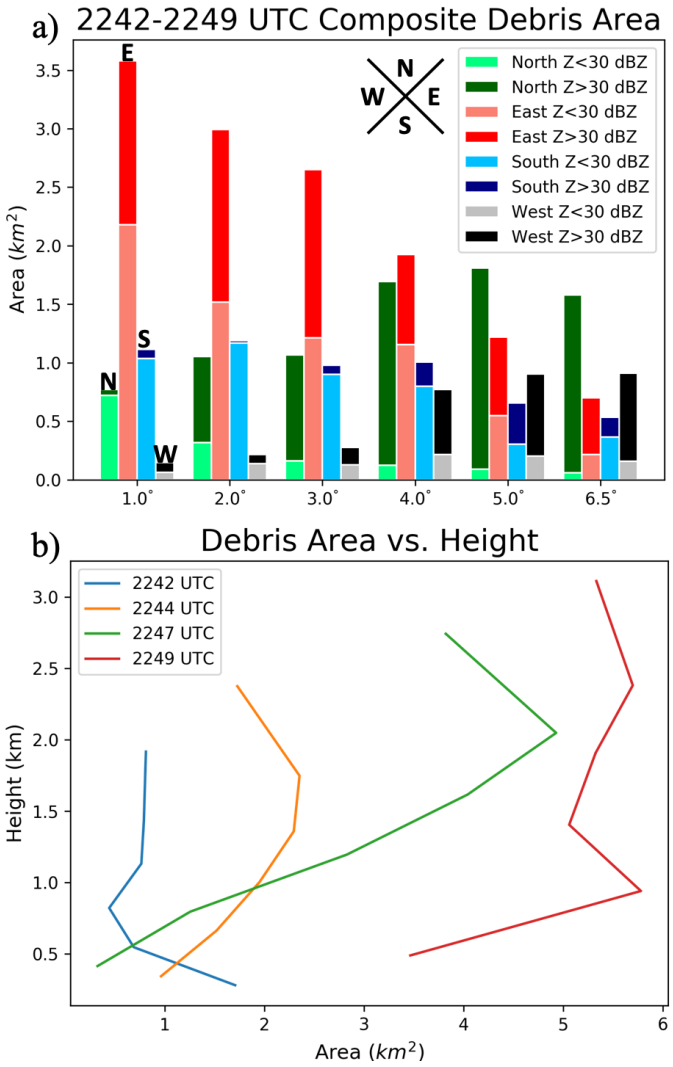


Figure 4.10: (a) OU-PRIME areal extent (km$^2$) of debris at 1.0°, 2.0°, 3.0°, 4.0°, 5.0°, and 6.5° in the northern (green), eastern (red), southern (blue), and western (black) quadrants. Quadrants are defined relative to the center of the tornado. Dark colors represent area with reflectivity >30 dBZ and light colors represent area with <30 dBZ reflectivity. (b) Area (km$^2$) of debris exhibiting $Z_H$ > 30 dBZ vs. height (km) valid at 2242 UTC (blue line), 2244 UTC (orange line), 2247 UTC (green line), and 2249 UTC (red line).

debris associated with an increase in the rotational velocity of the tornado late in the observation period (not shown). Debris would have been more likely to detrain farther from the tornado when tornado intensity was greater. In addition greater debris centrifuging, the increase in the intensity of the Norman-Little Axe tornado likely caused an increase in vertical debris flux, which would have resulted in the observed increase in the total volume of lofted debris. The temporal evolution of tornado intensity and its impact on the vertical profiles of polarimetric variables will be discussed in the next section.

The large area of debris to the east of the tornado in the low levels was largely due to the aforementioned debris 'tail' to the east of the Norman-Little Axe tornado, which was largest at 2242 UTC (Fig. 4.2a,d,g,j), but could also be seen to a lesser extent at 2244 UTC (Fig. 4.5a,d,g,j) and 2247 UTC (Fig. 4.6a,d,g,j). As previously discussed, the debris tail decreased in length and areal extent with height, which is one reason why the area of debris to the east of the tornado decreased with height. However, another factor in the upward decrease in area of debris to the east of the Norman-Little Axe tornado was the rotation of the TDS with height and redistribution of debris to the north, and to a lesser extent, to the west of the tornado (Fig. 4.11). At 2247 UTC, the major axis of the TDS was oriented nearly east-west (Fig. 4.11a,d,g). Going up in elevation, the major axis of the TDS rotated to the east-northeast (Fig. 4.11b,e,h) and then to the northeast (Fig. 4.11c,f,i). The TDS also became elongated as debris were transported to the north by storm relative winds (Fig. 4.13). From these observations it can be concluded that the areal extent of debris to the north of the tornado grew at the expense of the area of debris to the east of the tornado. This redistribution of debris to the north of the tornado is a near-real-time polarimetric radar verification of the observations from Snow et al. (1995) and (Magsig and Snow 1998) that the majority of debris is redistributed to the left of the tornado track.

The landspout tornado, while not lofting as much debris to higher altitudes as the Norman-Little Axe tornado, also exhibited an elongated TDS with tails of debris stretching to the south along the RFGF and to the north-northwest (Fig. 4.11c,f). Only a small

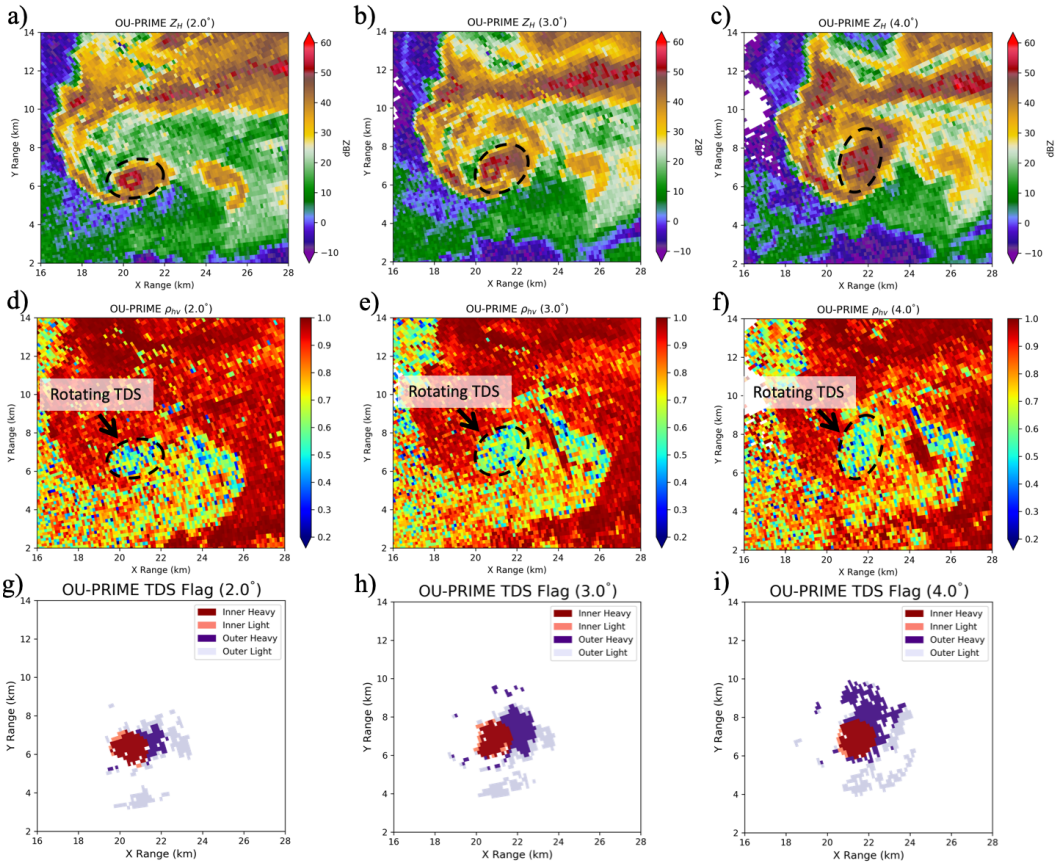


Figure 4.11: OU-PRIME PPI plots of (a–c) reflectivity (dBZ), (d–f) correlation coefficient, and (g–i) Norman-Little Axe tornado debris classification at (a,d,g) 2.0°, (b,e,h) 3.0°, and (c,f,i) 4.0° elevation valid at 2247 UTC.

arching band of precipitation separated the two TDSs as they converged toward a common point to the northeast of the Norman-Little Axe tornado. It is possible that debris were being drawn north and ingested into the storm-scale updraft that was located to the north of the two tornadoes (not shown).

At 2249 UTC, the Norman-Little Axe TDS maintained a northeastward orientation above the 4.0° elevation scan (Fig. 4.12). The Norman-Little Axe TDS became increasingly elongated with height, extending approximately 4 km along its major axis at 6.5° elevation (Fig. 4.12c,f,i,l). As noted at previous times, virtually all resolution volumes containing debris within the Norman-Little Axe tornado aloft exhibited $Z_H > 30$ dBZ (Fig. 4.12j-l). In contrast to the Norman-Little Axe tornado, the landspout TDS was much shallower than at previous times and did not loft debris above the 4.0° scan. As previously discussed, this may indicate that the landspout tornado had weakened by this time.

Dual-Doppler derived, mean storm-relative wind within 3 km of the Norman-Little Axe tornado at 2247 UTC veered with height (Fig. 4.13). In the low levels, mean storm relative flow was to the south, largely influenced by northerly winds within the RFD and east-northeasterly inflow into the tornado (Fig. 4.7). However, the mean storm relative winds shift to the northeast with height (Fig. 4.13) with mean winds of $\sim$20 m s$^{-1}$ to the northeast at 3.75 km ARL, approximately the altitude of the TDS at 6.5° elevation in Fig. 4.14c,f,i,l two minutes later at 2249 UTC. It is likely that the veering storm-relative wind profile was responsible for the rotation and elongation of the TDS to the northeast with height.

### 4.3.4 Dual-Wavelength Observations of Inner vs. Outer Debris

For the Norman-Little Axe tornado, the profiles of 'inner' debris within 1 km of the tornado, and 'outer' debris between a 1 and 3 km radius from the tornado were compared at C and S band (Fig. 4.14). At low levels, $Z_H$ was higher for inner debris than for outer debris (Fig. 4.14a,d). As previously discussed, $Z_H$ decreased slightly with height for

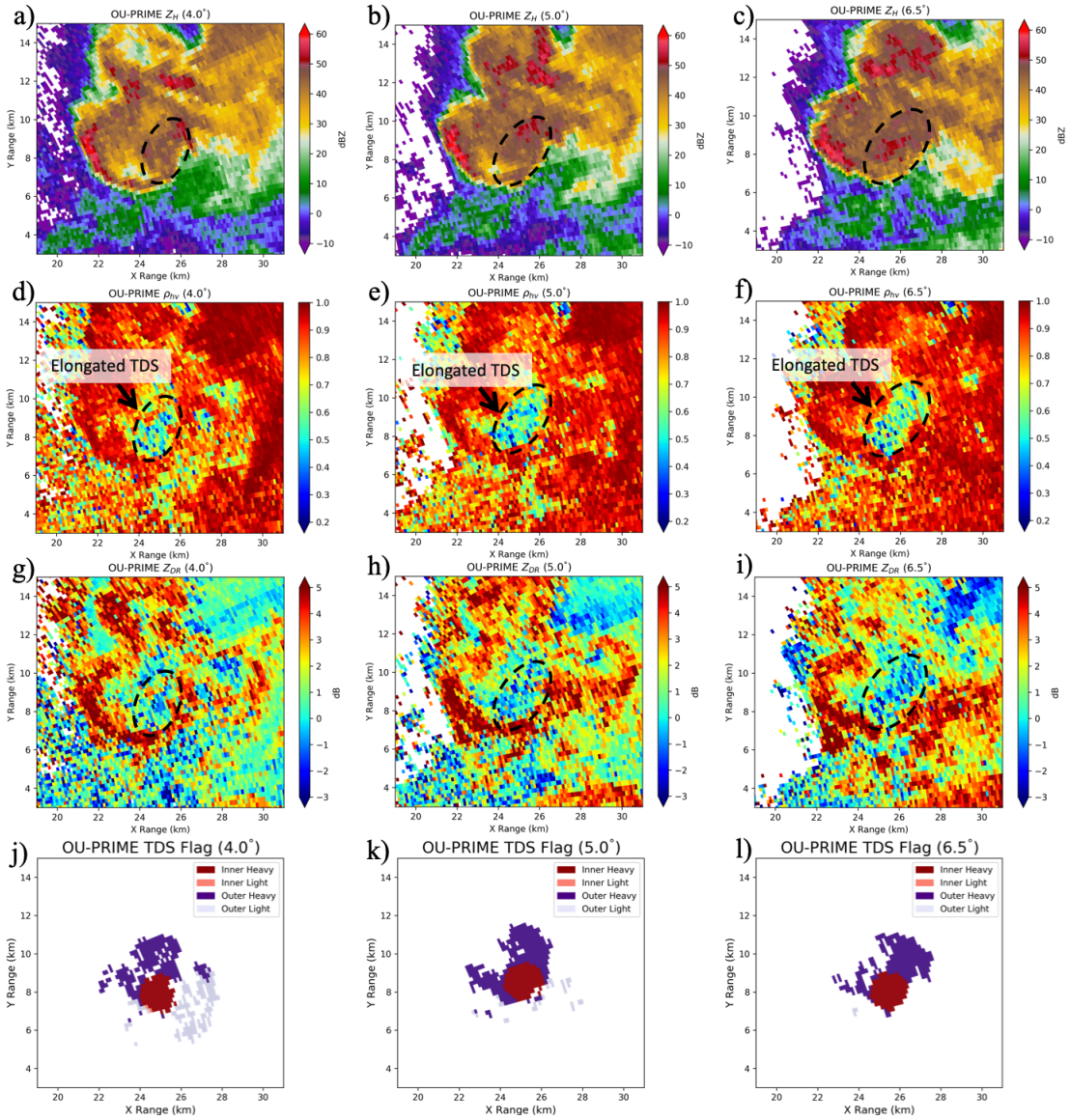


Figure 4.12: Same as Fig. 2 except at 4.0°, 5.0°, and 6.5° elevation (from left to right) valid at 2249 UTC.

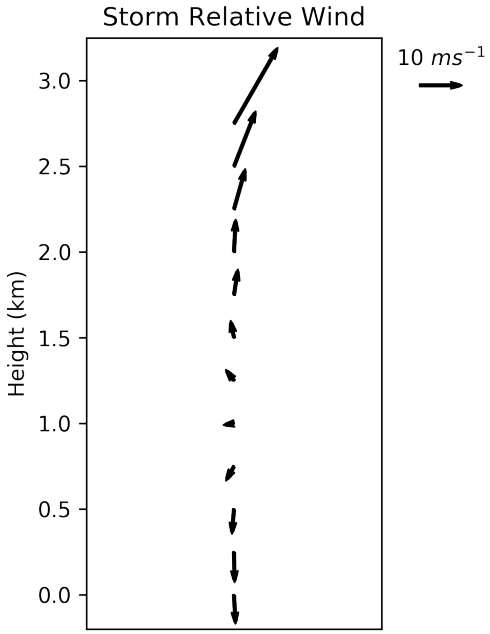


Figure 4.13: Dual-Doppler-derived mean storm relative horizontal wind profile, computed within a 3-km radius of the Norman-Little Axe tornado valid at 2247 UTC.

inner debris. However, for outer debris, $Z_H$ increased with height with median and 90th percentile values at S and C band becoming similar to their respective values for inner debris at 6.5° elevation. This occurred because larger debris were redistributed outward with height due to centrifuging and the northward transport of debris advecting debris away from the center (e.g., Fig. 4.11). Histograms of $Z_H$ (not shown) confirm that the distribution of $Z_H$ for outer debris at 6.5° was very similar to the distribution for inner debris at 1.0°. Additionally, the size distribution of debris likely narrowed with height due to the fallout of large debris causing more similar values of $Z_H$ between inner and outer debris at higher elevations. Median and 90th percentile $Z_H$ was approximately 7 dBZ higher at S band than at C band for inner debris. This was likely because volumes of inner debris were more likely to contain larger scatterers, which remain Rayleigh scatterers for larger sizes at S band than C band resulting in higher $Z_H$ (c.f., Figure 3 in Bodine et al. (2016b)). The dual-wavelength difference in $Z_H$ at low levels for outer debris was comparatively small with 1–2 dBZ differences in median and 90th percentile $Z_H$ below 1000 m ARL, likely because the debris sizes were much smaller for outer debris. The dual-wavelength difference in $Z_H$ for outer debris became greater above 1 km and more similar to the dual-wavelength difference for inner debris, going from a $\sim$ 3 dBZ mean difference below 1 km to a $\sim$ 9 dBZ mean difference between 1 and 2 km as larger debris particles were redistributed away from the tornado.

For both inner and outer debris, $Z_{DR}$ was larger at C band than S band (Fig. 4.14b,e). It is likely that C band was more sensitive to rain because many of the debris particles were non-Rayleigh scatterers allowing large raindrops to make up a larger proportion of the total Rayleigh scatterers. The dual-wavelength difference in median $Z_{DR}$ was greater for outer debris likely because more large raindrops were present at this range from the tornado (e.g., Fig. 4.4). Similarly, the 90th percentile values of $Z_{DR}$ were higher at both wavelengths for outer debris than inner debris because of greater concentrations of large raindrops at outer radii.

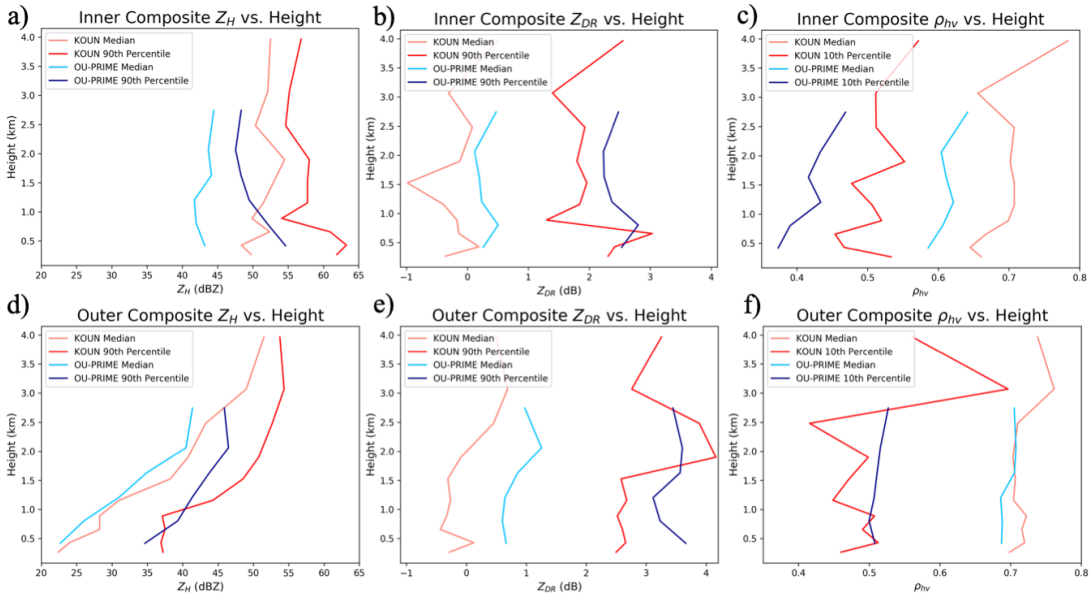


Figure 4.14: Composite profiles of (a,d) reflectivity (dBZ), (b,e) differential reflectivity (dB), and (c,f) correlation coefficient vs. height (km) for the western tornado valid from 2242–2249 UTC. Profiles in (a–c) are for inner debris (debris within a 1-km radius of the tornado center) and profiles in (d–f) are for debris farther than 1 km from the tornado center. Red lines indicate profiles from KOUN (S band) and blue lines are from OU-PRIME (C band). Light colors represent median values and dark colors represent median values.

Median and 10th percentile $\rho_{hv}$ was larger at S band than at C band (Fig. 4.14c) for inner debris. This is consistent with the findings of Bodine et al. (2014) and is due to a greater impact of resonance effects at C band due to a larger proportion of non-Rayleigh scatterers in a given volume containing debris. Additionally, C band is more sensitive to non-spherical shapes (Balakrishnan and Zrnić 1990), which would result in lower $\rho_{hv}$. At both S and C band, $\rho_{hv}$ increased with height for inner debris, likely due to the fallout of larger debris and consistent with the observations in Bodine et al. (2014). Conversely, differences in S- and C-band $\rho_{hv}$ were minimal for outer debris while median and 10th percentile values of $\rho_{hv}$ remained relatively constant with height in the lowest 2.5 km ARL (Fig. 4.14f). The smaller dual-wavelength differences in both $\rho_{hv}$ and $Z_H$ support the hypothesis that, in general, outer debris were comparatively smaller than inner debris. Additionally, both median and 10th percentile $\rho_{hv}$ were 0.1 higher for outer debris than inner debris suggesting proportionally fewer non-Rayleigh scatterers in the outer region. Unlike $Z_H$, however, the difference in $\rho_{hv}$ between S and C band did not increase with height for outer debris as inner debris were redistributed outward. Perhaps an increasing influence of precipitation hinted at by a slight positive trend in median $Z_{DR}$ with height (Fig. 4.14e) could explain the relatively constant $\rho_{hv}$ despite higher $Z_H$ from the introduction of larger debris particles from within the tornado. Regardless, it can be concluded that outer debris are likely to be smaller than inner debris on the whole at low levels with the debris characteristics becoming more similar between inner and outer debris at higher elevations due to the fallout and transport of inner debris away from the tornado.

## 4.4 Discussion

### 4.4.1 TDS Rotation

While the rotation of the TDS with height was something that was consistently observed in the Norman-Little Axe tornado, it is uncertain whether this TDS characteristic is commonplace among other tornadoes. For example, the Moore-Choctaw tornado, which was observed by OU-PRIME on the same day as the Norman-Little Axe tornado, was nearly circular in the low levels (c.f., Figure 2 in Griffin et al. (2017)) and remained relatively symmetric throughout the lowest 1.5 km ARL, only becoming slightly elongated to the northeast at higher elevation scans up to 2.5 km ARL which was approximately the top of the observed TDS (not shown). A small survey of recent tornadoes in the Oklahoma City metro[2] observed by KTLX also did not provide many observations of TDS rotation with height. However, in many instances it was difficult to determine the the shape and behavior of the TDS due to the range of the storms and relatively broad azimuthal sampling of the WSR-88Ds above 1.3°.

However, in our brief survey of central Oklahoma cases, there has been at least one instance of TDS rotation with height captured by KTLX. The 19 May 2013 Shawnee, Oklahoma, tornado passed very close to KTLX and at 2336 UTC, when the tornado was approximately 12 km in range, a north-south-oriented, elongated TDS was observed at 5° elevation ($\sim$ 1 km ARL, Fig. 4.15a,d). The TDS rotated counter-clockwise with height such that it was northwest-southeast oriented at 8° ($\sim$1.75 km ARL, Fig. 4.15c,f). The counter-clockwise rotation of an elongated TDS was very similar to the Norman-Little Axe tornado and demonstrates that the behavior of the Norman-Little Axe tornado was not a singular occurrence.

It may not be a coincidence that that the Shawnee tornado was the only KTLX case that unambiguously exhibited TDS rotation with height since it was one of the

[2]The survey included the 19 May 2013 Shawnee tornado, 20 May 2013 Moore tornado, and 31 May 2013 El Reno tornado, which all produced large, deep TDSs near KTLX.

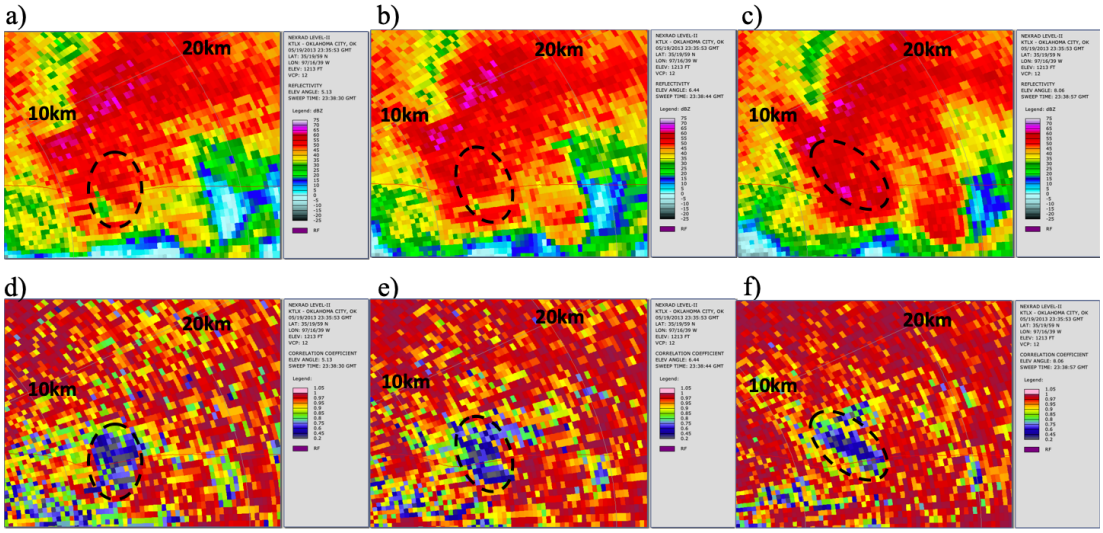


Figure 4.15: PPI plots of KTLX (a–c) reflectivity (dBZ) and (d–f) correlation coefficient at (a,d) 5°, (b,e) 6.5°, and (c,f) 8° elevation valid at 2336 UTC for the 19 May 2013 Shawnee, Oklahoma, tornado. Figures generated by the NOAA Weather and Climate Toolkit, available online at `https://www.ncdc.noaa.gov/wct/`. Rings represent range to radar (km).

best resolved tornadoes spatially due to its close range. However, the fact that the Moore-Choctaw tornado did not exhibit TDS rotation with height despite its relatively close range (∼20 km) and the 0.5° beamwidth of OU-PRIME means that in some cases the absence of TDS rotation is not simply a sampling issue. It is possible that not all TDSs experience such strongly veering storm-relative wind profiles in the near-tornado environment as was observed in the Norman-Little Axe tornado. Additionally, it may be that not all updraft structures support similar debris trajectories or that near-tornado downdrafts do not allow for debris to stay suspended long enough for the TDS to become elongated [3]. Or, it could be that there is some other control on TDS behavior that is only present in certain cases.

[3]The dual-Doppler volume was too shallow in the Moore-Choctaw case to compare the near-tornado wind profile with the Norman-Little Axe tornado.

### 4.4.2 Temporal Evolution of Polarimetric Profiles

Vertical profiles of polarimetric variables presented in the results section were temporally averaged and represented the the bulk characteristics of the TDS over a period of just under 10 min. However, some profiles changed drastically over the observation period. For example, within the Norman-Little Axe tornado, 90th percentile $Z_H$ for inner debris (Fig. 4.16a) decreased with height at a rate of 7.5 dBZ km$^{-1}$ at 2242 UTC (blue line). However, by 2249 UTC (red line), 90th percentile $Z_H$ only decreased in by ∼2 dBZ over the entire 2.5 km observed depth (∼1 dBZ km$^{-1}$). Additionally, 90th percentile $Z_H$ was at least 5 dBZ greater at 2249 UTC compared to 2242 UTC for all observed heights. Similarly, median $\rho_{hv}$ (Fig. 4.16b) increased with height at 2242 UTC (blue line), but the slope of $\rho_{hv}$ decreased with time and at 2249 UTC (red line) there was no consistent vertical trend. Additionally, median $\rho_{hv}$ decreased at all altitudes with time, which, along with the observed increase in 90th percentile $Z_H$ is likely due to the tornado producing greater damage at 2247 and 2249 UTC than at 2242 UTC, consistent with what was observed in Bodine et al. (2013) for other TDS cases. Descriptions of the damage survey from the event (available online at `https://www.ncdc.noaa.gov/stormevents/eventdetails.jsp?id=231948`) indicate that the Norman-Little Axe tornado produced increasing damage intensity throughout its lifecycle with the the most damage occurring approximately at the end of observation period. Moreover, observed OU-PRIME differential velocity (ΔV) at 1° elevation increased from ∼69 m s$^{-1}$ at 2242 UTC to a maximum of ∼83 m s$^{-1}$ at 2247 UTC (not shown) despite the beam height increasing from 280 m to 415 m ARL, respectively.

In general, the profiles in polarimetric variables became more homogeneous with height over time. It is possible that this means that the properties of debris in this column became more homogeneous during this time as well. This could be caused by one or a combination of multiple factors. First, the types of debris within the tornado itself could have become less variable over time. Additionally, large debris particles, which take longer to ascend, may not have had time to reach the upper portions of the TDS at 2242

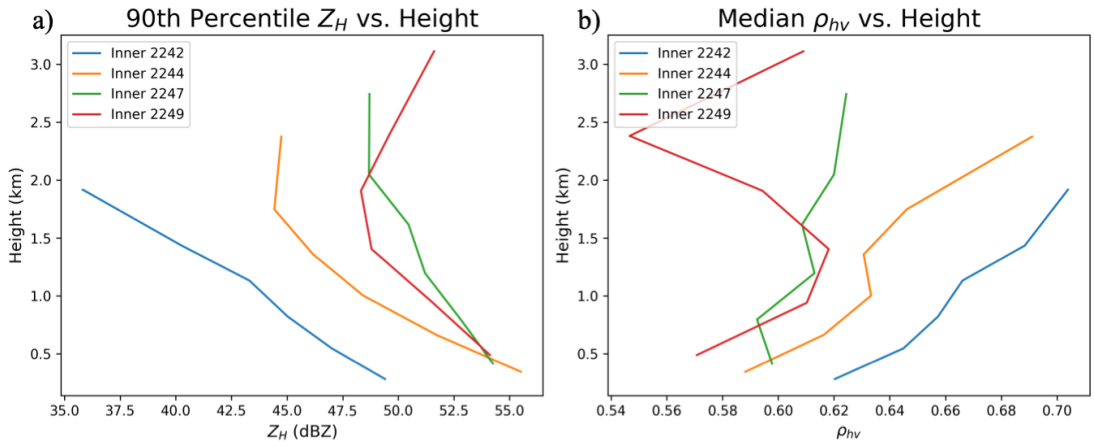


Figure 4.16: OU-PRIME (a) 90th percentile reflectivity (dBZ) and (b) median correlation coefficient vs. height (km) valid at 2242 UTC (blue line), 2244 UTC (orange line), 2247 UTC (green line), and 2249 UTC (red line) for debris within 1 km of the Norman-Little Axe tornado.

UTC, but by 2249 UTC they may have ascended to higher altitudes. Similarly, as the tornado increased in intensity, it is likely that it was more capable of lofting larger debris to higher altitudes. Finally, the fallout of previously lofted debris from aloft may have acted to homogenize the TDS by counteracting vertical size sorting that occurs when debris are initially lofted (i.e., smaller debris get lofted faster to higher altitudes). But, regardless of the responsible mechanism, it does appear that in this particular case the TDS became much more vertically homogeneous as it became longer lived. Whether this can be generalized among other TDSs remains a topic of future research.

## 4.5 Conclusions

The 10 May 2010 tornado outbreak provided a unique opportunity to compare two debris-lofting tornadoes of different intensities that were encountering similar land-cover due to their very close proximity to one another. The Norman-Little Axe tornado produced EF-4 damage and was associated with the parent mesocyclone of a long-lived supercell. A second tornado located along the gust front of the same supercell produced

EF-2 damage. Both TDSs associated with the two tornadoes exhibited appendages at some point during their respective lifecycles. The Norman-Little Axe TDS had a large tail of debris on its eastern side that shortened with height, but it could not be determined exactly what caused this appendage. The landspout tornado exhibited two small debris appendages, one on the northwest side of its TDS and one on the southeast side. While both appendages were along the RFGF, it can be inferred from dual-Doppler analyses that the southeastern appendage was associated with debris lofted by inflow into the tornado and the northwest appendage was likely associated with debris being ejected by the tornado. These are similar to the mechanisms for TDS appendages described in Houser et al. (2016) and Kurdzo et al. (2015), respectively, except happening simultaneously for the same TDS and in different directions of the ejected debris compared to Kurdzo et al. (2015).

The two tornadoes exhibited contrasting TDS characteristics. The landspout tornado had high $Z_H$ at its center surrounded by relatively lower $Z_H$ and at one point exhibited an annulus of low $\rho_{hv}$ at the periphery of its TDS, similar to Griffin et al. (2017); however, it unlikely that large tornado subvortices were present in this tornado like in the 10 May 2010 Moore-Choctaw case. Meanwhile, the Norman-Little Axe tornado had a WEH at its center and did not show any coherent features in $\rho_{hv}$. It was determined from a comparison of bulk polarimetric characteristics that median and 90th percentile $Z_H$ was larger in the Norman-Little Axe tornado, consistent with its greater damage intensity. Median and 90th percentile $\rho_{hv}$ and $Z_{DR}$ were also higher in the Norman-Little Axe tornado, likely due to precipitation entrainment. Despite differences in the overall magnitude and horizontal distribution of polarimetric variables, in both tornadoes $Z_H$ decreased with height, $\rho_{hv}$ increased with height, and $Z_{DR}$ was relatively constant with height.

The shape of the TDS and spatial distribution of debris within the Norman-Little Axe tornado did change significantly with height. At low levels, the TDS was elongated with an east-west orientation and the majority of the debris located to the east of the tornado.

As elevation increased, much of the debris to the east of the tornado was redistributed to the north and to a lesser extent, west, of the tornado. This was a byproduct of the TDS rotating and elongating with height such that the major axis of the TDS pointed toward the northeast at higher elevation angles. The rotation of the TDS with height was most prominent at the end of the observation period, when the tornado was producing the most intense damage. It is likely that a strongly veering storm-relative wind profile near the tornado was responsible for the redistribution of debris and TDS rotation with height by detraining and transporting debris in a preferential direction. Additionally, northeastward storm-relative winds above 2 km ARL were likely responsible for the elongation of the TDS in that direction. To the authors' knowledge, this is the first documentation of TDS rotation with height and the influence of the near-tornado mean wind profile on the TDS structure and serves as a polarimetric radar verification of previous observations from Snow et al. (1995) and Magsig and Snow (1998) that the majority of debris falls out to the left of the tornado track.

A novel dual-wavelength comparison of debris characteristics within the tornado ('inner') to debris between 1 and 3 km from the tornado ('outer') was performed. This provides a comparison of debris residing within the tornado to debris ejected into the nearby storm-scale flow (e.g., storm-scale updraft, RFD). S-band $Z_H$ was found to be larger than C-band $Z_H$ for both inner and outer debris with the greatest dual-wavelength differences occurring for debris within the tornado. This is likely due to larger debris being present within the tornado and is consistent with previous observations (Bodine et al. 2014) and simulations of debris radar signatures (Bodine et al. 2016b) that showed such differences result from resonance effects of large particles. In general, $Z_H$ was lower and $\rho_{hv}$ was higher for outer debris, which coupled with smaller dual-wavelength differences suggests that outer debris were smaller than inner debris. The dual-wavelength difference in $Z_H$ increased with height for outer debris and inner and outer $Z_H$ values at both wavelengths became much more similar at upper levels. This is likely due to debris within the tornado being redistributed outward with height from the effects of

centrifuging and advection away from the center of the tornado by the mean wind. The decreasing dual-wavelength differences with height, resulting from smaller dominant scatterer sizes and more similar dual-wavelength differences between inner and outer debris due to centrifuging, is consistent with simulations in Bodine et al. (2016b). Except, the observations in this study are at S and C band, and Bodine et al. (2016b) used simulated S- and X-band observations. The only appreciable dual-wavelength differences in $\rho_{hv}$ occurred for inner debris with lower $\rho_{hv}$ observed at C band than at S band due to increased resonance effects at C band for large scatterers.

As can be seen in this and other recent studies, it may be possible to infer many characteristics of the near-tornado wind field based solely on observations of debris using polarimetric radars (e.g., veering storm-relative wind profiles inferred from the elongation and rotation of the TDS). While many of the findings in this study are intuitive, more cases are needed in order to know whether observations like the differences in the debris characteristics of inner and outer debris can be generalized. Moreover, it appears that only a subset of TDSs rotate with height and additional dual-Doppler and high-resolution model datasets are needed to investigate the kinematic controls on this particular debris behavior. Finally, observations and polarimetric radar simulations with much finer-scale spatial and temporal resolution are needed in order to interrogate the the relationships between tornado intensity and structure and the manifestation of TDS appendages, polarimetric inhomogeneities, and the vertical distribution of debris.

# Chapter 5

# High-Temporal Resolution Observations of the 27 May 2015 Canadian, Texas, Tornado Using the Atmospheric Imaging Radar

In this chapter, observations collected by the Atmospheric Imaging Radar (AIR; Isom et al. 2013; Kurdzo et al. 2017) of the 27 May 2015, Canadian, Texas, tornado are presented. During this deployment, 20°-by-80° (elevation x azimuth) sector volumes were collected every 5.5 s at ranges as close as 6 km. The AIR captured the late-mature and decaying stages of the tornado. Early in the deployment, the tornado had a radius of maximum winds (RMW) of 500 m and exhibited maximum Doppler velocities near 65 m $s^{-1}$. Rapid changes associated with the dissipation stages of the tornado are documented. A 10-s resolution time-height investigation of vortex tilt and differential velocity ($\Delta$V) is presented and illustrates an instance of upward vortex intensification as well as downward tornado decay. Changes in tornado intensity over periods of less than 30 s coincided with rapid changes in tornado diameter. At least two small-scale vortices were observed being shed from the tornado during a brief weakening period. A persistent layer of vortex tilt was observed near the level of free convection, which separated two layers with contrasting modes of tornado decay. Finally, the vertical cross-correlation of vortex intensity reveals that apart from the brief instances of upward vortex intensification and downward decay, tornado intensity was highly correlated throughout the observation period.

## 5.1 Introduction

Toward the goal of a broader view of rapid tornado evolution, the present study interrogates close-range tornado observations collected by the AIR. The AIR is a mobile,

X-band phased-array radar that collects high-temporal resolution, vertically continuous volumetric observations of tornadoes. On 27 May 2015, the AIR collected 5.5-s temporal resolution observations of an EF-2 rated tornado near Canadian, Texas, with maximum Doppler velocities of 65 m $s^{-1}$ during the the scanning period and at its widest, had a radius of maximum winds (RMW) of 500 m. The nearly simultaneous volumetric data collection within the Canadian tornado provides a unique opportunity to interrogate the vertical structure of a tornado during decay without having to account for translation or evolution of the vortex between elevation scans.

This study documents the vertical evolution of tornado intensity during tornado decay with the goal of identifying if specific layers within the tornado are important for triggering tornado dissipation. Studies by French et al. (2014) and Houser et al. (2015) have previously documented tornado decay with high-temporal resolution and have provided early insight into the vertical behavior of tornadoes during dissipation. However, the data in this case have better spatial resolution compared to French et al. (2014) and better low-level coverage than Houser et al. (2015). Understanding where tornadoes first weaken and how decay evolves in time and space could inform future investigations into the vorticity budget of the tornado using models, multiple-Doppler analyses, or a combination of both (e.g., Marquis et al. 2012, 2016). In addition to contributing to a better understanding of why tornadoes dissipate, rapid observations that determine how late-lifecycle tornadoes behave have the potential to inform forecasters when to let warnings expire if phased-array radars are implemented operationally in the future.

In addition to investigating tornado decay, this study also documents two instances of small-scale vortices being shed from the parent tornado, which occur during a brief tornado weakening period and may have contributed to the transport of angular momentum away from the tornado. A detailed evolution of tornado tilt through multiple layers of the tornado is presented. French et al. (2014) previously found no relationship between tornado tilt and vortex intensity; however, this study calculates tornado tilt with much finer vertical resolution in order to investigate much smaller layers within the tornado

rather than just the overall tornado inclination. Finally, tornado intensity is compared to vortex diameter to interrogate the role of conservation of angular momentum on tornado intensity and the vertical cross-correlation of tornado intensity is analyzed.

## 5.2 Methods

### 5.2.1 Atmospheric Imaging Radar and Case Overview

The AIR is a mobile, rapid-scan, X-band, phased-array imaging radar designed and constructed by the ARRC (Isom et al. 2013). The AIR transmits a 20° in elevation by 1° in azimuth horizontally polarized fan beam and receives data using a 36-element array with a vertically oriented baseline. The 36 channels of received data are combined using digital beamforming (Mead et al. 1998) to reconstruct 20 1°-x-1° beams resulting in a simultaneous RHI with each pulse, which is mechanically steered in azimuth to collect volumetric data. In the present study, Fourier (non-adaptive) digital beamforming is used.

The 27 May 2015 Canadian, Texas, EF-2 tornado had a lifespan of approximately 10 min, forming around 2157 UTC and visually dissipating at 2207 UTC. Beginning at 2203 UTC, the AIR collected approximately 4.5 min of data in 20°-by-80° volumetric sectors with 5.5-s temporal resolution. The range to the tornado was between 5 and 6 km for the deployment with the closest distance occurring at the beginning of the sampling period. Corresponding beam heights range from 50 m to 2000 m above radar level (ARL) for the center of the beams between 0° and 20° elevation. The presented data are oversampled to 0.5° in both azimuth and elevation and have a 37.5-m gate spacing in range that is oversampled to 30 m (Kurdzo et al. 2014). For this case, the Nyquist velocity was 25 m $s^{-1}$ and the radar truck was level during data collection. Velocity aliasing was manually corrected during post processing. High spectrum width, low reflectivity data points were subjectively removed if their Doppler velocity looked suspect for all permutations of dealiasing. Spectrum width was used to identify large gradients in Doppler velocity and

aid in the identification of the zero isodop. However, in some instances ambiguities in the placement of zero isodop exist, especially regarding the distinction between folded outbound velocities and weak inbound velocities in the core of the tornado. For times with particularly high uncertainty, the position of the zero isodop was selected to best preserve temporal and vertical continuity. Nevertheless, changing the location of the zero isodop a few radials in either direction would have little or no impact on the presented results due to the displacement of the strongest Doppler velocities from the center of the tornado.

### 5.2.2 Time-Height Plots

The 5.5-s volumetric updates of the AIR can be leveraged to interrogate the vertical evolution of tornado characteristics. Time-height plots of differential velocity ($\Delta$V) and tornado vortex tilt are calculated for the entire 4.5-min deployment for the Canadian, Texas, tornado. For the time-height plots, a three-time (20-s) moving average is applied. An additional three-height (100-m) moving average is applied to the vortex tilt plots to filter out noise. The data are vertically interpolated to the beam heights of the first volume scan. Because the tornado was nearly stationary during the deployment, the maximum vertical interpolation is $\sim$20 m and the resulting changes in the data are negligible. Values of $\Delta$V are calculated by subjectively selecting the tornado center using radial velocity and the weak echo hole (WEH) as a first guess and searching for the maximum and minimum velocities within 1000 m. The locations of the maximum inbound and outbound velocities were manually checked to mitigate possible errors. Vortex tilt is calculated by determining the angle between the subjectively identified vortex center at the height above and height below a given analysis level (roughly 50 m above and below). The analyses were run multiple times with different subjectively chosen centers of the vortex and it was determined that the analyses were not qualitatively sensitive to small changes (on the order of tens of meters) in the choice of vortex center. Additionally, the

analyses were also not qualitatively sensitive to tilt being calculated over a 0.5°, 1.0°, or 2° angular depth.

### 5.2.3 Axisymmetric Wind Retrieval

Lee et al. (1999) used the assumption of axisymmetry to develop a method called the ground-based velocity track display (GBVTD) that retrieves the three-dimensional windfield within tropical cyclones. This technique has been subsequently applied to tornado vortices (e.g., Bluestein et al. 2003; Lee and Wurman 2005; Tanamachi et al. 2007; Kosiba and Wurman 2010; Wakimoto et al. 2012). This study uses a simplified GBVTD defined by Dowell et al. (2005) that only recovers the azimuthally averaged (zero wavenumber) radial and tangential velocities, $u$ and $v$. Previous studies to use this simplified GBVTD include Kosiba et al. (2008), Bodine et al. (2014), Griffin et al. (2017), and Mahre et al. (2018). For this case, $u$ and $v$ are calculated using 100-m-wide annuli at 50-m intervals. Vertical velocities are calculated by vertically integrating the radial mass flux using equation (2.2) in Nolan (2013). The center of the lowest beam included in the analyses was 50 m ARL, meaning that some of the low-level winds were not fully sampled, which could result in errors in the retrieved vertical velocities (Nolan 2013), especially for the first few analysis times when tornado inflow appears to be shallow. However, this dataset is much closer to the 'most probable' case in Nolan (2013) where mass flux in the lowest 40 m were neglected and errors were less extreme, compared to the case where the mass flux was neglected in the lowest 80 m.

Debris and hydrometeor centrifuging is known to bias radar-derived wind fields of tornadoes (Dowell et al. 2005; Wakimoto et al. 2012; Bodine et al. 2016b), and is difficult to account for since the dominant scatterer types are uncertain. Centrifuging in the axisymmetric wind retrieval is corrected for using equation (3.1) in Nolan (2013) that accounts for the outward bias in the tornado relative radial wind velocity owing to centrifugal accelerations. For this case, large debris were not visually observed within the tornado and therefore a relatively small specified maximum flow-relative radially outward velocity

estimate ($C_{max}$) of 4 m s$^{-1}$ is chosen. The centrifuging correction did not dramatically change the analyses, which were not qualitatively sensitive to $C_{max}$ values ranging from 4 to 12 m s$^{-1}$, similar to the maximum positive bias in radial velocity for hydrometeors found in Wakimoto et al. (2012) (cf., their Figure 9) and similar to the values tested by Kosiba and Wurman (2013).

### 5.2.4 Angular Momentum Budget

Axisymmetrtic angular momentum ($\Gamma = vr$) is calculated for the first seven volume scans when the tornado undergoes rapid transitions in structure and is well-sampled spatially. The time rate of change of angular momentum is given by the following equation adapted from Rasmussen and Straka (2007):

$$\frac{\delta\overline{\Gamma}}{\delta t} = -\frac{\delta\overline{u\Gamma}}{\delta r} - \frac{\delta\overline{w\Gamma}}{\delta z} + R \tag{5.1}$$

where $R$ is a residual term that is largely made up of the divergence of eddy angular momentum flux, which is indirectly calculated using the other three terms. The time rate of change of angular momentum is calculated by taking the difference in the angular momentum field between the first and last time in the analysis window (either 60 s or 20 s). The first two terms on the right hand side are the divergence of angular momentum flux, which is simply the advection of angular momentum assuming incompressibility, as is done in Rasmussen and Straka (2007). The advection terms are calculated by taking an average of the angular momentum advection terms over the entire analysis window. The angular momentum budgets use either three or seven volumes to compute the analyses for 20-s and 60-s windows, respectively.

## 5.3 Results

### 5.3.1 High-Temporal Resolution Observations

The maximum sampled intensity of the Canadian, Texas, tornado occurred at 22:03:52 UTC, in the first volume of data collected by the AIR (Fig. 5.1a-b). At this time, the tornado had maximum $\Delta$V of 110 m s$^{-1}$, a RMW ranging from 200 m at 100 m ARL (Fig. 5.2b) to 500 m at 500 m ARL (Fig. 5.2d), and a broad, 500-m wide region with Doppler velocities exceeding 40 m s$^{-1}$ in magnitude. Additionally, the tornado exhibited concentric WEHs similar to what has previously been observed by Wurman and Gill (2000), Wurman et al. (2007), Bluestein et al. (2007a), and Wakimoto et al. (2016). It is possible that the concentric WEHs represent different scatterer types (e.g., raindrops and small debris) similar to what was noted by Wakimoto et al. (2016). However, the AIR does not have dual-polarimetric capabilities to confirm the presence of debris. Additionally, the nearest WSR-88D is approximately 140 km away preventing adequate supplemental low-level polarimetric observations. RaXPol observations (Z. Wienhoff 2018, personal communication) from $\sim$2 min later did not show a polarimetric tornadic debris signature, but the lowest RaXPol scan was above where the AIR observed the inner WEH, which is hypothesized to be debris. The tornado rapidly weakened during the first minute of data collection (Fig. 5.1d,f). By 22:04:56 UTC, the maximum $\Delta$V decreased to $\sim$80 m s$^{-1}$ and only a $\sim$100-m wide region of Doppler velocities exceeding 40 m s$^{-1}$ in magnitude was present (Fig. 5.1f). The WEH rapidly filled in and became less symmetric during this weakening phase (Fig. 5.1c,e), becoming poorly defined at low levels by 22:04:56 UTC (Fig. 5.1e). By 22:05:18 UTC, the tornado diameter and intensity (Fig. 5.1h) was similar to what it was at 22:04:56 UTC, but a diffuse WEH became reestablished (Fig. 5.1g). The tornado persisted with similar intensity for approximately another minute before it completed its decay. The vertical and temporal evolution of tornado intensity will be discussed in further detail later in this section.

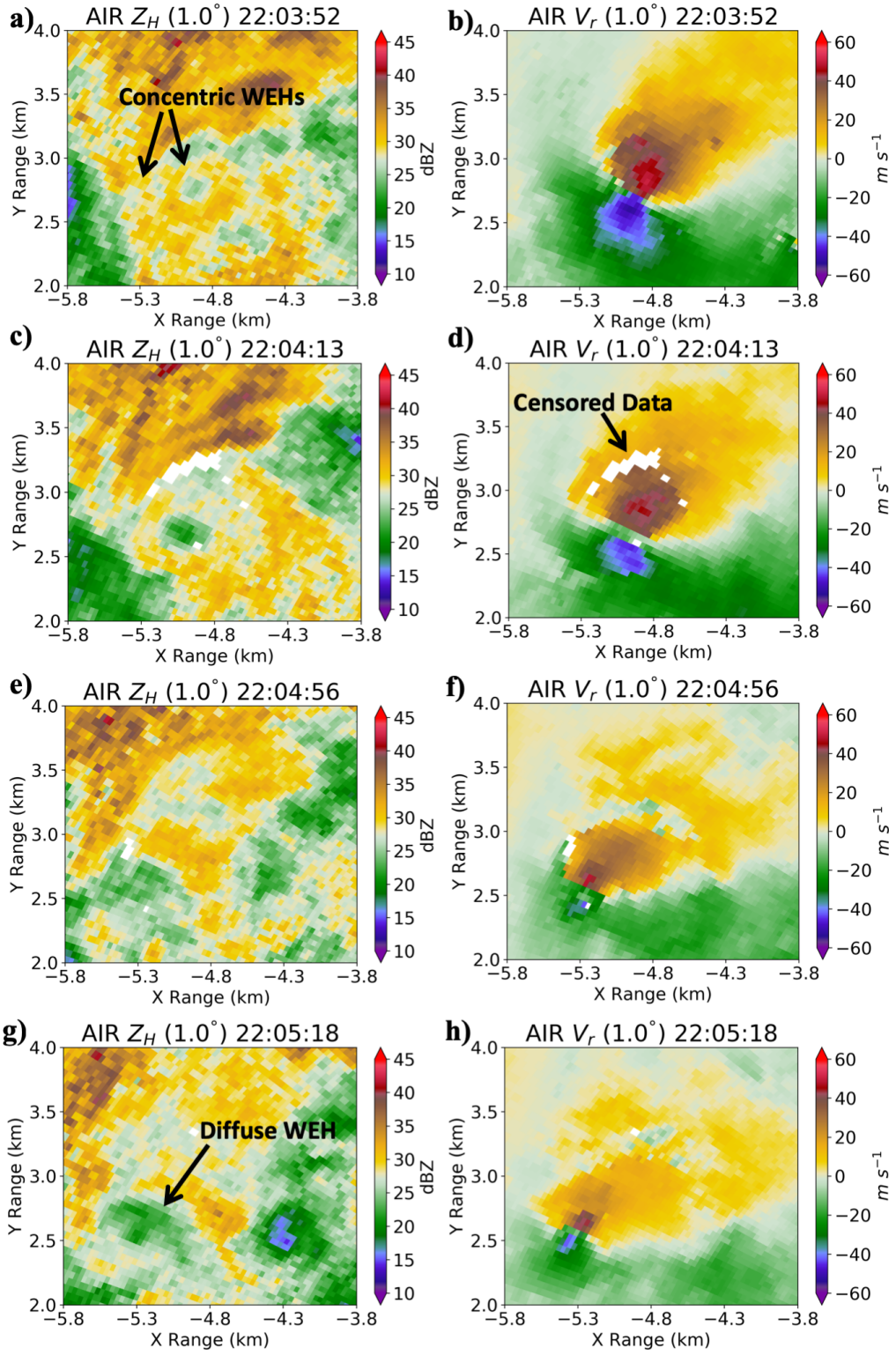


Figure 5.1: PPI plots of (a,c,e,g) reflectivity (dBZ) and (b,d,f,h) radial velocity (m s$^{-1}$) at 1° elevation at (a-b) 22:03:52, (c-d) 22:04:13, (e-f) 22:04:56, and (g-h) 22:05:18 UTC. White pixels here and elsewhere represent censored data.

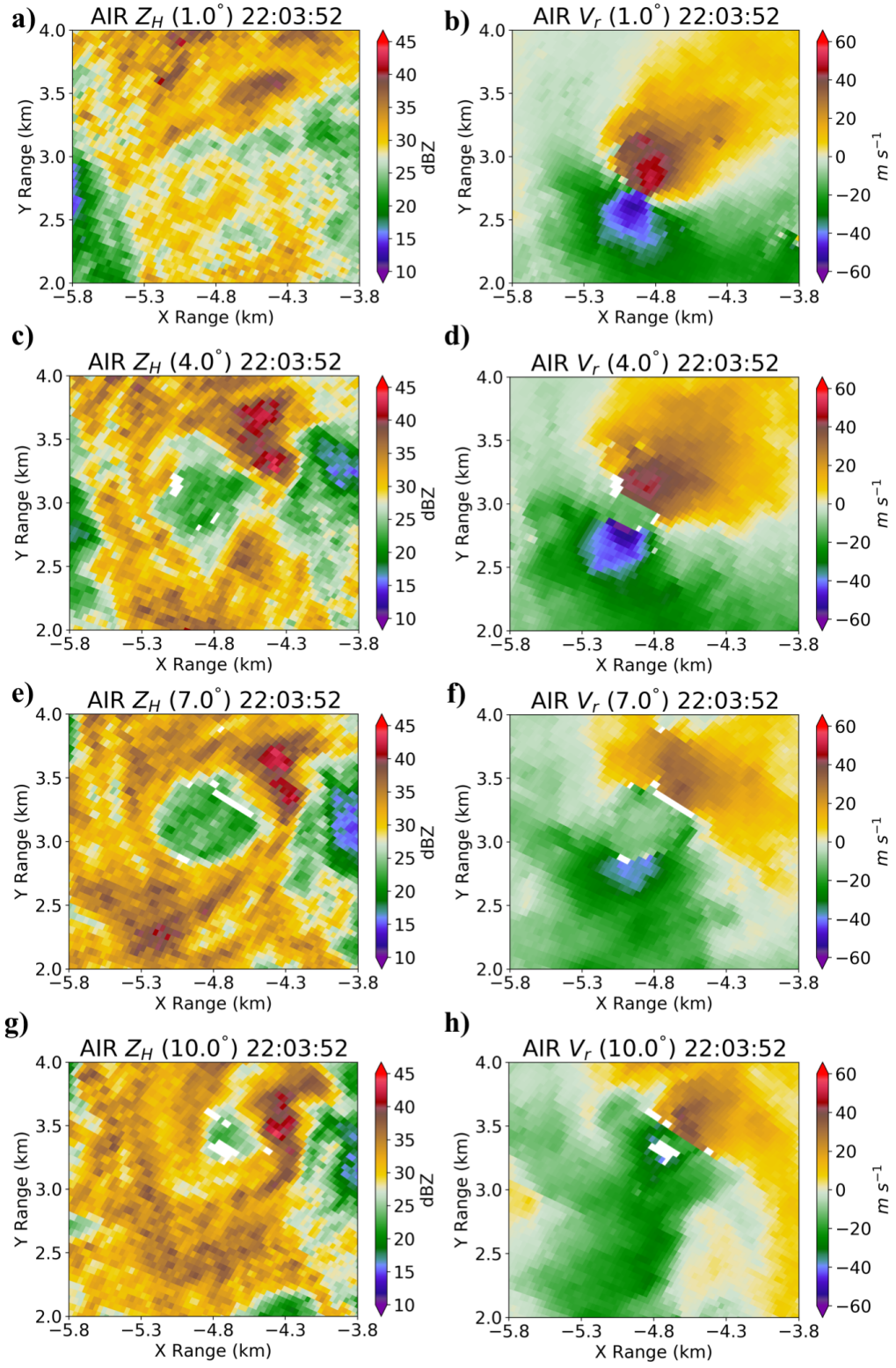


Figure 5.2: PPI plots of (a,c,e,g) reflectivity (dBZ) and (b,d,f,h) radial velocity (m s$^{-1}$) at (a-b) 1°, (c-d) 4°, (e-f) 7°, and (g-h) 10° elevation valid at 22:03:52 UTC. The elevations roughly correspond with 100 m, 400 m, 750 m, 1000 m ARL.

As noted by Kurdzo et al. (2017), an interesting feature of the Canadian tornado is the weak radial velocities in the core of the tornado (Fig. 5.2d,f) and large separation of the maximum inbound and maximum outbound radial velocities at early times, especially between 3–10° in elevation (400–1000 m ARL). A similar pattern of large separation between maximum inbound and outbound radial velocities with weak core Doppler velocities was observed by RaXPol in Wakimoto et al. (2016) when the 2013 El Reno tornado was exhibiting multiple vortex structure (cf., Figure 15, Wakimoto et al. (2016)). However, in the Canadian case these observations were seen at a beam height of ∼400–600 m compared to observations in Wakimoto et al. (2016), which were at 0.5° (below 100 m). At 1° elevation, the Canadian tornado instead exhibited a narrower core diameter[1] of ∼150 m (Fig. 5.2b). It must be noted that the AIR and RaXPol are both low-power radars, which may have less-sensitivity in areas of lower power, like the WEH. While the power returns in the WEH of the Canadian tornado were well above the noise floor of the AIR, the weak Doppler velocity structure in the core of tornadoes has not been observed by a higher-power radar; therefore, it is possible that the these observations are a radar artifact unique to low-power radars and not representative of the actual wind field.

Up to approximately 900 m ARL, the tornado widened to 600 m in diameter and weakened in intensity (Fig. 5.2d,f). Similar vertical structure to what is seen in the Canadian tornado can also be seen in model simulations of medium-swirl tornadoes with a narrow diameter near the surface and a larger diameter aloft (e.g., cf., Figure 5, Lewellen et al. (2000)). In the Lewellen et al. (2000) simulations, this widening of the vortex is associated with a transition from single-cell to two-cell vortex flow. Above ∼900 m, the tornado narrowed again (Fig. 5.2h) and maintained a similar 350-m diameter through the highest observed elevations (not shown). The WEH narrowed in response to the tightening of the vortex aloft (Fig. 5.2g) and is similar in structure to the bulging WEC

[1]Here and elsewhere in the paper, the tornado diameter is defined as the distance between the maximum outbound and maximum inbound Doppler velocities within the tornado.

structure noted in Bluestein et al. (2007b). The bulging structure of the vortex and WEH continued for approximately 30 s and is further discussed in Section 5.3.3.

A broken ring of high (>10 m $s^{-1}$) spectrum width was also observed at early times near the radius where the largest radial velocities were located (Fig. 5.3a). Similar spectrum width ring structure has also been observed by Wurman (2002) and Snyder and Bluestein (2014) in multiple-vortex tornadoes. Locally enhanced spectrum width near tornadic subvortices was likely due to high wind shear and turbulence. Additionally, strong radial gradients in tangential velocity are one requirement for subvortices to form (e.g., Rotunno 1978; Gall 1983; Lewellen et al. 2000), which would result in high spectrum width rings in an axisymmetric framework. Video of the Canadian tornado (Fig. S1 in the online supplemental material available at `https://drive.google.com/drive/folders/1sG9PEEBk9obq7cGv6vqlqffyj5yb4d1S?usp=sharing`) and enhanced shear regions along the zero isodop in Fig. 5.2b also indicate that multiple vortices were present near this time.

The AIR captured at least two instances of cyclonic vortices being shed by the main circulation in rapid succession over a period of one minute (Fig. 5.4). The vortices first appeared on the eastern side of the tornado near the RMW and translated eastward, well beyond the RMW of the tornado where tornado subvortices are normally located (e.g., Wurman 2002). After being shed, the vortices went through a brief intensification period and reached maximum $\Delta$V of 34 and 36 m $s^{-1}$, respectively. The maxima in intensity were reached at radii of approximately 500 m and 1000 m from the primary tornado, respectively. Maximum intensity for both vortices occurred at 22:04:56 UTC (Fig. 5.4f), approximately 30 s after they exited the parent cyclone. The shed vortices were largely confined to above 400–500 m ARL and only briefly appeared at lower elevation angles (not shown) at 22:04:56 and 22:05:07 UTC when the vortices were at maximum intensity. It is possible that the vertical elongation of the vortices combined with their brief intensification signifies that vortex stretching was occurring. The vortices translated slightly eastward while the main circulation moved to the west. There did not appear to be any

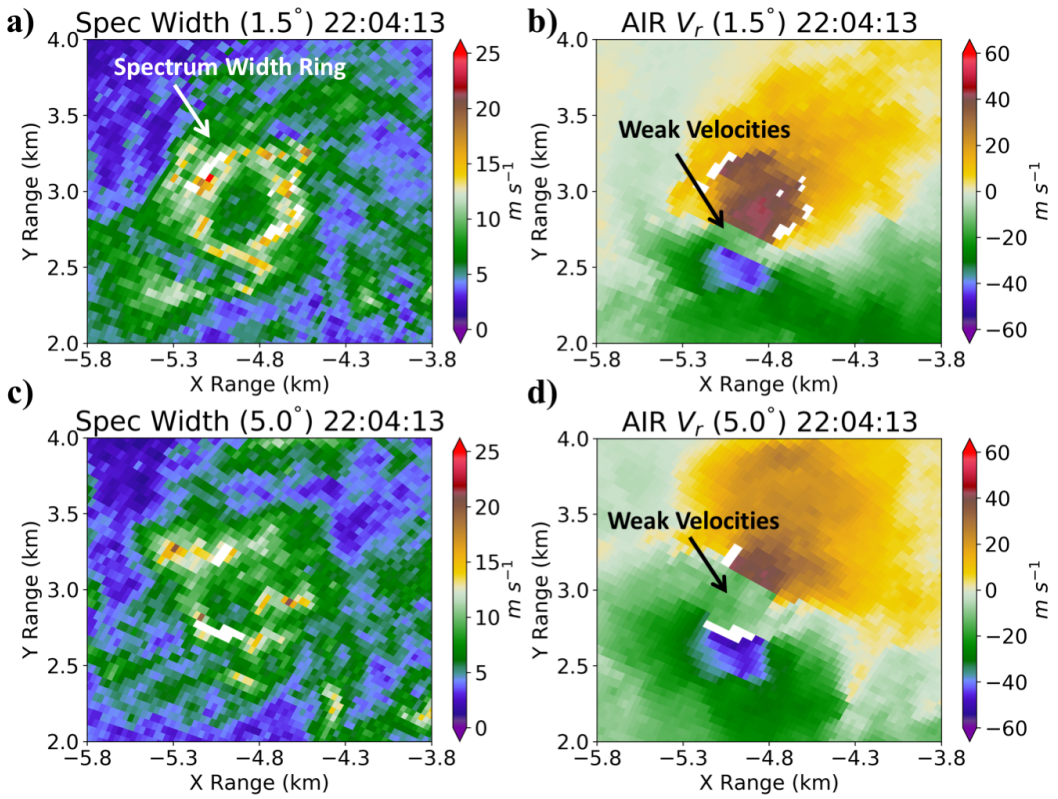


Figure 5.3: PPI plots of (a,c) spectrum width (m s$^{-1}$) and (b,d) radial velocity (m s$^{-1}$), at (a-b) 1.5° and (c-d) 5° elevation valid at 22:04:13 UTC.

clear evidence of a boundary that the shed vortices were traversing, nor was there any evidence of the vortices entering the tornado prior to being shed. As a result, the shed vortices may have acted to transport angular momentum away from the main circulation, which may have contributed to the weakening of the tornado.

The maximum $\Delta V$ during the deployment was $\sim$110 m s$^{-1}$ and occurred during the first two analysis times (Fig. 5.5). The strongest $\Delta V$ occurred in the lowest 700 m ARL. By 22:04:13 UTC, $\Delta V$ decreased to $\sim$70 m s$^{-1}$ in the low levels. The tornado briefly intensified at 22:04:56 UTC, following a $\sim$1-min, relatively weak period. The restrengthening occurred first in the low analysis levels and then simultaneously up to 500 m. Brief weakening followed by restrengthening of the low-level vortex could also be seen in visual observations of the tornado at this time (Fig. S1 0:45–1:15). This bottom-up strengthening is similar to what was observed in Mahre et al. (2018) in the mature stage and similar to the vertical evolution of tornadogenesis noted in French et al. (2013), except observed during the dissipation stage of the tornado in this case.

Following the brief restrengthening of the tornado at low levels, the Canadian tornado began a final weakening phase that culminated in tornado dissipation (Fig. 5.5). At all observed levels above 1.25 km ARL, $\Delta V$ decreased nearly simultaneously to $\sim$40 m s$^{-1}$ at 22:05:28 UTC. Over the next 2 min, the tornado decayed to a similar intensity in a downward direction in the layer between 400 and 1250 m ARL. Simultaneous weakening of the tornado occurred at 22:06:33 UTC between 150 and 400 m, approximately 1 min before similar tornado intensity was reached in the layer between 400 and 1000 m ARL. In the lowest 150 m, weakening of the tornado slightly preceded the simultaneous weakening over the 150–400 m layer by approximately 20 s. The downward decay region is similar to the inside out tornado decay noted by French et al. (2014) and Houser et al. (2015) except we do not have the observations above 2.5 km to compare the upper levels. Additionally, the decay in the Canadian case occurred in approximately 1–2 min, whereas in the 5 June 2009 Goshen tornado, decay took $\sim$3 min (French et al. 2014). The dense low-level observations provide insight into a non-descending tornado decay mode in the lowest

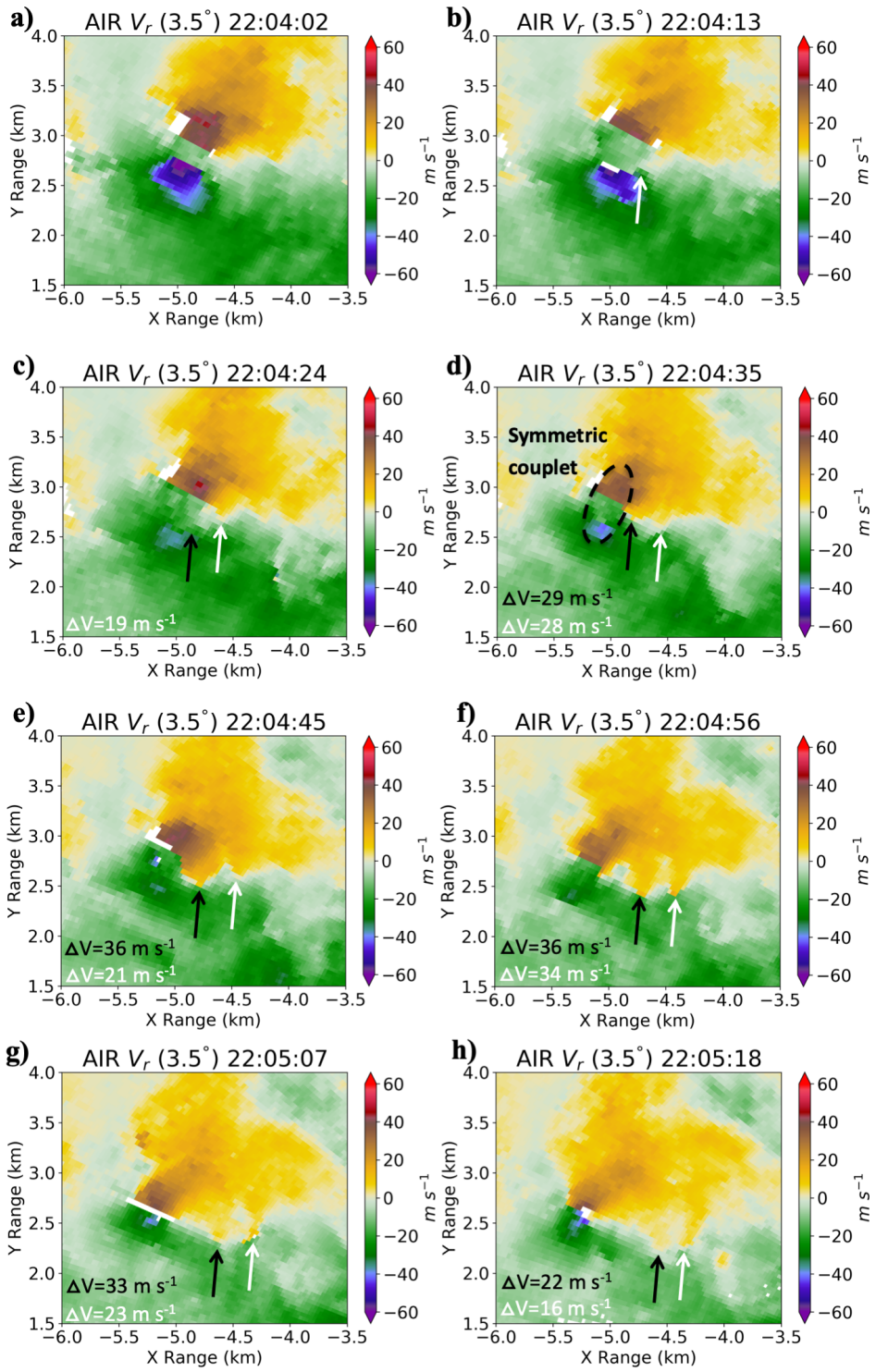


Figure 5.4: PPI plots of radial velocity (m s$^{-1}$) at (a) 22:04:02, (b), 22:04:13, (c) 22:04:24, (d) 22:04:35, (e) 22:04:45, (f) 22:04:56, (g) 22:05:07, and (h) 22:05:18 UTC at 3.5° elevation. Arrows indicate the location of the shed vortices. Maximum ΔV of each vortex is shown after it has been shed.

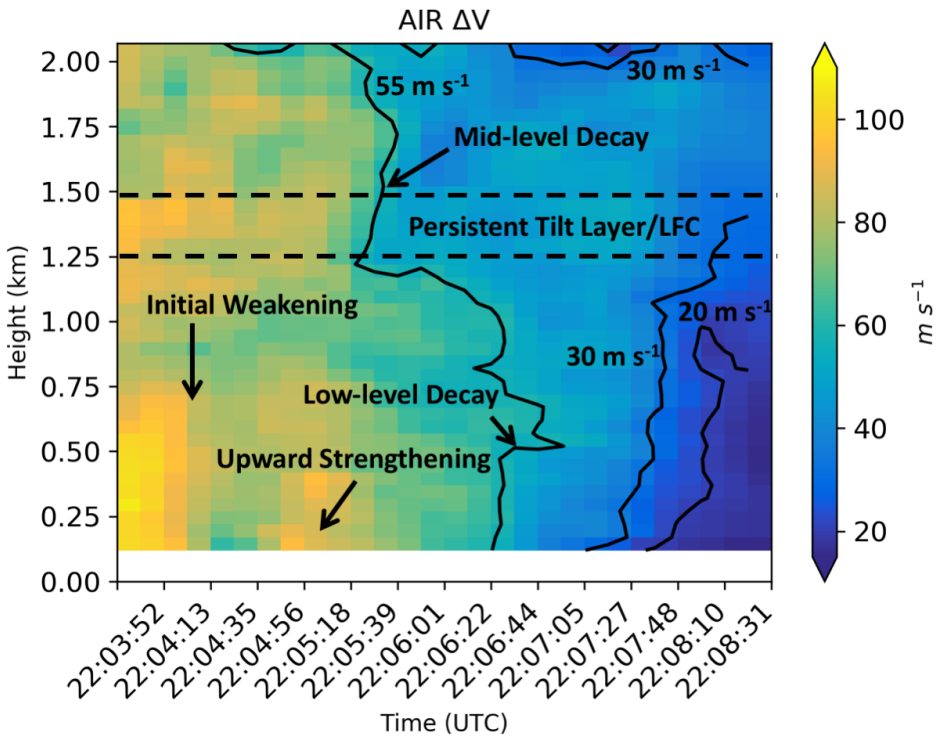


Figure 5.5: Time-height plot of maximum $\Delta V$ (m $s^{-1}$) within the tornado. Overlaid are the 55 m $s^{-1}$, 30 m $s^{-1}$, and 20 m $s^{-1}$ $\Delta V$ contours. Note that sampling of tornado intensity was not continuous, but rather there is approximately 10.5 s between each estimate of $\Delta V$.

400 m. The AIR sampled tornado decay with much better spatial resolution than what was sampled by the MWR-05XP during the Goshen tornado (1° beamwidth vs. 1.8° beamwidth for similar ranges to the tornado and 30 m vs. 150 m range resolution (French et al. 2014)). Also, the AIR sampled the lowest 1 km ARL of the Canadian tornado whereas RaXPol had poor low-level coverage of the 24 May 2011 El Reno tornado during decay (Houser et al. 2015). Differential velocity decreased within the analyzed column below the 55 m $s^{-1}$ threshold for tornado intensity noted by Houser et al. (2015) during the initial decay (Fig. 5.5). However, a funnel cloud was still present for approximately 1 min after this initial weakening (Fig. S1 3:00–4:00). The persistent funnel cloud coupled with $\Delta V > 40$ m $s^{-1}$ lead us to believe that this initial weakening was not the dissipation of the tornado. However, previous studies (e.g., Tanamachi et al. 2013; Wurman and Kosiba 2013) have examined tornadoes with similar intensity to the Canadian tornado at this stage of its lifecycle that did not exhibit funnel clouds; therefore, a funnel cloud is not a necessary condition for a tornado owing to its dependency on both vortex intensity and water vapor pressure.

After a minute of marginal tornado intensity, the vortex decayed beginning around 22:07:27 UTC in the lowest 1.25 km ARL while it maintained $\Delta V$ of $\sim$40 m $s^{-1}$ above this altitude. Below 750 m ARL, the tornado weakened in an upward direction. Video of tornado decay (Fig. S1 3:15–4:00) also illustrated upward dissipation of the funnel cloud at this time. However, the upward dissipation of the funnel cloud may also have been the result of upward advection of drier air. Above 750 m ARL, the tornado dissipated nearly simultaneously (Fig. 5.5) , similar to what was observed in the 24 May 2011 El Reno, Oklahoma, tornado at altitudes above 1 km ARL (Houser et al. 2015). The $\Delta V$ threshold of 30 m $s^{-1}$ best captures the tornado decay based on the dissipation of the funnel cloud; however, the rapid decrease in $\Delta V$ from in excess of 40 m $s^{-1}$ to less than 20 m $s^{-1}$ in less than 30 s means that any threshold between 20 and 40 m $s^{-1}$ (not shown) would also approximately discriminate between tornadic and nontornadic intensity. These lower $\Delta V$

thresholds for tornado criteria agree well with other previous work (e.g., Alexander and Wurman 2008; Marquis et al. 2012; Kosiba and Wurman 2013; French et al. 2013).

### 5.3.2 Rapid Tornado Evolution

During the initial weakening phase, the Canadian tornado undergoes rapid changes in axisymmetric vortex flow with substantial changes in three-dimensional winds seen between the 10–20 s intervals shown (Fig. 5.6). Initially, maximum tangential velocity is ∼50 m $s^{-1}$ and an axial downdraft is observed above 500 m ARL with weak vertical motion below it (arrows, Fig. 5.6a). The radius of maximum winds (RMW) is ∼150 m. Inflow into the tornado at this time was likely shallow and is largely below the lowest analysis level (50 m). While this can lead to significant errors in the derived vertical velocities (Nolan 2013), locally strong divergent flow in the radial component of motion near the axis of rotation (not shown) suggest that a downdraft is present. We expect that insufficient sampling of low-level inflow prevents an updraft from being resolved at larger radii aloft (i.e., a two-cell vortex flow). Evidence of tornado subvortices discussed in the previous section would support this hypothesized two-cell vortex flow. Moreover, low-level tangential velocities exceed tangential velocities aloft, which would suggest a downward-directed, dynamic perturbation pressure gradient force (e.g., Church et al. 1979; Davies-Jones 1986; Wakimoto and Liu 1998; Lewellen et al. 2004, 2008; Bluestein 2013) and further support the validity of the derived axial downdraft.

Over the next minute, axisymmetric tangential velocity decreases, especially in the lowest 400 m. Initially, the stronger tangential velocities are observed near the surface (lowest 400 m ARL) and the RMW expands with height (Fig. 5.6a). Twenty seconds later, the depth of tangential velocities exceeding 35 m $s^{-1}$ shrinks to the lowest 200 m ARL (Fig. 5.6b), with some residual tangential velocities exceeding 30 m $s^{-1}$ between 200–600 m ARL at 400 m in radius. At this time (22:04:13 UTC), radial outflow becomes apparent near and outside of the RMW, which may be contributing to the weakening of the tornado during this period. By 22:04:24 UTC (Fig. 5.6c), the tangential wind structure

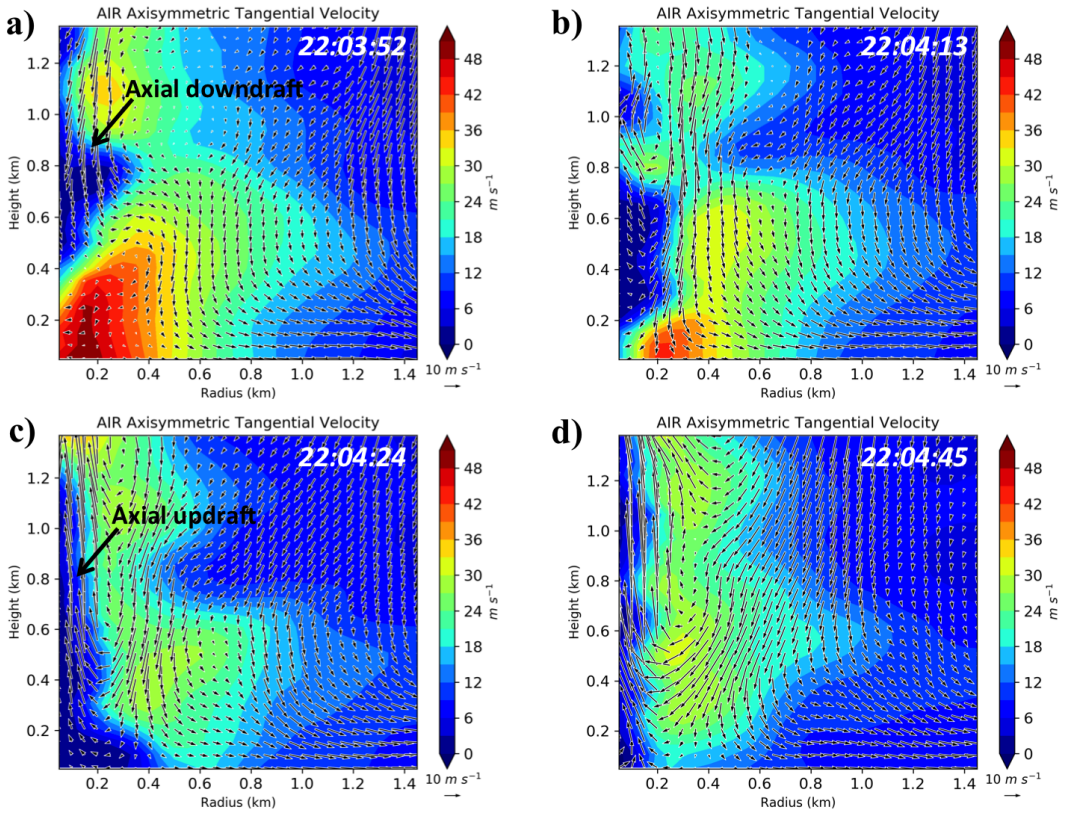


Figure 5.6: Axisymmetric tangential velocity (shaded, m $s^{-1}$) at (a) 22:03:52, (b) 22:04:13, (c) 22:04:24, and (d) 22:04:45 UTC. Arrows represent secondary circulation wind vectors (m $s^{-1}$) comprised of radial and vertical velocities from the axisymmetric wind retrieval.

is disorganized with very weak velocities near the surface, consistent with the weakening evident in $\Delta V$ (Fig. 5.5). Stronger tangential motions become better established in a column by 22:04:45 UTC (Fig. 5.6d), preceding the period of restrengthening evident in Fig. 5.5. Additionally, comparatively strong inflow has become reestablished within the RMW, which has moved slightly outward to $\sim$300 m.

Between 22:03:52–22:04:24 UTC, vertical motion near the center of the tornado rapidly reverses direction and an axial updraft becomes established in place of the initial axial downdraft (Fig. 5.6a,c). The weakening of the low-level tangential winds would reduce any downward-directed, dynamic perturbation pressure gradient force and could allow for vertical motion to change direction. It is also possible that a strengthening and deepening inflow layer contributes to a larger region of observed updraft. Shortly after the period shown in Fig. 5.6, the Canadian tornado narrowed such that it could no longer be well sampled in an axisymmetric sense and thus analysis of times beyond 22:05:18 UTC are not conducted.

Axisymmetric reflectivity (Fig. 5.7) is observed to change rapidly during the initial weakening of the Canadian tornado, with the evolution of the weak echo column (WEC) appearing to occur in direct response to changes in vortex flow. The observed evolution of the WEC can be feasibly explained by the radial and vertical advection of hydrometeors by the secondary circulations, which adds confidence to the qualitative characteristics of the derived wind field. Initially, the WEC bulges out from a 300-m radius to 500-m radius between 500 and 800 m ARL where strong divergence is present (Fig. 5.7a). One explanation could be a vortex breakdown flow type where an abrupt increase in divergence and core radius is observed above the vortex breakdown altitude. At 22:04:13 UTC, there is no longer a downdraft with associated divergent flow near the axis of the tornado and single-cell vortex flow develops (Fig. 5.7b). The WEC bulge is still present but descends about 200 m compared to Fig. 5.7a. Downward vertical motion has become established between 200 m and 500 m in radius, bringing a region of higher reflectivity toward the surface at the periphery of the tornado. By 22:04:24 UTC, the transition

region between the narrow and wide WEC has descended another 100 m within the peripheral downdraft regime and the single-cell vortex flow has strengthened with inflow toward the center of the tornado beginning to develop between 200 m and 600 m ARL (Fig. 5.7c). By 22:04:45 UTC, the WEC has a radius of 300 m throughout the analyzed depth (Fig. 5.7d). The abrupt narrowing of the WEC may be aided by the robust inflow into the center of the tornado that has become established in the lowest 600 m, which could transport descending hydrometeors or other scatterers inward toward the axis of the tornado. The drastic change in vortex flow and response of the WEC column occurs at 10–20 s intervals and highlights the rapid changes that can occur within tornadoes.

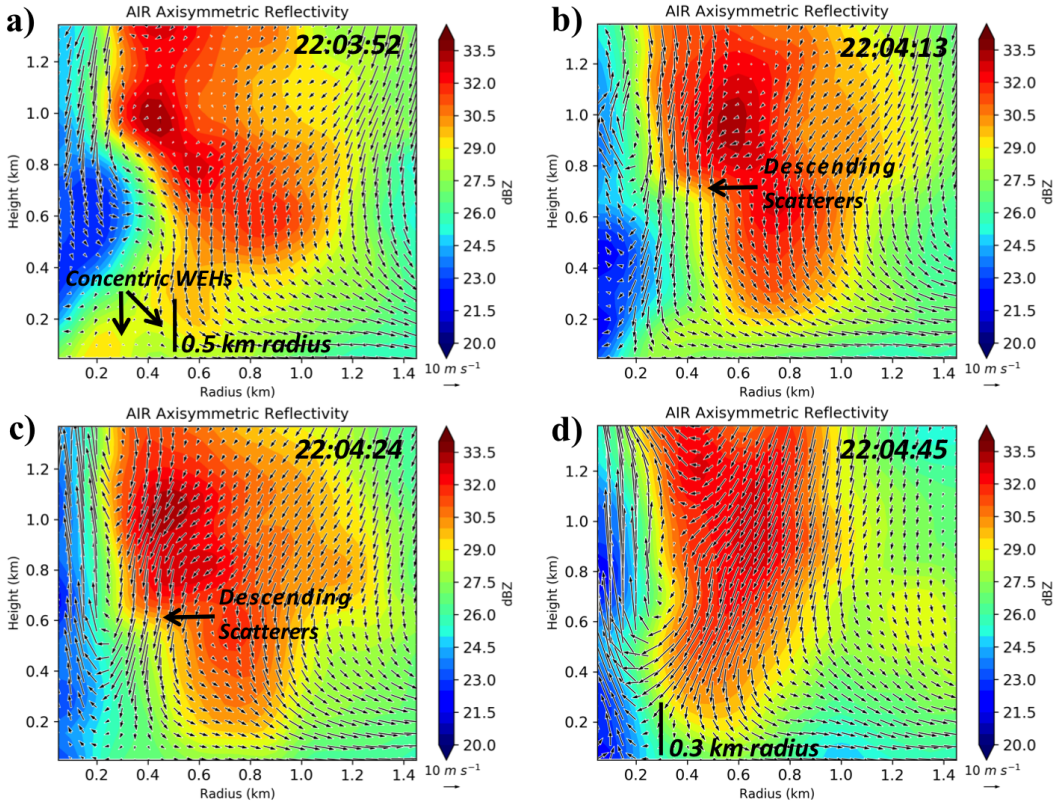


Figure 5.7: The same as Fig. 5.6 except for axisymmetric reflectivity (shaded, dBZ).

In addition to illustrating the rapid evolution of the WEC, Fig. 5.7a also provides an axisymmetric view of the concentric WEHs first noted in Fig. 5.1a. The inner band of enhanced reflectivity is disconnected from any regions of higher reflectivity aloft and extends below the analysis domain, whereas the outer WEH is part of the continuous

region of high reflectivity that extends through the top of the analysis domain. The contrasting vertical structure of the two WEHs supports the hypothesis that they represent different regimes of scatterers. It is speculated that the inner WEH is comprised of light debris that are lofted from the surface and the outer WEH represents descending rainbands at the periphery of the tornado. However, in the absence of polarimetric data, this hypothesis cannot be confirmed.

### 5.3.3 Angular Momentum Budget

During the initial weakening of the tornado, maximum axisymmetric angular momentum ($\Gamma$) decreases from in excess of 19000 $m^2$ $s^{-1}$ (Fig. 5.8a) to less than 15000 $m^2$ $s^{-1}$ (Fig. 5.8d) in approximately one minute. The most significant decrease in $\Gamma$ occurs below 600 m ARL. Throughout this period, the location of the maximum $\Gamma$ remains constant at approximately 600 m in height and 900 m in radius and is in a region characterized by downward and outward velocities. The time rate of change of $\Gamma$ (Fig. 5.9a) is $\sim$-100 $m^2$ $s^{-2}$ between 400 and 1100 m in radius and below 600 m ARL and is near zero elsewhere.

Lower angular momentum air is advected into the region of maximum $\Gamma$ between 400 and 1200 m in radius and just above 600 m ARL (Fig. 5.9b). The low angular momentum air originates aloft and is advected into the region of maximum $\Gamma$ by a downdraft as can be seen in Fig. 5.8. This downdraft also transports high angular momentum downward toward the surface and outward to larger radii as illustrated by the positive angular momentum advection regions in the lower right hand corner of Fig. 5.9b. This pattern of downward and outward angular momentum advection is consistent with the findings of Rasmussen and Straka (2007) during tornado decay. The downdraft between 600–1000 m in radius, which is acting to transport angular momentum away from the tornado at larger radii, also acts to increase convergence into the axis of the tornado within the RMW. Increased flow into the center of the tornado results in a positive angular momentum advection term at small radii (Fig. 5.9b) meaning that inward transport

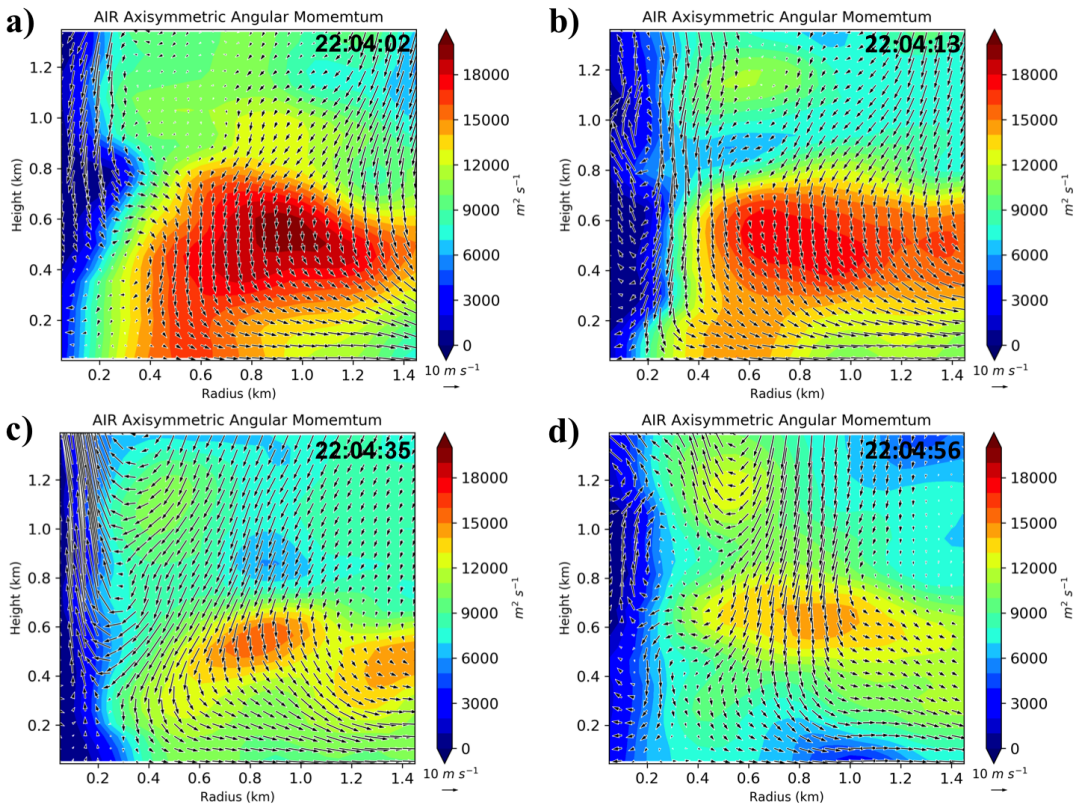


Figure 5.8: Axisymmetric angular momentum (shaded, $m^2\ s^{-1}$) at (a) 22:04:02, (b) 22:04:13, (c) 22:04:35, and (d) 22:04:56 UTC. Arrows represent secondary circulation wind vectors ($m^2\ s^{-1}$) comprised of radial and vertical velocities from the axisymmetric wind retrieval.

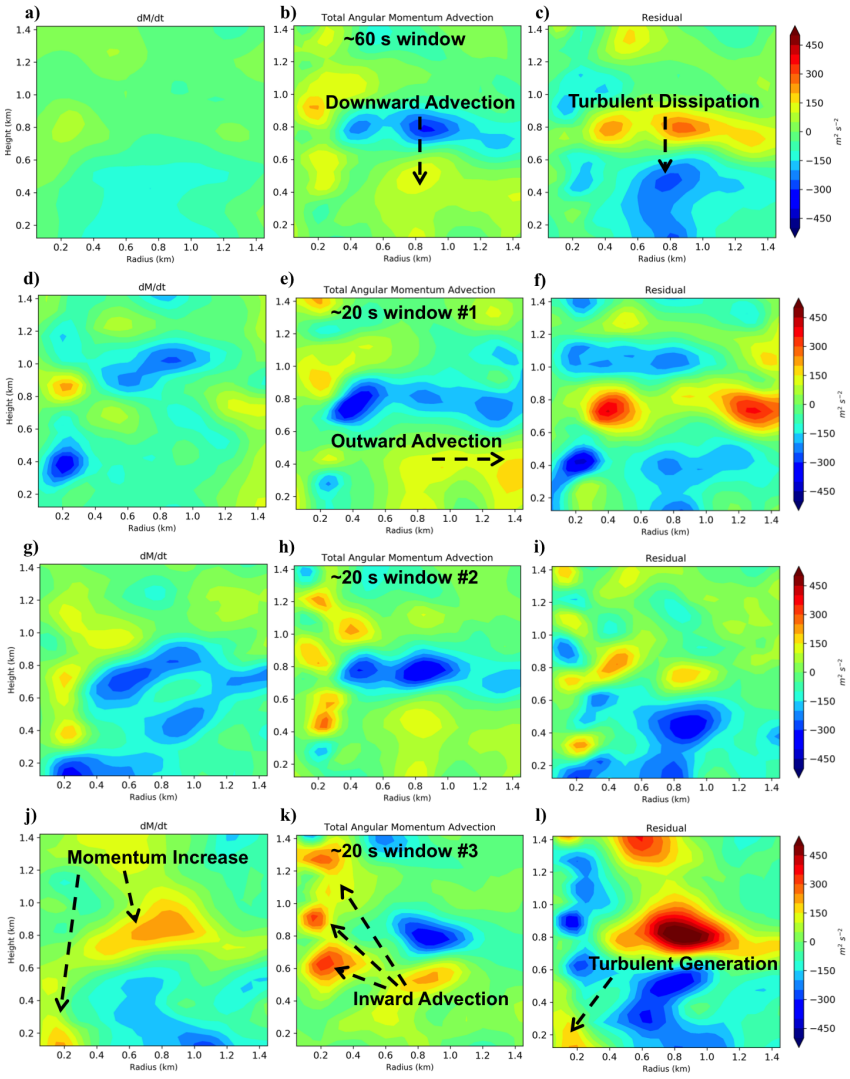


Figure 5.9: Axisymmetric (a,d,g,j) time rate of change (shaded, $m^2\ s^{-2}$), (b,e,h,k) advection (shaded, $m^2\ s^{-2}$), and (c,f,i,l) eddy flux convergence (shaded, $m^2\ s^{-2}$) of angular momentum valid for the (a-c) 22:03:52–22:04:56 UTC timeframe, (d-f) 22:03:52–22:04:13 UTC timeframe, (g-i) 22:04:13–22:04:35 UTC timeframe, and (j-l) 22:04:35–22:04:56 UTC timeframe. The left column represents the time rate of change of angular momentum calculated by taking difference in the angular momentum field between the first and last time in the analysis window. The middle column represents the average advection of angular momentum by the secondary circulation during the analysis window. The right column is largely representative of the turbulent creation and dissipation of angular momentum.

of angular momentum is still occurring, a requirement for tornado maintenance (e.g., Marquis et al. 2012). Eddy angular momentum flux (Fig. 5.9c), acts as a low-level sink of angular momentum, especially in the region where large values of angular momentum are advected downward. The loss of angular momentum near the ground agrees with the findings of Rasmussen and Straka (2007) and is likely due to surface friction. Overall, the high-temporal observations are consistent with the lower-resolution observations in Rasmussen and Straka (2007) that downward and outward advection and subsequent dissipation of angular momentum by surface friction occurs during tornado decay.

The high-temporal updates of the AIR can also be leveraged to test the sensitivity of the angular momentum budget to the length of the analyzed window. The budget was calculated over the same 60-s period using three 20-s windows of data (Fig. 5.9d). It can be seen that the values of the time rate of change of $\Gamma$ are larger and more variable on the shorter time scales (Fig. 5.9 d,g,j). Except near the core of the tornado, total angular momentum advection is largely insensitive to the length of the analyzed window (Fig. 5.9 e,h,k). Near the core, inward angular momentum advection strengthens at the end of the analyzed window (Fig. 5.9k) as single-cell vortex flow becomes established and the previously discussed axial updraft forms and strengthens (Fig. 5.8c). It is possible that the increase in inward advection of angular momentum during this period contributes to the brief strengthening of the tornado noted in Fig. 5.5 and further evidenced by the positive time rate of change regions in Fig. 5.9j. Similar to the time rate of change term, the eddy angular momentum flux term is larger and more variable at shorter timescales (Fig. 5.9 f,i,l). The magnitude of the eddy angular momentum flux term is particularly large late in the analyzed period (Fig. 5.9l), and is responsible for the positive time rate of change of angular momentum in the bottom region of the tornado core. Because the advection term remains relatively constant throughout much of the domain, this means that the eddy angular momentum flux term is contributing more to the time rate of change of $\Gamma$ when calculating the budget over a shorter analysis window. It is likely that

the eddy flux term becomes more important on shorter timescales due to the short-lived nature of turbulent eddies.

### 5.3.4 Tornado Tilt

The Canadian, Texas, tornado became increasingly tilted through all depths beginning at 22:05:39 UTC and lasting through tornado dissipation (Fig. 5.10a). The increase in tornado tilt corresponded with the initial stage of tornado decay in Fig. 5.5. Increase in tornado tilt was maximized in the 0.1–0.5 km and 0.1–1.0 km layers, where tilt increased from approximately 25° to 55° and from 35° to 55°, respectively. The increase in tilt was the result of the low-level vortex becoming increasingly displaced to the west of the the mid-level vortex (Fig. 5.10b). While the Canadian tornado at the lowest elevation angle (black) moved steadily westward, higher up, between 1 and 2 km ARL (red), the Canadian tornado looped cyclonically and moved only slightly westward during dissipation. This tornado motion likely resulted in the tornado becoming occluded as the low-levels became displaced to the west of the mesocyclone above 1 km as well as to the west of the position of the rear-flank gust front (not shown).

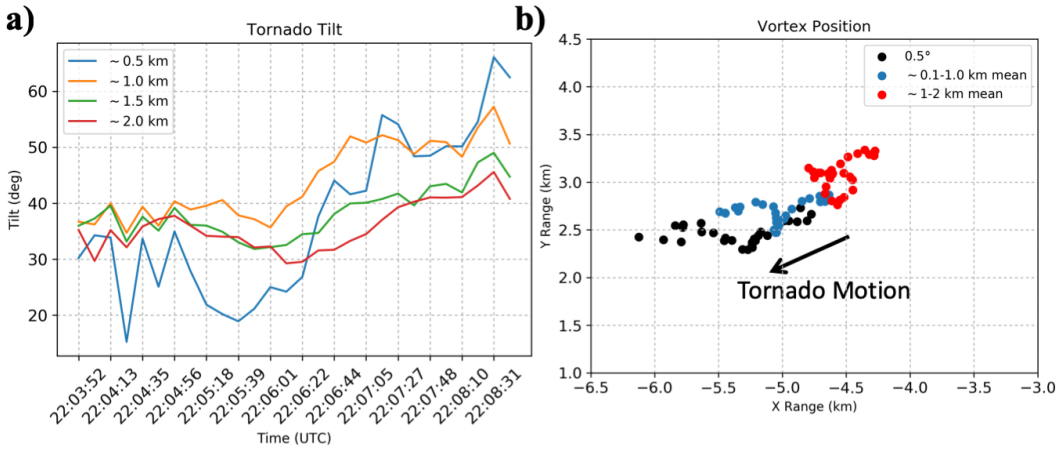


Figure 5.10: (a) Tornado tilt (°) between the lowest elevation angle (∼ 0.1 km) and 0.5 km (blue), 1.0 km (orange), 1.5 km (green), and 2.0 km (red). (b) Tornado center at the lowest elevation angle (black) and mean tornado center in the 0.1–1.0 km layer (blue) and 1.0–2.0 km layer (red). Storm motion is from right to left at all levels.

The direction of tilt in the 0.1–2.0 km ARL (0.5–20°) layer was to the northeast for the entirety of the deployment (Fig. 5.11), which is similar to the 0-3 km environmental wind shear vector (not shown). Similar northeastward tilt has been noted previously (e.g., Tanamachi et al. 2012, 2013; French et al. 2014) and appears to be a common orientation for supercellular tornadoes in the northern hemisphere. The tilt direction changed from toward the NNE to toward the ENE during the tornado decay period. This clockwise shift in tilt direction corresponded with the westward motion of the low-level vortex relative to the upper levels of the vortex (Fig. 5.10b). The largest change in tilt direction started at 22:05:39 UTC (Fig. 5.11), when the first tornado decay period began (Fig. 5.5) and the aforementioned increase in tilt occurred.

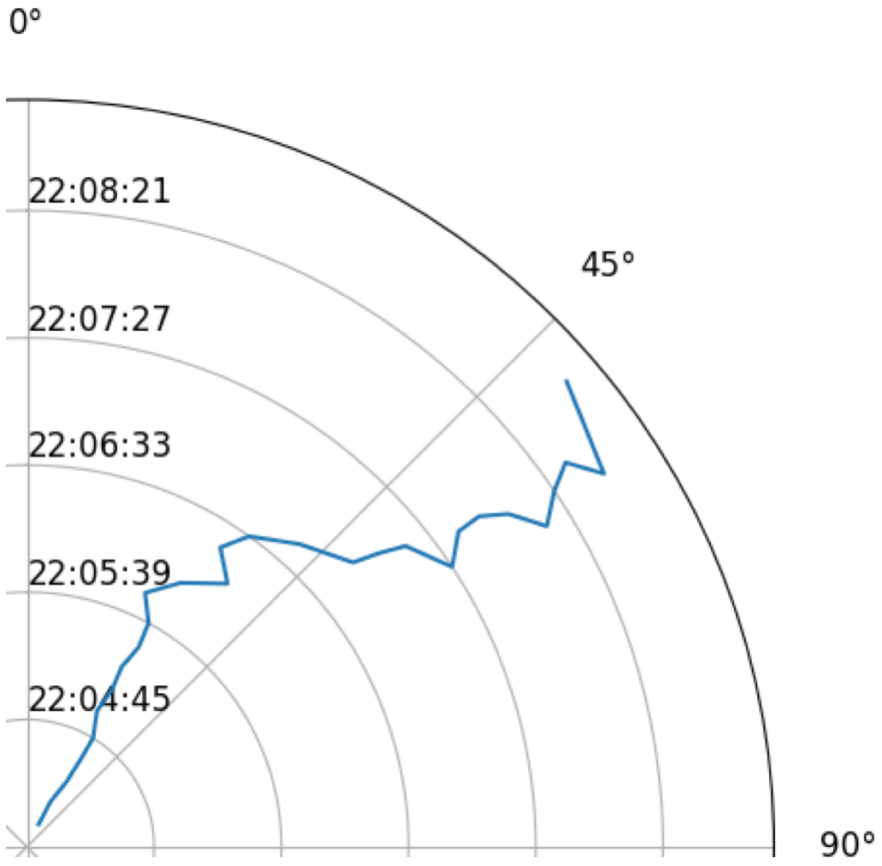


Figure 5.11: Direction of vortex tilt between 0.1 and 2.0 km ARL in clockwise degrees from north. Radial axis is time in UTC.

The simultaneous RHIs collected by the AIR also allows for the interrogation of the vertical shape of the tornado in greater detail (Fig. 5.12). Early on in the deployment when the tornado was at its observed maximum diameter and intensity, the tornado was nearly upright with minimal vortex tilt below the cloud base (Fig. 5.12a,d). As previously mentioned, the tornado became increasingly tilted late in its lifecycle (Fig. 5.12b,d). A rapid increase in tilt was observed between 400 and 700 m ARL during the 22:06:01–22:06:44 UTC period (Fig. 5.12c-d). The formation of the region of vortex tilt in excess of 70° corresponded temporally with the downward tornado decay observed in Fig. 5.5 and was located at the bottom of the of the vertical layer where downward decay occurred. Interestingly, the layer with the largest tilt, between 400 and 700 m ARL, exhibited the slowest decrease in $\Delta$V (Fig. 5.5)[2] and has relatively high $\Delta$V compared to the layer below with less tilt, opposite of the inverse relationship between vortex intensity and tornado tilt observed by French et al. (2014). Another feature of interest was a layer of persistent tilt (40-50°) above the cloud base between 1.25 and 1.5 km ARL. This region of persistent tilt also divided the aforementioned temporally separate mid-and low-level decay in Fig. 5.5. Speculation regarding the significance of this layer is reserved for Section 4a. An additional layer of persistent tilt was located between 750 and 1000 m ARL, near the cloud base. At the beginning of the decay phase corresponding to the photograph in Fig. 5.12b, the region of tilt near the cloud base either disappeared or descended and merged with the aforementioned high-tilt region between 400 and 700 m ARL.

### 5.3.5 Vertical Cross-Sections

A simultaneously collected RHI through the concentric WEHs (Fig. 5.13a) reveals that the inner bands of enhanced reflectivity were disconnected from any regions of higher

[2]Note that the slowest decay occurring in the most tilted layer means that the downward decay may have been slower than what is presented due to biases owing to tornado geometry.

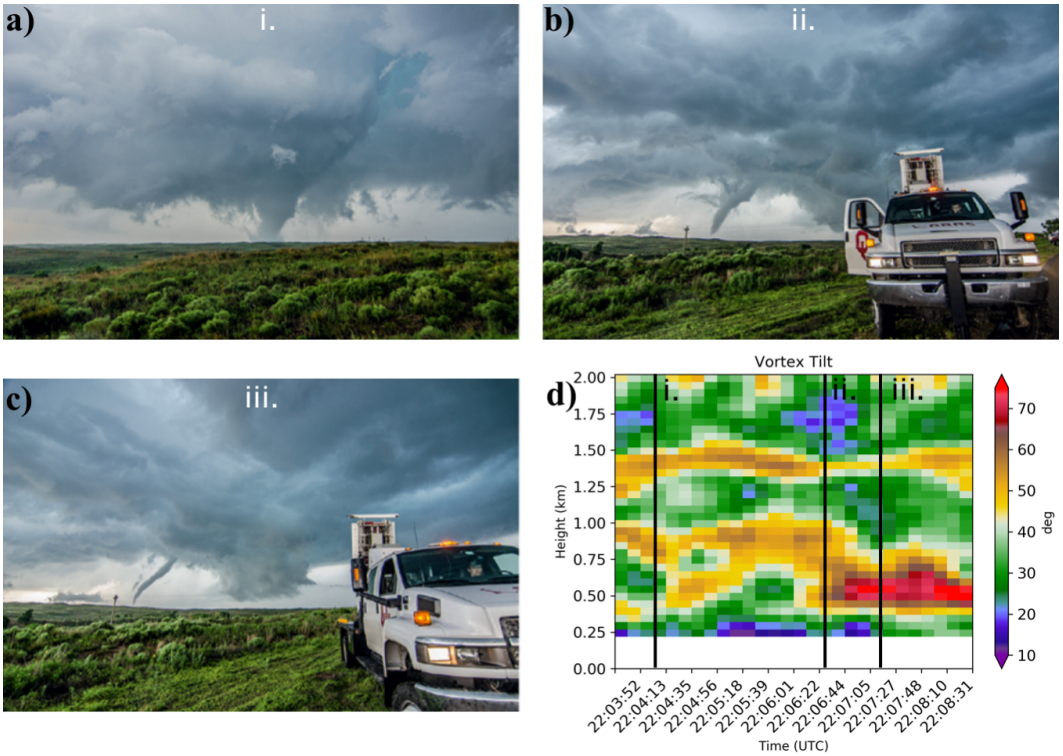


Figure 5.12: Photographs at (a) 2204, (b) 2206, and (c) 2207 UTC and (d) a time-height plot of filtered vortex tilt (°). Vertical lines i, ii, iii in (d) correspond with (a-c) respectively. Photographs adapted from Kurdzo et al. (2017).

reflectivity aloft and extended below the lowest observed elevation (Fig. 5.13b). Conversely, the outer bounds of the larger WEH were part of a continuous region of high reflectivity that extended through 20° in elevation. While the outer WEC extended higher than the 750 m illustrated in Fig. 5.13b, the tornado tilts out of the RHI plane, precluding observation of the feature through a deeper layer. Regardless, the contrasting vertical structure of the WECs in the low levels supports the hypothesis that the two WECs represented different types of scatterers. It is speculated that the inner WEH was comprised of light debris that were lofted from the surface and the outer WEH represented descending rainbands at the periphery of the tornado. However, in the absence of polarimetric data, this hypothesis cannot be confirmed.

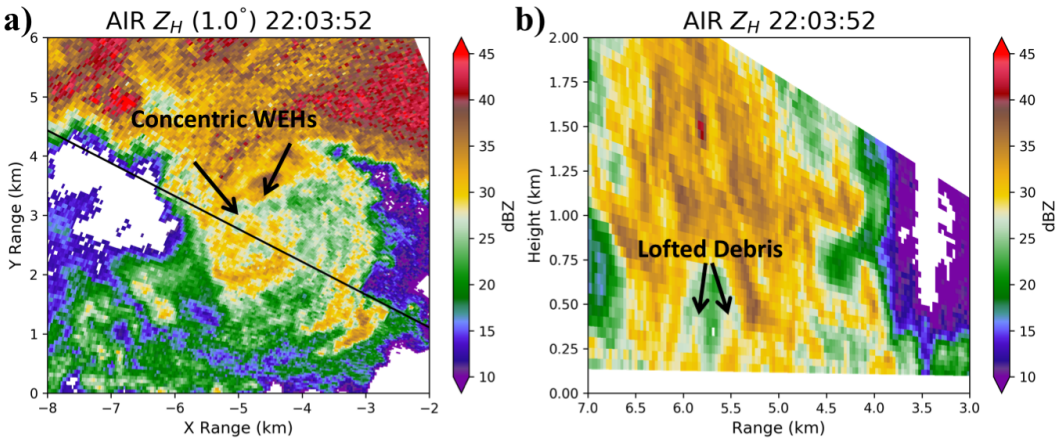


Figure 5.13: (a) PPI plot of reflectivity (dBZ) at 1° elevation and (b) RHI of reflectivity (dBZ) valid at 22:03:52 UTC. Black line in (a) represents the location of the RHI in (b).

To better observe the vertical structure of the WEH, azimuth height indicators (AHIs) consisting of a vertical cross-section along a constant range are constructed (Fig. 5.14a). While these AHIs are not simultaneous, they only represent a span of ∼5 s of data, and therefore are comparable to traditional RHIs collected by mechanically steered radars. Because the Canadian tornado was tilted to the northeast (Fig. 5.11), this geometry better captures a deeper layer of the WEC along the direction of tornado tilt. However, the tapered nature of the WEC above 1.25 km ARL and the disappearance of the WEC above 1.5 km (Fig. 5.14b) are artifacts of the tornado tilting out of the AHI plane within

the persistent tilt layer between 1.25 and 1.5 km ARL. In contrast, the abrupt narrowing of the WEC at 1 km ARL is not an artifact of tornado tilt since the AHI bisects the WEH at its widest point beneath 1 km (Fig. 5.14c) and just above 1 km (Fig. 5.14d). While there was no observed vertical gradient in $\Delta V$ in this layer (Fig. 5.5), there was an appreciable narrowing of the RMW (Fig. 5.2f,h). Beneath the height of the abrupt narrowing, the WEC slightly broadened with height resulting a bulging structure similar to what was observed by Bluestein et al. (2007b) (cf., Figure 13, Bluestein et al. (2007b)).

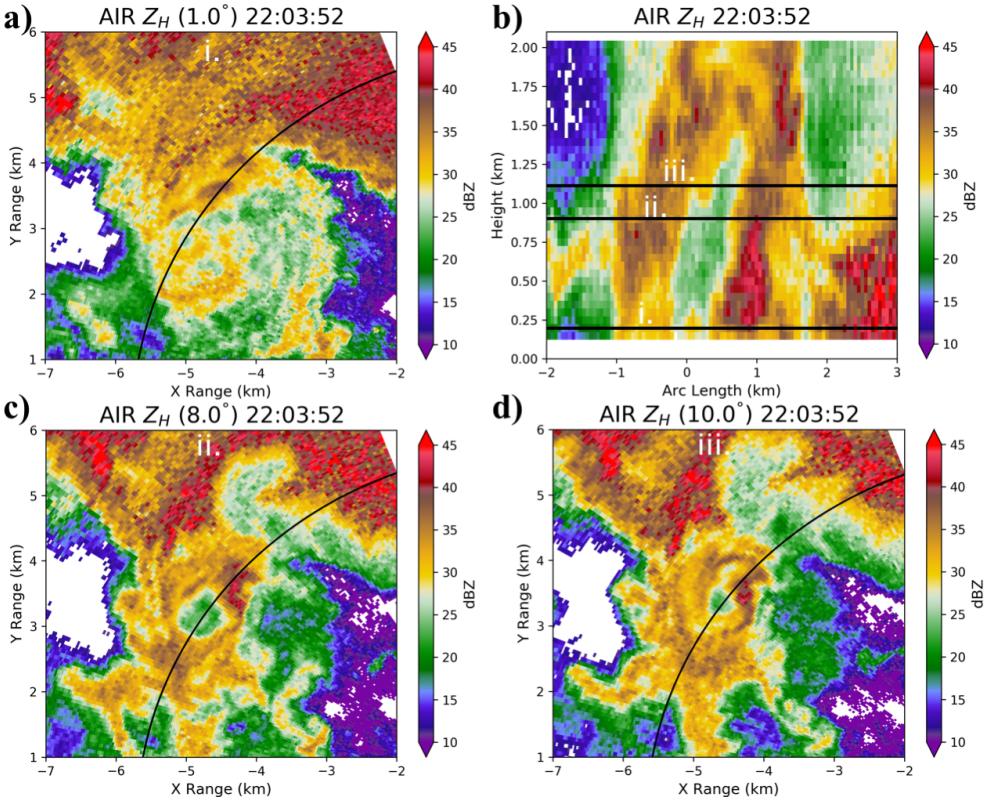


Figure 5.14: (a,c,d) PPI plots of reflectivity (dBZ) at 1°, 8°, and 10° respectively and (b) AHI of reflectivity (dBZ) valid at 22:03:52 UTC. Horizontal lines i, ii, iii in (b) correspond with (a,b,d) respectively. Black lines in (a,c,d) represent the location of the AHI in (b).

As previously mentioned, the Canadian tornado became increasingly tilted late in its lifecycle (Fig. 5.12). A simultaneous RHI was taken through the tornado (Fig. 5.15) near time ii in Fig. 5.12b,d. The tilt of the tornado at this time was 45-50° from vertical in the layer between 400 and 750 m ARL. Differential velocity was computed in both the vertical

(Fig. 5.15b) and horizontal (Fig. 5.15c-d) planes. As expected from a tornado that was tilted approximately 45° from vertical, the magnitude of vertical shear was similar to the magnitude of horizontal shear with $\Delta$V between 50 and 60 m $s^{-1}$ depending on the choice of elevation angle for PPIs and radial for RHIs. The vertical shear in Fig. 5.15b is due to the tornado being partially tilted into the horizontal plane, which results in the RHI bisecting outbound velocities on the north side of the tornado in the low levels (Fig. 5.15c) and inbound velocities on the south side of the tornado aloft (Fig. 5.15d). The largest vertical gradient in Doppler velocity at 6 km in range was largely contained within the the 400–700 m layer ARL where the tornado was also the most tilted (Fig. 5.12d). The horizontal vorticity associated with the tilted vortex was strong enough to centrifuge hydrometeors and cause a WEH to appear (Dowell et al. 2005) in the horizontal plane (Fig. 5.15a). The center of this WEH bisected the layer where the strongest vertical gradient in Doppler velocity was observed.

## 5.4 Discussion

### 5.4.1 Persistent Vortex Tilt Layer and Tornado Decay

The persistent region of enhanced vortex tilt between 1.25 and 1.5 km ARL (Fig. 5.12d) coincided with the level that separated the temporally displaced mid- and low-level vortex decay near the end of the Canadian tornado lifecycle (Fig. 5.5). Additionally, the maximum tornado intensity observed at the beginning of the deployment as well as the brief restrengthening of the tornado that occurred shortly thereafter was confined to within the lowest 1 km (Fig. 5.5). It is hypothesized from this body of circumstantial evidence that the vertical layer around $\sim$1.25 km ARL was particularly relevant to the Canadian tornado.

The Dodge City, Kansas, 00Z sounding was launched approximately one hour after the Canadian tornado occurred, and despite the approximately 200 km that separate the locations, the surface conditions at Dodge City (DDC) were nearly identical to those in

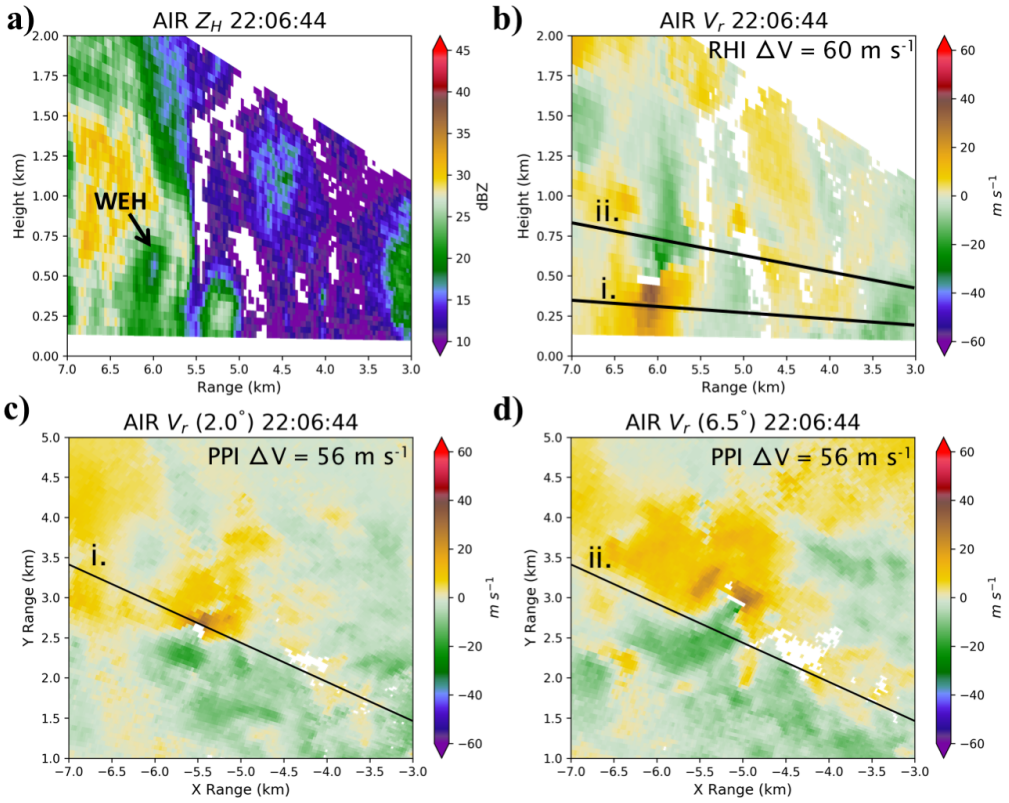


Figure 5.15: RHI plots of (a) radial velocity (m s$^{-1}$) and (b) reflectivity (dBZ) and PPI plots of radial velocity (m s$^{-1}$) at (c) 2° and (d) 6.5° elevation valid at 22:06:44 UTC. The tornado is very tilted through the 400–700 m layer (see Fig. 5.12d) as evidenced by the shift in vortex position between (c) and (d). Strong horizontal vorticity is evident through this layer with slightly larger ΔV in the RHI scan compared to the PPI scans. Black lines i and ii in (b) correspond with the elevation angles in (c-d) respectively. Black lines in (c-d) correspond with the location of the RHIs in (a-b).

Canadian, Texas at the time of the tornado (Fig. 5.16a). Additionally, environmental temperatures at 700 mb (Fig. 5.16b) and 500 mb (Fig. 5.16c) were also similar at DDC and Canadian, Texas, and the regional environment was relatively uniform. Thus, it is assumed that the DDC sounding (Fig. 5.16b) was at least somewhat representative of the environmental thermodynamic profile in Canadian, Texas. The level of free convection (LFC) at DDC was at approximately 760 mb, corresponding to ∼1500 m above ground level (AGL) at the sounding site. Replacing the surface conditions of the DDC sounding with the ASOS observations in Canadian, Texas, at the time of the tornado (not shown) lowers the LFC to 800 mb or 1250 m ARL, which is within the layer of enhanced vortex tilt.

The transition from forced to free ascent by parcels within the tornado may have caused a change in parcel trajectory and might explain the tilted nature of the vortex in this layer, especially given that the layer between 1 and 2 km exhibited considerable environmental wind shear (Fig. 5.16d). In this scenario, ascent, which was forced beneath the LFC, would have been slower than above the LFC where parcels were positively buoyant. As a result, more horizontal advection would have occurred beneath the LFC than above it. The vertical gradient in vertical velocity necessary for increased tilt in this layer is similar to what was inferred by French et al. (2014) when discussing the increased vertical vorticity stretching that may occur near the LFC. Differential horizontal advection in this layer would be enhanced if the near-storm environment beneath the LFC were particularly stable. A stable layer would also have contributed to the observed vertical discontinuity in tornado decay similar to what was observed by Houser et al. (2015). Within the stable layer, parcels would not be accelerated upward by the buoyancy force, which in turn weakens vertical gradients in vertical velocity and subsequently limits the stretching of vertical vorticity. If negatively buoyant air were to be ingested into the updraft, within and above a stable layer the vertical gradient in vertical velocity could even become negative, rapidly reducing vortex strength through horizontal divergence.

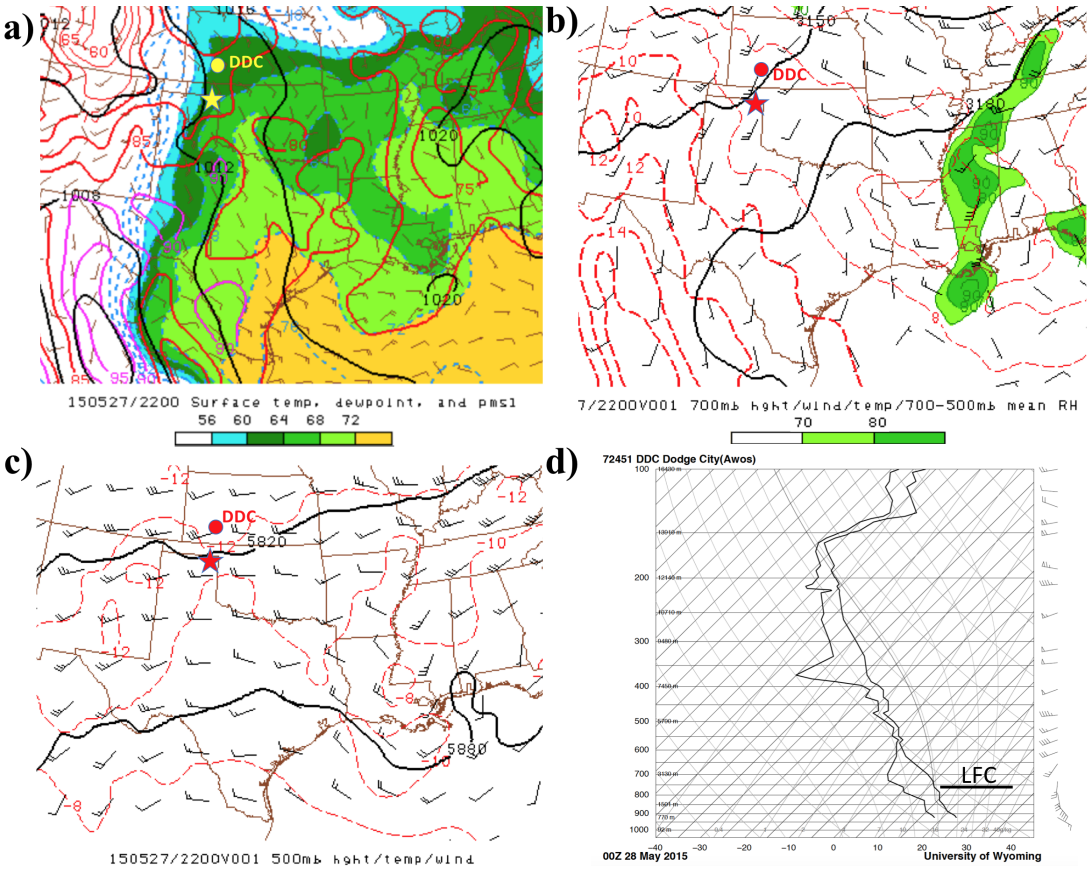


Figure 5.16: Storm Prediction Center mesoanalysis of (a) surface temperature (red lines, °F), mean sea level pressure (black lines, mb), and dewpoint temperature (shaded, °F), (b) 700 mb height (black lines, m), temperature (red lines, °C), and 700-500 mb mean RH (shaded, %), and (c) 500 mb height (black lines, m) and temperature (red lines, °C) valid at 2200 UTC on 27 May 2015. The star indicates the location of Canadian, Texas, and the circle indicates the location of Dodge City, Kansas. Archived mesoananalyses are available online at `http://www.spc.noaa.gov/exper/ma_archive/`. (d) Skew-T diagram of the vertical sounding launched at Dodge City, Kansas, valid at 00 UTC on 28 May 2015. Archived soundings are available online at `http://weather.uwyo.edu/upperair/sounding.html`.

However, a near-storm sounding would be necessary to assess whether a small stable layer was present.

Changes in inflow characteristics associated with tornado occlusion may impact vortex strength above the LFC on a different timescale than below the LFC. The gradual, downward vortex weakening in Fig. 5.5 might first occur just above the LFC where the buoyancy force plays an important role in accelerating parcels and stretching vorticity. Vortex decay below the LFC may lag mid-level decay because ascent is forced by a dynamic pressure gradient force that is modulated by mid-level vortex strength. This possible explanation would be in agreement with the tornado occlusion mechanism for tornado decay hypothesized in French et al. (2014), where tornadoes first weaken just above the level of occlusion and then dissipate in an "inside out" fashion. Additionally, the 5 June 2009 Goshen County, Wyoming, tornado was observed to intensify much more rapidly above the LFC than below the LFC (French et al. 2013), which further supports the theory that the LFC demarks a boundary in tornado structure and evolution.

While the LFC appears to separate two dissipation modes, there are many additional factors that may contribute to tornado intensity. A comparison of tornado diameter to tornado intensity (Fig. 5.17) reveals that tornado intensity was anti-correlated with the distance between the location of maximum and minimum Doppler velocity within the tornado. During the brief restrengthening period between 22:04:13 and 22:05:18 UTC, tornado diameter decreased from approximately 700 m to between 100 and 200 m. The tightening of the vortex was confined to the lowest 750 m ARL, the same depth over which tornado intensity increased. Conversely, the near simultaneous weakening of the tornado above 1250 m ARL at 22:05:28 UTC occurred at the same time vortex diameter doubled from ∼300–400 m to ∼700–800 m within the same vertical layer. Tornado intensity at this time approximately halved from $\Delta$V of near 90 m s$^{-1}$ to $\Delta$V less than 50 m s$^{-1}$, which implies that angular momentum remained relatively constant during this weakening period. Finally, between 500 and 1000 m ARL, downward broadening of the tornado coincided with downward decay. The tornado widened nearly simultaneously

in the lowest 500 m at 22:06:22 UTC, approximately at the same time the tornado weakened within the same layer. While it is expected that a decrease in overall angular momentum occurred during tornado decay (Rasmussen and Straka 2007; Atkins et al. 2012), it appears that over short time periods the conservation of angular momentum at least partially contributes to changes in the magnitude of $\Delta$V as the Canadian tornado underwent changes in diameter. The inverse relationship between the magnitude of $\Delta$V and the radius of maximum winds is consistent with the behavior of of the 5 June 1999 Bassett, Nebraska, tornado (Bluestein et al. 2003) except in this case the relationship was investigated at each elevation angle through a 2 km depth and not just a single level. However, the behavior of the Canadian tornado is dissimilar to the 15 May 1999 Stockton, Kansas, tornado where both tangential velocity and tornado diameter decreased simultaneously during decay (Tanamachi et al. 2007), illustrating a range of late lifecycle tornado behaviors.

### 5.4.2 Vertical Correlation in Vortex Intensity

Differential Velocity ($\Delta$V) at all heights was highly correlated with $\Delta$V at the lowest analysis level at zero lag for the deployment period (Fig. 5.18). High correlation at lag 0 suggests that changes in vortex intensity occurred largely simultaneously in the vertical. Values of correlation were greater than 0.97 for all heights in the analysis. The linear decrease in correlation throughout most of the analysis signifies that correlation with near-surface intensity was inversely related to the vertical displacement from the surface, likely as intensity changes aloft became slightly less in phase with changes near the surface. However, correlation at non-zero lags (not shown) was approximately 0.05 lower with each increasing lag[3]. This further suggests that simultaneous changes in intensity were more prevalent than directional changes in intensity (i.e. upward or downward strengthening

[3]In this case, a negative lag would mean that changes near the surface preceded changes aloft (i.e., upward strengthening/weakening) and a positive lag means that changes aloft preceded changes near the surface (downward strengthening/weakening).

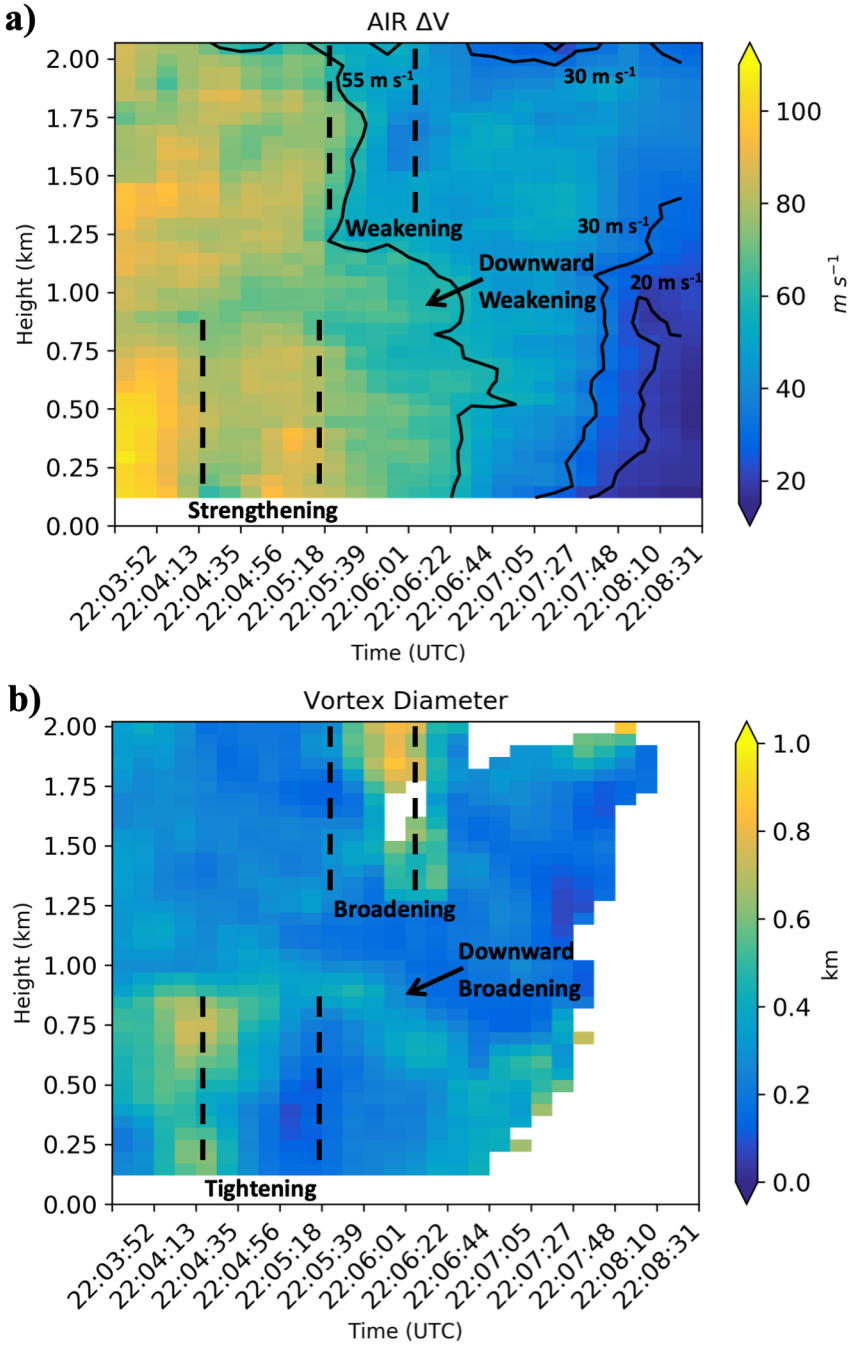


Figure 5.17: Time-height plots of (a) maximum ΔV (m $s^{-1}$) as in Fig. 5.5 and (b) the distance (km) separating maximum inbound and maximum outbound velocities used to calculate ΔV in (a). Vortex diameter is thresholded on ΔV beneath 40 m $s^{-1}$ where diameter calculations became much noisier.

or weakening of the vortex) in the Canadian tornado similar to what was observed during the majority of the 24 May 2011 El Reno case (Houser et al. 2015). Recall that there was one noted instance of upward tornado strengthening in the Canadian tornado (Fig. 5.5), but the restrengthening was brief and occurred above the lowest few analysis levels the intensification occurred simultaneously rather than upward in direction. As a result, no signal was found at negative lags and therefore it is not shown. Additionally, the Canadian tornado was observed to decay in a downward direction between 400 and 1250 m ARL (Fig. 5.5); however, analysis of correlation at positive lags was inconclusive and are not included. It is likely that the relatively small number of data points that encompassed the observed upward and downward changes in vortex intensity caused their signal to be washed out by the highly correlated nature of the vortex over the length of the full deployment. The directional changes in vortex intensity are important to understanding the behavior of the Canadian tornado during decay, but they do not characterize tornado behavior for the majority of observed period.

The high correlation of vortex intensity at all heights with the low-level vortex in the Canadian tornado contrasts with other recent high-temporal observations of tornadoes. French et al. (2014) noted that low-level vortex intensity in the 5 June 2009 Goshen County, Wyoming, EF2 tornado was often anti-correlated with mid-level intensity. This was largely due to the oscillatory nature of low-level vortex strength. However, French et al. (2014) were comparing average tornado intensity below 2 km with average intensity above 2 km, which sometimes extended above 5 km ARL, whereas all of the observations in the Canadian case were below 2 km. Similar to the Goshen County tornado, the 16 May 2015 Tipton, Oklahoma, tornado also exhibited periodic changes in low-level vortex intensity, which often decorrelated vortex intensity in the lowest 500–700 m from vortex intensity above 700 m (Mahre et al. 2018). Periodic changes in low-level tornado intensity have also been observed by Wurman et al. (2013) using high-temporal resolution mobile radar data. Additionally, the Tipton tornado experienced one instance of pronounced upward tornado intensification, although this may be due to debris-induced biases (Mahre

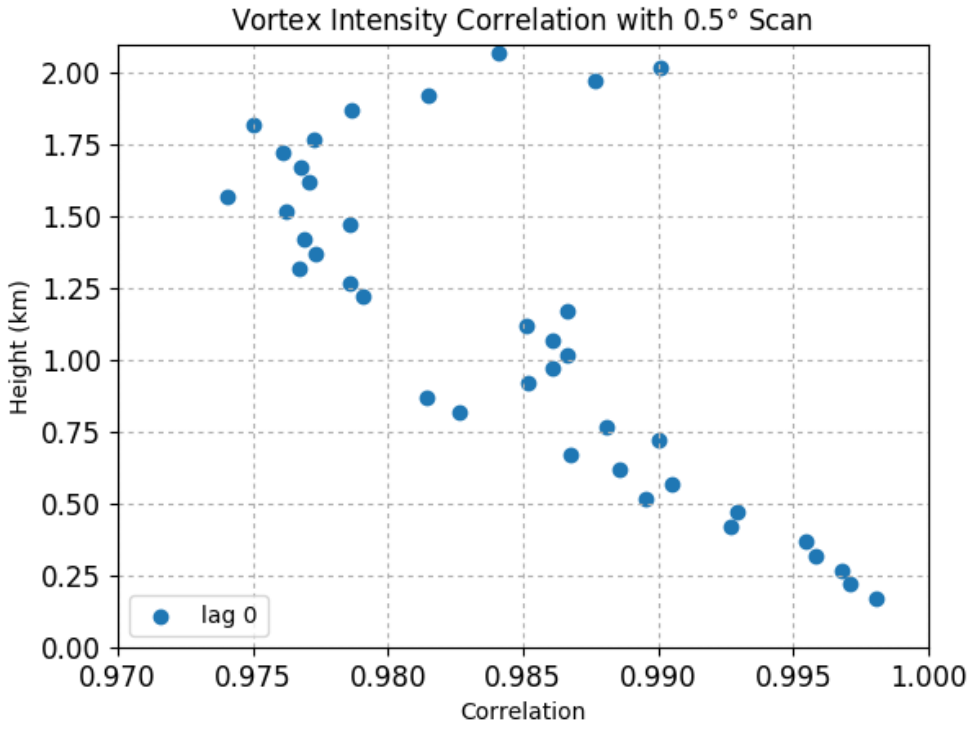


Figure 5.18: Cross-correlation at lag 0 of $\Delta V$ at each height (km) with the 0.5° scan. The calculation was performed over the 22:03:52–22:07:37 UTC time period when $\Delta V$ exceeded 40 m $s^{-1}$ throughout the majority of the observed depth. High correlation at lag 0 suggests that changes in vortex intensity occur largely simultaneously in the vertical.

et al. 2018). The Canadian tornado did not exhibit strong periodicity in low-level vortex intensity during the observed period; however, these observations were during the late-mature to dissipation stages whereas the Tipton observations were during the mature stage, so caution is required when comparing the two cases. Perhaps there is some mechanism for periodic oscillations in tornado intensity that is less likely to occur late in the tornado lifecycle, e.g., because the tornado and mesocyclone are less vertically stacked. However, it can be concluded that during the late mature and decay phases of the Canadian tornado, changes in vortex intensity in the lowest 2 km were largely non-periodic and were highly correlated with tornado intensity at the lowest analysis level.

## 5.5 Conclusions

On 27 May 2015, the AIR collected 4.5 min of sector volumes with 5.5-s temporal resolution during the late-mature and decay stages of the Canadian, Texas, tornado. At the beginning of the deployment, maximum $\Delta$V within the tornado was observed to be 110 m $s^{-1}$. At this time, the tornado vortex widened from a small diameter vortex near the surface to a wide vortex with weak Doppler velocities in its core aloft and then back to a small diameter vortex above the cloud base. Broken rings of enhanced spectrum width at the radius of maximum winds, and regions of enhanced shear along the zero isodop were also observed, suggesting that the Canadian tornado initially had multiple-vortex structure. Additionally, small-scale vortices were observed to exit the tornado and translate eastward beyond the RMW, each of which went through brief periods of intensification after being shed.

A weakening of the vortex occurred soon after the beginning of the dataset with $\Delta$V decreasing from 110 to 80 m $s^{-1}$ in less than 30 s. The weakening from peak vortex strength was accompanied by a change from an axial downdraft to an axial updraft in the axisymmetric framework. A reversal in the direction of the dynamic perturbation pressure gradient force associated with the decrease in low-level tangential velocities

may have contributed to the change in axial flow. Additionally, the weak echo column narrowed in response to the change in vortex flow characteristics, narrowing as inflow intensified and hydrometeors or other scatterers from an intensifying downdraft outside the RMW became entrained. Finally, axisymmetric angular momentum decreased significantly during the initial weakening period. At large radii, angular momentum was advected downward and away from the center of the tornado and into regions near the surface where turbulence acted as an angular momentum sink. Advection of angular momentum away from the tornado may have been aided by the rapid shedding of subvortices that was observed during this timeframe. Overall, the angular momentum budget findings agree with observations by Rasmussen and Straka (2007) of vortex decay, but the current study illustrates these changes with much higher temporal resolution data. At small radii, angular momentum was advected inward, which allowed for the continued maintenance of the tornado. Additionally, a novel time-sensitivity analysis was performed and it was determined that the time rate of change of angular momentum was larger and more variable at shorter timescales and that this was largely due to a greater contribution from the eddy angular momentum flux term. Meanwhile, the advection term was largely insensitive to the length of the analysis window.

A brief, bottom-up intensification of the Canadian tornado occurred following the weak period, coinciding with a narrowing of the tornado. The bottom-up intensification is similar to what has been previously noted by French et al. (2014) and Mahre et al. (2018), except observed here near the decay of the tornado. After the brief reintensification, the largest weakening of the tornado occurred. During this period, $\Delta$V decreased to 40 m s$^{-1}$.

The decay of the vortex first occurred simultaneously in the column above 1.25 km ARL and dissipation progressed in a downward direction over the next minute. An increase in tornado diameter occurred simultaneously with the observed decreases in $\Delta$V. The downward dissipation is similar to the "inside out" decay that was noted in French et al. (2014) and Houser et al. (2015) with the exception that the top half of the hypothesized "inside out" decay occurred above what the AIR observed in the Canadian

case and this study includes observations in the lowest 1000 m unlike Houser et al. (2015). Additionally, tornado decay occurred much more rapidly than was noted in French et al. (2014) and occurred in multiple modes, i.e., downward decay between 400 and 1250 m, simultaneous decay between 150 and 400 m, and decay in the lowest 150 m slightly preceding decay between 150 and 400 m.

Apart from the brief upward intensification and downward decay periods, vortex intensity throughout the analyzed depth was highly correlated with intensity at the lowest analysis level and changes in intensity occurred nearly simultaneously in the vertical. The largely simultaneous vertical changes in vortex intensity were similar to what was observed in the 24 May 2011 El Reno, Oklahoma, tornado (Houser et al. 2015), but dissimilar to the anti-correlated low-level and mid-level tornado strength exhibited by the 5 June 2009 Goshen County, Wyoming, tornado (French et al. 2014) and the 16 May 2015 Tipton, Oklahoma, tornado (Mahre et al. 2018).

During decay, the Canadian tornado also became increasingly tilted in the low levels. The increase in tilt is the result of the low levels of the tornado becoming increasingly displaced to the west of the vortex above 1 km, which potentially resulted in the tornado becoming occluded. Additionally, a persistent region of enhanced tilt was noted between 1.25 and 1.5 km ARL throughout the entire deployment. This height was the same that separated the mid-level and low-level decay at the end of the Canadian tornado lifecycle, and roughly corresponds with the level of free convection, which may help explain both the enhanced tilt and early vortex decay in this region.

While the Canadian tornado is only one case in a growing list of high-temporal resolution tornado observations, it illustrates how rapidly tornado structure can change. Additionally, when considered alongside other recent high-temporal tornado datasets, the Canadian case also exemplifies the diversity of tornado behavior that exists within even a small sample of cases. While similarities are noted between the behavior of the Canadian tornado and tornadoes in other high-temporal datasets, many differences between the tornadoes were highlighted in this case. More high-temporal observations are

needed in order to properly document the range of tornado behavior at short time scales and begin to understand the mechanisms that drive different rapid tornado evolutionary modes. It is our hope that a C-band, dual-polarimetric version of the AIR currently under development (PAIR; Salazar-Cerreño et al. 2017) will facilitate future high-temporal resolution observations of tornadoes in addition to providing information on the evolution of tornadic debris and hydrometeor distributions in supercells.

# Chapter 6

# Conclusions and Recommendations for Future Work

In this chapter, conclusions from the dual-Doppler and polarimetric radar observations of tornadic debris as well as high-temporal resolution mobile radar observations of tornado decay are presented. Then, recommendations for future working using the PAIR and polarimetric radar simulations are discussed.

## 6.1 Conclusions

The objectives of this study were to relate tornado- and storm-scale kinematic processes to the distribution, behavior, and polarimetric characteristics of tornadic debris as well as motivate future rapid-scan polarimetric radar studies of tornadoes through high-temporal resolution observations of tornado features that evolve on very short timescales. Background on tornado lifecycle and structure in addition to background on selected polarimetric signatures in supercells were provided in Chapter 2. In Chapter 3, polarimetric radar and dual-Doppler observations were utilized to relate the near-tornado wind field to heterogeneities within the TDS. A broader look at storm-scale debris sedimentation and a dual-wavelength comparison of debris within a tornado to debris outside the tornado was provided in Chapter 4. Finally, high-temporal resolution radar observations of tornado decay were interrogated in Chapter 5.

Polarimetric radar observations of the 10 May 2010 Moore-Choctaw tornado collected by OU-PRIME revealed a large, heterogeneous TDS with pockets of locally enhanced $Z_H$ and locally reduced $Z_{DR}$ and $\rho_{hv}$ located near the RMW. Dual-Doppler analyses indicated that at low levels two large tornado subvortices were collocated with the extrema in $Z_H$ and $\rho_{hv}$ and the minima in $Z_{DR}$ was located at the periphery and in the wake of the subvortices. Farther aloft, a bifurcated distribution in $\rho_{hv}$ was observed with higher values of $\rho_{hv}$ collocated with an updraft in the dual-Doppler analyses and lower values

of $\rho_{hv}$ collocated with a downdraft. In axisymmetric vertical cross-sections through the tornado, the polarimetric heterogeneities manifested as $Z_H$, $Z_{DR}$, and $\rho_{hv}$ annuli located near the RMW that all widened with height, likely due to the effects of debris centrifuging.

Comparisons of OU-PRIME radar observations of the 10 May 2010 Norman-Little Axe tornado to a nearby landspout tornado revealed contrasting TDS characteristics. The Norman-Choctaw tornado exhibited a WEH, whereas the landspout tornado had a local maxima in $Z_H$ at its center in addition to exhibiting an annulus of $\rho_{hv}$ at the periphery of its TDS. Median and 90th percentile $Z_H$ were larger in the Norman-Little Axe tornado consistent with its greater damage intensity. Additionally, median and 90th percentile $\rho_{hv}$ were also larger in the Norman-Little Axe tornado, likely due to precipitation entrainment. Both TDSs had appendages at different points in their respective lifecycles, with the landspout tornado exhibiting two appendages at one point. One of these appendages was collocated with inflow into the tornado, as indicated by dual-Doppler analyses, and one was collocated with outflow from the tornado. These two relationship are similar to the mechanisms for TDS appendage formation described in Houser et al. (2016) and Kurdzo et al. (2015), respectively, except happening simultaneously for the same TDS. The Norman-Little Axe tornado rotated and elongated to the northeast with height and a vertical profile of dual-Doppler winds revealed that this may have been due to strongly veering and increasingly northeastward storm-relative winds with height. This serves as the first polarimetric radar verification of previous observations by Snow et al. (1995) and Magsig and Snow (1998) that the majority of debris falls out to the left of the tornado track.

Dual-wavelength comparisons of debris within the Norman-Little Axe tornado ('inner') to debris near or falling out of the tornado ('outer') revealed that S-band $Z_H$ was larger than C-band $Z_H$ for both inner and outer debris. The greatest dual-wavelength differences in $Z_H$ and lowest values of $\rho_{hv}$ were observed for inner debris, likely due to increased particle sizes and associated resonance effects. Dual-wavelength differences in $Z_H$ decreased with height for inner debris and increased with height for outer debris. As

a result, inner and outer $Z_H$ values at both wavelengths became more similar at upper levels. This was likely due to debris within the tornado being redistributed outward with height from the effects of centrifuging and advection away from the center of the tornado by the mean wind. These observations are consistent with simulations in Bodine et al. (2016b) except for S and C band instead of S and X band. The decreasing dual-wavelength differences with height for inner debris are likely due to smaller dominant scatterer sizes due to the fallout of the largest debris particles. The only appreciable dual-wavelength differences in $\rho_{hv}$ occurred for inner debris with lower $\rho_{hv}$ observed at C band than at S band due to increased resonance effects a C band for large scatterers.

High-temporal resolution radar observations collected by the AIR reveal that the 27 May 2015 Canadian, Texas, tornado exhibited multiple modes of tornado decay. The decay of the vortex first occurred simultaneously in the column above 1.25 km ARL and dissipation progressed downward over the next minute. An increase in tornado diameter occurred simultaneously with the observed decrease in $\Delta$V above 1.25 km. Between 400 and 1250 m ARL, downward dissipation was observed, similar to the "inside out" decay that was noted in French et al. (2014) and Houser et al. (2015) with the exception that the top half of the hypothesized "inside out" decay occurred above what the AIR observed in the Canadian case. This study also includes observations in the lowest 1000 m unlike Houser et al. (2015). Simultaneous decay was observed between 150 and 400 m, and decay in the lowest 150 m slightly preceded decay between 150 and 400 m.

During decay, the Canadian tornado became increasingly tilted in the low levels. The increase in tilt was the result of the low levels of the tornado becoming increasingly displaced to the west of the vortex above 1 km, which potentially resulted in the tornado becoming occluded. Additionally, a persistent region of enhanced tilt was noted between 1.25 and 1.5 km ARL throughout the entire deployment and corresponded to the height that separated the mid-level and low-level decay at the end of the Canadian tornado life-cycle. Just prior to tornado decay, a brief weakening of the tornado was observed. This weakening coincided with small-scale vortices being shed from the tornado. Following

the brief weakening, a brief, bottom-up intensification, coinciding with a narrowing of the tornado, was observed. The bottom-up intensification is similar to what has been previously noted by French et al. (2014) and Mahre et al. (2018), except observed during the decay of the tornado. Apart from the brief upward intensification and downward decay periods, vortex intensity throughout the analyzed depth was highly correlated with intensity at the lowest analysis level and changes in intensity occurred nearly simultaneously in the vertical. The largely simultaneous vertical changes in vortex intensity were similar to what was observed in the 24 May 2011 El Reno, Oklahoma, tornado (Houser et al. 2015), but dissimilar to the anti-correlated low-level and mid-level tornado strength exhibited by the 5 June 2009 Goshen County, Wyoming, tornado (French et al. 2014) and the 16 May 2015 Tipton, Oklahoma, tornado (Mahre et al. 2018).

## 6.2 Recommendations for Future Work

### 6.2.1 Polarimetric Atmospheric Imaging Radar

While the 2-min temporal resolution data provided by OU-PRIME for this study were sufficient to infer many tornado- and storm-scale processes, radar data with temporal resolution sufficient to resolve tornado evolution ($\sim$10 s) are necessary to fully interrogate the relationship of the debris field to near-tornado kinematic processes and to investigate the response of the debris field to rapid changes in vortex structure. As discussed in Chapter 1, the Polarimetric Atmospheric Imaging Radar (PAIR, Yu et al. 2015; Salazar-Cerreño et al. 2017) will soon be capable of volumetrically resolving rapid tornado evolution while providing the polarimetric data necessary to identify tornadic debris. The near-simultaneous vertical cross-sections collected by the system will mean that a steady-state assumption when investigating the vertical structure of tornadoes and supercells will be much more appropriate than what is implied when using volumetric data collected over a 2-min period. Additionally, the mobile nature of the PAIR will provide superior spatial resolution to the OU-PRIME data used in this study since the PAIR will

usually be less than 10 km from the tornado. This would allow for the interrogation of debris processes on the tornado-scale for smaller tornadoes and on the sub-tornado-scale for large tornadoes.

By performing similar analyses to the ones presented in this study, the PAIR will provide greater certainty in the relationships between polarimetric and kinematic relationships. Dual-Doppler analyses using data from two rapid-scan radars would provide the ability to check whether all of the inferred relationships in this study are consistent in time. This is especially important for investigating short-lived phenomena such as tornado subvortices. Additionally, rapid-scan dual-Doppler would provide the context necessary investigate the formation mechanisms for TDS asymmetries such as debris appendages. Moreover, the response of the debris field to rapid changes in tornado structure and behavior could be investigated. For example, the PAIR could document the response of the debris field to something similar to the rapid change from a medium-swirl drowned vortex jump tornado structure to a low-swirl single-cell vortex like what was seen in the Canadian, Texas tornado in Chapter 5. Similarly, the response to a rapidly evolving debris field from changing surface conditions could be examined.

One particularly useful analysis tool that could be utilized with PAIR data would be to run high-temporal resolution debris trajectories using dual-Doppler syntheses with another rapid-scan radar. The rapid-scan data would minimize the the temporal interpolation of the wind field and improve the accuracy of the trajectories. Trajectories for different debris species with a range of aerodynamic properties could be computed to investigate the differential sedimentation of debris (Fig. 6.1a). Calculating and binning the number of debris trajectories in tornado-relative reference frame (Fig. 6.1b) will provide insight into polarimetric asymmetries within a TDS. For example, it may be possible to determine whether larger debris with lower $\rho_{hv}$ collect within downdrafts near the tornado while smaller debris remain within localized updrafts as hypothesized in Chapter

3 (Fig. 3.10). Simulations of debris trajectories using high-resolution simulations of supercells resolving tornadoes would also be beneficial for comparisons to radar-computed debris trajectories.

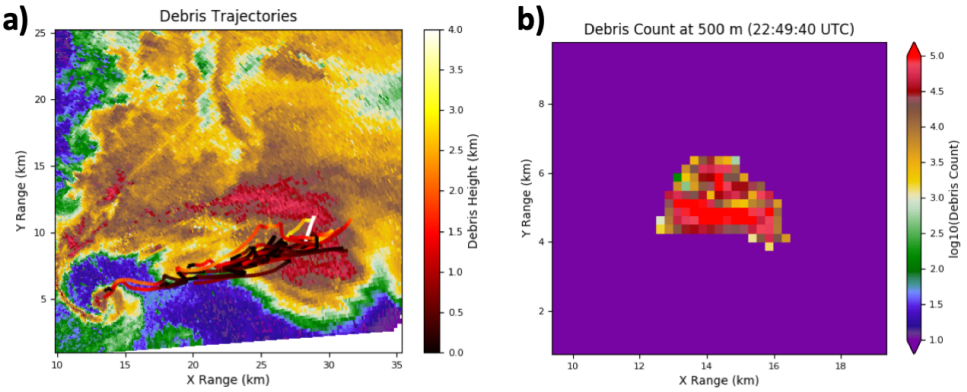


Figure 6.1: PPI plot of (a) OU-PRIME reflectivity overlaid with forward trajectories for leaves color coded by height above ground level and (b) binned $\log_{10}$(debris count) for leaves in a tornado relative reference frame.

In addition to debris studies, the PAIR can continue the tornado research of the AIR. Of particular interest should be studying the vertical evolution of vortex intensity during tornadogenesis and tornado decay. Recent rapid-scan radar observations have shown that tornadogenesis occurs nearly exclusively in a simultaneous or slightly upward fashion (e.g., French et al. 2013; Houser et al. 2015). However, more cases are needed in order to generalize that all tornadoes develop in this fashion. Moreover, more research is needed to investigate why tornadoes develop nearly simultaneously. As an example, the AIR captured tornadogenesis in the 23 May 2016 Woodward, Oklahoma, tornado, and in this case vertically simultaneous tornadogenesis occurred when a low-level vortex became spatially phased with the low-level and mid-level mesocyclone (Fig. 6.2). However, this vertical stacking of the vortices was short lived and the tornado quickly dissipated. More cases are required to determine whether this is a common tornadogenesis mechanism and assess if a more prolonged vertical stacking would have been more conductive to a longer-lived tornado.

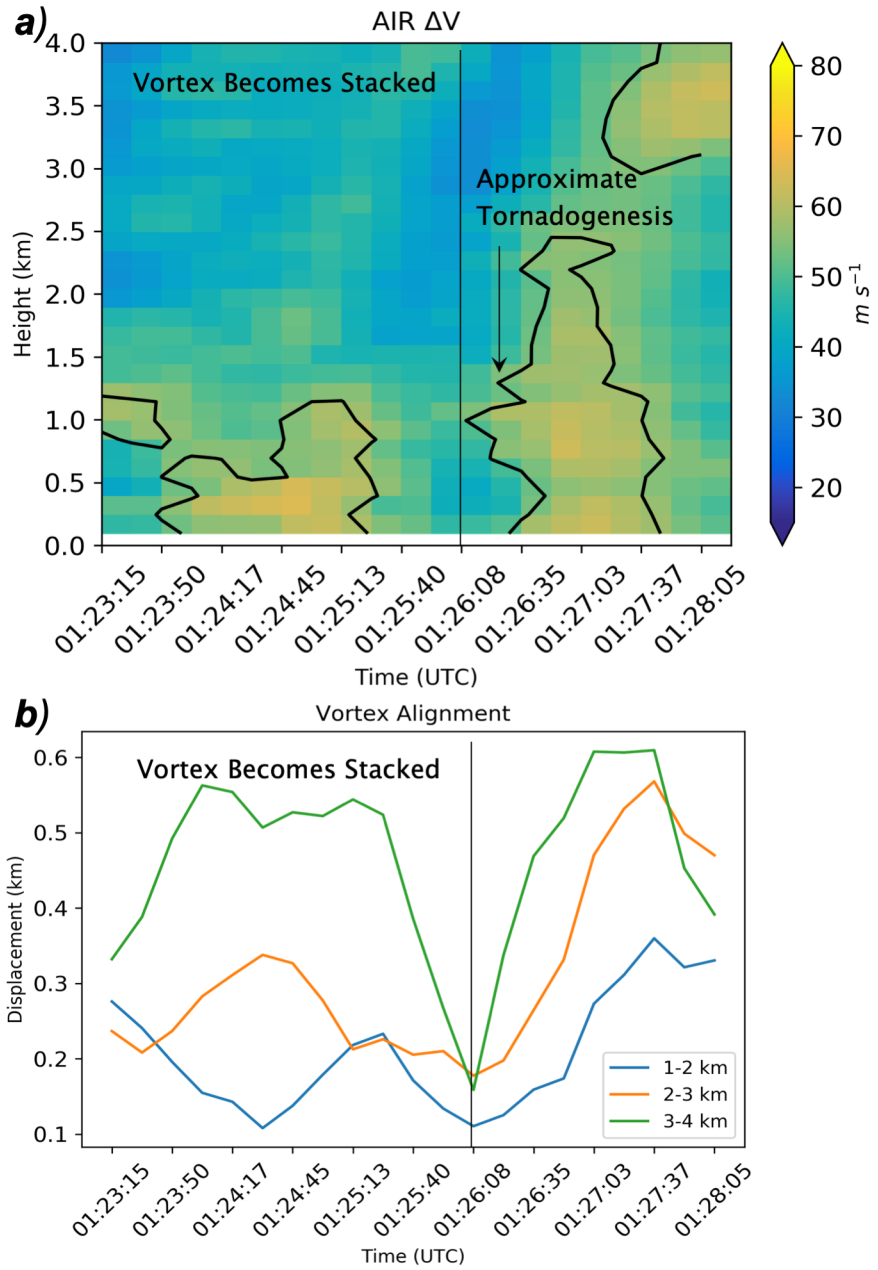


Figure 6.2: (a) Time-height plot of maximum ΔV (m $s^{-1}$) and (b) the distance between the mean position of the Woodward tornado in the lowest 1 km and the mean position of the vortex between 1-2 km (blue), 2-3 km (orange), and 3-4 km (green).

Mature tornadoes have shown a diversity in behavior when observed at high-temporal resolution. The 5 June 2009 Goshen County, Wyoming, tornado exhibited periodic tornado intensity that was sometimes correlated and sometimes anti-correlated with mesocyclone intensity (French et al. 2014). Meanwhile, the 24 May 2011 El Reno, Oklahoma, tornado exhibited periodic tornado intensity that was correlated with mesocyclone intensity (Houser et al. 2015) and the 16 May 2015 Tipton, Oklahoma, tornado exhibited low-level vortex periodicity that was anti-correlated with vortex intensity aloft (Mahre et al. 2018). The Canadian, Texas, tornado in this study exhibited vertically correlated vortex strength and did not exhibit periodic changes in intensity. A large number of cases needs to be collected to determine the relative frequency of these tornado behaviors and to begin to investigate the mechanisms that control periodic changes in tornado intensity and why only some tornadoes are correlated with mesocyclone intensity.

Additional research is also needed on tornado dissipation mechanisms. While inside out tornado decay appears to be commonly observed during decay, near-storm thermodynamic observations and modeling research is needed to verify the dynamic and thermodynamic processes that lead to this dissipation mode. Mobile mesonet or unmanned aircraft systems (UAS) observations of the position and thermodynamic characteristics of the cold pool could provide insight on the occlusion process and the vertical layering of processes that occur. Near storm-soundings could provide information on potential mesoscale controls on where tornado dissipation may initiate by identifying the near-storm LFC or measuring any stable inversions. It is possible that the recent Targeted Observation by Radars and UAS of Supercells (TORUS) field campaign may have serendipitously collected the necessary observations to investigate these processes already.

### 6.2.2 SimRadar

In addition to observational studies, future modeling studies are required to systematically and experimentally isolate the behavior of debris in tornadoes. Currently,

the most well equipped tool to model TDSs is SimRadar (Cheong et al. 2017), a physically based radar simulator that combines large-eddy simulation (LES), air drag models, and radar cross-section (RCS) measurements of debris. SimRadar allows researchers to investigate how different debris species behave in different realistic tornado flow types (Fig. 6.3) based on air drag models and then provides simulated dual-polarization time series and radar moments for a range of radar setups for mixed debris volumes based on RCS measurements.

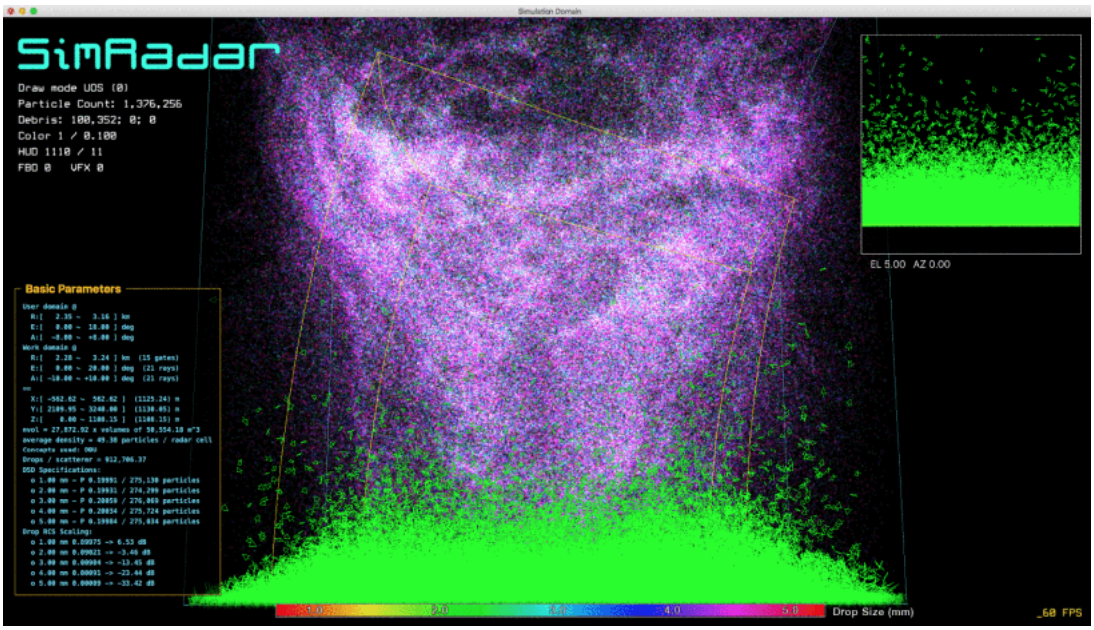


Figure 6.3: Graphical output from SimRadar showing the vertical plane of an LES tornado simulation with lofted raindrops (purple) and leaves (green).

There are a number of model experiments that are motivated by this study. In Chapter 3, observations of locally enhanced $Z_H$ and locally reduced $\rho_{hv}$ were observed in large tornado subvortices, hypothesized to be due to greater debris concentrations and perhaps larger mean debris size. Additionally, negative $Z_{DR}$ was observed at the periphery and in the wake of these subvortices. Preliminary analyses of a high-swirl tornado indicate that the tornado subvortex $Z_H$ signature can be replicated using SimRadar (Fig. 6.4). Orientation analyses, similar to those in Umeyama et al. (2018), should be performed in the future to investigate whether common debris alignment occurs at the periphery

or in the wake of these subvortices. Additionally, lower $\rho_{hv}$ was observed in downdrafts compared to updrafts in the Moore-Choctaw tornado. SimRadar should be used to investigate the differential sedimentation of debris species within tornado updrafts and downdrafts.

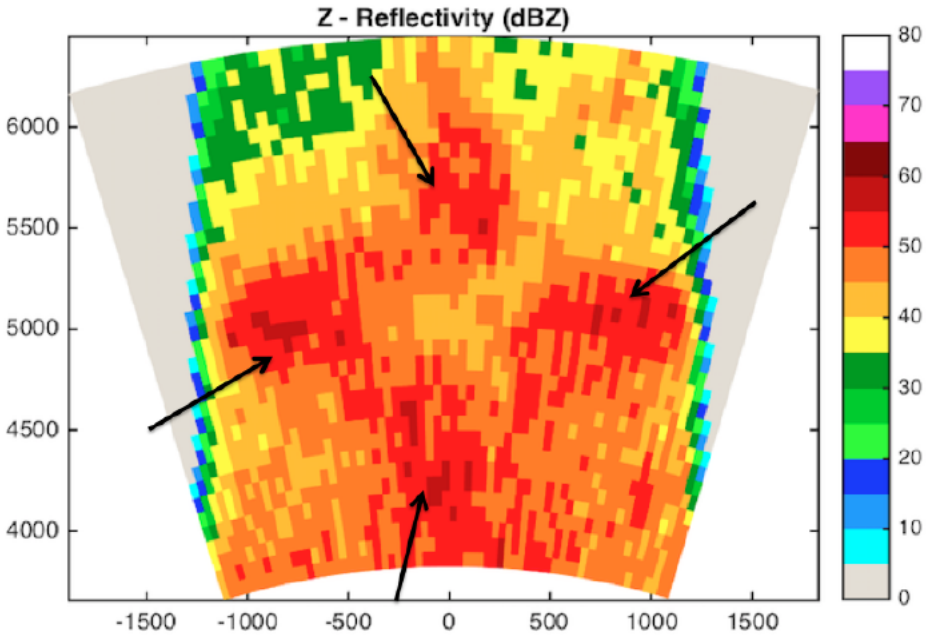


Figure 6.4: Simulated $Z_H$ for a high-swirl LES. Arrows indicate the position of large tornado subvortices.

It was observed in Chapter 4 that the vertical profiles of polarimetric variables became more homogeneous with time and were most vertically homogeneous when the tornado was at maximum intensity. SimRadar should be used to investigate the tornado lifecycle controls on the vertical distribution of debris and whether vertical size sorting of debris becomes less prominent over time in strong tornadoes (e.g., perhaps large debris are lofted to higher altitudes given enough residence time within the tornado updraft). Additionally, the vertical profiles of polarimetric variables should be investigated for different tornado intensities. Perhaps only strong tornadoes are capable of producing vertically homogeneous polarimetric profiles because weaker tornadoes cannot loft large debris to higher elevations.

In Chapter 5, the AIR observed a rapid change from a medium-swirl drowned vortex jump to a low-swirl single-cell vortex. In addition to investigating how swirl ratio controls the distribution of tornadic debris, SimRadar could be used to interrogate the behavior of debris during the transition from one tornado structure to another. Of interest could be the latency between the transition of the vortex from one flow structure to another and the transition of the debris from one distribution to another. It is also possible that the transition from one flow structure to another creates a hybrid debris distribution that is unlike the TDS structure of a steady-state low-, medium-, or -high swirl tornado. These simulations can also be compared to new rapid-scan observations of tornadic debris collected by the PAIR.

## Bibliography


Alderman, E. J., K. K. Droegemeir, and R. P. Davies-Jones, 1999: A numerical simulation of cyclic mesocyclogenesis. *J. Atmos. Sci.*, **56**, 2045–2069.

Alexander, C., and J. Wurman, 2008: Updated mobile radar climatology of supercell tornado structure and dynamics. *Preprints, 24th Conf. on Severe Local Storms, Amer. Meteor. Soc.*, Savannah, GA.

Ashley, W. S., and S. M. Stradler, 2016: Recipe for disaster: How the dynamic ingredients of risk and exposure are changing the tornado disaster landscape. *Bull. Amer. Meteor. Soc.*, **97**, 767–786.

Atkins, N. T., A. McGee, R. Ducharme, R. M. Wakimoto, and J. Wurman, 2012: The LaGrange tornado during VORTEX2. Part II: Photogrammetric analysis of the tornado combined with dual-Doppler radar data. *Mon. Wea. Rev.*, **140**, 2939–2958.

Balakrishnan, N., and D. S. Zrnić, 1990: Use of polarization to characterize precipitation and discriminate large hail. *J. Atmos. Sci.*, **47**, 1525–1540.

Barnes, S., 1964: A technique for maximizing details in numerical weather map analysis. *J. Appl. Meteor.*, **3**, 396–409.

Barnes, S., 1973: *Mesoscale Objective Map Analysis Using Weighted Time-Series*. NOAA TM ERL NSSL.

Bluestein, H., M. French, I. PopStefanija, R. Bluth, and J. Knorr, 2010: A mobile, phased-array Doppler radar for the study of severe convective storms. *Bull. Amer. Meteor. Soc.*, **91**, 579–600.

Bluestein, H., and A. Pazmany, 2000: Observations of tornadoes and other convective phenomena with a mobile, 3-mm wavelength, Doppler radar: The spring 1999 field experiment. *Bull. Amer. Meteor. Soc.*, **81**, 2939–2951.

Bluestein, H. B., 2013: *Severe Convective Storms and Tornadoes, Observations and Dynamics*. Springer-Verlag Berlin Heidelberg, 456 pp.

Bluestein, H. B., M. M. French, R. L. Tanamachi, S. Frasier, K. Hardwick, F. Junyent, and A. Pazmany, 2007a: Close-range observations of tornadoes in supercells made with a dual-polarization, X-band, mobile Doppler radar. *Mon. Wea. Rev.*, **135**, 1522–1543.

Bluestein, H. B., W.-C. Lee, M. Bell, C. C. Weiss, and A. L. Pazmany, 2003: Mobile Doppler radar observations of a tornado in a supercell near Bassett, Nebraska, on 5 June 1999. Part II: Tornado-vortex structure. *Mon. Wea. Rev.*, **131**, 2968–2984.

Bluestein, H. B., C. C. Weiss, M. M. French, E. M. Holthaus, R. L. Tanamachi, S. Frasier, and A. L. Pazmany, 2007b: The structure of tornadoes near Attica, Kansas on 12 May 2004: High-resolution, mobile, Doppler radar observations. *Mon. Wea. Rev.*, **135**, 475–506.

Bodine, D. J., M. R. Kumjian, R. D. Palmer, P. L. Heinselman, and A. V. Ryzhkov, 2013: Tornado damage estimation using polarimetric radar. *Wea. Forecasting*, **28**, 139–158.

Bodine, D. J., T. Maruyama, R. D. Palmer, C. J. Fulton, H. B. Bluestein, and D. C. Lewellen, 2016a: Sensitivity of tornado dynamics to debris loading. *J. Atmos. Sci.*, **73**, 2783–2801.

Bodine, D. J., R. Palmer, T. Maruyama, C. Fulton, Y. Zhu, and B. L. Cheong, 2016b: Simulated frequency dependence of radar observations of tornadoes. *J. Atmos. Oceanic Technol.*, **33**, 1825–1842.

Bodine, D. J., R. D. Palmer, and G. Zhang, 2014: Dual-wavelength polarimetric radar analyses of tornadic debris signatures. *J. Appl. Meteor. Climatol.*, **53**, 242–261.

Bohonos, J. J., and D. E. Hogan, 1999: The medical impact of tornadoes in North America. *J. Emerg. Med.*, **17**, 67–73.

Brandes, E. A., 1978: Mesocyclone evolution and tornadogenesis: Some observations. *Mon. Wea. Rev.*, **106**, 635–647.

Brandes, E. A., 1984: Vertical vorticity generation and mesocylcone sustenance in tornadic thunderstorms: The observational evidence. *Mon. Wea. Rev.*, **112**, 2253–2269.

Bringi, V. N., and V. Chandrasekar, 2001: *Polarimetric Doppler Weather Radar: Principles and Applications*. Cambridge University Press, 636 pp.

Brown, R. A., and V. T. Wood, 2012: The tornadic vortex siganture: An update. *Wea. Forecasting*, **27**, 525–530.

Burgers, J. M., 1948: A mathematical model illustrating the theory of turbulence. *Adv. Appl. Mech.*, **1**, 197–199.

Caylor, I. C., and A. J. Illingworth, 1987: Radar observations and modeling of warm rain initiation. *Quart. J. Roy. Meteor. Soc.*, **113**, 1171–1191.

Cheong, B. L., D. J. Bodine, C. J. Fulton, S. M. Torres, T. Maruyama, and R. D. Palmer, 2017: SimRadar: A polarimetric radar time-series simulator for tornadic debris studies. *IEEE Trans. Geosci. Rmote Sens.*, **55**, 2858–2870.

Church, C. R., J. T. Snow, G. L. Baker, and E. M. Agee, 1979: Characteristics of tornado-like vortices as a function of swirl ratio: A laboratory investigation. *J. Atmos. Sci.*, **36**, 1755–1776.

Coffer, B. E., and M. D. Parker, 2017: Simulated supercells in nontornadic and tornadic VORTEX2 environments. *Mon. Wea. Rev.*, **145**, 149–180.

Coleman, T. A., and P. G. Dixon, 2014: An objective anlaysis of tornado risk in the United States. *Wea. Forecasting*, **29**, 366–376.

Conway, J. W., and D. S. Zrnić, 1993: A study of production and hail growth using dual-Doppler and multiparamter radars. *Mon. Wea. Rev.*, **121**, 2511–2528.

Crowe, C. C., C. J. Schultz, L. D. Carey, and W. A. Petersen, 2012: Use of dual-polarization signatures in diagnosing tornadic potential. *Electronic J. Operational Meteor.*, **13**, 57–78.

Dahl, J. M., M. D. Parker, and L. J. Wicker, 2014: Imported and storm-generated near-ground vertical vorticity in a simulated supercell. *J. Atmos. Sci.*, **71**, 3027–3051.

Davies-Jones, R. P., 1986: *Thunderstorm Morphology and Dynamics*. University of Oklahoma Press, 432 pp.

Dawson II, D. T., E. R. Mansell, Y. Jung, L. J. Wicker, M. R. Kumjian, and M. Xue, 2014: Lo-level $Z_{DR}$ signatures in supercell forward flanks: The role of size sorting and melting of hail. *J. Atmos. Sci.*, **71**, 276–299.

Doviak, R. J., and D. S. Zrnić, 1993: *Doppler Radar and Weather Observations*. 2nd ed., Dover Publications, Mineola, New York.

Dowell, D., and H. Bluestein, 2002: The 8 June 1995 McLean, Texas, storm. Part I: Observations of cyclic tornadogenesis. *Mon. Wea. Rev.*, **130**, 2626–2648.

Dowell, D. C., C. R. Alexander, J. M. Wurman, and L. J. Wicker, 2005: Centrifuging of hydrometeors and debris in tornadoes: Radar-reflectivity patterns and wind-measurement errors. *Mon. Wea. Rev.*, **133**, 1501–1524.

French, M., H. Bluestein, I. PopStefanija, C. Baldi, and R. Bluth, 2013: Reexamining the vertical development of tornadic vortex signatures in supercells. *Mon. Wea. Rev.*, **141**, 4576–4601.

French, M., H. Bluestein, I. PopStefanija, C. Baldi, and R. Bluth, 2014: Mobile, phased-array, Doppler radar observations of tornadoes at X band. *Mon. Wea. Rev.*, **142**, 1010–1036.

French, M. M., D. Burgess, E. R. Mansell, and L. Wicker, 2015: Bulk hook echo raindrop sizes retrieved using mobile, polarimatric Doppler radar observations. *J. Appl. Meteor. Climatol.*, **54**, 423–450.

Gall, R. L., 1983: A linear analysis of the multiple vortex phenomenon in simulated tornadoes. *J. Atmos. Sci.*, **40**, 2010–2024.

Griffin, C. B., D. J. Bodine, and R. D. Palmer, 2017: Kinematic and polarimetric radar observations of the 10 May 2010, Moore-Choctaw, Oklahoma, tornadic debris signature. *Mon. Wea. Rev.*, **145**, 2723–2741.

Houser, J., H. Bluestein, and J. Snyder, 2015: Rapid-scan, polarimetric, Doppler radar observations of tornadogenesis and tornado dissipation in a tornadic supercell: The "El Reno, Oklahoma" storm of 24 May 2011. *Mon. Wea. Rev.*, **143**, 2685–2710.

Houser, J. L., H. B. Bluestein, and J. Snyder, 2016: A finescale radar examination of the tornadic debris signature and weak-echo reflectivity band associated with a large, violent tornado. *Mon. Wea. Rev.*, **144**, 4101–4130.

Hubbert, J., V. N. Bringi, L. D. Carey, and S. Bolen, 1998: CSU-CHILL polarimetric measurements from a severe hailstorm in eastern Colorado. *J. Appl. Meteor.*, **37**, 749–755.

Isom, B., and Coauthors, 2013: The Atmospheric Imaging Radar: Simultaneous volumetric observations using a phased array weather radar. *J. Atmos. Ocean. Technol.*, **30**, 655–675.

Joss, J., and A. Waldvogel, 1970: Raindrop size distribution and doppler velocites. *Preprints, 14th Conf. on Radar Meteorology*, Amer. Meteor. Soc., Ed.

Knox, J. A., and Coauthors, 2013: Tornado debris characterisitics and trajectories during the 27 April 2011 super outbreak as determined using social media data. *Bull. Amer. Meteor. Soc.*, **94**, 1371–1380.

Koch, S. E., M. desJardins, and P. J. Kocin, 1983: An interactive Barnes objective map analysis scheme for use with satellite and conventional data. *J. Clim. Appl. Meteor.*, **22**, 1487–1503.

Kosiba, K., and J. Wurman, 2010: The three-dimensional axisymmetric wind field structure of the Spencer, South Dakota, 1998 tornado. *J. Atmos. Sci.*, **67**, 3074–3083.

Kosiba, K. A., R. J. Trapp, and J. Wurman, 2008: An analysis of the axis-symmetric three-dimensional low level wind field in a tornado using mobile radar observations. *Geophys. Res. Lett.*, **35 (L05805)**, 1–6.

Kosiba, K. A., and J. M. Wurman, 2013: The three-dimensional structure and evolution of a tornado boundary layer. *Wea. Forecasting*, **28**, 1552–1561.

Kumjian, M. R., 2011: Precipitation properties of supercell hook echoes. *Electron. J. Severe Storms Meteor.*, **6 (5)**.

Kumjian, M. R., 2013a: Principles and applications of dual-polarization weather radar. Part 1: Description of the polarimetric radar variables. *J. Oper. Meteor.*, **1**, 226–242.

Kumjian, M. R., 2013b: Principles and applications of dual-polarization weather radar. Part 2: Warm and cold season applications. *J. Oper. Meteor.*, **1**, 243–264.

Kumjian, M. R., A. Khain, N. Benmoshe, E. Ilotoviz, A. Ryzhkov, and V. T. Phillips, 2014: The anatomy and physics of $Z_{DR}$ columns: Investigating a polarimetric radar signature with a spectral bin microphysical model. *J. Appl. Meteor. Climatol.*, **53**, 1820–1843.

Kumjian, M. R., J. C. Picca, S. M. Ganson, A. V. Ryzhkov, J. Krause, D. S. Zrnić, and A. Khain, 2010a: Polarimetric radar characteristics of large hail. *Preprints, 25th Conference of Severe Local Storms, Amer. Meteor. Soc., Denver, CO.*

Kumjian, M. R., and A. Ryzhkov, 2010: The impact of evaporation on polarimetric characteristics of rain: Theoretical model and practical implications. *J. Appl. Meteor. Climatol.*, **49**, 1247–1267.

Kumjian, M. R., and A. V. Ryzhkov, 2008: Polarimetric signatures in supercell thunderstorms. *J. Appl. Meteor. Climatol.*, **48**, 1940–1961.

Kumjian, M. R., and A. V. Ryzhkov, 2009: Storm-relative helicity revealed from polarimetric radar measurements. *J. Atmos. Sci.*, **66**, 667–685.

Kumjian, M. R., A. V. Ryzhkov, V. M. Melnikov, and T. J. Schuur, 2010b: Rapid-scan super-resolution observations of a cyclic supercell with a dual-polarization WSR-88D. *Mon. Wea. Rev.*, **138**, 3762–3786.

Kurdzo, J. M., D. J. Bodine, B. L. Cheong, and R. D. Palmer, 2015: High-temporal resolution polarimetric X-band Doppler radar observations of the 20 May 2013 Moore, Oklahoma tornado. *Mon. Wea. Rev.*, **143**, 2711–2735.

Kurdzo, J. M., B. L. Cheong, R. D. Palmer, G. Zhang, and J. Meier, 2014: A pulse compression waveform for improved-sensitivity weather radar observations. *J. Atmos. Oceanic Technol.*, **31**, 2713–2731.

Kurdzo, J. M., and Coauthors, 2017: Observations of severe local storms and tornadoes with the Atmospheric Imaging Radar. *Bull. Amer. Meteor. Soc.*, **98**, 915–935.

Lee, W. C., B. J.-D. Jou, P.-L. Chang, and S.-M. Deng, 1999: Tropical cyclone kinematic structure retrieved from single-Doppler radar observations. Part I: Doppler velocity patterns and the GBVTD technique. *Mon. Wea. Rev.*, **127**, 2419–2439.

Lee, W.-C., and J. Wurman, 2005: Diagnosed three-dimensional axisymmetric structure of the Mulhall tornado on 3 May 1999. *J. Atmos. Sci.*, **62**, 2373–2393.

Lemon, L. R., and C. A. Doswell, 1979: Severe thunderstorm evolution and mesocyclone structure as related to tornadogenesis. *Mon. Wea. Rev.*, **107**, 1184–1197.

Leslie, L. M., 1971: The development of concentrated vorticies: A numerical study. *J. Fluid Mech.*, **48**, 1–21.

Lewellen, D. C., B. Gong, and W. S. Lewellen, 2004: Effects of debris on near-surface tornado dynamics. *22nd Conf. on Severe Local Storms, Hyannis, MA, Amer. Meteor. Soc.*

Lewellen, D. C., B. Gong, and W. S. Lewellen, 2008: Effects of finescale debris on near-surface tornado dynamics. *J. Atmos. Sci.*, **65**, 3247–3262.

Lewellen, D. C., and W. S. Lewellen, 2007a: Near-surface intensification of tornado vorticies. *J. Atmos. Sci.*, **64**, 2176–2194.

Lewellen, D. C., and W. S. Lewellen, 2007b: Near-surface vortex intensification through corner flow collapse. *J. Atmos. Sci.*, **64**, 2195–2209.

Lewellen, D. C., W. S. Lewellen, and J. Xia, 2000: The influence of a local swirl ratio on tornado intensification near the surface. *J. Atmos. Sci.*, **57**, 527–544.

Loeffler, S. D., and M. R. Kumjian, 2018: Quantifying the separation of enhanced $Z_{DR}$ and $K_{DP}$ regions in nonsupercell tornadic storms. *Wea. Forecasting*, **33**, 1143–1157.

Magsig, M. A., and J. T. Snow, 1998: Long-distance debris transport by tornadic thunderstorms. Part I: The 7 May 1995 supercell thunderstorm. *Mon. Wea. Rev.*, **126**, 1430–1449.

Mahre, A., J. M. Kurdzo, D. J. Bodine, C. B. Griffin, R. D. Palmer, and T.-Y. Yu, 2018: Analysis of the 16 May 2015 Tipton, Oklahoma, EF-3 tornado at high spatiotemporal resolution using the Atmospheric Imaging Radar. *Mon. Wea. Rev.*, **146**, 2103–2124.

Majcen, M., P. Markowski, Y. Richardson, D. Dowell, and J. Wurman, 2008: Mulipass objective analyses of Doppler radar data. *J. Atmos. Ocean. Technol.*, **25**, 1845–1858.

Markowski, P. M., 2002: Hook echoes and rear-flank donwdrafs: A review. *Mon. Wea. Rev.*, **130**, 852–876.

Markowski, P. M., J. M. Straka, and E. N. Rasmussen, 2002: Direct surface thermodynamic observations within the rear-flank downdrafts of nontornadic and tornadic supercells. *Mon. Wea. Rev.*, **130**, 1692–1721.

Marquis, J., Y. Richardson, P. Markowski, D. Dowell, and J. Wurman, 2012: Tornado maintenance investigated with high-resolution dual-Doppler and EnKF analysis. *Mon. Wea. Rev.*, **140**, 3–27.

Marquis, J., Y. Richardson, P. Markowski, J. Wurman, K. Kosiba, and P. Robinson, 2016: An investigation of the Goshen County, Wyoming, tornadic supercell of 5 June 2009 using EnKF assimilation of mobile mesonet and radar observations collected during VORTEX2. Part II: Mesocyclone-scale processes affecting tornado formation, mainenance, and decay. *Mon. Wea. Rev.*, **144**, 3441–3463.

Marquis, J., Y. Richardson, J. Wurman, and P. Markowski, 2008: Single- and dual-Doppler analysis of a tornadic vortex and surrounding storm scale flow in the Crowell, TX, supercell of 30 April 2000. *Mon. Wea. Rev.*, **136**, 5017–5043.

Mead, J., G. Hopcraft, S. J. Frasier, B. D. Pollar, C. D. Cherry, D. H. Schaubert, and R. E. McIntosh, 1998: A volume-imaging radar wind profiler for atmospheric boundary layer turbulence studies. *J. Atmos. Oceanic Technol.*, **15**, 849–859.

NCDC, 2015: *Billion-dollar weather and climate disasters: Overview.* [Available online at http://www.ncdc.noaa.gov/billions/.], National Climatic Data Center.

Nolan, D. S., 2013: On the use of Doppler radar-derived wind fields to diagnose the secondary circulations of tornadoes. *J. Atmos. Sci.*, **70**, 1160–1171.

Oye, R., C. Mueller, and S. Smith, 1995: Software for radar translation, visualization, editing, and interpolation. *Preprints, 27th Conf. on Radar Meteorology, Vail, CO, Amer. Meteor. Soc., 359–361.*

Palmer, R. D., and Coauthors, 2011: The 10 May 2010 tornado outbreak in central Oklahoma: Potential for new science with high-resolution polarimetric radar. *Bull. Amer. Meteor. Soc.*, **92**, 871–891.

Park, H., A. Ryzhkov, D. Zrnić, and K. Kim, 2009: The hydrometeor classification algorithm for the polarimetric wsr-88d: Description and application to an mcs. *Wea. Forecasting*, **24**, 730–748.

Pauly, P. M., and X. Wu, 1990: The theoretical, discrete, and actual response of the Barnes objective scheme for one- and two-dimensional fields. *Mon. Wea. Rev.*, **118**, 1145–1163.

Pazmany, A., J. Mead, H. Bluestein, J. Snyder, and J. Houser, 2013: A mobile rapid-scanning X-band polarimetric (RaXPol) Doppler radar system. *J. Atmos. Ocean. Technol.*, **30**, 1398–1413.

Potvin, C., D. Betten, L. Wicker, K. Elmore, and M. Biggerstaff, 2012: 3DVAR versus traditional dual-doppler wind retrievals of a simulated supercell thunderstorm. *Mon. Wea. Rev.*, **140**, 3487–3494.

Rankine, W. J. M., 1882: *A Manual of Applied Physics.* 10th ed., Charles Griffin & Co., 663 pp.

Rasmussen, E., and J. Straka, 2007: Evolution of low-level angular momentum in the 2 June 1995 Dimmitt, Texas, tornado cyclone. *J. Atmos. Sci.*, **64**, 1365–1378.

Rasmussen, E. N., J. M. Straka, R. P. Davies-Jones, C. A. Doswell, F. H. Carr, M. D. Eilts, and D. R. MacGorman, 1994: Vertification of the Origins of Rotation in Tornadoes Experiment: VORTEX. *Bull. Amer. Meteor. Soc.*, **75**, 995–1006.

Romine, G. S., D. W. Burgess, and R. B. Wilhelmson, 2008: A dual-polairzation-radar-based assessment of the 8 May 2003 Oklahoma City area tornadic supercell. *Mon. Wea. Rev.*, **136**, 2849–2870.

Rotunno, R., 1978: A note on the stability of a cylindrical vortex sheet. *J. Fluid Mech.*, **87**, 761–771.

Rotunno, R., 1986: Tornadoes and tornadogenesis. *Mesoscale Meteorology and Forecasting*, 414–436.

Ryzhkov, A., D. Burgess, D. Zrnić, T. Smith, and S. Giangrande, 2002: Polarimetric analysis of a 3 May 1999 tornado. *Preprints, 21th Conf. on Severe Local Storms*, Amer. Meteor. Soc., Ed., San Antonio, TX.

Ryzhkov, A. V., M. R. Kumjian, and S. M. Ganson, 2013: Polarimetric radar characteristics of melting hail. Part I: Theoretical simulations using spectral microphysical modleing. *J. Appl. Meteor. Climatol.*, **52**, 2849–2870.

Ryzhkov, A. V., T. J. Schuur, D. W. Burgess, P. L. Heinselman, S. E. Giangrande, and D. S. Zrnić, 2005a: The joint polarization experiment: Polarmetric rainfall measurements and hydrometeor classification. *Bull. Amer. Meteor. Soc.*, **86**, 809–824.

Ryzhkov, A. V., T. J. Schuur, D. W. Burgess, and D. S. Zrnić, 2005b: Polarimetric tornado detection. *J. Appl. Meteor.*, **44**, 557–570.

Saari, M. D., R. M. Lawton, C. J. Schultz, and L. D. Carey, 2014: Early characteristics of the polarimetric tornadic debris signature associated with the 20 May 2013 Newcastle-Moore, Oklahoma, tornado. *J. Oper. Meteor.*, **2**, 110–114.

Salazar-Cerreño, J. L., and Coauthors, 2017: Development of a mobile C-band polarimetric atmospheric imaging radar(PAIR). *97th AMS Annual Meeting*, Seattle, WA, Amer. Meteor. Soc.

Schueth, A., and C. C. Weiss, 2018: Comparing observations and simulations of the streamwise vorticity current in a tornadic supercell storm. *Preprints, 29th Conference of Severe Local Storms, Amer. Meteor. Soc., Stowe, VT.*

Schultz, C. J., and Coauthors, 2012a: Dual-polarization tornadic debris signatures Part I: Examples and utility in an operational setting. *Electronic J. Operational Meteor.*, **13**, 120–137.

Schultz, C. J., and Coauthors, 2012b: Dual-polarization tornadic debris signatures Part II: Comparisons and caveats. *Electronic J. Operational Meteor.*, **13**, 138–158.

Schwarz, C. M., and D. W. Burgess, 2011: Supercell polarimetric signatures at X-band: Data from VORTEX2. *35th Conf. on Radar Meteorology*, Amer. Meteor. Soc., Ed., 7B.4.

Seliga, T. A., and V. N. Bringi, 1976: Potential use of radar differential reflectivity measurements at orthogonal polarizations for measuring precipitation. *J. Appl. Meteor.*, **15**, 69–76.

Skow, K. D., and C. Cogil, 2017: A high-resolution aerial survey and radar analysis of quasi-linear convective system surface vortex damage paths from 31 August 2014. *Wea. Forecasting*, **32**, 441–467.

Smith, R. K., and L. M. Leslie, 1978: Tornadogenesis. *Quart. J. Roy. Meteor. Soc.*, **104**, 189–199.

Snow, J. T., A. L. Wyatt, A. K. McCarthy, and E. K. Bishop, 1995: Fallout of debris from tornadic thunderstorms: A historical perspective and two examples from VORTEX. *Bull. Amer. Meteor. Soc.*, **76**, 1777–1790.

Snyder, J., and H. Bluestein, 2014: Some considerations for the use of high-resolution mobile radar data in tornado intensity determination. *Wea. Forecasting*, **29**, 799–827.

Snyder, J. C., H. B. Bluestein, D. T. Dawson II, and Y. Jung, 2017: Simulations of polarimetric, X-band radar signatures in supercells. Part II: $Z_{DR}$ columns and rings and $K_{DP}$ columns. *J. Appl. Meteor. Climatol.*, **56**, 2001–2026.

Snyder, J. C., and A. V. Ryzhkov, 2015: Automated detection of polarimetric tornado debris signatures using a hydrometeor classification algorithm. *J. Appl. Meteor. Climatol.*, **54**, 1861–1870.

Straka, J. M., E. N. Rasmussen, R. P. Davies-Jones, and P. M. Markowski, 2007: An observational and idealized numerical examination of low-level counter-rotating vortices toward the rear flank of supercells. *Electronic J. Severe Storms Meteor.*, **2**, 1–22.

Sullivan, R. D., 1959: A two-cell vortex solution of the Navier-Stokes euqations. *J. Aerospace Sci.*, **26**, 767–768.

Tanamachi, R. L., H. B. Bluestein, J. B. Houser, S. J. Frasier, and K. M. Hardwick, 2012: Mobile X-band, polarimetric Doppler radar observations of the 4 May 2007 Greensburg, Kansas, tornadic supercell. *Mon. Wea. Rev.*, **140**, 2103–2125.

Tanamachi, R. L., H. B. Bluestein, W. C. Lee, M. Bell, and A. L. Pazmany, 2007: Ground-based velocity track display (GBVTD) analysis of W-band radar data in a tornado near Stockton, Kansas on 15 May 1999. *Mon. Wea. Rev.*, **135**, 783–800.

Tanamachi, R. L., H. B. Bluestein, M. Xue, W. C. Lee, K. Orzel, S. Frasier, and R. M. Wakimoto, 2013: Near-surface vortex structure in a tornado and in a sub-tornado-strength convective-storm vortex observed by a mobile, W-band radar during VORTEX2. *Mon. Wea. Rev.*, **141**, 3661–3690.

Tanamachi, R. L., and P. L. Heinselman, 2016: Rapid-scan, polarimetric observations of central Oklahoma severe storms on 31 May 2013. *Wea. Forecasting*, **31**, 19–42.

Taylor, G. I., 1938: The spectrum of turbulence. *Proc. Roy. Soc. London*, **A164**, 476–490.

Trapp, R. J., and R. P. Davies-Jones, 1997: Tornadogenesis with and without a dynamic pipe effect. *J. Atmos. Sci.*, **54**, 113–133.

Umeyama, A., B. L. Cheong, S. Torres, and D. Bodine, 2018: Orientation analysis of simulated tornadic debris. *J. Atmos. Oceanic Technol.*, **35**, 993–1010.

Van Den Broeke, M. S., 2015: Polarimetric tornadic debris signature variability and debris fallout signatures. *J. Appl. Meteor. Climatol.*, **54**, 2389–2405.

Van Den Broeke, M. S., 2017: Polarimetric radar metrics related to tornado life cycles and intensity in supercell storms. *Mon. Wea. Rev.*, **145**, 3671–3686.

Van Den Broeke, M. S., and S. T. Jauernic, 2014: Spatial and temporal characteristics of polarimetric tornadic debris signatures. *J. Appl. Meteor. Climatol.*, **53 (10)**, 2217–2231.

Vivekanandan, J., D. S. Zrnić, S. M. Ellis, D. Oye, A. V. Ryzhkov, and J. Straka, 1999: Cloud microphysics retrieval using S-band dual-polarization radar measurements. *Bull. Amer. Meteor. Soc.*, **80**, 381–388.

Wakimoto, R. M., N. T. Atkins, K. M. Butler, H. B. Bluestein, K. Thiem, J. Snyder, and J. Houser, 2015: Photogrammetric analysis of the 2013 El Reno tornado combined with mobile X-band polarimetric radar data. *Mon. Wea. Rev.*, **143**, 2657–2683.

Wakimoto, R. M., and C. Liu, 1998: The Garden City, Kansas, storm during VORTEX 95. Part II: The wall cloud and tornado. *Mon. Wea. Rev.*, **126**, 393–408.

Wakimoto, R. M., P. Stauffer, W. C. Lee, N. T. Atkins, and J. Wurman, 2012: Finescale structure of the LaGrange, Wyoming tornado during VORTEX2: GBVTD and photogrammetric analyses. *Mon. Wea. Rev.*, **140**, 3397–3418.

Wakimoto, R. M., Z. Wienhoff, H. B. Bluestein, and D. Reif, 2018: The Dodge City tornadoes on 24 May 2016: Damage survey, photogrammetric analysis combined with mobile polarimetric radar data. *Mon. Wea. Rev.*, **146**, 3735–3771.

Wakimoto, R. M., and Coauthors, 2016: Areal damage survey of the 2013 El Reno tornado combined with mobile radar data. *Mon. Wea. Rev.*, **144**, 1749–1776.

Wang, Y., and T. Yu, 2015: Novel tornado detection using an adaptive neuro-fuzzy system with S-band polarimetric weather radar. *J. Atmos. Oceanic Technol.*, **32**, 195–208.

WDTB, 2013: *Dual-polarization radar training.* [Available online at http://www.wdtb.noaa.gov/courses/dualpol/index. html.], National Weather Service Warning Decision Training Branch.

Weiss, C. C., T. Cermak, R. Metzger, A. Reinhart, and P. Skinner, 2014: Insights into tornado structure afforded by high-frequency mobile radar. *27th Conference on Severe Local Storms, Madison, Wisconsin, American Meterological Society, P9.4.*

Wicker, L. J., and R. B. Wilhelmson, 1995: Simulation and analysis of tornado development and decay within a three-dimensional supercell thunderstorm. *J. Atmos. Sci.*, **52**, 2675–2703.

Wurman, J., 2002: The multiple-vortex structure of a tornado. *Wea. Forecasting*, **17**, 473–505.

Wurman, J., and S. Gill, 2000: Fine-scale radar observations of the Dimmitt, Texas (2 June 1995), tornado. *Mon. Wea. Rev.*, **128**, 2135–2164.

Wurman, J., and K. Kosiba, 2013: Finescale radar observations of tornadoes and mesocyclone structures. *Wea. Forecasting*, **28**, 1157–1174.

Wurman, J., K. Kosiba, and P. Robinson, 2013: In situ, Doppler radar, and video observations of the interior structure of a tornado and the wind-damage relationship. *Bull. Amer. Meteor. Soc.*, **94**, 835–846.

Wurman, J., and M. Randall, 2001: An inexpensive, mobile, rapid-scan radar. *Preprints, 30th Int. Conf. on Radar Meteorology, Munich, Germany, American Meteorological Society, P3.4.*

Wurman, J., Y. Richardson, C. Alexander, S. Weygandt, and P. F. Zhang, 2007: Dual-Doppler and single-Doppler analysis of a tornadic storm undergoing mergers and repeated tornadogenesis. *Mon. Wea. Rev.*, **135**, 736–758.

Wurman, J., J. Straka, and E. Rasmussen, 1996: Fine-scale Doppler radar observations of tornadoes. *Science*, **272**, 1774–1777.

Yu, T., and Coauthors, 2015: MRI: Development of a mobild C-band polarimetric imaging radar. *National Science Foundation Proposal*, 1–15.

Zrnić, D., and Coauthors, 2007: Agile-beam phased array radar for weather observations. *Bull. Amer. Meteor. Soc.*, **88**, 1753–1766.

Zrnić, D. S., and A. V. Ryzhkov, 1999: Polarimetry for weather surveillance radars. *Bull. Amer. Meteor. Soc.*, **80**, 389–406.

Appendix

# Appendix A

## List of Acronyms

| | |
|---|---|
| AIR | Atmospheric Imaging Radar |
| AHI | Azimuth Height Indicator |
| AGL | Above Ground Level |
| ARL | Above Radar Level |
| ARRC | Advanced Radar Research Center |
| CAPPI | Constant-Altitude Plan Position Indicator |
| DDC | Dodge City, Kansas |
| DPE | Dynamic Pipe Effect |
| EF | Enhanced Fujita |
| GBVTD | Ground-Based Velocity Track Display |
| HYSPLIT | Hybrid Single-Particle Lagrangian Integrated Trajectory |
| LES | Large-Eddy Simulation |
| LFC | Level of Free Convection |
| MWR-05XP | Meteorological Weather Radar 2005 X-band Phased Array |
| OPAWS | Observation Processing and Wind Synthesis |
| OU-PRIME | University of Oklahoma's Polarimetric Radar for Innovations in Meteorology and Engineering |
| PAIR | Polarimetric Atmospheric Imaging Radar |
| PPI | Plan Position Indicator |
| RaXPol | Rapid-Scanning, X-band, Polarimetric Doppler Radar |
| RCS | Radar Cross-Section |
| RHI | Range Height Indicator |
| RFD | Rear-Flank Downdraft |
| RFGF | Rear-Flank Gust Front |

| | |
|---|---|
| RFGFS | Rear-Flank Gust Front Surge |
| RMW | Radius of Maximum Winds |
| SNR | Signal-to-Noise Ratio |
| SRH | Storm-Relative Helicity |
| STSR | Simultaneous Transmit Simultaneous Receive |
| TDS | Tornadic Debris Signature |
| UTC | Coordinated Universal Time |
| VCP | Volume Coverage Pattern |
| WEC | Weak Echo Column |
| WEH | Weak Echo Hole |
| WSR-88D | Weather Surveillance Radar 1988 Doppler |

# Appendix B

## List of Symbols

| | |
|---|---|
| $C_{max}$ | Specified maximum flow-relative radially outward velocity estimate (m $s^{-1}$) |
| $K_{DP}$ | Specific Differential Phase (° $km^{-1}$) |
| $r$ | Radius from tornado center (m) |
| $u$ | Radial velocity (m $s^{-1}$) |
| $U$ | True radial wind velocity (m $s^{-1}$) |
| $U_{bias}$ | Radial velocity bias introduced by debris centrifuging (m $s^{-1}$) |
| $U_{mod}$ | Biased radial wind velocity (m $s^{-1}$) |
| $v$ | Tangential velocity (m $s^{-1}$) |
| $V_r$ | Radial velocity (m $s^{-1}$) |
| $V_{dual}$ | Dual-Doppler derived tangential velocity (m $s^{-1}$) |
| $V_{single}$ | Single-Doppler derived tangential velocity (m $s^{-1}$) |
| $Z_{DR}$ | Differential reflectivity (dB) |
| $Z_H$ | Radar reflectivity factor at horizontal polarization (dBZ) |
| $\delta$ | Limiting spatial resolution (m) |
| $\Delta$V | Differential velocity (m $s^{-1}$) |
| $\gamma$ | Second-pass convergence parameter |
| $\kappa$ | Smoothing Parameter ($km^2$) |
| $\Phi_{DP}$ | Differential Phase (°) |
| $\rho_{hv}$ | Co-polar cross-correlation coefficient |
| $\zeta$ | Vertical vorticity ($s^{-1}$) |